Acoustical Physics, Vol. 49, No. 3, 2003, pp. 241–262. Translated from Akusticheskiĭ Zhurnal, Vol. 49, No. 3, 2003, pp. 293–317.

Noise Control Problems of Passenger Airplanes (A Review)

V. M. Kuznetsov

State Research Center Zhukovskiĭ Central Aerohydrodynamics Institute, ul. Radio 17, Moscow, 105005 Russia

e-mail: vmkuznetsov@mtu-net.ru

Received May 30, 2002

Abstract—The consequences of the introduction of new international standards and regulations that impose limitations on the community noise of passenger airplanes and restrict the operation of noisy airplanes are analyzed. The need in developing new methods for reducing the aircraft noise is stated. The main noise sources inherent in passenger airplanes of different types are considered. The ways of increasing the efficiency of noise-suppressing systems used in power plants and the ways of reducing the intensity of airplane noise sources are determined. The methods for reducing the noise both inside and outside an airplane are described. © *2003 MAIK "Nauka/Interperiodica".*

INTRODUCTION

The problems of noise control in aviation, which arose in the middle of the twentieth century with the beginning of intense operation of jet airliners, are still quite topical and form an important part of the global environmental concerns of humanity. In recent years, the growing public resentment towards the adverse effects of aircraft noise on local communities has resulted in setting new international standards that impose stronger limitations on the noise produced by passenger airplanes in the residential areas near airports. The passenger airplanes designed in the last few years are less noisy, as compared to the airplanes designed at the early stage of passenger aviation. However, because of the growth of the total amount of air conveyances and the increasing intensity of airplane operation, the environmental conditions near airports cannot be noticeably improved and may even become worse in the next ten years, if no considerable progress is achieved in the development of technologies for noise control in aviation [1, 2]. For the Russian specialists in aviation acoustics, the problem of primary concern is to provide the competitive ability of Russian airliners from the viewpoint of community noise they produce, as well as from the viewpoint of the acoustic comfort in their cabins.

INTERNATIONAL REQUIREMENTS FOR THE NOISE OF SUBSONIC PASSENGER AIRPLANES

The problem of reducing the level of aviation noise is one of the main aviation-related environmental problems and is of primary concern to international environmental and aviation organizations. The noise levels in airport areas are regulated by the requirements of Annex 16 of the ICAO (International Civil Aviation Organization) Standard and, in Russia, additionally, by the AP-36 Aviation Rules, which determine the standard noise levels depending on the date of application for the airworthiness certificate of a given aircraft.

The standards for the community noise are set depending on the maximal take-off mass of an airplane and specified for three fixed reference points near the runway. These points characterize the main stages of the flight: the take-off, for which the reference point is at the side of the runway, and the climb and descent, for which the reference points lie on the runway axis (Fig. 1). The standard noise requirements are expressed as effective perceived noise levels (EPNL) with allowance for the noise spectral composition and duration. If the application for the airworthiness certificate was submitted before October 1977, the requirements formulated in Chapter 2 of Annex 16 of the ICAO Standard are in effect; if the application was submitted later, more stringent requirements formulated in Chapter 3 of the same document should be met (Fig. 2). The modern

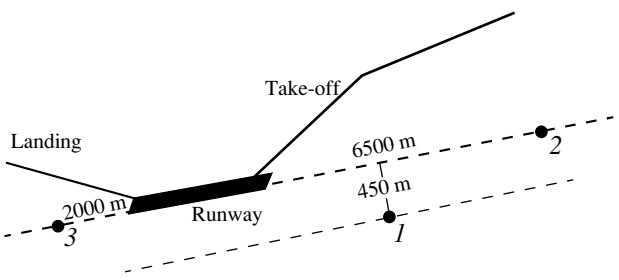

Fig. 1. Reference points on the ground near the runway for the acoustic certification.

1063-7710/03/4903-0241$24.00 © 2003 MAIK "Nauka/Interperiodica"

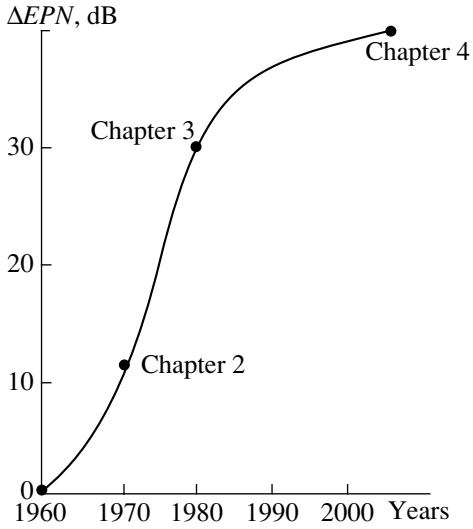

Fig. 2. Growing requirements for the community noise of airplanes.

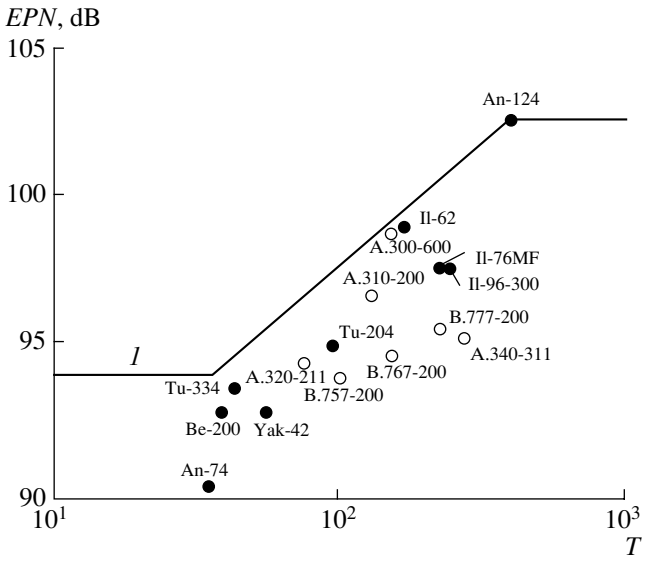

Fig. 3. Airplane noise levels at reference point 1 lying at the side of the runway. (*1*) The solid line displays the requirements of Chapter 3 of the ICAO Standard.

Russian airplanes, Il-96-300 and Tu-204 with PS-90A Russian engines, which were accepted for regular flights in the 1990s, had been designed to satisfy the community noise standards of Chapter 3 (Fig. 3).

In 2001, the ICAO issued a new standard for aircraft noise, which comes into effect on January 1, 2006 and imposes more stringent requirements on the community noise; i.e., the new standard of Chapter 4 of Annex 16 will be introduced. According to this standard, the noise levels from a new airplane, when summarized over three reference points, must be 10 EPN dB lower than the allowable noise levels given in Chapter 3 (Fig. 2). In addition, the decrease in the noise levels at any two points of measurement should be no less than 2 EPN dB. The purpose of the new standard is a further decrease in the community noise near airports.

For the same purpose, resolution A.28.3 of the ICAO assembly prohibits the use of airplanes that do not meet the noise standards of Chapter 3 or that only meet the requirements of Chapter 2. This prohibition has been in effect since April 1, 2002. The ICAO committee on aviation-caused environmental problems is also considering the possibilities for a gradual exclusion of airplanes that meet the requirements of Chapter 3 with a narrow noise level margin. The European Community passed a resolution that limits the use of airplanes modified and recertified as complying with the requirements of Chapter 3. These are the airplanes whose acoustic characteristics were improved to fit the standards of Chapter 3 after a modification of their power plants, but such airplanes still remain noisier than modern passenger airplanes. The resolution introduces rules of operation that prevent the adverse effects of, e.g., old foreign airplanes, on the acoustic conditions in European airports.

Thus, the decisions taken by the ICAO in 2001 and imposing more stringent requirements on the aviation noise result in various kinds of limitations and bans that have been introduced by international organizations to prevent the operation of noisy airplanes in airports. Obviously, the imposition of more stringent requirements on the community noise levels of airplanes is in line with the general prospects of air transport development. Therefore, the solution of the complex scientific and engineering problems related to the improvement of the acoustic characteristics of passenger airplanes is the major task of today's aviation acoustics.

NOISE OF A SUBSONIC JET AIRPLANE

The community noise levels of subsonic passenger airplanes gradually decreased over the last 30–35 years (Fig. 4). This decrease was achieved on the basis of an increase in the efficiency of the fuel consumption and a decrease in the noise generated by the high-velocity exhaust jets of the engines. The main noise sources of a modern by-pass turbojet engine are the jet and the fan, while the internal combustion chamber and the turbine stages usually make a smaller contribution to the total noise produced by the engine.

A decrease in the noise intensity is obtained with the help of engineering developments and the use of effective means of sound absorption in the ducts of the power plants [3–5]. For example, a noise reduction in by-pass turbojet engines with a low by-pass ratio $m < 2$ (where m is the ratio of the gas flow rate through the outer duct to the gas flow rate through the inner duct) was achieved by using a common mixing chamber for the high-velocity outer and low-velocity inner flows,

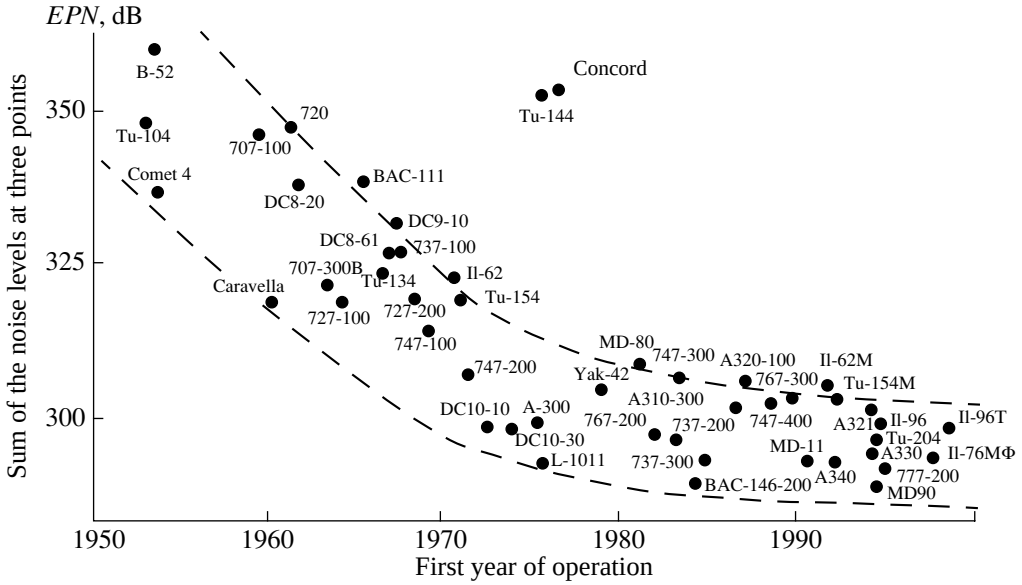

Fig. 4. Tendency for a decrease in the community noise levels of airplanes.

i.e., through a reduction of the exhaust velocity of the engine (Fig. 5).

A substantial decrease in the aircraft noise levels was obtained with the appearance of by-pass turbojet engines with high by-pass ratios $m = 5–8$ and relatively low exhaust velocities of jets. Since, for the engines of latest designs, the exhaust jet is no longer the main source of noise, a further reduction of aircraft noise is mainly related to the suppression of noise generated at the engine inlet or to a balanced noise suppression (in the inlet duct, chevron nozzles, flow mixers, and the engine exhaust) [6–8].

The noise of the engine fan is determined by the inhomogeneities of the oncoming flow interacting with hard surfaces and contains two components: the discrete tones due to the interaction of the wakes of the rotor and stator blades and the broadband noise generated by the turbulent oncoming flow. In modern engines, a decrease in the fan noise is achieved owing to the optimization of the blade shape, the limitation of the number of inlet guide vanes, the decrease in both rate of rotation and number of blades, the optimal combination of the fan blades with the stator blades, and, hence, the reduction of the effects of interactions between the rotating blades and the flow inhomogeneities and between the inhomogeneous flows and the stator blades.

The noise intensity at the engine inlet can be reduced by introducing a sound-absorbing treatment in the air intake ducts, which consists of sound-absorbing structures tuned to the absorption of the fan noise (Fig. 6a). These structures have been repeatedly improved in order to raise their efficiency, to simplify their manufacture technology, and to reduce their weight. The importance of investigations aimed at the development of noise suppression systems of high acoustic efficiency for the ducts of power plants is determined by the necessity for the Russian airliners to satisfy the new severe requirements imposed by the ICAO on the aircraft noise, because it is the necessary condition for their operation at international airports [9, 10].

NOISE SUPPRESSION SYSTEMS FOR POWER PLANTS

In the ducts of the power plants of airplanes with by-pass turbojet engines, such as the widely used Tu-154M (Fig. 5a), sound-absorbing structures (SASs) in the form of one- or two-layer honeycomb sandwiches of the resonance type with perforated panels are commonly used (Fig. 6). The geometric parameters of the SAS (the height of the honeycomb filler, the perforation percentage, the hole diameter, and the thickness of the face panel) are chosen so as to provide the maximum noise suppression at the blade frequency of the fan impeller ($1.5 < f < 2.5$ kHz). However, when this noise component is suppressed, its harmonics with frequencies up to 5–6 kHz persist in the community noise of the airplane. A further increase in the efficiency of SASs, which is dictated by the ever-increasing requirements for the aircraft noise, necessarily involves the suppression of the high-frequency noise components, which correspond to the second and third harmonics of the blade frequency of the fan impeller, without reducing the efficiency of noise suppression at the fundamental frequency. To reduce the levels of the high-frequency noise components, it is necessary to use multiparameter SASs with an improved acoustic efficiency [11, 12].

The single-layer resonance-type SASs widely used in aircraft power plants have a number of disadvan-

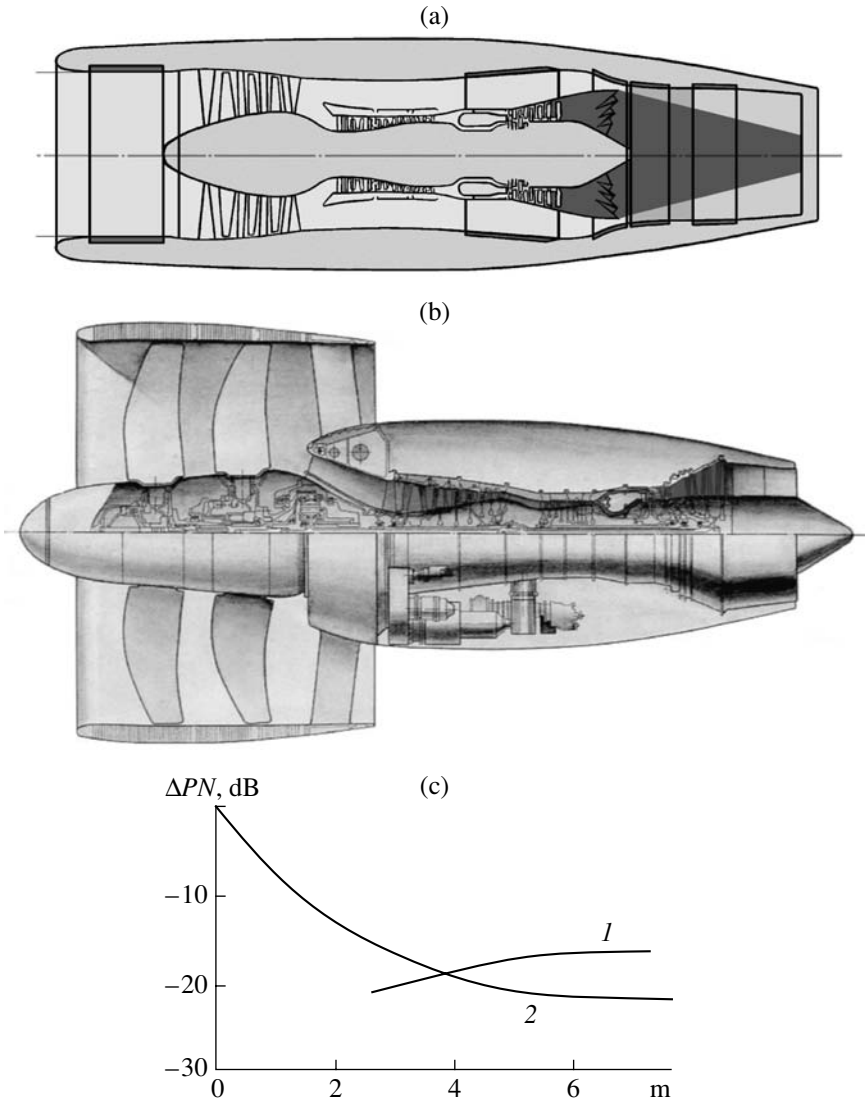

Fig. 5. Examples of engine designs with (a) low and (b) high by-pass ratios. (c) Dependence of noise produced by (*1*) the fan with a noise suppressing system and (*2*) the jet on the by-pass ratio.

tages. In addition to the insufficiently wide absorption band, they exhibit a dependence on the sound pressure level and, hence, on the engine operation mode. Evidently, single-layer honeycomb SASs cannot reduce the power plant noise to a level that complies with the new severe requirements for the aircraft noise and the limitations for the airplane operation. Therefore, in the last few years, the research and production enterprises of the aviation industry were working on the scientific and engineering problems concerned with the increase in the efficiency of noise-suppressing systems for aircraft engines.

One of the main reserves for raising the efficiency of noise suppression in the engine ducts is the increase in the sound attenuation at the fundamental blade frequency of the fan impeller and its harmonics and the simultaneous extension of the attenuation band to higher frequencies without any changes in the length of the treatment (SAS) along the duct axis. An increase in the attenuation at a fixed frequency can be achieved, on the one hand, by choosing the parameters of the SAS on the basis of a detailed study of the field structure in the duct and, specifically, with allowance for the parameters of the boundary layer and the real velocity profile; on the other hand, it can be achieved by making the conditions of sound propagation more complicated: for example, various inserts treated with sound-absorbing material and oriented along the duct can be introduced into the latter. The attenuation band can be extended by using more complex SASs with a greater number of geometric parameters, so that these SASs affect the acoustic impedance of the structure. In the last few years, at the Zhukovskiĭ Central Aerohydrodynamics Institute, new methods have been developed for

increasing the efficiency of sound suppression in the ducts of aircraft engines on the basis of determining the optimal impedance of the duct walls and the "realization" of this impedance by using specially designed SASs [12, 13]. Particular attention has been given to studying the ways of increasing the efficiency of multilayer combined structures with varying geometry along the duct by using resonant structures of different shapes, volume absorbers, composite materials, and perforated and grid panels. By varying the parameters of the SAS, changing the resonant frequency of the structures, and extending the absorption band, it is possible to considerably enhance the sound attenuation in the engine ducts.

Formulation of the Problems of Determining the Efficient SAS

In the general form, the problem of sound propagation and attenuation in a duct with an SAS treatment becomes complicated when the effect of the flow with parameters varying along the duct is taken into account. Since an exact solution of the problem of sound propagation in an inhomogeneous duct with a flow is impossible, various analytic and numerical methods are developed for obtaining approximate particular solutions. The problem becomes even more complicated when the effect of the boundary layer formed at the surfaces bounding the flow is considered. Of practical interest is the general solution to this problem for the case of the acoustic field generated by a simple source. For example, one can construct the Green function for the Blokhintsev equation in the principal small-parameter approximation for a smoothly inhomogeneous treated duct with a subsonic compressible flow when the boundary layer is ignored. The presence of the boundary layer manifests itself, first, in the refraction of sound, which leads to a change in the angle of the sound wave incidence on the duct wall and to the attenuation in the course of the propagation, and, second, in the formation of hydrodynamic disturbances in the boundary layer under the effect of sound, so that these disturbances, being convected by the flow, give rise to acoustic disturbances. The solution to the problem with allowance for only the refractive effect of the boundary layer was obtained for an axisymmetric duct with a subsonic compressible flow on the condition that the cross section and the wall impedance of the duct slowly vary along its axis [14]. As a result, the solution to the waveguide problem of the sound propagation in a smoothly inhomogeneous duct in the presence of a potential flow was obtained and the Green function that determines the general solution for a given distribution of sources was constructed.

A theoretical problem of special interest is the determination of the optimal geometric and aeroacoustic parameters of SASs on the basis of the real spectral characteristics of acoustic fields in the ducts, the boundary layer flow parameters at the duct walls, and the mean velocity profiles in the duct. The parameters of the SAS should be determined so as to affect both the discrete components and the broadband part of noise produced by the engine. Evidently, to reduce the levels of discrete components, it is expedient to use resonant structures, while, for reducing the broadband noise, volume absorbers are preferable. The goal of the studies carried out in the last few years was the development of high-efficiency multiparameter SASs that combine

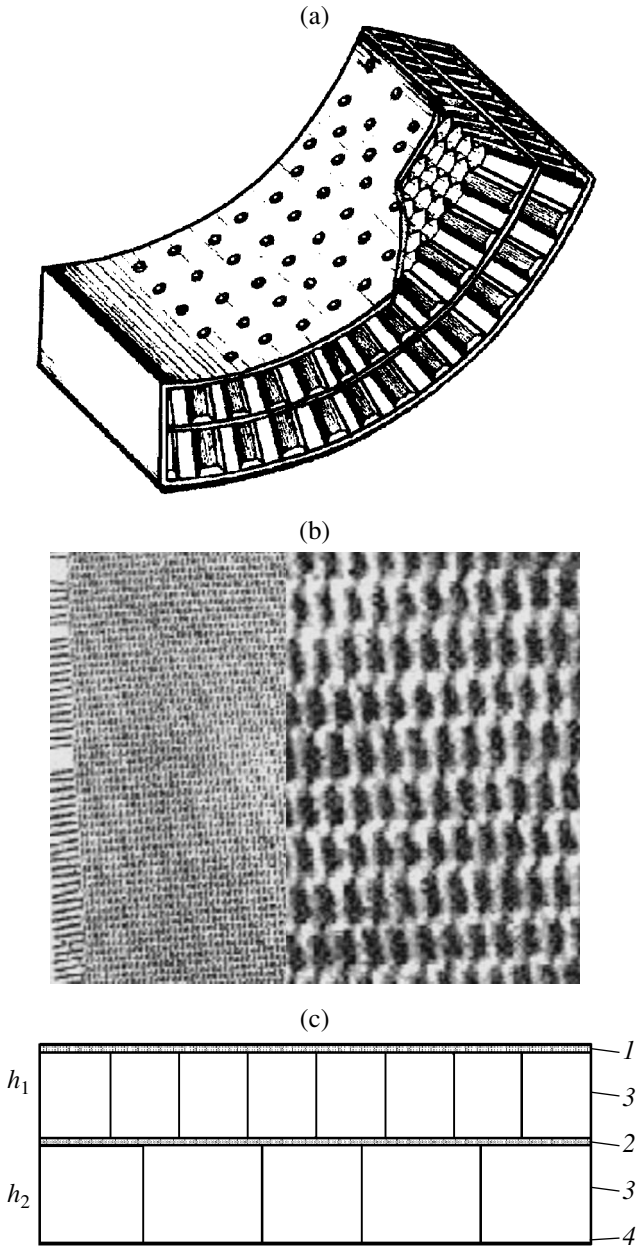

Fig. 6. Variants of a two-layer treatment with perforated and microporous layers. (a) A two-layer sound-absorbing treatment with a perforated surface layer; (b) photographs of a grid layer with different magnifications; (c) schematic representation of a two-layer treatment: (*1*, *2*) perforated or grid layers, (*3*) honeycomb filler, and (*4*) rigid base.

the properties of resonant structures and volume absorbers.

One can separate several important problems concerned with the development of high-efficiency SASs. One of them is the detailed study of the mechanisms of sound absorption in perforated panels with the aim of developing better methods for determining the impedance characteristics of SASs. The second problem is concerned with studying the effect of an increase in the number of degrees of freedom of a resonant structure on its acoustic efficiency. By controlling the degrees of freedom, it is possible to extend the frequency band of effective noise suppression without increasing the area of the sound suppressing system. This problem deals with multilayer and combined SASs. The next important problem is related to studying the efficiency of microporous permeable panels as absorbing layers. Microporous panels are manufactured using different technologies. The Russian mass production materials include grid panels with a serge weaving (Fig. 6b).

In designing SASs for engine ducts, the fundamental problem is to obtain the maximum possible attenuation at a given frequency or in a given frequency band with a limited length of the treatment. This refers in full measure to the ducts of engines with a high by-pass ratio, where the possibilities of mounting the SAS are limited (Fig. 5b) while a considerable reduction of the noise levels is required at both the blade frequency and its harmonics. For real power plant duct lengths in the frequency band under consideration, it is appropriate to use the method of determining the optimal impedance of SASs from the condition of the maximal ratio of acoustic energy flows at the inlet and outlet of the muffler duct [11]. Using the solution to the problem of determining the optimal attenuation in a treated duct on the basis of calculating the energy flow from a point source positioned symmetrically with respect to the walls, it is possible to calculate the geometric parameters of the SAS from the condition that the impedance is optimal and to determine the dependences of the optimal impedance and the maximum possible attenuation in the duct on both frequency and distance from the source.

The optimal sound attenuation in a duct with a source lying on the duct axis is achieved when the impedances of the SAS on opposite walls are equal. However, most of the real sources of engine noise do not lie in the middle of the duct, and the equality of the SAS impedances on opposite walls is unnecessary. With the introduction of an additional argument, namely, the impedance of the second wall, the solution of the problem is considerably complicated, because, in this case, the acoustic field in the duct is a function of many variables. On the other hand, the introduction of the variability of the SAS impedance extends the possibilities for raising the efficiency of the system of noise suppression in the duct. If the source is not in the middle of the duct, the maximal attenuation at a given frequency occurs at certain unequal values of the SAS admittance on opposite duct walls [12]. In this case, the attenuation is higher than the attenuation achieved when the source lies in the middle of the duct, as well as when the treatment impedance takes equal values on opposite duct walls.

Multilayer SASs

The sound attenuation in a duct with a two-layer SAS can be determined with different optimization conditions. The geometric parameters of a two-layer structure, namely, the depth of the air cavities of the layers and the perforation percentage of the panels, can be calculated from the condition that its impedance takes optimal values at two frequencies simultaneously. The optimal impedance at each frequency can be determined in two ways: on the assumption that the impedance values on opposite duct walls are different and on the assumption that these values are equal. For example, in the cases considered in [12], the efficiency of a two-layer structure coincides with the optimal one at the maxima of the frequency characteristics of attenuation. On the whole, the structure, whose geometric parameters are determined on the assumption that the impedance takes different values on opposite walls, proves to be more efficient. The dips in the frequency characteristics of attenuation are related to the limited attenuation bands of individual layers, which presumably is a consequence of the presence of a large associated mass of the perforated panels. Hence, using two-layer treatments, it is possible to make their impedances equal to the optimal values corresponding to the maximal attenuation at two frequencies simultaneously. As a result, the frequency spectrum of attenuation is broadened compared to the case of single-layer structures. To obtain more uniform frequency characteristics of attenuation, it is expedient to use fine-pore grids with a small associated mass and also to use structures containing several layers.

The use of thin smooth permeable grids (Fig. 6b) as absorbing layers of the SAS offer considerable promise. Experimentally, it was found that the impedance of a single-layer grid structure is independent of the sound pressure level and that the associated mass of such a structure is small, at least when the structure is relatively deep [15]. These facts, along with the smoothness of the surface layer, make such structures attractive for use in the ducts of aircraft engines, where it is necessary that the SAS be effective in a wide range of engine operation modes, from landing to take-off.

To calculate the impedance of a structure with a grid layer, one has to use rather complicated mathematics based on the Green function approach. The main effects that should be taken into account in calculating the impedance of a single-layer structure include the losses due to the viscosity and the heat transfer in the pores of the surface grid and at the walls of the air cavity (resonator), as well as the effect of the lateral and rear walls

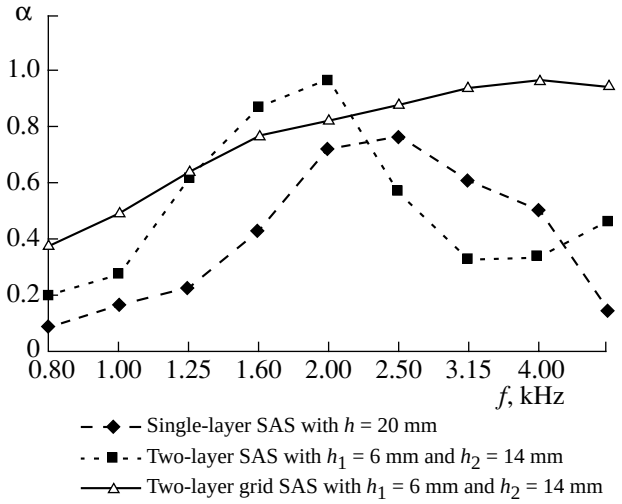

Fig. 7. Comparison between the sound absorption coefficients of a single-layer SAS, a two-layer SAS with perforated panels, and a two-layer grid SAS.

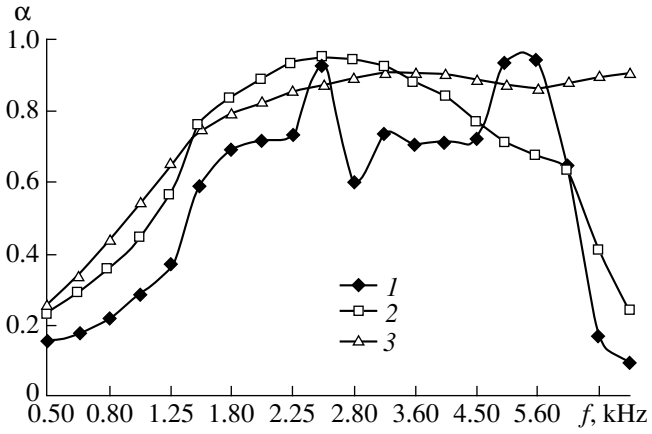

Fig. 8. Frequency dependences of the sound absorption coefficient for two-layer structures: (*1*) with perforated panels, (*2*) with a perforated surface panel and an inner grid panel, and (*3*) with grid panels.

on the associated mass [15]. The inclusion of the losses due to the viscosity and the heat transfer at the walls of the air cavity is possible through the introduction of the appropriate wall admittance of the nonlocally reacting type. The losses in the holes of the grid strongly depend on the shape and dimensions of the holes; in particular, in the case of a serge weaving, the holes have smooth inlets and outlets, which hinders the formation of jet flows [16, 17]. This fact partially accounts for the weak dependence of the impedance on the sound pressure level.

The impedance of a two-layer structure is a sum of the impedance of the surface grid, the inertial impedance of the surface grid with a load equal to the internal layer impedance, the inertial impedance of the surface grid with a load corresponding to an infinite column thickness, and the impedance of the first layer (without the surface grid) loaded with the impedance of the second layer [13]. When the depth of the first layer is small, the two-layer structure behaves as a single-layer one of the total thickness with a higher resistance and a lower resonance frequency. The latter is caused by the higher inertial parameter due to the effect of the second layer. As the depth of the first layer increases, a second resonance emerges at a higher frequency. Simultaneously, the first resonance shifts to lower frequencies. The operating range of such a two-layer structure is the wide frequency band that covers both resonance frequencies.

Owing to the small associated mass, the grid structures, especially the two-layer ones, offer advantages over the structures with perforated panels from the viewpoint of their bandwidth and sound absorption coefficient [15]. Figure 7 presents a comparison between the sound absorption coefficients measured experimentally for single-layer and two-layer SASs with perforated panels and a two-layer grid SAS. The sound absorption coefficient α of a two-layer structure with perforated panels has two maxima corresponding to two tuning frequencies (the second peak is beyond the operating range of the experimental setup). The large resistance and inertial mass of this structure are undesirable, because, in the corresponding frequency region, the frequency characteristic of sound attenuation in the duct will exhibit a dip. A correct choice of the geometric parameters of a two-layer SAS with a perforated panel should make the spike in the real part of the impedance as small as possible or shift it to the edge of the frequency range of interest. In the case of a two-layer grid structure, because of the small associated mass and a moderate resistance value, the frequency characteristic of the absorption coefficient has a single smooth maximum without any dips. This structure provides a sufficiently high sound absorption coefficient within the whole frequency range of practical interest. One can see that a two-layer grid structure has a wider frequency characteristic of α compared to the two-layer structure with perforated panels.

If the surface layer of the treatment may be fouled so that the grid structure may loose its absorbing properties, it is expedient to use combined two-layer SASs with the surface layer in the form of a perforated panel and the inner layer in the form of a grid panel. Figure 8 compares the characteristics of the sound absorption coefficient obtained for three variants of two-layer structures: with two perforated panels, with a perforated surface panel and an inner grid panel, and with two grid panels. The geometric parameters of the first and second layers of the SAS were chosen so as to make them best suitable for using the structures in the ducts of modern engines. From the viewpoint of the sound absorption efficiency, the SAS with a perforated surface panel and an inner grid panel occupies the inter-

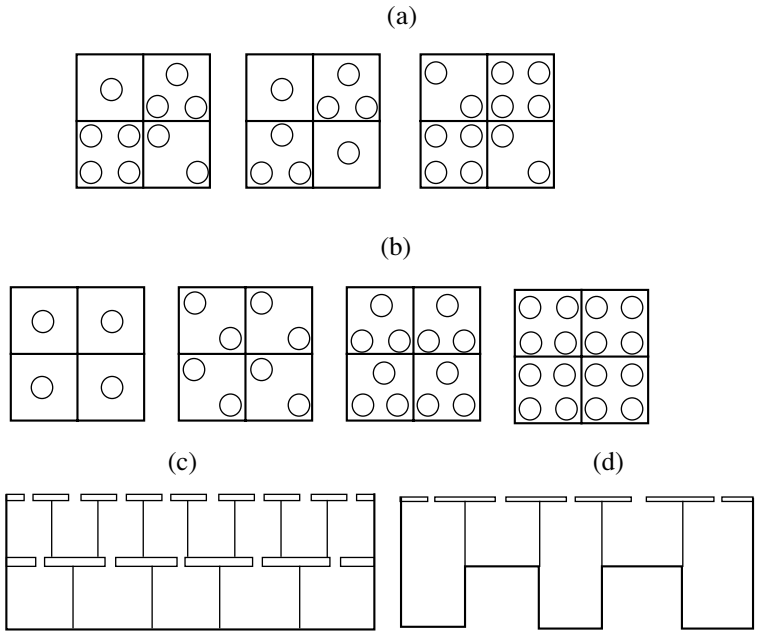

Fig. 9. Samples of (b, c) homogeneous and combined SASs (a) with different perforations of the surface layer and (d) with different resonator volumes.

mediate place between the two-layer SASs with perforated panels and grids.

The purpose of research carried out in this area is the choice of micron grids that are most suitable for power plants of airplanes, as well as the refinement of the effect of the interaction between the perforated surface panel and the grid panel and between two grids in order to determine the optimal distance between them and the optimal combination of their parameters.

Combined SASs

An extension of the absorption band to both higher and lower frequencies is possible by using multiparameter treatments, i.e., combined two-layer structures of different thicknesses with a varying perforation of surface layers [18].

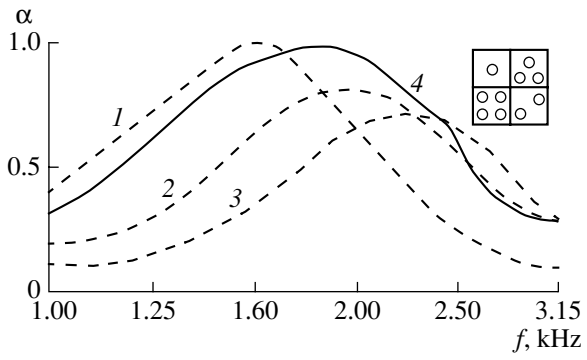

Fig. 10. Frequency dependences of the sound absorption coefficient for a combined SAS (—) and for homogeneous SASs (– – –) with a hole diameter d = 2 mm and different perforation percentages of the surface panel: F = (*1*) 6, (*2*) 9, (*3*) 12, and (*4*) (3 ∪ 6 ∪ 9 ∪ 12)%; L_{inc} = 140 dB.

For the practical application in air intake ducts, the structures most suitable from the viewpoint of extending their absorption band are combined SASs with an absorbing surface that consists of resonator units repeated in two mutually perpendicular directions, each unit consisting of several resonators tuned to different frequencies. The resonators forming a unit are tuned by varying the perforation percentage or the resonator volume in neighboring cells (Fig. 9). If we draw an analogy to a two-layer structure, whose impedance is determined as a series connection of impedances of its constituent elements, the impedance of the combined structure under consideration can be represented as a parallel connection of the elements forming the unit. To make the frequency characteristic of absorption as uniform as possible in a wide frequency band, it is necessary to choose the appropriate geometric parameters of the cells forming a unit with allowance for the effect they produce on each other.

An exact determination of the impedance of a combined structure consisting of several differently tuned cells usually presents a complex diffraction problem, which requires solving the wave equation with a periodically inhomogeneous surface. By introducing a set of limitations concerning the conditions of the sound incidence and the relations between the geometric parameters and the sound wavelength, one can obtain an approximate expression for the impedance of a combined sound-absorbing structure [3]. For this purpose, it is sufficient to know the impedance of each of the

homogeneous structures, whose elements form the combined SAS, and the fraction the area of each element makes of the total area of the unit.

The comparative study of combined resonant SASs that was carried out at normal sound incidence by a high-level interferometer showed a considerable extension of the frequency characteristics of the absorption coefficient α, as compared to the corresponding characteristics of the homogeneous SASs whose elements form the combined SAS (Fig. 10). The combined SAS under investigation had the form of a unit of four isolated resonant cells, which were tuned to an individual frequency each and, pairwise, to two resonance frequencies or three different frequencies. The frequency characteristic of a combined SAS consisting of four different cells actually represents the envelope of the characteristics of α of three homogeneous SASs. The fourth cell with the minimal perforation percentage $F = 3\%$, which has the maximal resistance compared to the other three cells, made practically no contribution to the total absorption. To extend the frequency characteristic of the sound absorption coefficient, it is important to provide the maximal efficiency of all cells of the structure. This presents the subject of the inverse problem, which consists in the determination of the parameters of a combined SAS from the condition that the sound absorption coefficient α be maximal in the given frequency band.

It is well known that the impedance of a resonant structure strongly depends on the intensity level of the incident sound. The characteristics of sound absorption by combined SASs that were obtained for different sound pressure levels L_{inc} at the sample surface showed a decrease in their nonlinearity. Figure 11 presents the results of studying the sound absorption coefficient of a combined SAS, whose cells have different hole diameters d, and a similar SAS, whose inner partitions are eliminated. One can see that, in the second case, i.e., for a homogeneous structure with holes of different diameter, the sound absorption coefficient strongly depends on the sound pressure level at the sample surface. For a combined SAS consisting of four cells with holes of different diameter, the effect of sound level variation is considerably reduced, which is an important advantage from the point of view of its application in the ducts of an aircraft engine.

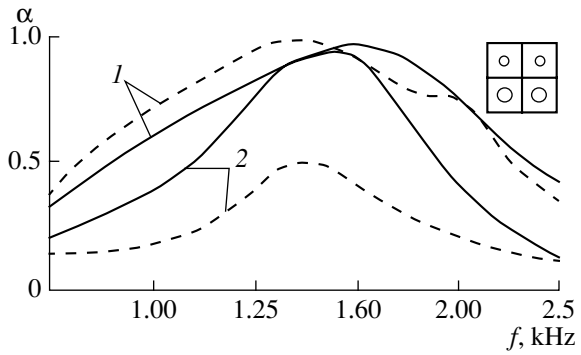

Fig. 11. Effect of the sound pressure level at the surface of an SAS with hole diameters d = 1, 2, 3, and 4 mm on the sound absorption coefficient for L_{inc} = 110 (- - -) and 140 dB (—): (*1*) a combined structure and (*2*) a structure without inner partitions.

Low-Frequency SASs

An effective reduction of the engine noise level in the low-frequency region is possible with the use of small-size low-frequency resonators. The absorption band can be extended by changing the geometric parameters of resonators and the perforation percentage of the surface layer. The use of such structures is expedient for engines with a superhigh by-pass ratio $m \geq 10$ or for cowled propfans and, in particular, for the NK-93 engine that is under development in Russia. Such engines exhibit a noise spectrum with a spectral maximum shifted to lower frequencies, as compared to the spectral maxima characterizing the noise of modern by-pass turbojet engines; namely, this maximum occurs at frequencies of 300–500 Hz. To reduce the noise levels in this frequency region, the honeycomb resonant SASs are unsuitable because of their relatively large thickness required in this case. A decrease in the SAS thickness to 40–70 mm can be achieved through structural changes that cause a considerable increase in the associated mass and, hence, a resonance frequency shift to the low-frequency region. The corresponding means may be grids introduced in the air cavities or pipes of different length and diameter.

In each section, the system of resonators may include, for example, two or three resonators tuned to different frequencies and positioned close to each other. Each resonator consists of a rectangular cavity with holes in the form of a throat oriented toward the incident sound. The use of pipes of sufficient length and width makes it possible to reduce the total height of the sound-absorbing section due to the increase in the associated mass (Fig. 12). The resonators belonging to the same section are tuned to different frequencies, which allows the extension of the absorption band. Tuning is possible by choosing the appropriate lengths and diameters of the pipes and the volume of each resonator within a given section.

The results of testing by a low-frequency interferometer showed that an increase in the pipe length δ and a decrease in the throat diameter d lead to a decrease in the resonance frequency (Figs. 12a and 12b). The frequency characteristic of the sound absorption by a combined structure consisting of several resonators is in fact the envelope of the characteristics of individual elements. The use of metal grids placed in the resonator throat leads to an extension of the frequency characteristic of sound absorption (Fig. 12c), while the resonance frequency remains practically unchanged.

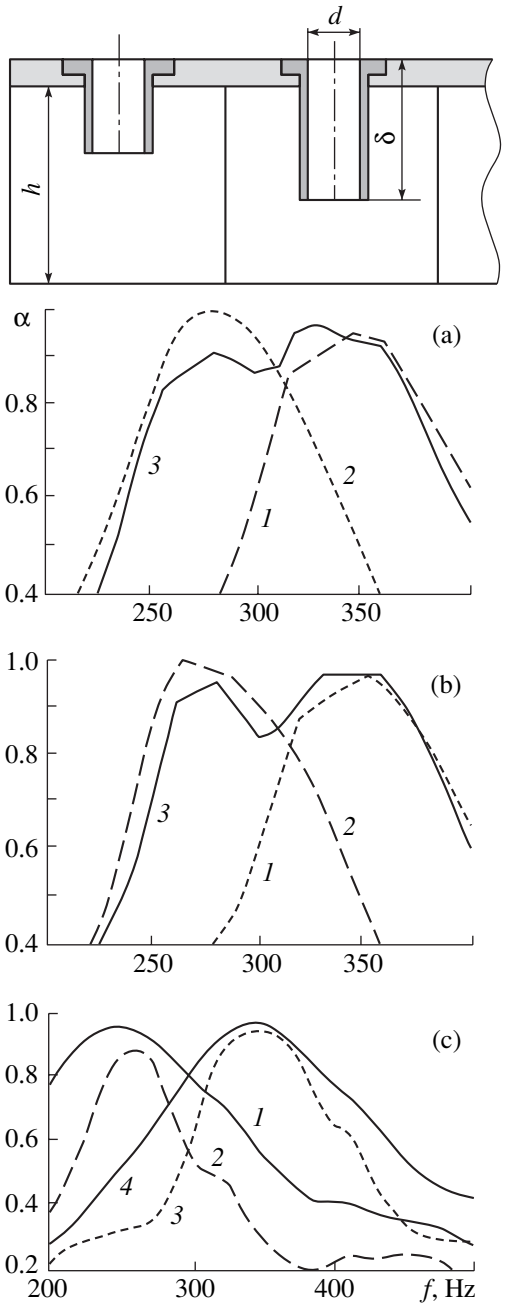

Fig. 12. Frequency dependence of the sound absorption coefficient of a resonant structure: (a) $h = 50$ mm, $d = 20$ mm, the perforation percentage is $F = 5.5\%$, and $\delta = (1)$ 20, (2) 40, and (3) an inhomogeneous structure with $\delta = 20$ and 40 mm; (b) $h = 50$ mm, $\delta = 20$ mm, $d = (1)$ 20, (2) 15 mm, and an inhomogeneous structure with $d = 15$ and 20 mm; (c) $d = 20$ mm, $\delta = 20$ mm, and $h = (1, 2)$ 100 and (3, 4) 50 mm for a structure (1, 4) with and (2, 3) without a metal grid.

The use of pipes of different lengths and diameters makes it possible to design variants of combined SASs by analogy with those considered above and intended for noise suppression in the higher frequency region. To prevent the undesired sound generation, low-resistance grids may be placed at the pipe inlet.

Multisectional SASs

Studies that are of practical interest from the point of view of obtaining the maximum sound attenuation in the power plant ducts are those aimed at increasing the efficiency of sections or combinations of sound-absorbing treatments with different parameters and properties [18]. The efficiency of a two-section treatment may be even higher than the algebraic sum of the individual efficiencies of the two sections. Presumably, this is related to the presence of the impedance jump, which causes the reflection of sound waves and the transformation of low-order modes to higher-order ones, while the latter are more efficiently absorbed by the treatment. The tuning frequency of a two-section SAS is intermediate between the tuning frequencies of the two sections.

To provide the required efficiency of the system of noise suppression in a power plant, it is necessary to use several structures with different geometric parameters, i.e., to use a multisectional treatment. One can construct many combinations of SASs with different tuning frequencies and different area of their mounting, so that each of these combinations will provide the required frequency band of noise suppression. In practice, the parameters of interest of an SAS include the area of the sections and their tuning frequencies; a multisectional SAS should provide the required efficiency of noise suppression and have the minimal area. In other words, it is necessary to solve the problem of a balanced noise reduction by each of the sections, so that the resulting frequency characteristic of this SAS be close to the required one, e.g., in the sense of the rms approximation. For example, for the outer contour duct of an engine with a high by-pass ratio, the problem can be solved as follows. We assume that the duct can be divided into sections that have the form of pieces of a ring channel with a constant height within each section, while the heights of different sections may be different. Each section is treated with SASs over the whole lateral inner surface. The number of sections, their initial dimensions, and the preliminary tuning frequencies of the SASs are determined. Then, for the duct under consideration, the optimal impedances of each of the sections are determined for the least attenuated mode. From the optimal impedance, the perforation percentage and the depth of the air cavity are determined at the preliminary tuning frequency of each of the pieces with given initial dimensions. The necessary dimensions of the sections and the frequencies corresponding to maximal attenuation are determined so as to make the calculated attenuation spectrum as close as possible to that required for the power plant under consideration.

NOISE PROBLEMS OF A SUPERSONIC PASSENGER AIRPLANE

The necessity to satisfy the requirements imposed on the community noise in airport areas leads to an

unordinary situation in connection with the development and possible operation (expected in the second decade of the XXI century) of supersonic transport aircraft of the second generation (SST-2) in both Russia and western countries. The experience gained from the operation of the first-generation SST, Tu-144 and Concord, which were developed in the late 1960s, showed that, to satisfy the currently effective requirements of Chapter 3 of the ICAO Standard, it is necessary to reduce the noise level produced by these airplanes at the take-off conditions by about 20 dB [19, 20] (Fig. 4). The acuteness of the problem of the SST noise suppression is determined by the necessity of using engines with a high thrust-to-weight ratio to provide a cruising flight with a supersonic speed. The issue velocity of the power plants of both Tu-144 and Concord reached a value of 900 m/s and was more than 1.5 times higher than the outflow velocity of the engines of subsonic passenger airplanes used at that time. For comparison, note that, in the engines of modern subsonic passenger airplanes, which allow a further strengthening of the noise standards, the issue velocities are within 300–350 m/s.

The possibility of providing low levels of community noise near airports is the decisive condition for the beginning of the operation of SST-2, and this possibility depends on the development of efficient methods for suppressing the jet noise of these airplanes [21, 22]. A possible solution to this problem may be the use of engines with a variable operation cycle, namely, a bypass turbojet engine for the take-off and landing and a turbojet engine for the cruiser flight. However, the variation of the operation cycle alone is not enough to satisfy the requirements imposed on the community noise by, e.g., Chapter 3 of the ICAO Standard, and it is necessary to use the latest advances in jet noise control. The noise control methods that were recently developed in connection with the SST-2 operation problem include intensification of the jet mixing with the surrounding medium, reduction of the resulting issue velocity, and passive sound absorption [23–26]. The intensification of the jet mixing processes can be achieved by varying the parameters of the flows in the inner and outer engine contours and by using a multielement or multilobe nozzle in combination with an ejector. In this case, it is desirable that the flow velocity at the ejector outlet be comparable with the issue velocity of modern engines.

In an engine with a variable operation cycle, the jet mixing can be accelerated by using the so-called “inverted” velocity and temperature profiles of the engine outlet flow, when the high-head and high-temperature flow occurs in the outer contour [19]. Model studies showed that the use of the inverted profile of the flow parameters leads to a decrease in the maximum levels of the jet noise by 5–7 dB and to a decrease in the acoustic power by up to 5 dB. An additional decrease in the noise levels may be achieved by creating a gaseous shield between the exhaust flow and the observer, e.g., by separating part of the gas flow downstream from the combustion chamber to form a secondary heated flow that is parallel to the main one [27]. In this case, the acoustic effect is based on the reflection and refraction of sound waves as a result of their passage through the gas layer. A considerable reduction of the noise levels, by about 10 dB, is observed in the high-frequency region at the observation angles corresponding to the directions of the most intense jet noise radiation. Evidently, to obtain the maximal acoustic effect, it is expedient to use certain combinations of jet noise control methods.

In the development of the power plants for SPA-2, an especially important problem is the design of an efficient ejector muffler that suppresses the jet noise at the take-off and landing stages of the flight and is eliminated from the flow or partially transformed to a streamlined body at the cruiser flight stage (Fig. 13a). The difficulties encountered in designing an ejector device are related to the problems of obtaining a perfectly expanded main flow for a wide range of pressure ratios and engine operation modes, as well as obtaining acceptable thrust characteristics of engines at real operating conditions. An ejector device should be designed so as to minimize the noise of wave structures in the flow by creating optimal systems of variable geometry for the exhaust nozzles.

The acoustic effect achieved with the use of an ejector muffler occurs at the expense of the reduction of the flow velocity in the zone of mixing with the surrounding medium. For example, in an axisymmetric ejector device consisting of a shell, an ejector, a central body, and hollow pylons, an efficient mixing of the main flow with the ejected air results from the flow separation into a number of jets of smaller transverse size and the ejection of the surrounding air into the mixing zone through additional windows in the lateral walls (Fig. 13b). At the stage of the supersonic cruiser flight, the pylons are transformed so that they close the external airflow and form the supersonic part of the nozzle with a low thrust loss. A similar structure is used in the rectangular multielement ejector nozzle consisting of a shell, corrugations, central body, lateral walls, and leafs of the ejector [23].

In ejector mufflers, one can distinguish two characteristic zones of jet mixing (Fig. 14). One of them lies at the outlet of the corrugated nozzle elements. In this zone, the high-speed jets are mixed with ejected air. Since the characteristic size of the flow is determined by the geometric dimensions of individual lobes, the noise generated by this part of the flow is a high-frequency noise, which is usually called the “lobe noise.” The second characteristic zone of mixing lies at the ejector outlet where the issuing flow is mixed with surrounding air. Since the flow has a greater transverse dimension and a lower velocity, the noise from this part of the flow is a low-frequency one and is called the “mixing noise.” An approximate evaluation of these

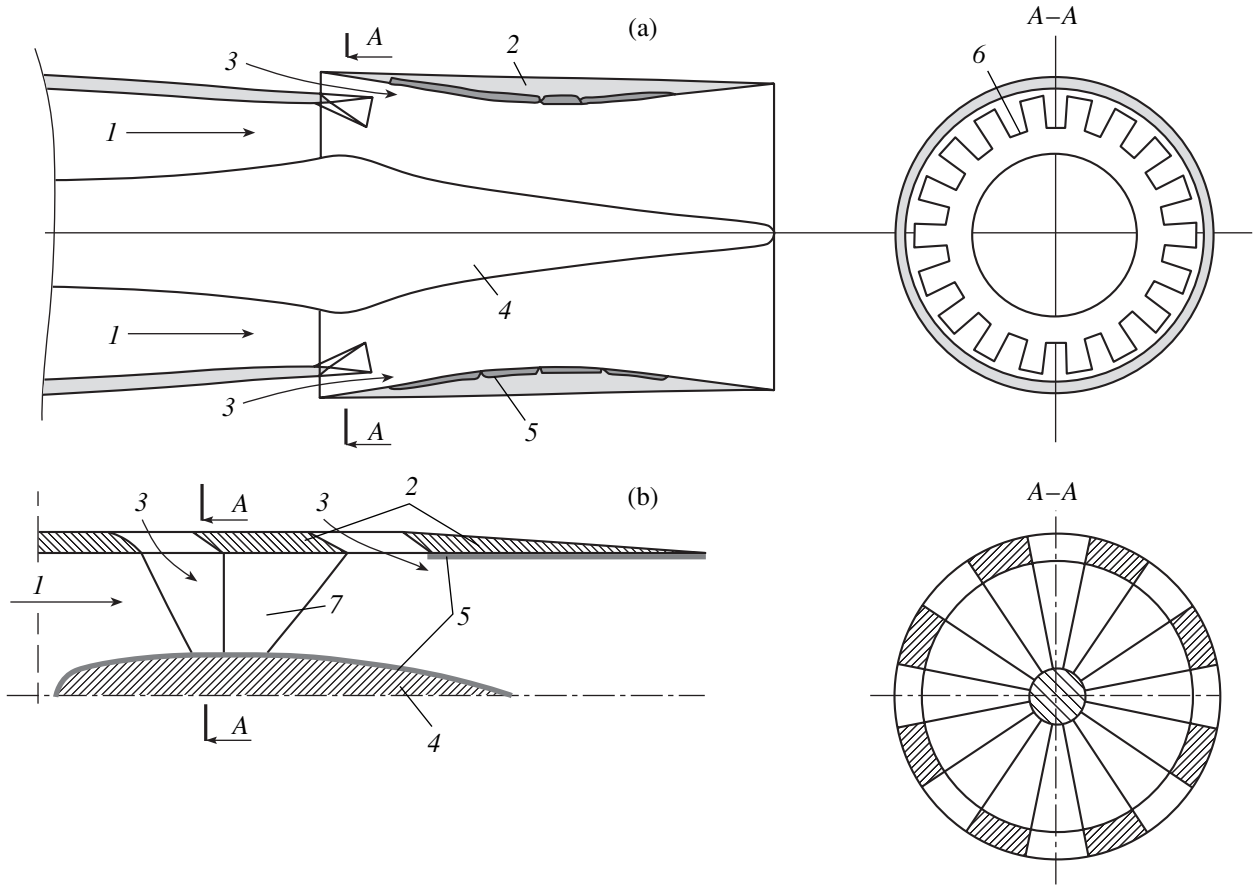

Fig. 13. Noise-suppressing ejector nozzles with the air ejection (a) through an annular slot and (b) through additional windows: (*1*) main flow, (*2*) ejector, (*3*) ejected air, (*4*) central body, (*5*) sound-absorbing treatment, (*6*) corrugated nozzle, and (*7*) pylons.

noise components is possible on the basis of the determination of the main gas-dynamic and geometric parameters of the flow with the use of the theory of flow mixing in an ejector [20]. The acoustic efficiency of ejector nozzles, which was measured at static takeoff and landing conditions, proved to be as high as 15–17 dB in the intervals of frequencies and observation angles corresponding to most intense noise radiation (Fig. 15).

A further reduction of the noise level can be achieved using SASs mounted on the inner surface of the ejector [28] (Fig. 14). The parameters of the SAS should be adjusted so as to provide the maximum suppression of the high-frequency lobe noise. Along with solving the direct problem, which consists in the determination of the acoustic field formed in the ejector duct under consideration as a function of the aeroacoustic parameters of the duct and, specifically, of the treatment impedance, it is of practical interest to solve two inverse problems: first, to determine the preferable or optimal values of the treatment impedance that provide the maximum sound attenuation in the duct and, second, to determine the geometric parameters of multiparameter sound-absorbing treatments so as to make their real impedance as close as possible to the optimal value in the given frequency range. In this case, the attenuation provided by the specific treatment will be the maximum possible one in the given frequency range.

It should also be noted that, because of the severe weight and area limitations, the sound-absorbing treatments mounted on the duct walls must have the highest possible efficiency. The solution of the direct problem for, e.g., a point source localized in the region of the maximal flow noise generation, should be performed with allowance for the refraction and reflection effects arising at the flow layer boundaries and in the boundary layer and affecting the mode structure of the field in the duct and, hence, the parameters of the SAS [29]. The optimal impedance is determined from the condition of minimal energy at the outlet of the treated part of the ejector duct. For example, the solution of a number of problems for single-layer, two-layer, and combined treatments was obtained for a rectangular duct with identical SASs mounted on its opposite sides [30]. Single-layer honeycomb resonant structures provide the maximum possible attenuation at their tuning frequencies, and a two-layer structure provides the maximal attenuation at two frequencies simultaneously. Experi-

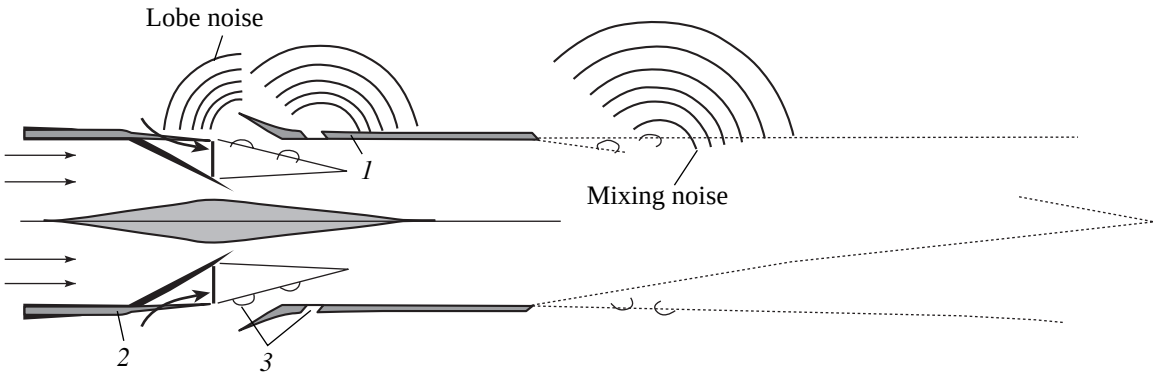

Fig. 14. Increase in the acoustic efficiency of an ejector nozzle: (*1*) the optimization of the parameters of SASs, (*2*) the change in the initial nozzle configuration, and (*3*) the increase in the efficiency of air ejection and the intensification of the flow mixing.

mental studies were performed with two-layer structures made of composite materials, including perforated sheets and baffles attached to them so as to form resonant air cavities. It was found that, in the presence of sound-absorbing treatments in the ejector duct, a noise reduction of 11 dB can be achieved in a wide frequency range.

Recent studies show that a promising SST-2 can fit the current ICAO Standard for community noise of passenger airplanes if a by-pass engine with an ejector muffler is used at take-off and landing and the optimal operation procedures are used in the course of the flight. To satisfy the new, more stringent requirements imposed on the community noise near airports, it is necessary to apply a variety of noise-control techniques.

ACOUSTIC FIELD OF AN AIRPLANE WITH PROPFAN ENGINES

The operating experience gained with various airplanes shows that the use of propellers provides higher economical efficiency of aircraft power plants, as compared to turbojet engines, for the speeds of flight corresponding to Mach numbers less than 0.75 [31]. The An-70 Russian–Ukrainian airplane is the world's first airplane with a propfan power plant, which includes an eight-blade front propeller and a six-blade rear propeller. This airplane has remarkably good take-off and landing characteristics.

To obtain preliminary estimates of the noise characteristics of this airplane, the acoustic field generated by a propfan was measured in a "flying" laboratory [32]. The main noise sources of a coaxial propfan were analyzed: the noise level produced by the rotation of the eight-blade front propeller L_8, the noise level produced by the rotation of the six-blade rear propeller L_6, and the noise level L_{int} caused by the aerodynamic interaction between the blades of the propellers in the coaxial configuration with unequal numbers of blades in the front and rear propellers (Fig. 16). In the zone of propeller rotation $\bar{x} = 0$ (where $\bar{x} = x/D_p$, x is the distance from the plane of rotation of the front propeller along the fuselage, and D_p is the propeller diameter), the total acoustic load level L_t on the fuselage is determined by the noise components caused by the rotation of the front and rear propellers, namely, by the first harmonics of the noise produced by the rotation of these propellers with the frequencies f_8 and f_6, respectively.

The narrow-band analysis in the high-frequency region of the noise spectra revealed many discrete components at the frequencies f_p representing combinations of the rotation frequencies of the front and rear propellers (Fig. 17). The directivity of these noise components L_p is more uniform than that of the harmonics of the rotation noise. The intensity of the discrete noise components at the combination frequencies is determined by the aerodynamic interaction of the propellers and the effects of the interaction of the vortex wakes and pressure fields produced by the propellers. In the coaxial configuration, the rear propeller operates in a field of velocities varying in azimuth and produced by the front propeller; the blades of the front propeller produce a

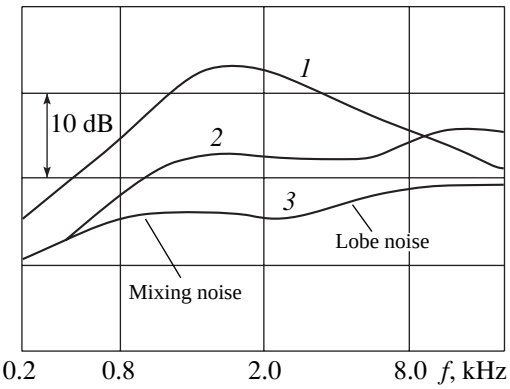

Fig. 15. Noise spectra in the direction of the maximal noise radiation from the jets issuing from the nozzles: (*1*) initial circular nozzle, (*2*) ejector nozzle of Fig. 13a, and (*3*) ejector nozzle of Fig. 13b.

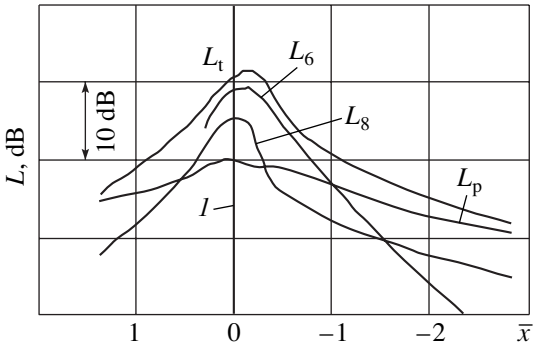

Fig. 16. Distribution of acoustic load levels along the fuselage surface; (*1*) the solid vertical line represents the plane of rotation of the front propeller.

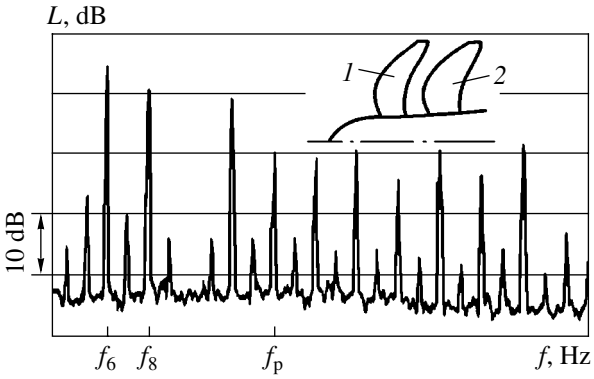

Fig. 17. Noise spectrum of a coaxial propfan; (*1*) the eight-blade front propeller and (*2*) the six-blade rear propeller.

vortex sheet that is incident on the blades of the rear propeller. The most intense vortices can be the end ones formed by the front propeller blades at off-design conditions. It was found that, in the spectral characteristics of a coaxial propfan noise, the relation between the levels of the discrete components and the broadband noise is determined by the geometric and aerodynamic parameters of the propellers, the operating mode of the power plant, and the airflow conditions around the propellers.

The pronounced directivity of the propeller noise harmonics and the presence of many discrete high-frequency noise components may cause problems for a passenger airplane with a propfan power plant as to the acoustic comfort inside the plane and the community noise limits determined by the ICAO Standard.

Effective measures for reducing the propeller noise include an increase in the number of blades, a decrease in their relative thickness, a more swept shape, and the optimal choice of the load distributions over the blade surfaces and the blade geometry that reduce the wave processes in the airflow around the blades [33–35]. A decrease in the levels of the discrete noise components at the combination frequencies can be achieved by changing the rotation rates of the front and rear propellers and by increasing the distance between the planes of blade rotation, i.e., by reducing the aerodynamic interaction of the propellers. Some of the methods of noise reduction are ineffective for supersonic and close-to-supersonic velocities of the flow around the blades. The possibilities offered by other methods, such as a decrease in the relative thickness and an increase in the width of the blades, proved to be practically exhausted because of the technological difficulties in manufacturing this kind of blade. Therefore, to reduce the propeller noise and the loads on the airplane fuselage, it is necessary to consider specific methods, such as the choice of the optimal load distribution over the blade surface and the blade geometry that reduce the wave processes in the flow around the blade and, hence, reduce the corresponding noise levels. In this case, the calculation of the field of pressure disturbances caused by coaxial propellers with blades of an arbitrary shape is based on the determination of the fields of forces acting in the blade cross sections and the determination of the effects produced in the surrounding medium by the aerodynamic loads applied to the blades. It should be noted that the measures taken with the aim of reducing the noise must not affect the aerodynamic characteristics of the propellers.

Currently, in the studies of the possibilities of increasing the efficiency of power plants, some attention is also paid to propellers and coaxial propfans mounted in ring cowls. At equal thrusts, the diameter of a cowled propeller is smaller than that of an open propeller, which makes it possible to realize different configurations of power plants in the airplanes.

Let us list the possible contradictory consequences of the use of a cowled propfan for solving the acoustic problems of airplanes. The specific feature of the configuration with a cowled coaxial propfan is the presence of pillars supporting the cowl, while, in a turbojet engine, they may be an integral part of the stator. Under the assumption that the noise caused by the interaction of propellers produces the same effect as the noise of the rotor–stator interaction with the same axial separation of blades, a cowled coaxial propfan is characterized by the additional noise due to the interaction of the propeller with the pillars, as compared to an open propfan.

With the same engine length, the structure of a cowled propfan requires a decrease in the distance between the rows of propeller blades, as compared to an open propfan, which inevitably leads to higher noise levels due to the interaction between the propellers. At the same time, with the same thrust of the power plants, the end velocities of the blades of a cowled propfan are smaller, which results in a less intense noise radiation. However, the inner wall boundary layer in the cowl causes perturbations of the oncoming airflow at the ends of the propeller blades, which may cause an increase in the noise radiation. In addition, in such a

structure, it is difficult to realize propeller blades with large sweep angles to obtain lower noise levels at cruising speeds. On the other hand, the presence of a cowl screens the propfan noise and provides the possibility of mounting SASs on the inner surfaces.

To obtain an exact description of the sound field of a cowled coaxial propfan, one needs exact information on the additional mechanisms of blade loading due to the nonstationary aerodynamic interaction between the blade rows and the effects of interactions of ring vortices, the vortex sheet behind the blades, and the flow inhomogeneities caused by one of the blade rows and interacting with other blade rows. In addition, it is necessary to describe the additional noise sources that appear when the propeller operates at a nonzero angle of attack or an inhomogeneous velocity field, as well as the noise sources due to the flow interaction with the pillars supporting the cowl. The multitude of the mechanisms of noise generation in a cowled coaxial propfan complicates the development of the noise computation methods and the parametric studies of the acoustic characteristics of an airplane.

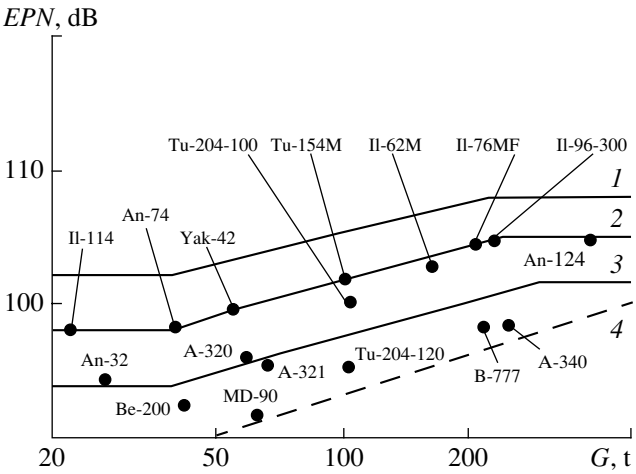

Fig. 18. Noise levels from different airplanes at reference point 3 (at landing); the noise limits according to (*1*) Chapter 2, (*2*) Chapter 3, and (*3*) Chapter 4 of the ICAO Standard; and (*4*) the noise levels expected for the flow noise from the airframe.

FLOW NOISE FROM THE AIRFRAME ELEMENTS

In the development of the new generation of passenger airplanes with low noise levels, in addition to the problem of further suppression of the power plant noise, the problems of reducing the flow noise caused by the airflow around the airframe elements, the high-lift devices, and the landing gear of the airplane become increasingly important [10, 36]. One can consider the noise of the flow around the airframe elements as the lower limit for the reduction of the airplane noise. For example, at landing conditions, the noise levels produced by the power plant of a modern airplane are close to the noise levels produced by the airflow around the landing gear, the high-lift devices, and the airframe (Fig. 18). The studies in this area are especially topical for the large passenger airplanes under development.

The noise of the flow around the airframe elements is determined by the fluctuations of the parameters of turbulent flows in the slots formed by the slats and flaps at take-off and landing conditions, in the boundary layers at the skin surfaces, and in the wakes behind the airframe elements (Fig. 19). The most intense noise is generated by the flow around the landing gear, the flaps of the trailing edge of the wing, and the slots in the leading edge of the wing.

As a rule, the acoustic disturbances generated by these sources cannot be fully calculated because of the complex structure of the fields of the turbulent stress tensor in the flows and the fluctuating forces acting on the airplane surfaces in the real flows around the airframe elements. Therefore, the evaluation of the noise sources is performed using both numerical methods and experimental data obtained in the model conditions or in the conditions imitating real stages of flight. In numerical calculations, the attention is focused on the determination of the turbulent flow structure resulting from the flow around the airframe elements [37]. For example, it was shown that the noise generated by the flow around the flaps is caused by intense pressure fluctuations related to the fluctuations of the vorticity field near the flap edges.

The approaches currently used for estimating the flow noise around the airframe are based on the measurements of the airplane noise with the engines operating in reduced power conditions and on the determination of the dependences of the noise characteristics on the speed of flight, the airplane weight, the position of the high-lift devices, etc. Such an approach allows one to estimate the acoustic characteristics of the flow noise from the airframe only when the configurations of the initial and calculated airplanes are geometrically similar. Other approaches are associated with the determination of the noise generated by the flows around individual elements: the slats, the wing, the flaps, the landing gear, etc. in a wind tunnel whose working section contains a sound-absorbing treatment [38, 39].

From the point of view of reducing the noise intensity, the most difficult source is the airflow around the landing gear. In studying the formation of this source, an important role is played by the experimental aeroacoustic studies in conditions close to those of real operation, along with the studies of the flow noise around large-scale models. The studies of the flow noise around full-scale landing gears of modern airplanes show that, when the landing gear enters the oncoming airflow, the most noticeable increase in the spectral noise levels occurs in the region of low acoustic frequencies. A decrease in the flow noise levels can be

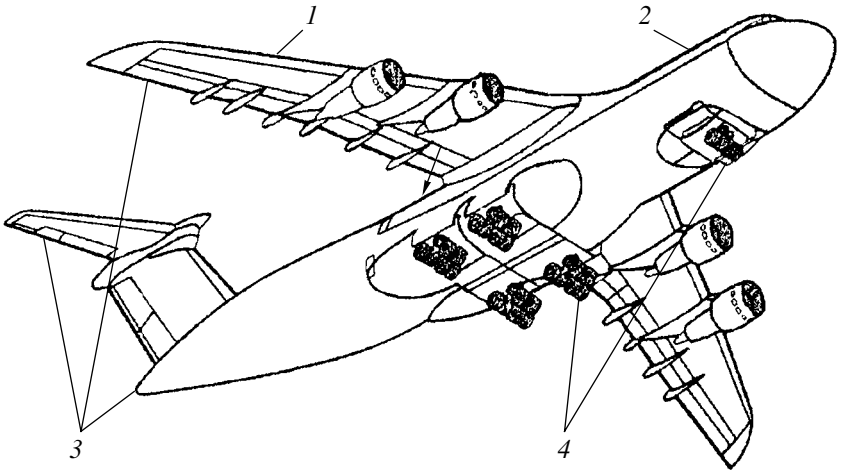

Fig. 19. Sources of the flow noise produced by the airframe of an airplane: (*1*) the flow around the slats and the flow separation from the surface; (*2*) the boundary layer at the fuselage surface; (*3*) the turbulent wakes and vortex formations behind the trailing edge of the wing, flaps, fuselage, and tail unit; and (*4*) the flow around the landing gear.

achieved by making the landing gear streamlined and by using fairings and interceptors.

The flow noise around the high-lift devices is mainly generated by the complex vortex structures accompanying the formation of the lift of the wing (Fig. 20). Currently, an especially important problem is the determination of the relation between the noise intensity and the geometry of the high-lift devices. The dominant noise source formed in the airflow around a slat is the turbulent flow accelerated in the slot of the slat and convected past the rear edge of the slat [38, 40]. In addition, the flow in the slot is combined with the nonstationary flow component. The vortex separation from the lower edge of the slat gives rise to low-frequency discrete components. Moreover, the flow around the devices providing the deflection of the slat surfaces gives rise to a small-scale turbulence in the slot flow, which leads to a noise generation in the high-frequency region [41, 42].

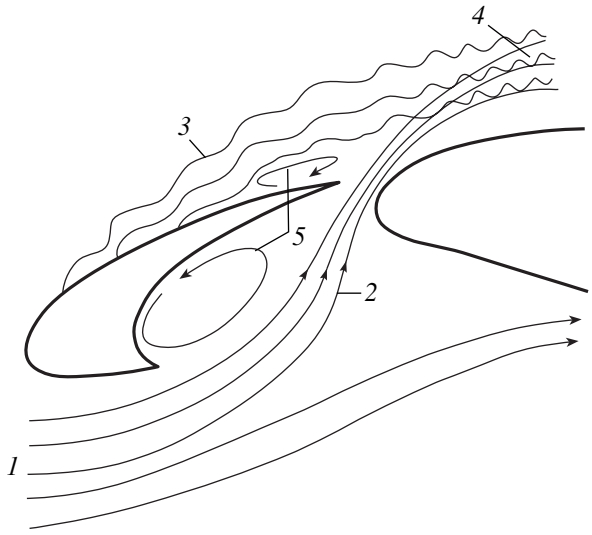

Fig. 20. Possible mechanisms of noise generation by the flow around the slat: (*1*) the oncoming airflow; (*2*) the flow through the slot between the slat and the wing; (*3*) the flow separation from the slat surface and the build-up of the flow instability; (*4*) the interaction of the flows; and (*5*) the vortex formation.

Noticeable noise levels can also be generated by the flow around some auxiliary load-bearing elements, e.g., braces or control elements of the high-lift devices. If one airframe element falls into the wake of another element, e.g., the flap falls into the wake of the landing gear pillars, the noise level may increase. The levels of the flow noise from the airframe elements can be reduced by developing a rational structural scheme, in which the noise-generating elements do not come into the turbulent wake formed by the airframe elements located upstream from them, or by reducing to the maximal possible extent the mutual effects of the elements in the flow.

The introduction of more stringent limitations for airplane noise will not only restrict the production of airplanes with imperfect acoustic characteristics but also initiate the development of new types of airplanes. The current problem of reducing the noise levels by 10–15 dB within 20–25 years may require the realization of structural schemes in which the fuselage structure and the engine configuration in the airplane will be based on entirely new ideas. For example, according to one of the concepts, the structure of the wing gradually passes into the fuselage structure, and the power plant is mounted on the upper surface of the whole airplane structure. The airplanes of the "flying wing" type may have a lower weight compared to conventional structures and, hence, may be less noisy with the same passenger capacity and flight range. The important feature

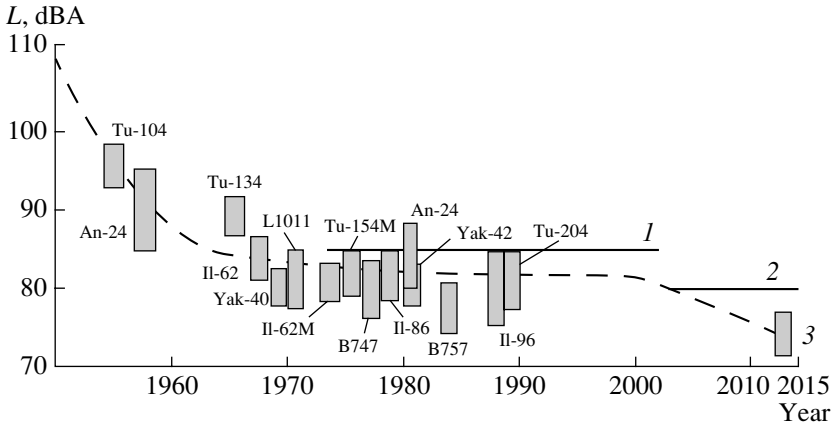

Fig. 21. Tendency toward the noise level decrease in the cabins of passenger airplanes: (*1*) the GOST 20296 State Standard; (*2*) the newly proposed GOST State Standard; and (*3*) a future airliner.

of this configuration is that, in the flying wing scheme, the fuselage will prevent the propagation of the power plant noise toward the ground and will exhibits better aerodynamic characteristics at take-off and landing; hence, the flow noise around the airframe elements will be considerably reduced.

INTERIOR NOISE OF PASSENGER AIRPLANES

The competitive ability of airplanes is determined by both their community noise characteristics and the acoustic comfort in their cabins. In Russia, the allowable noise levels in airplane cabins and the corresponding measurement techniques are regulated by the GOST 20296-81 State Standard. International standards for the interior noise of airplanes have not yet been devised. Large companies of the aircraft industry usually establish their own standards for the allowable noise levels to provide the acoustic comfort inside the airplanes and to make the latter competitive (Fig. 21).

From the scientific point of view, the problem of providing the allowable noise levels in aircraft cabins includes the study of the mechanisms of the energy transformation from pressure fluctuation fields to sound via thin-wall structures and the study of the noise control techniques suitable for acoustic fields in aircraft cabins.

A popular method of noise reduction in cabins is the use of sound-insulating structures which simultaneously serve as heat insulators. A typical sound-insulating structure (Fig. 22) consists of two impermeable layers (the fuselage skin and the interior panel), between which layers of a sound-absorbing material are fixed. The sound-proofing properties of this structure may vary within wide limits, depending on the filling factor of the sound-absorbing layers in the space between the skin and the interior panel, the compression of these layers, the acoustic properties of the layer material, and the surface mass of the interior panel. To provide a better effect of the second wall, a vibration insulation is necessary between the interior panels and the fuselage structure. As a rule, in the board structures of passenger airplanes with turbojet engines, the space between the fuselage and the interior panel is filled with a soft loose-fiber material made of extra-thin fibers (1–3 μm in diameter) with a low mass per unit volume

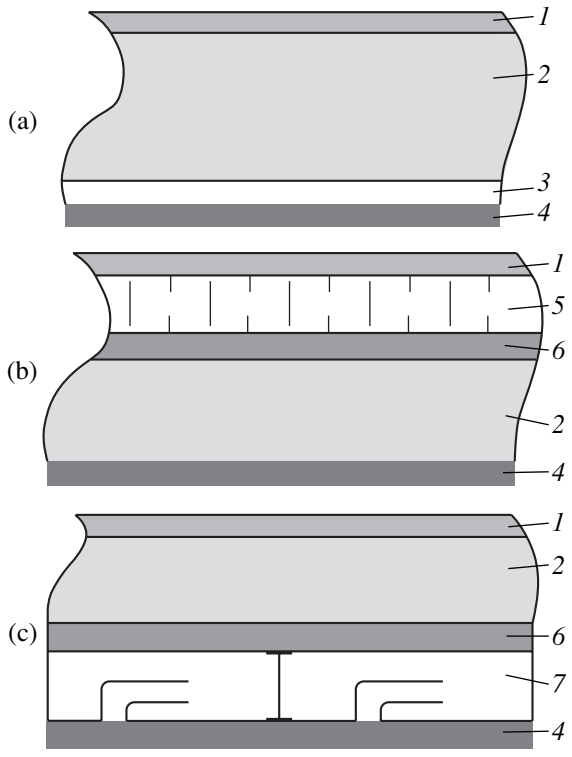

Fig. 22. Schematic representations of the (a) conventional and (b, c) advanced sound-insulating structures: (*1*) skin, (*2*) heat and sound insulation, (*3*) air gap, (*4*) interior panels, (*5*) honeycomb, (*6*) vibration-absorbing coating, and (*7*) resonator.

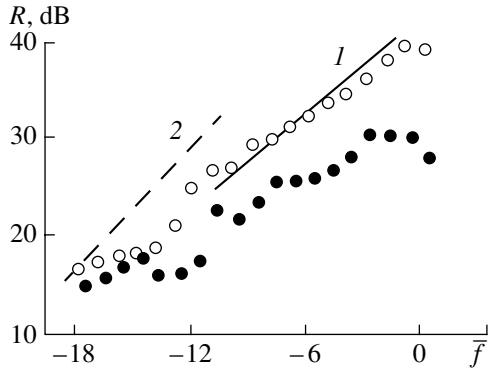

Fig. 23. Frequency dependence of the sound-proofing coefficient of an airplane panel (○) treated with a layer of vibration-absorbing material and (●) without this layer.

(10–20 kg/m^3). The total mass of this heat-insulating sound-proofing material may constitute a considerable part of the take-off mass of the airplane: up to 0.5%. Therefore, the problem of increasing the acoustic efficiency of such materials is quite topical [43].

In the last few years, studies of acoustic characteristics of various loose-fiber materials produced in Russia and in other countries by different technologies were carried out [44–46]. The materials had different fiber diameters (from 0.7 to 25 μm) and volume densities (from 9 to 100 kg/m^3). The analysis of the experimental results made it possible to construct general universal characteristics of sound attenuation in these materials with the use of dimensionless parameters. The resulting computational model developed for a wide frequency range can serve for the optimization of heat-insulating sound-proofing structures used in airplane cabins, as well as for the development of the corresponding recommendations for the manufacturers.

An effective way to enhance the dissipative properties of the board structures is to mount vibration-absorbing treatments with a high loss coefficient (higher than 0.2) on their surfaces [47]. For example, the sound-proofing property of a stiffened panel is considerably improved if this panel is treated with a layer of a vibration-absorbing material of the SKL type (Fig. 23). In the medium- and high-frequency regions $f > 400$ Hz, or at $\bar{f} = 10\log f/f_{cr} > -11$, where f_{cr} is the critical frequency of wave coincidence, the measured values of the sound-proofing coefficient R differ little from the results of calculations by the "mass law" with allowance for the panel skin and the treatment of the panel (curve *1*). In the low-frequency region, the actual efficiency of the vibration-absorbing treatment is lower than that calculated by the mass law with allowance for the mass of the skin, the stringers, and the treatment (curve *2*).

The experimental investigations show that the use of conventional heat-insulating sound-proofing treatments and a vibration-absorbing treatment on the skin surface of the fuselage panel is ineffective in the low-frequency region from the point of view of sound insulation, because the dominant role of the panel resonance modes is not reduced to any considerable extent in the low-frequency region, while the inertial properties of the panel are used insufficiently. Because of the effect of the resonance modes and the relatively large distance between the load-bearing elements, the mass of the load-bearing framing of the fuselage structure has a minor effect on the sound insulation in the low-frequency region. At low frequencies, the effect of the sound-absorbing structures can be enhanced by increasing the gap between the skin and the interior panel. However, even when the gap is large, the effect of the second wall is practically insignificant for the frequencies $f \le 250$ Hz, i.e., in the frequency range corresponding to the most intense noise radiation of the turbofan or propeller power plants of airplanes. For example, a decrease in the noise level in the cabin of an Il-114 airplane requires a considerable improvement of the sound insulation of its board at low frequencies, which cannot be achieved with conventional sound-insulating structures. The necessity to maintain the interior noise levels in the low-frequency region below the allowable limit in airplanes with propeller and turboprop engines is one of the most complicated problems in aviation acoustics.

To satisfy the requirements of the State Standard for the acoustic comfort in airplane cabins, it is necessary to raise the sound-proofing ability of the board structures in the narrow low-frequency bands corresponding to the fundamental blade frequency of propellers and its low-frequency harmonics. In the region of these sound frequencies, the sound-proofing ability of layered structures is limited by the mass law and determined by the surface mass of the structures. The required increase in the sound-proofing ability of the airplane board at low frequencies cannot be achieved with the structures of allowable mass that are conventionally used in aviation. The problem of reducing the low-frequency noise in the cabin can be solved by taking a set of measures that include the application of active methods and different unconventional passive methods of noise suppression [47–49]. To increase the sound-proofing ability of a structure, it is possible to use such active methods that immediately affect the physical processes governing the sound energy transfer through it. One of these methods (characterized by a high efficiency) is the use of mass simulators of the load-bearing framing of the fuselage and acoustic resonators, which hinder the sound transmission through the interior panels. Another effective method of low-frequency noise reduction is the synchrophasing of propellers; the

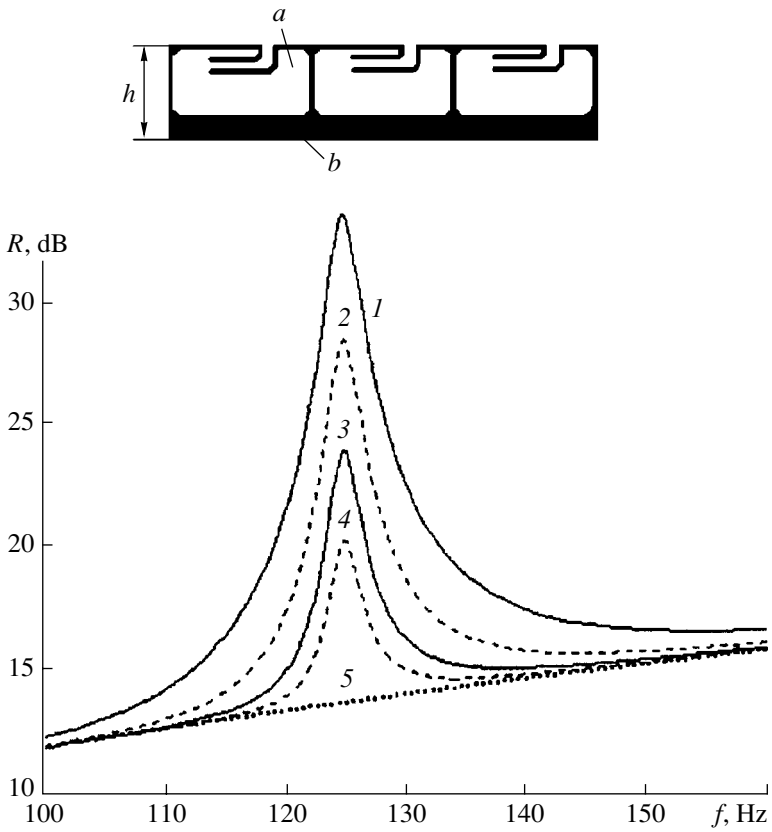

Fig. 24. Sound-proofing coefficient of a panel with and without resonators: (*a*) resonator, (*b*) panel; h = (*1*) 8, (*2*) 4, (*3*) 2, and (*4*) 1 cm; (*5*) panel without resonators.

main difficulty in its realization is the complexity of the design and mass production of the equipment maintaining the operating modes of all engines in the preset limits of possible variation.

The specialists in aeroacoustics pay special attention to the active methods of interior noise suppression. The main effort in developing the active systems of noise suppression is aimed at reducing the effect of broadband and discrete low-frequency noise components on the passengers of airplanes with propeller or turbofan power plants. The studies include the development of individual noise-proofing means for passengers and the development of "antinoise" systems optimally distributed over the cabin and the fuselage structure. The difficulties in the practical application of antinoise systems include not only their complexity and high cost, but also their labor-consuming mounting and tuning in the airplane cabins. Therefore, the studies concerned with the development of efficient and practicable methods of low-frequency noise reduction are of practical significance.

The sound-proofing property of the board of a propeller airplane can be enhanced by using resonant systems mounted on the interior panels [49, 50]. The good prospects for this method are determined not only by its acoustic efficiency but also by the possibility of its practical realization. As an example, Fig. 24 schematically represents a panel with a resonant system and displays the frequency characteristic of the sound-proofing coefficient R of a panel with the resonant system for different values of the acoustic layer thickness h and the sound-proofing coefficient of a panel of the same surface mass without the resonant system. A computational model was developed for evaluating the acoustic efficiency of such systems when included in the board structure of the airplane fuselage with allowance for the elastic-inertial properties of the fuselage skin with stiffening ribs (with stringers and frames), acoustic characteristics of heat-insulating sound-proofing layered treatments, vibroacoustic characteristics of the interior panels with resonant systems, and characteristics of the acoustic volume of the airplane cabin. The results of calculations and laboratory experiments provide the possibility of determining the most promising structures with resonant systems, which should be used in airplanes for reducing the interior noise at the fundamental blade frequency of the propeller and at its lower harmonics. The important condition for the efficiency of these systems is their optimal distribution over the fuselage structures and the passenger cabin.

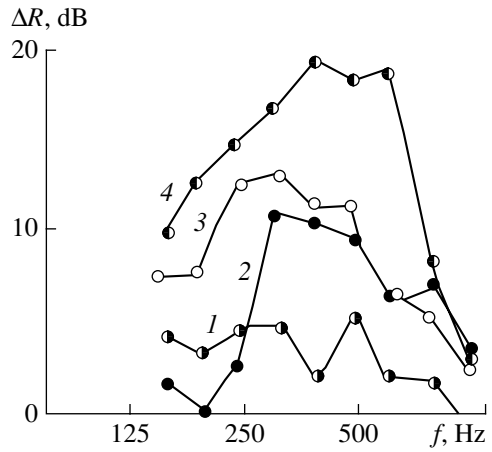

Fig. 25. Frequency dependence of the sound-proofing coefficient of a cylindrical airplane panel supplemented with (*1*) duralumin stringers with a density of 0.4 kg/m and rubber strips with densities of (*2*) 0.4, (*3*) 1.1, and (*4*) 1.5 kg/m.

Recently, a new method was proposed and studied to improve the sound insulation by mass simulators of the stiffening ribs of fuselage structures [47]. The essence of the method consists in mounting additional linear elements on the fuselage skin, so that these elements simulate the stiffening ribs in terms of the linear mass and are made of materials with a lower Young's modulus and a higher loss coefficient than the material of the panel elements (the skin and the stiffening ribs). Such mass simulators of the load-bearing framing make it possible, first, to artificially reduce the interval between the linear elements and, hence, to increase the upper cutoff frequency of the frequency band where the "nonresonant" sound insulation is determined not only by the mass of the skin but also by the mass of the stiffening ribs and their simulators. Second, the use of mass simulators with a rather strong dissipation reduces the effect of the resonance excitation of the panel on its sound-proofing property because of the introduction of additional loss. Third, with the introduction of the mass simulators, the role of the inertial properties of the structure eigenmodes becomes more significant.

The fundamental possibility of raising the sound-proofing abilities of plane and cylindrical fuselage panels at low frequencies by introducing stiffening rib simulators was confirmed experimentally. Specifically, experimental evaluation of the efficiency of mounting rubber strips with different linear mass on cylindrical fuselage panels with a large curvature radius (2.8 m) was carried out [47]. It was shown that the mass of the simulators enhances the inertial properties of the modes that predominate in the sound energy transfer at low frequencies, while the artificial decrease in the intervals between the concentrated linear masses (the stiffening ribs and their simulators) extends the frequency band where the mass of the load-bearing elements affects the sound insulation. In addition, since the rubber simulators of the load-bearing framing have stronger dissipative properties than those of an untreated panel, their mounting on the panel reduces the effect of resonance vibrations on the sound insulation. Owing to the effect of the aforementioned factors, the mounting of simulators on untreated panels makes the sound-proofing properties of the latter comparable with those calculated by the mass law with allowance for the total mass of the skin, the stiffening ribs, and their simulators. Figure 25 presents the results of studying the effect of the rubber strips mounted in the middle of a stringer cell on the sound-proofing coefficient of a cylindrical panel. One can see that, in the frequency range $f > 250$ Hz, the mounting of duralumin stringers is less effective than the similar mounting of rubber strips with the same linear mass density. As the linear density of the rubber strips increases, the increase in the sound-proofing coefficient becomes greater and reaches, e.g., a value of 12 dB when the total mass of the panel increases approximately twofold. The use of simulators of the load-bearing framing is expedient in certain local zones of the fuselage, e.g., in the zone of maximal acoustic loads caused by the power plant. The calculations show that the use of simulators of the load-bearing framing in the zone of the maximal acoustic loads on the fuselage surface of a short-range airplane may provide an additional decrease in the interior noise levels by 8–10 dB.

Thus, a considerable reduction of the noise levels in airplane cabins can be achieved by increasing the efficiency of the sound-insulating board structures. The acoustic comfort in the cabin can be improved with the use of resonant systems in the interior panels, the use of materials with enhanced sound-absorbing properties, vibration-absorbing materials that improve the sound insulation at resonance frequencies, materials with combined properties, and multilayer sound-insulating structures made of new materials and optimized with allowance for the effects of the space–time structure of the aeroacoustic fields at the outer fuselage surface.

A reduction of the noise levels inside and outside a passenger airplane is possible only by the combined solution of many problems concerned with decreasing the intensity of the power plant noise sources and with developing high-efficiency sound-absorbing and sound-insulating materials and airplane structures. The reduction of the noise produced by the airplanes, both currently in operation and under development, is the problem of prime importance, and this problem is directly related to the competitive ability of Russian aircraft engineering.

The research and design projects concerned with noise control in aviation are included in the Federal Special-purpose Program "Development of Civil Avia-

tion Engineering in Russia for the period from 2002 to 2010 and up to 2015."

REFERENCES

1. V. M. Kuznetsov, in *Proceedings of XI Session of the Russian Acoustical Society* (NII SF RAASN, Moscow, 2001), Vol. 4, p. 128.
2. V. M. Kuznetsov and A. G. Munin, in *Plenary Report of First Joint CEAS/AIAA Aeroacoustics Conference, Münich, Germany, 1995*, CEAS/AIAA-95-003, p. 1.
3. A. F. Sobolev, N. M. Solov'eva, and R. D. Filippova, Akust. Zh. **41**, 146 (1995) [Acoust. Phys. **41**, 124 (1995)].
4. V. M. Kuznetsov and A. G. Munin, in *Central Aerohydrodynamics Institute: Main Stages of Scientific Activity* (Nauka, Moscow, 1996), pp. 556–569.
5. V. F. Kop'ev, in *Proceedings of X Session of the Russian Acoustical Society* (NII SF RAASN, Moscow, 2000), Vol. 4, p. 99.
6. G. Raman and D. K. McLaughlin, in *Proceedings of 5th AIAA/CEAS Aeroacoustics Conference, Seattle, WA, 1999*, AIAA-99-1915, p. 1.
7. A. J. Bradley, Aeronaut. Q. **104** (1037), 301 (2000).
8. A. C. Powell and J. S. Preisser, in *Proceedings of 22nd International Congress of Aeronautical Sciences, Harrogate, UK, 2000*, p. 1.
9. V. F. Samokhin, in *Proceedings of III Scientific Conference on Hydroaviation: Hydroaerosalon-2000* (Tsentr. Aerogidrodin. Inst., Moscow, 2000), p. 270.
10. V. M. Kuznetsov and A. G. Munin, Tr. Tsentr. Aerogidrodin. Inst., No. 2634, 14 (1999).
11. A. F. Sobolev, Akust. Zh. **40**, 837 (1994) [Acoust. Phys. **40**, 742 (1994)].
12. A. F. Sobolev, Akust. Zh. **45**, 404 (1999) [Acoust. Phys. **45**, 357 (1999)].
13. A. F. Soblolev, Akust. Zh. **46**, 536 (2000) [Acoust. Phys. **46**, 466 (2000)].
14. A. F. Sobolev, Akust. Zh. **41**, 301 (1995) [Acoust. Phys. **41**, 260 (1995)].
15. V. M. Kuznetsov, É. G. Maslova, A. F. Sobolev, and R. D. Filippova, Tekh. Vozdushn. Flota, Nos. 2–3, 29 (1999).
16. C. Tam and K. Kurbatskii, in *Proceedings of 5th AIAA/CEAS Aeroacoustics Conference, Seattle, WA, 1999*, AIAA-99-1850, p. 311.
17. M. Choudhari, M. Khorrami, and J. Edwards, in *Proceedings of 5th AIAA/CEAS Aeroacoustics Conference, Seattle, WA, 1999*, AIAA-99-1851, p. 1.
18. V. Kuznetsov, A. Sobolev, E. Maslova, *et al.*, in *Proceedings of 2nd AIAA/CEAS Aeroacoustics Conference, 1996*, AIAA-96-1681, p. 1.
19. V. M. Kuznetsov, in *Proceedings of First Joint CEAS/AIAA Aeroacoustics Conference, Münich, Germany, 1995*, CEAS/AIAA-95-147, p. 1.
20. V. M. Kuznetsov, S. Y. Makashov, and A. F. Sobolev, in *Proceedings of 3rd AIAA/CEAS Aeroacoustics Conference, Atlanta, GA, 1997*, AIAA-97-1621, p. 255.
21. V. M. Kuznetsov and S. Y. Makashov, in *Proceedings of 7th International Congress on Sound and Vibration, Germany, 2000*, Vol. 3, p. 1187.
22. S. Yu. Krasheninnikov, A. K. Mironov, and E. V. Pavlyukov, in *Proceedings of 6th International Symposium on Transport Noise and Vibration, St. Petersburg, 2002.*
23. V. M. Kuznetsov and S. Y. Makashov, in *Proceedings of 5th CEAS/AIAA Aeroacoustics Conference, Bellevue, WA, 1999*, AIAA-99-1927, p. 826.
24. V. M. Kuznetsov, A. G. Munin, and A. F. Sobolev, in *Proceedings of 22nd International Congress of Aeronautical Sciences, ICAS 2000, Harrogate, UK, 2000*, p. 1.
25. V. K. Zhitinev, V. M. Kuznetsov, S. Yu. Krasheninnikov, A. K. Mironov, and E. V. Pavlyukov, RF Patent No. 2,153,091 (2000).
26. S. Yu. Krasheninnikov and A. K. Mironov, in *Proceedings of 5th International Symposium on Transport Noise and Vibration, St. Petersburg, 2000.*
27. V. M. Kuznetsov and A. A. Potokin, Akust. Zh. **44**, 239 (1998) [Acoust. Phys. **44**, 196 (1998)].
28. V. M. Kuznetsov, A. F. Sobolev, and E. G. Maslova, in *Proceedings of 4th AIAA/CEAS Aeroacoustics Conference, Toulouse, 1998*, AIAA-98-2324, p. 721.
29. A. F. Sobolev, Akust. Zh. **47**, 273 (2001) [Acoust. Phys. **47**, 226 (2001)].
30. V. M. Kuznetsov, É. G. Maslova, and A. F. Sobolev, Tr. Tsentr. Aerogidrodin. Inst., No. 2634, 51 (1999).
31. E. V. Vlasov, V. I. Ganabov, V. M. Kuznetsov, *et al.*, Tr. Tsentr. Aerogidrodin. Inst., No. 2614, 1 (1996).
32. V. M. Kuznetsov, in *Proceedings of 6th International Symposium on Transport Noise and Vibration, St. Petersburg, 2002.*
33. V. M. Kuznetsov, V. I. Ganabov, L. S. Krymova, and S. Y. Makashov, in *Proceedings of 15th Aeroacoustics Conference, Long Beach, CA, 1993*, AIAA-93-4444, p. 1.
34. V. M. Kuznetsov and S. Y. Makashov, in *Proceedings of 3rd International Congress on Air and Structure-Borne Sound and Vibration, Montreal, 1994*, p. 1253.
35. V. M. Kuznetsov, L. S. Krymova, and S. Y. Makashov, in *Proceedings of CEAS Forum on Aeroacoustics of Rotors and Propellers, Rome, 1999*, p. 108.
36. V. M. Kuznetsov and A. G. Munin, in *Aeronautical Acoustics. Encyclopedia* (Mashinostroenie, Moscow, 2002), Chap. 4, pp. 701–726.
37. F. T. Brooks and W. M. Humphreys, in *Proceedings of 6th AIAA/CEAS Aeroacoustics Conference, Hahaina, Hawaii, 2000*, AIAA-2000-1975, p. 1.
38. W. Dobzzynski and M. Pott-Pollenske, in *Proceedings of 7th AIAA/CEAS Aeroacoustics Conference, Maastricht, 2001*, AIAA-2001-2158, p. 1.
39. M. M. Henk and P. Sijtsma, in *Proceedings of AIAA/CEAS Aeroacoustics Conference, Maastricht, 2001*, AIAA-2001-2170, p. 1.

40. S. Olson, F. O. Thomas, and R. C. Nelson, in *Proceedings of 7th AIAA/CEAS Aeroacoustics Conference, Maastricht, 2001*, AIAA-2001-2156, p. 1.

41. M. Yu. Zaĭtsev, V. F. Kop'ev, and A. N. Kotova, Akust. Zh. **47**, 793 (2001) [Acoust. Phys. **47**, 699 (2001)].

42. A. S. Ginevskiĭ, E. V. Vlasov, and R. K. Karavosov, *Acoustic Control of Turbulent Flows* (Fizmatlit, Moscow, 2001).

43. V. M. Kuznetsov and A. G. Munin, Tr. Tsentr. Aerogidrodin. Inst., No. 2647, 3 (2002).

44. A. A. Tkachev, in *Proceedings of XI Session of the Russian Acoustical Society* (NII SF RAASN, Moscow, 2001), Vol. 4, p. 100.

45. A. A. Tkachev, Tr. Tsentr. Aerogidrodin. Inst., No. 2647, 23 (2002).

46. A. Yu. Golubev, L. Ya. Kudisova, and V. B. Kuznetsov, Tr. Tsentr. Aerogidrodin. Inst., No. 2647, 65 (2002).

47. A. A. Tkachev, Tr. Tsentr. Aerogidrodin. Inst., No. 2634, 41 (1999).

48. V. T. Dedesh, Yu. I. Kalinin, and V. M. Kuznetsov, RF Inventor's Certificate No. 023357 (1999).

49. B. M. Efimtsov and L. A. Lazarev, Tr. Tsentr. Aerogidrodin. Inst., No. 2634, 32 (1999).

50. B. M. Efimtsov and L. A. Lazarev, Tr. Tsentr. Aerogidrodin. Inst., No. 2647, 35 (2002).

Translated by E. Golyamina

Acoustical Physics, Vol. 49, No. 3, 2003, pp. 263–268. Translated from Akusticheskiĭ Zhurnal, Vol. 49, No. 3, 2003, pp. 318–324.

Acoustic Properties of Marine Animals Forming Deep Scattering Layers of the Ocean

I. B. Andreeva† and L. L. Tarasov

Andreev Acoustics Institute, Russian Academy of Sciences, ul. Shvernika 4, Moscow, 117036 Russia

e-mail: tarasov@akin.ru

Received December 14, 2001

Abstract—Acoustic models are considered for different animals that inhabit the deep scattering layers of the ocean and form a scattered acoustic field. These animals are divided into several groups that differ in their acoustic properties: fish with and without swim bladders, crustaceans, small squids, and other animals whose bodies consist of soft tissues and have no hard or gaseous inclusions. Normalized criteria are chosen for the quantitative comparison of the scattering properties of the animals. For the animals of each group, computational models are presented and analyzed. Generalized curves are constructed for the quantitative comparison of the backscattering cross sections of animals from different groups and of different sizes at different sound frequencies. In addition, these curves allow one to estimate the absolute values and the frequency characteristics of the scattering cross sections of animals for wide frequency and size ranges. © *2003 MAIK "Nauka/Interperiodica".*

One of the widespread acoustic inhomogeneities of the water column of the deep ocean is represented by the deep scattering layers (DSL), i.e., horizontally extended assemblages of small marine animals. In constructing an acoustic model for the DSL, information is needed on the acoustic properties of the marine animals inhabiting these layers and responsible for the scattered field. The animals can be divided into several different groups that differ in their acoustic properties: fish with and without swim bladders, crustaceans, small squids, and various animals with soft tissues of the body without hard or gaseous inclusions. In this paper, we present the comparative estimates of the scattering cross sections of the main inhabitants of the deep scattering layers. These estimates were obtained using theoretical models and formulas approximating the experimental data and are undeniably approximate for several reasons: first, because of the variety of forms and structures of the bodies of animals belonging to each of the groups; second, because of the impossibility of taking into account the details of the body structure of the live animals in the model; and, third, because of the lack of experimental data on the acoustic and mechanical properties of the live tissues and on the direct measurements of the scattering properties of individual inhabitants of the DSL. One of the last publications in this area of research is the paper by Benoit-Bird and Whitlov [1].

To remove the ambiguity related to the difference in the size of the animals of the same group, we use normalized characteristics for the purposes of comparison: the backscattering cross section σ normalized to the squared typical size l of an animal, $\sigma^* = \sigma/l^2$, and also the size l normalized to the sound wavelength λ, $l^* = l/\lambda$. Below, the latter will be called normalized size or normalized frequency, or simply frequency.

The typical size of the animals in the DSL is within 1 to 20 cm. The acoustic properties of the DSL are best studied in the frequency range within 1–20 kHz. We will assign the values $l^* < 1$ to the low-frequency range and the values $l^* > 1$ to the high-frequency range.

We start with the low-frequency range and the models for fish with swim bladders. Such a model was first proposed in [2], where expressions were obtained for the resonance frequency (f_r) and the scattering cross sections in the range $ka \ll 1$, where a is the radius of the sphere whose volume equals that of the swim bladder. The first of these expressions has the form

$$\omega_r = 2\pi f_r = \frac{1}{a}\sqrt{\frac{3\gamma P + 4\mu}{\rho}}. \quad (1)$$

Here, P is the static pressure at the depth where the fish is located, $\gamma = c_p/c_v = 1.4$ is the specific heat ratio for gas at constant pressure and volume, ρ is the water density, and μ is the shear modulus of live tissues surrounding the bladder. For an open-bladder fish whose swim bladder volume does not depend on depth, we can set $a \cong 0.05l$. Introducing the corresponding corrections in Eq. (1) and the following formulas, we can write them in a form more convenient for practical calculations.

Among all the quantities in Eq. (1), the shear modulus is the least studied, and all information available to us about this quantity is presented in the publications by Lebedeva [3, 4]. We used these data to construct the dependence $\mu_t(f)$ shown in Fig. 1. In this figure, the shaded area characterizes the scatter of the experimen-

† Deceased.

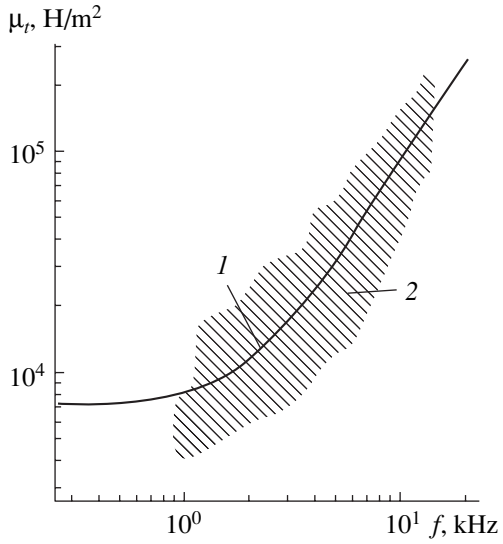

Fig. 1. Experimental data for the shear modulus of live tissues: (*1*) the average value (approximately) and (*2*) the data scatter region.

tal data. Because of a certain indeterminacy of these results, many of the following calculations are performed for two values of the shear modulus: $\mu = \mu_{min} = 0.3\mu_t$ and $\mu = \mu_{max} = 3.0\mu_t$, which covers the major part of the shaded area in Fig. 1.

Figure 2 shows the dependence of the resonance frequency on the radius a and on the fish length $l = 20a$ (the lower horizontal scale). The plots are constructed for different depths of the fish and for different values of the shear modulus. The plots in Fig. 2 show that the aforementioned scatter of the shear modulus values does not lead to a significant indeterminacy of the resonance frequencies; for the most part, they are determined by the size of the fish and by its depth. The resonance frequencies (excluding very large fish at very small depths) remain in the frequency range from several to ten or twenty of kilohertz.

Taking into account the aforesaid relation between the size of a fish and its swim bladder, the backscattering cross section can be written in the form [2]

$$\sigma = \frac{2.5 \times 10^{-3} l^2 Q^2}{\left(\frac{\omega_r^2}{\omega^2} - 1\right)^2 Q^2 - \frac{\omega_r^2}{\omega^2}}, \qquad (2)$$

where Q is the quality factor of the oscillatory system formed by the swim bladder and the tissues of the fish body. The sound scattering by such an oscillatory system can be considered isotropic. This determines the simple relation of the total and backscattering cross sections of a fish with a swim bladder at low frequencies: $\sigma_0 = 4\pi\sigma$.

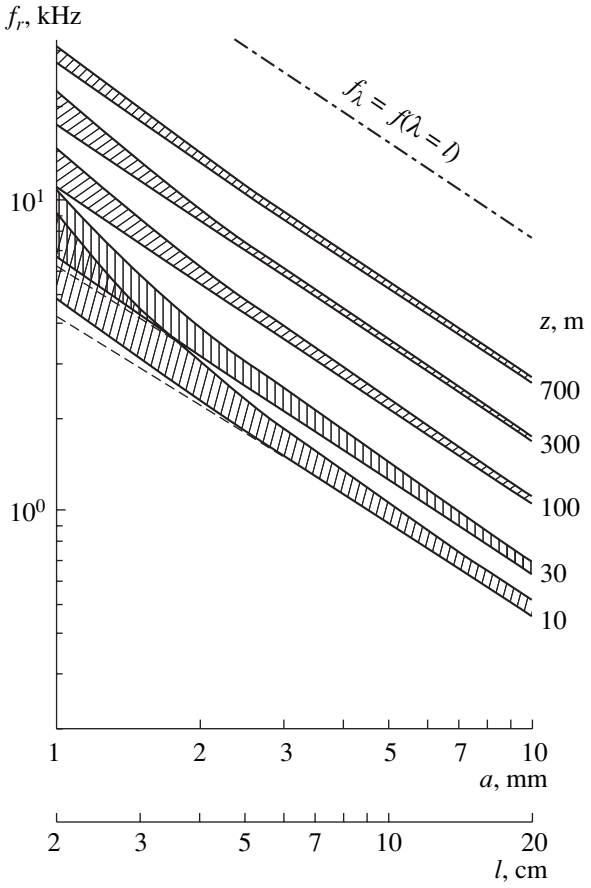

Fig. 2. Resonance frequency versus the fish size at different depths z. The lower boundary of each shaded region corresponds to $\mu = \mu_{min}$, and the upper boundary, to $\mu = \mu_{max}$. The dashed lines corresponds to free gas bubbles in water.

The physical nature of the quality factor was considered in [5], where it was shown that its value is almost totally determined by two kinds of losses: the scattering loss (η_s) and the shear loss (η_μ) in live tissues surrounding the swim bladder. The quality factor can be written in the form

$$Q = \left(\frac{1}{\eta_s + \eta_\mu}\right) = \left(\frac{1}{c}\sqrt{\frac{3\gamma P + 4\mu}{\rho}} + \frac{0.2\mu}{3\gamma P + 4\mu}\right)^{-1}. \qquad (3)$$

The results of calculations show that the ratio of these two kinds of losses depends on the size of the fish, its depth, and the quantity μ. The fraction of the shear loss is maximal for small fish at shallow depths, where it approaches 100%, but this fraction decreases almost to 50% as the depth increases to 1000 m. For relatively large fish in the DSL ($l \cong 20$ cm), the shear loss almost disappears at large depths and the quality factor is determined only by the scattering loss. The values of both kinds of losses depend on the shear modulus and, therefore, on the resonance frequency. All these facts make the dependence of the quality factor on the fish size ambiguous. The calculations performed using

Eq. (3) showed that, for real possible variations of the parameters involved in this formula, the quantity Q can change from 4 to 15.

Figure 3 presents the resonance curves $\sigma(f)$ corresponding to a fish length of 10 cm, two depths, and two extreme values of the shear modulus. The resonance backscattering cross section, σ_r, can reach hundreds of square centimeters, the width of the resonance region is small, and the resonance frequency strongly varies only as the depth changes. The shear modulus noticeably affects only the resonance cross section value. At frequencies below the resonance region, the scattering cross section decreases as f^4; above this region, the cross section decreases slower and, for $ka \cong 0.3l^* \cong 0.3$, this model ceases to be valid for estimations.

At relatively high frequencies, $l^* > 1$, the role of the swim bladder in the sound scattering from fish decreases and the scattering ceases to be isotropic. The measurements performed at the Andreev Acoustics Institute showed that, in the high-frequency region, both the scattering pattern and the backscattering diagram of fish have maxima, which correspond to the insonification of the "flattest" parts of the fish body (the side surface, the back, and the belly), and dips, which correspond to the head and tail aspects. The form of these experimental angular dependences was described in detail by Andreeva and Samovol'kin [6].

Love [7] carried out a comprehensive study to determine the characteristics of the scattering cross section of fish in the high-frequency region. In his generalizing work [7], on the basis of ample experimental data, he showed that the scattering cross sections of fish, with or without swim bladder, differ little from one another in the high-frequency region. Therefore, they can be combined into a single group; for $l^* \cong 1$–15, they are almost independent of the parameter l^*. Love considered the dependence of the backscattering cross sections on the fish insonification aspect and presented the numerical characteristics for all possible aspects. For the quantitative description, he chose the quantity $4\pi\sigma^*$.

Let us present some values of the normalized backscattering cross sections calculated on the basis of the data taken from [7]. For the dorsal insonification aspect, $\sigma^* = \sigma_1^* = 3.3 \times 10^{-3}$; this quantity being averaged over all aspects yields $\langle\sigma^*\rangle = 1.6 \times 10^{-3}$. These values are practically independent of the normalized fish length when $l^* = 1$–15.

For estimating the backscattering cross sections of fish without swim bladders in the low-frequency region, we have no reliable experimental or calculated data. As an approximation, such estimates can be obtained on the basis of the high-frequency values of σ^* for $l^* \cong 1$ by calculating the dependence $\sigma^*(l^*)$ corresponding to the decay law proportional to $(l^*)^4$ in the low-frequency range. For such estimates, we need to omit the transition region near $l^* \cong 1$ and restrict our consideration to the values $l^* < 0.3$. Using the aforementioned value $\sigma_1^* = 3.3 \times 10^{-3}$, for $l^* = 0.01$, we obtain the normalized backscattering cross section of fish without swim bladders $\sigma^* \cong 10^{-10}$. This value is much smaller than the typical values for fish with swim bladders not only in the resonance region but outside it as well.

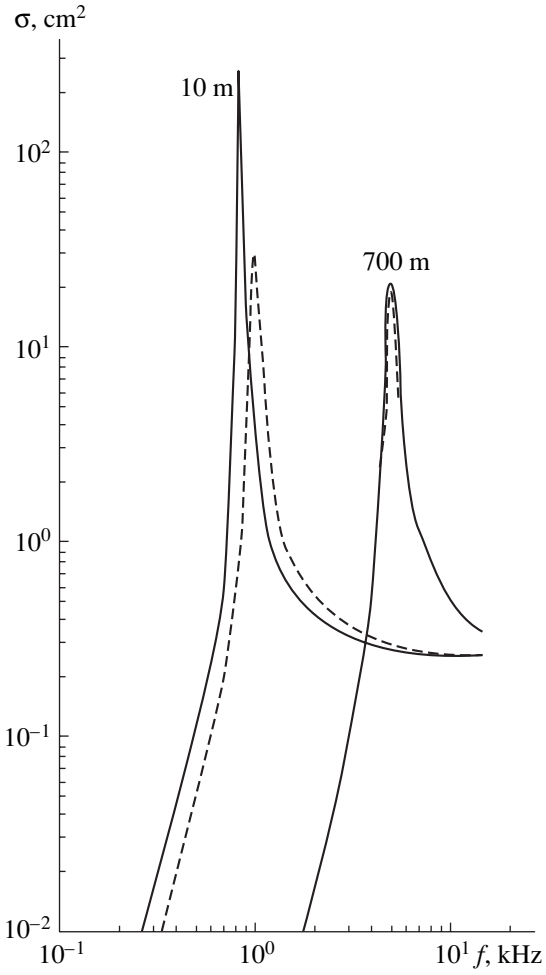

Fig. 3. Resonance curves for the backscattering cross sections of 10-cm-long fish with swim bladders for different depths and shear modulus values. The solid lines refer to $\mu = 0.3\mu_t$, and the dashed lines, to $\mu = 3\mu_t$.

Figure 4 presents the frequency dependences of the normalized backscattering cross sections for the fish models described above. At low frequencies, these dependences for fish with a swim bladder, for the aforementioned reasons, are not uniquely related to the fish size and the insonifying frequency. Therefore, these dependences are represented in Fig. 4 by shaded regions *1* and *2*. Region *1* approximately bounds the possible values of the scattering cross sections σ_r^* at the resonance frequency of the swim bladder. The calculations of the quantity σ_r^* corresponding to region *1* were performed for typical fish sizes from 3 to 20 cm and depths from 30 to 1000 m. In region *1*, the values

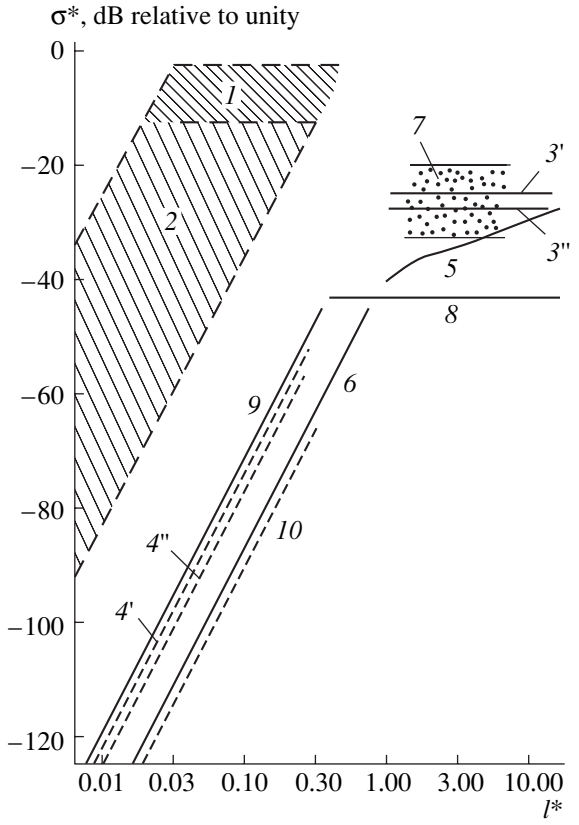

Fig. 4. Comparative estimates of the normalized frequency characteristics and backscattering cross sections of animals belonging to acoustically different groups in the DSL: (*1*) at resonance frequencies; (*2*) fish with swim bladders at frequencies below the resonance region; (*3*') fish according to the data of [7] for the dorsal insonification aspect; (*3*") fish according to the data of [7]: the average value over all aspects; (*4*' and *4*") fish without bladders for levels *3*' and *3*", respectively; (*5* and *6*) small crustaceans: calculations by formulas (4) and (5), respectively; (*7*) squids; (*8* and *9*) animals with soft homogeneous body tissues: formulas (6) and (7), respectively; and (*10*) the conditional animal with the same tissues.

of σ_r^* vary from 0.04 to 0.5 and correspond to fish with a normalized length l^* from 0.03 to 0.3. The large number of affecting factors hinders a more exact determination of the boundaries of this region. However, for each particular case, the calculation can be performed by the formulas presented above. At frequencies below the resonance, the scattering cross sections decrease by the law that rapidly approaches the fourth power of frequency, $(l^*)^4$, which determines the boundaries of region *2*.

Line *3*' in this figure corresponds to the value σ_1^*, while line *3*", to the value $\langle\sigma^*\rangle$ averaged over all possible insonified aspects (according to the data from [7]). Lines *4*' and *4*" determine the approximate dependences for fish without swim bladders in the low-frequency range. These lines are drawn on the basis of levels *3*' and *3*", respectively. Since such estimates are insufficiently strict, the low-frequency branches of the calculated dependences $\sigma^*(l^*)$, as well as the boundaries of regions *1* and *2*, are represented by dotted lines.

The second group of marine animals in the DSL, after fish, consists of crustaceans whose typical size is several centimeters; the most massive part of the crustacean body contains muscular tissues surrounded by a thin but much harder chitin testa. In its shape, this part is similar to a somewhat curved cylinder or an ellipsoid of revolution; its length is considered as the typical size of the crustacean, l. To describe the scattering properties of the animals of this group, theoretical models were developed and experimental data on the scattering cross sections were approximated. The main problems related to this subject were considered in detail in [8], and here we use the basic results of this publication.

Despite the apparent simplicity of the shape of the crustacean body, all computational models are described by rather cumbersome formulas. From our point of view, their complexity is inconsistent with the inaccuracy of initial data, namely, the scarcity of the data on the properties of the live tissues and on the angular dependences of the sound scattering by live crustaceans. For numerical estimates, it is expedient to use relatively simple approximate formulas obtained from the sufficiently large experimental data arrays, while the theoretical models can be used for clearing up the role of various factors affecting the process of the sound scattering by crustaceans and for explaining some effects observed in the measurements.

Most data used for constructing the empirical dependence $\sigma^*(l^*)$ were obtained for the mesopelagic crustaceans freely swimming in a fish pond or in the sea [8]. The special case is the investigation of freshwater shrimps whose size and body structure are similar to marine crustaceans [6]. The measurements testify to the closeness of their acoustic characteristics. In addition, the investigations of the freshwater shrimps are valuable, because they were carried out with live animals by the unique measuring system at the Andreev Acoustics Institute, to which the delivery of live crustaceans from the ocean is practically impossible. These experiments provided reliable records of the scattering patterns and angular dependences of the backscattering cross sections of crustaceans with the insonification and scattering angles smoothly varying within 360° [8].

The angular pattern of the backscatter from crustaceans is similar to that obtained for fish in the high-frequency region: it also has the typical maxima corresponding to the side and dorsal insonification aspects and the dips for the head and tail aspects. However, the experiments also revealed significant differences. The maxima are not "monolithic," as for fish, but represent groups of narrow peaks whose number and height grow with increasing frequency. We do not know any appropriate quantitative description of the complex shape of these angular characteristics of crustaceans in the high-frequency region. In most cases, in the full-scale sound-

ing of crustacean assemblages, the irregularity of the angular characteristic of each of them is automatically smoothed out: the sounding directional pattern simultaneously spans a large number of species whose orientation relative to the horizon undergoes small and random variations. The analysis of the experimental directional patterns of the backscatter shows that the effective "smoothed" cross section is, by a factor of 2–3, smaller than the calculated value of σ_{max} corresponding to the dorsal aspect of the model considered in [8]. All these facts testify to the advantage of the empirical formulas over the computational models.

In our previous paper [8], we considered the numerous results of measuring the backscattering cross sections of crustaceans in water when individual crustaceans or their assemblages were insonified from above. The experiments were carried out by different authors, by different methods of measurement, and at different frequencies. These results were recalculated to the quantities $\sigma^*(l^*)$ chosen for comparing the acoustic properties of different animals. On the basis of the set of these data, two empirical formulas [8] were proposed for practical estimates of the backscattering cross sections of crustaceans that inhabit the DSL. These formulas differ in frequency ranges. For high frequencies at dorsal (or side) insonification aspect, it has the form

$$\sigma^* = 7 \times 10^{-5} \times 10^{-0.13 l^*}, \text{ for } l^* \cong 1.1\text{–}15. \quad (4)$$

For the low-frequency region, for any aspect, we have

$$\sigma^* = 10^{-4} (l^*)^4, \text{ for } l^* < 1.1. \quad (5)$$

These formulas correspond to curves *5* and *6* in Fig. 4. In the high-frequency part, in contrast to the dependence $\sigma^*(l^*)$ for fish, a noticeable growth of the normalized scattering cross sections of crustaceans is observed as the frequency increases. Andreeva and Lysak [9] proposed a computational model for a crustacean to explain this feature. It was shown that, at low frequencies, for $l^* = 2\text{–}3$, the scattered field is small and determined mainly by the soft tissues of the body. As l^* increases to 10–20, the scattered field noticeably grows due to the contribution introduced by the testa of the crustacean.

The information on the backscatter of acoustic waves by small squids is presented in [1]. It was obtained for several kinds of squids whose size (the length of the mantle) l was approximately within 1 to 5 cm, while the sound frequency used in the experiment was 200 kHz. This corresponds to the interval $l^* = 1.2\text{–}6.2$. In the cited experiment [1], the target strength $TS = 10 \log \sigma$ expressed in decibels per unit area was chosen for the characterization of the backscattering cross section. These data, being recalculated to the normalized scattering cross sections and the squid length, are shown in Fig. 4 as region *7*. The vertical size of this region corresponds to the difference in σ^* obtained for different kinds of small squids. Approximations constructed for the data that were obtained for individual kinds of squids studied by the authors [1] show that the quantity σ^* almost does not depend on l^* for the aforementioned interval of values of the quantity l^*.

Consider now the scattering cross sections of the last group of DSL inhabitants: marine animals whose bodies consist of soft homogeneous tissues and have no hard or gaseous inclusions. Experimental and theoretical investigations concerned with this issue were performed for the Black Sea jellyfish, and the results of these studies are presented in [6, 10]. The experiments were carried out in the frequency range from 20 to 200 kHz for $l^* > 1$. In the low-frequency range, the measurements proved to be impossible because of the smallness of the scattering cross sections. The corresponding theoretical model was constructed using the small perturbation method.

Experimentally, it was found that, on the average, the backscattering cross section of jellyfish does not depend on its insonification aspect. This allowed us to propose a model of spherical shape with a volume equal to that of the scattering object. To make the comparison with other types of scatterers more convenient, the model diameter is also designated by l. For such a model, we proposed simplified semiempirical formulas that rather accurately describe the backscattering cross sections of jellyfish, when averaged over all insonifying aspects, in both high- and low-frequency ranges. In the plane $\sigma(l)$, these models define two linear segments approximating the theoretical curve with a sufficient accuracy. In the high-frequency region, it is a horizontal line $\sigma = \frac{l^2}{64}(\delta K)^2$, and, in the low-frequency region, a sloping line $\sigma = 1.9 l^2 (\delta K)^2 (l/\lambda)^4$. Here, $\delta K = (K - K_0)/K_0$, where K_0 is the bulk modulus of water and K is that of the scatterer tissues. The value of δK was chosen according to the experimental results on the basis of the best agreement of the calculated and measured values of σ in the high-frequency region. In the region $l^* \ll 1$, the straight line almost coincides with the calculated curve. The optimal position of the boundary between high- and low-frequency linear approximations corresponds to $l \cong 0.3\lambda$ and almost does not depend on the variations of the quantity δK within a factor of 2–3.

Passing to the normalized values of the size (frequency) and the backscattering cross section, we obtain simple formulas convenient for calculating the characteristics $\sigma^*(l^*)$ for jellyfish-like inhabitants of the DSL. In the high-frequency range, we have

$$\sigma^* \cong 2.5 \times 10^{-5}, \text{ for } l^* > 0.3, \quad (6)$$

and, in the low-frequency range, we have

$$\sigma^* \cong 3 \times 10^{-3} (l^*)^4, \text{ for } l^* < 0.3. \quad (7)$$

The results of calculation by these formulas are represented in Fig. 4 by lines *7* and *8*. These expressions can be used for estimating the scattering properties of other animals of this group that have substantially different

configurations only after the applicability of the spherical model to these animals is additionally investigated.

The general consideration of Fig. 4 allows one, in a wide range of normalized frequencies from $l^* \ll 1$ to $l^* \cong 10$–15, to compare the sound intensities backscattered by the animals of the DSL that have the same size but belong to different groups from the viewpoint of their acoustic properties.

Although the estimates presented above are fairly rough, it is clear that, in the low-frequency range, the scattering cross section of fish with swim bladders is several orders of magnitude greater than the scattering cross sections of any other animals of the same size in the DSL. In the high frequency range $l^* > 1$, the normalized backscattering cross sections of most animals are much greater than at low frequencies. However, the fish with a swim bladder is again the exception, for which the high-frequency values of σ^* remain smaller than the resonance values pertaining to low frequencies.

Of special interest are the relatively high values of the low-frequency scattering cross sections of jellyfish. Apparently, this can be explained by the inadequacy of the normalization chosen for the animals of this group, which substantially differ in their model shape from other animals. The volumes of fish and crustacean models of the same size l only slightly differ from one another, because both have a strongly elongated form. The volume of the spherical model of jellyfish of the same size l is much greater, and this difference is not compensated by the normalization accepted for low frequencies. Let us consider a conditional animal that is close in shape to crustaceans and fish, but, in acoustic–mechanical properties, to jellyfish. In this case, we can show that its backscattering cross section at low frequencies will be an order of magnitude smaller than that corresponding to line *8* in Fig. 4. The dashed line *10* shown in this figure corresponds to the conditional animal.

The increase in the normalized backscattering cross section of crustaceans in the high-frequency region of l^* is determined by the peculiarities of their body structure: the presence of a compact hard testa surrounding the soft tissues. Its contribution to the field scattered by a crustacean noticeably grows as the frequency increases. Neither fish nor jellyfish have similar features of the body structure.

The plots in Fig. 4 allow one to estimate the absolute values of the backscattering cross sections of the animals that inhabit the DSL, as well as their frequency characteristics $\sigma(f)$. For each value of l^*, at a chosen size l, there is a corresponding sound frequency $f = c(l^*/l)$, and vice versa, for each frequency f there is a corresponding normalized value of $l^* = l/\lambda$. This allows one, from the plots of Fig. 4, to determine the normalized value of σ^* for animals of each group for any specific values of l and f and to calculate the absolute value of the backscattering cross section by the formula $\sigma(f) = \sigma^* l^2$.

As an example, we consider the numerical characteristics of the scattering from a 5-cm-long crustacean at a frequency of 5 kHz (the wavelength $\lambda = 30$ cm). For this case, we have the normalized value $l^* = 0.17$ and, according to curve *6* in Fig. 4, the normalized scattering cross section is $\sigma^* = -75$ dB relative to unity, or $\sigma^* \cong 3 \times 10^{-8}$. The absolute value of the backscattering cross section can be easily evaluated as $\sigma = \sigma^* l^2 = 7.5 \times 10^{-7}$ cm^2. To obtain the corresponding frequency characteristic, one has to repeat this calculation for other frequencies in the high-frequency region, while, in the low-frequency range, one should use the fact that the variations of σ at l = const are proportional to f^4.

Thus, the plots shown in Fig. 4 not only give a clear idea about the relationship of the intensity of sound waves scattered by the animals of different groups in the DSL but also allow one to readily estimate the absolute values of the backscattering cross sections in a wide frequency range for animals of different sizes.

ACKNOWLEDGMENTS

We are grateful to our late colleague V.G. Samovol'kin, who made an invaluable contribution to the experimental research into the subject of this paper.

This work was supported by the Russian Foundation for Basic Research, project no. 01-05-64735.

REFERENCES

1. K. J. Benoit-Bird and W. L. Whitlov, J. Acoust. Soc. Am. **110**, 812 (2001).
2. I. B. Andreeva, Akust. Zh. **10**, 20 (1964) [Sov. Phys. Acoust. **10**, 17 (1964)].
3. L. P. Lebedeva, Akust. Zh. **11**, 197 (1965) [Sov. Phys. Acoust. **11**, 163 (1965)].
4. L. P. Lebedeva, Dissertation (Acoustics Inst.–Oceanology Inst., USSR Academy of Sciences, Moscow, 1966).
5. I. B. Andreeva, in *Acoustics of the Ocean*, Ed. by L. M. Brekhovskikh (Nauka, Moscow, 1974), pp. 491–558.
6. I. B. Andreeva and V. G. Samovol'kin, *Scattering of Acoustic Waves from Marine Animals* (Agropromizdat, Moscow, 1986).
7. R. H. Love, J. Acoust. Soc. Am. **62**, 1397 (1977).
8. I. B. Andreeva and L. L. Tarasov, Akust. Zh. **49** (2) (2003) (in press).
9. I. B. Andreeva and D. P. Lysak, Okeanologiya (Moscow) **25**, 425 (1985).
10. I. B. Andreeva and L. L. Tarasov, Okeanologiya (Moscow) **25**, 43 (1985).

Translated by Yu. Lysanov

Acoustical Physics, Vol. 49, No. 3, 2003, pp. 269–275. Translated from Akusticheskiĭ Zhurnal, Vol. 49, No. 3, 2003, pp. 325–331.

Is It Possible to Determine the Type of Fastening of a Vibrating Plate from Its Sounding?

A. M. Akhtyamov

Department of Differential Equations, Bashkortostan State University, ul. Frunze 32, Ufa, Bashkortostan, 450074 Russia

e-mail: AkhtyamovAM@mail.ru

Received January 24, 2002

Abstract—The problem of determining the type of fastening of a circular plate inaccessible to direct observation from the natural frequencies of its symmetric flexural vibrations is considered. The uniqueness theorem for the solution to this inverse problem is proved, and a method for the reconstruction of unknown boundary conditions is indicated. An approximate formula for the determination of unknown boundary conditions from three natural frequencies is obtained. It is assumed that the natural frequencies can be given approximately, within a certain accuracy. The method of an approximate calculation of unknown boundary conditions is illustrated by four examples of different cases of the plate fastening (a free support, an elastic fixing, a floating fixing, and a free edge). © *2003 MAIK "Nauka/Interperiodica".*

INTRODUCTION

Circular plates are parts of various devices. If it is impossible to observed the plate directly, the only source of information on the possible defects of its fastening can be the natural frequencies of its flexural vibrations. A question arises: "Is it possible to determine unambiguously the type of fastening of a circular plate from the natural frequencies of its symmetric flexural vibrations?" This paper gives and substantiates a positive answer to this question.

Similar problem statements were proposed in [1–9]. These papers can be conventionally divided into three groups.

The first group is related to the problems of acoustic diagnosis. For example, a question was put in [1]: "Is it possible to determine the shape of a drum from its sounding?" Problems of acoustic diagnosis of mechanisms were solved in [2, 3]. The size of an object and its location in a chamber were determined in [4] from the natural frequency shifts. One more paper [5] was devoted to the method of detecting the railway sleepers that lost close contact with the railroad bed by means of impact excitation of vibrations and analysis of the resulting acoustic signals. Unlike all these and similar papers, below, we determine not the shape of a region, the dimensions of an object, or its position but the conditions of the plate fastening.

The second group of papers is devoted to the problem of noise suppression in car and aircraft engines. However, in the papers devoted to this topic, the solutions that satisfy the necessary requirements to noise, pressure, and other parameters, are sought (see, e.g., [6]). Inverse boundary problems are also formulated in these papers. For example, conditions at the input and output of exhaust pipes and pipe systems were studied in [7, 8]. Contrary to these studies, this paper studies not the conditions at the input and output of pipe systems but the boundary conditions for the plate vibration problem.

In the third group of papers, so-called inverse spectral problems are considered. In these papers, it is necessary to reconstruct the coefficients of a differential equation and the boundary conditions (see [9], for example). However, in these studies, not a single spectrum is used as the data for the reconstruction of the boundary conditions (as in this paper) but several spectra or other additional spectral data (for example, the spectral function, the Weyl function, or the so-called weight numbers). Moreover, the main purpose of these studies is the reconstruction of the coefficients in an equation and not in the boundary conditions, whereas the purpose of the present paper is the reconstruction of the boundary conditions of a spectral problem with known coefficients in an equation from a single spectrum.

Thus, this paper differs from the papers of the aforementioned three groups in both formulation and method of solution.

My previous papers [10, 11] were devoted to the reconstruction of boundary conditions of spectral problems, and, in our common work with I.Sh. Akhatov [12], the fastening at one end of a rod was determined from the natural frequencies. The present paper continues the studies described in these papers.

Let us give the mathematical formulation of the problem before describing the methods of its solution.

1063-7710/03/4903-0269$24.00

FORMULATION OF THE INVERSE PROBLEM

The problem on symmetric vibrations of a circular plate is reduced [13] to the following spectral problem:

$$\frac{d^4y}{dr^4} + \frac{2}{r}\frac{d^3y}{dr^3} - \frac{1}{r^2}\frac{d^2y}{dr^2} + \frac{1}{r^3}\frac{dy}{dr} - \lambda^4 y = 0, \quad (1)$$

$$U_1(y) = 0, \quad U_2(y) = 0. \quad (2)$$

Here, $U_i(y) = \sum_{j=1}^{4} a_{ij} (L_j y)_{r=a}$ $(i = 1, 2)$ are the linear forms characterizing the plate fastening, where

$$L_1 y(r) = y(r),$$

$$L_2 y(r) = \frac{dy(r)}{dr},$$

$$L_3 y(r) = \frac{d^2y(r)}{dr^2} + \frac{\nu}{r}\frac{dy(r)}{dr},$$

$$L_4 y(r) = \frac{d}{dr}\left(\frac{d^2y(r)}{dr^2} + \frac{1}{r}\frac{dy(r)}{dr}\right),$$

$\lambda = (\rho h \omega^2/D)^{1/4}$, a is the plate radius, ω is the frequency parameter, D is the flexural rigidity of the plate, ν is the Poisson ratio, h is the thickness, and ρ is the density.

Let us denote the matrix consisting of the coefficients a_{ij} of the forms $U_1(y)$ and $U_2(y)$ by A, and its minors, by M_{ij}:

$$A = \begin{Vmatrix} a_{11} & a_{12} & a_{13} & a_{14} \\ a_{21} & a_{22} & a_{23} & a_{24} \end{Vmatrix}, \quad M_{ij} = \begin{vmatrix} a_{1i} & a_{1j} \\ a_{2i} & a_{2j} \end{vmatrix}.$$

The determination of the forms $U_1(y)$ and $U_2(y)$ is equivalent to the determination of a linear span $\langle \mathbf{a}_1, \mathbf{a}_2 \rangle$ constructed using the vectors $\mathbf{a}_i = (a_{i1}, a_{i2}, a_{i3}, a_{i4})^T$ $(i = 1, 2)$.

Different cases of circular plate fastening are given in [14–16]. They are listed below together with their corresponding matrices A.

1. Clamping: $\begin{Vmatrix} 1 & 0 & 0 & 0 \\ 0 & 1 & 0 & 0 \end{Vmatrix}$;

2. Free support: $\begin{Vmatrix} 1 & 0 & 0 & 0 \\ 0 & 0 & 1 & 0 \end{Vmatrix}$;

3. Free edge: $\begin{Vmatrix} 0 & 0 & 1 & 0 \\ 0 & 0 & 0 & 1 \end{Vmatrix}$;

4. Floating fixing: $\begin{Vmatrix} 0 & 1 & 0 & 0 \\ 0 & 0 & 0 & 1 \end{Vmatrix}$;

5. Five different kinds of elastic fixing:

$$\begin{Vmatrix} 0 & 1 & 0 & 0 \\ c_1 & 0 & 0 & 1 \end{Vmatrix}; \quad \begin{Vmatrix} 1 & 0 & 0 & 0 \\ 0 & -c_2 & 1 & 0 \end{Vmatrix}; \quad \begin{Vmatrix} 0 & 0 & 1 & 0 \\ c_1 & 0 & 0 & 1 \end{Vmatrix};$$

$$\begin{Vmatrix} 0 & 0 & 0 & 1 \\ 0 & -c_2 & 1 & 0 \end{Vmatrix}; \quad \begin{Vmatrix} c_1 & 0 & 0 & 1 \\ 0 & -c_2 & 1 & 0 \end{Vmatrix}.$$

It is necessary to note that, in all nine cases, we have

$$M_{14} = 0, \quad \text{and} \quad M_{23} = 0. \quad (3)$$

Therefore, in terms of the spectral problem given by Eqs. (1) and (2), the above inverse problem is formulated as follows: the coefficient a_{ij} of the forms $U_1(y)$ and $U_2(y)$ of the problem given by Eqs. (1) and (2) are unknown; the rank of the matrix A constructed from these coefficients is equal to two, and the minors M_{14} and M_{23} of this matrix are equal to zero; and the nonzero eigenvalues λ_k of the problem given by Eq. (1) are known. It is necessary to reconstruct the linear span $\langle \mathbf{a}_1, \mathbf{a}_2 \rangle$ of the vectors $\mathbf{a}_i = (a_{i1}, a_{i2}, a_{i3}, a_{i4})^T$ $(i = 1, 2)$.

Note that we deal with the uniqueness of the reconstruction of the linear span rather than of all coefficients a_{ij}, since, for example, the boundary conditions

$$y(r) = 0, \quad \frac{dy(r)}{dr} = 0$$

and

$$y(r) - \frac{dy(r)}{dr} = 0, \quad y(r) + \frac{dy(r)}{dr} = 0$$

at $r = a$ are equivalent, while their corresponding coefficients a_{ij} are different.

UNIQUENESS OF THE SOLUTION TO THE INVERSE PROBLEM

Let us consider the following spectral problem together with the problem set by Eqs. (1) and (2):

$$\frac{d^4y}{dr^4} + \frac{2}{r}\frac{d^3y}{dr^3} - \frac{1}{r^2}\frac{d^2y}{dr^2} + \frac{1}{r^3}\frac{dy}{dr} - \lambda^4 y = 0, \quad (4)$$

$$\tilde{U}_1(y) = 0, \quad \tilde{U}_2(y) = 0. \quad (5)$$

Here, $\tilde{U}_i(y) = \sum_{j=1}^{4} b_{ij} (L_j y(r))_{r=a}$ $(i = 1, 2)$ are the linear forms characterizing the plate fastening.

Let us denote the matrix constructed from the coefficients b_{ij} of the forms $\tilde{U}_1(y)$ and $\tilde{U}_2(y)$ by B, and its minors, by $\tilde{M}_{ij}$:

$$B = \begin{Vmatrix} b_{11} & b_{12} & b_{13} & b_{14} \\ b_{21} & b_{22} & b_{23} & b_{24} \end{Vmatrix}, \quad M_{ij} = \begin{vmatrix} b_{1i} & b_{1j} \\ b_{2i} & b_{2j} \end{vmatrix}.$$

We denote the linear span of the vectors $\mathbf{b}_i = (b_{i1}, b_{i2}, b_{i3}, b_{i4})^T$ $(i = 1, 2)$ by $\langle \mathbf{b}_1, \mathbf{b}_2 \rangle$.

Theorem of the uniqueness of solution to the inverse problem. Let the following conditions be valid:

$$\operatorname{rank} A = \operatorname{rank} B = 2, \tag{6}$$

$$M_{14} = \tilde{M}_{14} = M_{23} = \tilde{M}_{23} = 0. \tag{7}$$

If the nonzero eigenvalues $\{\lambda_k\}$ of the problem given by Eqs. (1) and (2) and the nonzero eigenvalues $\{\tilde{\lambda}_k\}$ of the problem defined by Eqs. (4) and (5) are identical with allowance for their multiplicity, the linear spans $\langle \mathbf{a}_1, \mathbf{a}_2 \rangle$ and $\langle \mathbf{b}_1, \mathbf{b}_2 \rangle$ are also identical.

Proof. A general solution to the problem on vibrations of a circular plate (see [14]) is the function

$$y(r) = y(r, \lambda) = C_1 J_0(\lambda r) + C_2 I_0(\lambda r),$$

where standard notations for Bessel functions are used.

The boundary conditions $U_i(y) = 0$, $i = 1, 2$ are used to determine the constants C_1 and C_2. The equation for frequencies is obtained from the condition of the existence of a nonzero solution for C_i. The latter solution exists if and only if [17] the determinant of the corresponding system

$$\Delta(\lambda) \equiv \begin{vmatrix} U_1(J_0) & U_1(I_0) \\ U_2(J_0) & U_2(I_0) \end{vmatrix}$$

is equal to zero.

Applying the Laplace theorem to calculate the determinants, we obtain

$$\begin{aligned} \Delta(\lambda) \equiv {} & M_{12}[(L_1J_0)(L_2I_0) - (L_2J_0)(L_1I_0)] \\ & + M_{13}[(L_1J_0)(L_3I_0) - (L_3J_0)(L_1I_0)] \\ & + M_{14}[(L_1J_0)(L_4I_0) - (L_4J_0)(L_1I_0)] \\ & + M_{23}[(L_2J_0)(L_3I_0) - (L_3J_0)(L_2I_0)] \\ & + M_{24}[(L_2J_0)(L_4I_0) - (L_4J_0)(L_2I_0)] \\ & + M_{34}[(L_3J_0)(L_4I_0) - (L_4J_0)(L_3I_0)]. \end{aligned} \tag{8}$$

Using Eq. (7), we obtain

$$\begin{aligned} \Delta(\lambda) \equiv {} & M_{12}[(L_1J_0)(L_2I_0) - (L_2J_0)(L_1I_0)] \\ & + M_{13}[(L_1J_0)(L_3I_0) - (L_3J_0)(L_1I_0)] \\ & + M_{24}[(L_2J_0)(L_4I_0) - (L_4J_0)(L_2I_0)] \\ & + M_{34}[(L_3J_0)(L_4I_0) - (L_4J_0)(L_3I_0)]. \end{aligned} \tag{9}$$

From the properties of the Bessel functions J_0 and I_0, it follows that the function $\Delta(\lambda)$ is an entire function of the first order. Since $\Delta(\lambda) \not\equiv 0$, from the Hadamard factorization theorem (see [18]), it follows that the determinant $\Delta(\lambda)$ of the set of equations

$$U_1(y) = 0, \quad U_2(y) = 0$$

for the determination of the constants C_i and the determinant $\tilde{\Delta}(\lambda)$ of the set of equations

$$\tilde{U}_1(y) = 0, \quad \tilde{U}_2(y) = 0$$

for the determination of the constants $\tilde{C}_i$ are connected by the relation

$$\Delta(\lambda) \equiv C\lambda^k e^{a\lambda} \tilde{\Delta}(\lambda), \tag{10}$$

where a is a real number, k is a nonnegative integer number, and C is a nonzero constant.

Since $y(r, -\lambda) = y(r, \lambda)$, $\Delta(\lambda)$ and $\tilde{\Delta}(\lambda)$ are even functions of λ. Then, we find from Eq. (10) that $a = 0$ and $k = 2m$.

Hence,

$$\begin{aligned} & (M_{12} - C\lambda^{2m}\tilde{M}_{12}) f_1(\lambda) \\ & + (M_{13} - C\lambda^{2m}\tilde{M}_{13}) f_2(\lambda) \\ & + (M_{24} - C\lambda^{2m}\tilde{M}_{24}) f_3(\lambda) \\ & + (M_{34} - C\lambda^{2m}\tilde{M}_{34}) f_4(\lambda) \equiv 0, \end{aligned} \tag{11}$$

where

$$\begin{aligned} f_1(\lambda) &= (L_1J_0)(L_2I_0) - (L_2J_0)(L_1I_0), \\ f_2(\lambda) &= (L_1J_0)(L_3I_0) - (L_3J_0)(L_1I_0), \\ f_3(\lambda) &= (L_2J_0)(L_4I_0) - (L_4J_0)(L_2I_0), \\ f_4(\lambda) &= (L_3J_0)(L_4I_0) - (L_4J_0)(L_3I_0). \end{aligned}$$

Let us show that m is equal to zero. Let us assume the contrary. Let $m \neq 0$. Expanding the functions $f_i(\lambda)$ ($i = 1, 2, 3, 4$) into the Maclaurin series, we find, with the help of the MAPLE software, that the functions

$$f_1(\lambda),\ f_2(\lambda),\ f_3(\lambda),\ f_4(\lambda),$$
$$\lambda^{2m} f_1(\lambda),\ \lambda^{2m} f_2(\lambda),\ \lambda^{2m} f_3(\lambda),\ \lambda^{2m} f_4(\lambda)$$

at $m \neq 0$ form a system of linearly independent functions. Taking this fact into account, we obtain from Eq. (11) the relations

$$M_{12} = \tilde{M}_{12} = M_{13} = \tilde{M}_{13} = M_{24} = \tilde{M}_{24} = M_{34} = \tilde{M}_{34} = 0,$$

which, together with Eq. (7), contradict the condition given by Eq. (6), according to which the rank of the matrix A is equal to two. Thus, $m = 0$.

By virtue of the linear independence of the functions

$$f_1(\lambda),\ f_2(\lambda),\ f_3(\lambda),\ f_4(\lambda)$$

we obtain from Eq. (11) the equation

$$(M_{12}, M_{13}, M_{14}, M_{23}, M_{24}, M_{34})^T = C(\tilde{M}_{12}, \tilde{M}_{13}, \tilde{M}_{14}, \tilde{M}_{23}, \tilde{M}_{24}, \tilde{M}_{34})^T, \quad (12)$$

which is equivalent to proportionality of the bivectors $\mathbf{a}_1 \wedge \mathbf{a}_2$ and $\mathbf{b}_1 \wedge \mathbf{b}_2$.

It is known (see [19]) that there is a natural bijective correspondence between the classes of proportional nonzero bivectors and two-dimensional subspaces of the vector space. In this correspondence, the vector product $\mathbf{x}_1 \wedge \mathbf{x}_2$ of the vectors of the arbitrary subspace basis $\mathbf{x}_1$, $\mathbf{x}_2$ answers to each subspace, and the subspace $\langle \mathbf{x}_1, \mathbf{x}_2 \rangle$ answers to each bivector $\mathbf{x}_1 \wedge \mathbf{x}_2$.

Therefore, from Eq. (12), it follows that $\langle \mathbf{a}_1, \mathbf{a}_2 \rangle = \langle \mathbf{b}_1, \mathbf{b}_2 \rangle$, which was to be proved.

Remark 1. The conditions given by Eqs. (7) do not limit the physical formulation of the problem. They are needed only to reconstruct the boundary conditions from three natural frequencies and not from a greater number of them.

METHOD OF RECONSTRUCTING THE BOUNDARY CONDITIONS FROM THREE NATURAL FREQUENCIES

From the proven uniqueness theorem, it follows that it is sufficient to use the first n eigenvalues to reconstruct the boundary conditions approximately. The corresponding method is described in [12]. It is based on the possibility of the reconstruction of the entire function $\Delta(\lambda)$ by all its zeros with the help of the Weierstrass function (an infinite product) and the approximate reconstruction of the function $\Delta(\lambda)$ by its first n zeros with the help of a finite product with a large number of factors.

Another way to reconstruct the boundary conditions is the method based on solving a set of linear algebraic equations. It is simpler in use and more precise (since there is no error accumulation).

Let λ_1, λ_2, and λ_3 be the first three eigenvalues of the spectral problem set by Eqs. (1) and (2), i.e., three first roots of the function $\Delta(\lambda)$. It follows from Eq. (9) that λ_1, λ_2, and λ_3 satisfy the equations

$$\Delta(\lambda_j) = M_{12} f_1(\lambda_j) + M_{13} f_2(\lambda_j) + M_{24} f_3(\lambda_j) + M_{34} f_4(\lambda_j) = 0, \quad j = 1, 2, 3. \quad (13)$$

Equations (13) represent a set of three equations in four unknowns M_{12}, M_{13}, M_{24}, and M_{34}. As it follows from the uniqueness theorem, this set has a solution that is unique, accurate to a constant. Thus, Eqs. (13) uniquely within a constant determine the bivector

$$(M_{12}, M_{13}, M_{14}, M_{23}, M_{24}, M_{34})^T = \mathbf{a}_1 \wedge \mathbf{a}_2,$$

from which the boundary conditions are determined by the method developed in [12].

If the first three eigenvalues λ_j of the problem given by Eq. (1) are known only approximately,

$$\lambda_j \approx \mu_j \quad (j = 1, 2, 3),$$

the inverse problem of the determination of boundary conditions can be solved approximately. To do this, we substitute the values of μ_j (j = 1, 2, 3), which approximately coincide with the first three positive eigenvalues, into Eq. (13). We obtain a set of three homogeneous algebraic equations in four unknowns M_{12}, M_{13}, M_{24}, and M_{34}:

$$M_{12} f_1(\mu_j) + M_{13} f_2(\mu_j) + M_{24} f_3(\mu_j) + M_{34} f_4(\mu_j) \approx 0. \quad (14)$$

The resulting set of equations has an infinite number of solutions. From the proved uniqueness theorem, it follows that unknown minors can be determined approximately, accurate to a coefficient. Thus, if μ_j (j = 1, 2, 3) differ from the first three eigenvalues only slightly, the resulting set of equations must have a rank equal to three and a solution determined accurate to a constant. Calculations conducted using MAPLE software confirm this statement. Unknown minors are determined accurate to a constant. In this case, the order of the calculation error almost does not differ from the order of the error of closeness between the values of μ_j and λ_j and only in some cases can grow by four orders. However, the main advantage of this method is the fact that only the first three eigenvalues are needed for its realization.

EXAMPLES

Let us consider the application of the method for the determination of the boundary conditions from the eigenvalues by using specific examples. In all examples considered below, we assume for definiteness that the plate radius is equal to unity and the Poisson ratio ν is equal to 1/3 (according to Wertheim).

Example 1 (Free Support)

If

$$\mu_1 = 2.232449096, \quad \mu_2 = 5.455111632, \quad \mu_3 = 8.613495974$$

are the values of $(\rho h \omega_i^2 / D)^{1/4}$ that correspond to the three natural frequencies ω_i determined by a frequency meter, the solution to the set of equations (14) determined accurate to a constant has the form

$$M_{34} = 10^{-13}, \quad M_{24} = -0.6198612900 \times 10^{-12}, \quad M_{12} = -0.2186626466 \times 10^{-9}, \quad M_{13} = 0.2380103959. \quad (15)$$

In addition, according to the problem statement, we have $M_{14} = 0$ and $M_{23} = 0$.

Let us determine the linear span corresponding to these minors. Let $\mathbf{x} = (x_1, x_2, x_3, x_4)^T$ be an arbitrary vector of the desired linear span $\langle \mathbf{a}_1, \mathbf{a}_2 \rangle$. In this case, the coordinates of the vector $\mathbf{x}$ satisfy the condition

$$\operatorname{rank}\begin{Vmatrix} a_{11} & a_{12} & a_{13} & a_{14} \\ a_{21} & a_{22} & a_{23} & a_{24} \\ x_1 & x_2 & x_3 & x_4 \end{Vmatrix} = 2. \qquad (16)$$

Since

$$M_{13} = \begin{vmatrix} a_{11} & a_{13} \\ a_{21} & a_{23} \end{vmatrix} \neq 0,$$

condition (16) is equivalent to vanishing of both minors bordering M_{13}.

Expanding the corresponding determinants with respect to the third line, we obtain

$$x_1 M_{23} - x_2 M_{13} + x_3 M_{12} = 0,$$
$$x_1 M_{34} - x_3 M_{14} + x_4 M_{13} = 0.$$

We substitute the values of M_{ij} [Eqs. (15)] into these equations. The values of M_{12}, M_{23}, M_{14}, and M_{34} can be set equal to zero (the accuracy is 10^{-8}, i.e., rather high). Therefore, we can assume that $x_2 = 0$ and $x_4 = 0$, and an arbitrary vector of the desired linear span has the form $\mathbf{x} = (x_1, 0, x_3, 0)^T$.

As the base vectors for this linear span, we can choose, for example, the vectors

$$\mathbf{a}_1 = (1, 0, 0, 0)^T \text{ and } \mathbf{a}_2 = (0, 0, 1, 0)^T.$$

Therefore, the desired boundary conditions have the form

$$L_1 y(r) = y(r) = 0,$$
$$L_3 y(r) = \frac{d^2 y(r)}{dr^2} + \frac{\nu}{r}\frac{dy(r)}{dr} = 0.$$

This means that the edge inaccessible to direct observation is freely supported.

It is necessary to note that the type of fastening of the plate edge is determined correctly. The values of μ_1, μ_2, and μ_3 given above approximately coincide with the first three roots of the equation $\Delta(\lambda) = 0$. The accuracy of the approximation is equal to 10^{-9}.

Example 2 (Elastic Fixing)

If

$$\mu_1 = 3.822859373, \quad \mu_2 = 7.014140157$$
$$\mu_3 = 10.172993460$$

are the values of $(\rho h \omega_i^2 / D)^{1/4}$ corresponding to the three natural frequencies ω_i determined by a frequency meter, the solution to the set of equations (14) determined accurate to a constant has the form

$$M_{13} = 0.7280190 \times 10^{-8}, \quad M_{12} = -0.1458655,$$
$$M_{24} = -0.1458655, \quad M_{34} = 10^{-11}.$$

We can assume approximately that the bivector $\mathbf{a}_1 \wedge \mathbf{a}_2$ is equal to

$$(M_{12}, M_{13}, M_{14}, M_{23}, M_{24}, M_{34})^T = (-1, 0, 0, 0, 1, 0)^T$$

accurate to a constant. The approximation accuracy is 10^{-7}.

Let us determine the linear span corresponding to this bivector. Let $\mathbf{x} = (x_1, x_2, x_3, x_4)^T$ be an arbitrary vector of the desired linear span $\langle \mathbf{a}_1, \mathbf{a}_2 \rangle$. In this case, the coordinates of the vector $\mathbf{x}$ satisfy the condition

$$\operatorname{rank}\begin{Vmatrix} a_{11} & a_{12} & a_{13} & a_{14} \\ a_{21} & a_{22} & a_{23} & a_{24} \\ x_1 & x_2 & x_3 & x_4 \end{Vmatrix} = 2. \qquad (17)$$

Since

$$M_{12} = \begin{vmatrix} a_{11} & a_{12} \\ a_{21} & a_{22} \end{vmatrix} \neq 0,$$

condition (17) is equivalent to vanishing of both minors bordering M_{12}.

Expanding the corresponding determinants with respect to the third line, we obtain

$$x_1 M_{23} - x_2 M_{13} + x_3 M_{12} = 0,$$
$$x_1 M_{24} - x_2 M_{14} + x_4 M_{12} = 0.$$

The values of M_{13}, M_{23}, and M_{14} can be set equal to zero (the accuracy is equal to 10^{-7}, i.e., rather high). Therefore, we can assume that $-x_3 = 0$ and $x_1 - x_4 = 0$, and an arbitrary vector of the desired linear span has the form $\mathbf{x} = (x_1, x_2, 0, x_1)^T$.

As the base vectors of this linear span, we can choose, e.g., the vectors

$$\mathbf{a}_1 = (0, 1, 0, 0)^T \text{ and } \mathbf{a}_2 = (1, 0, 0, 1)^T.$$

Therefore, the desired boundary conditions have the form

$$L_2 y(r) = \frac{dy(r)}{dr} = 0,$$
$$(L_1 + L_4) y(r) = y(r) + \frac{d}{dr}\left(\frac{d^2 y(r)}{dr^2} + \frac{1}{r}\frac{dy(r)}{dr}\right) = 0.$$

Precisely these boundary conditions (the first kind of elastic fixing $c_1 = 1$) were used in selecting the values of μ_1, μ_2, and μ_3, which coincide with an accuracy of 10^{-9} with the first three roots of the corresponding characteristic equation $\Delta(\lambda) = 0$.

Example 3 (Floating Fixing)

If

$$\mu_1 = 3.831705970, \quad \mu_2 = 7.015586670,$$
$$\mu_3 = 10.17346814,$$

we have, accurate to a constant,

$$M_{13} = 0.3403043 \times 10^{-6}, \quad M_{12} = -0.2587103 \times 10^{-5},$$
$$M_{24} = -0.6014163, \quad M_{34} = 10^{-9}.$$

We can approximately assume that the bivector $\mathbf{a}_1 \wedge \mathbf{a}_2$ is equal, accurate to a constant, to

$$(M_{12}, M_{13}, M_{14}, M_{23}, M_{24}, M_{34})^T$$
$$= (0, 0, 0, 0, 1, 0)^T.$$

The approximation accuracy is 10^{-5}.

Therefore, the desired boundary conditions have the form

$$L_2 y(r) = \frac{dy(r)}{dr} = 0,$$

$$L_4 y(r) = \frac{d}{dr}\left(\frac{d^2 y(r)}{dr^2} + \frac{1}{r}\frac{dy(r)}{dr}\right) = 0.$$

The values of μ_1, μ_2, and μ_3, which coincide with an accuracy of 10^{-9} with the first three roots of the corresponding characteristic equation $\Delta(\lambda) = 0$, were selected according to these conditions.

Example 4 (Free Edge)

If

$$\mu_1 = 3.012657950, \quad \mu_2 = 6.205965863,$$
$$\mu_3 = 9.371213583,$$

we have

$$M_{24} = 10^{-9}, \quad M_{34} = 0.1454148,$$
$$M_{13} = -0.6555181 \times 10^{-7},$$
$$M_{12} = -0.8146801 \times 10^{-6}.$$

We can assume approximately that the bivector $\mathbf{a}_1 \wedge \mathbf{a}_2$ is equal, accurate to a constant, to

$$(M_{12}, M_{13}, M_{14}, M_{23}, M_{24}, M_{34})^T$$
$$= (0, 0, 0, 0, 0, 1)^T.$$

The approximation accuracy is 10^{-6}.

Therefore, the desired boundary conditions have the form

$$L_3 y(r) = \frac{d^2 y(r)}{dr^2} + \frac{\nu}{r}\frac{dy(r)}{dr} = 0,$$

$$L_4 y(r) = L_4 y(r) = \frac{d}{dr}\left(\frac{d^2 y(r)}{dr^2} + \frac{1}{r}\frac{dy(r)}{dr}\right) = 0.$$

This means that the edge inaccessible to direct observation is free.

It is necessary to note that, as in the preceding example, the values of μ_1, μ_2, and μ_3 approximately coincide with the first three roots of the characteristic equation $\Delta(\lambda) = 0$ corresponding to a free edge. (The approximation accuracy is 10^{-7}.)

Remark 2. How essential is the utilization of precisely the first nonzero eigenvalues for the approximate reconstruction of the boundary conditions? Maybe it is sufficient to use an arbitrary finite set of eigenvalues (natural frequencies) for this purpose? Let us consider an example showing that even the utilization of an infinite set of nonzero eigenvalues as the reconstruction data still does not guarantee the uniqueness of the reconstruction of the boundary conditions.

For a plate with a free edge in the case of large k and symmetric vibrations, the eigenvalues λ_k are almost equal to the values $\lambda_k = k\pi$ (see [13]), while, for a plate clamped along its contour at large λ_k and symmetric vibrations, the problem eigenvalues λ_k are almost equal to the values $\lambda_k = (k + 1)\pi$. If we ignore the sequence order of eigenvalues, starting from the eighth one, they almost coincide on the set of numbers $\{k\pi\}$.

Therefore, totally different boundary conditions correspond to the infinite set of eigenvalues $\{k\pi\}$ ($k = 8, 9, 10, \ldots$). Thus, for the uniqueness of the reconstruction of boundary conditions, it is essential to use precisely the first nonzero eigenvalues.

Thus, the type of fastening of a circular plate can be fully determined from the first natural frequencies measured by a frequency meter with a certain error.

ACKNOWLEDGMENTS

I am grateful to I.Sh. Akhatov, M.A. Il'gamov, and S.F. Urmancheev for useful discussions. This work was supported by the Russian Foundation for Basic Research, project no. 01-01-0096.

REFERENCES

1. M. Kac, Am. Math. Monthly **73** (4), 1 (1966).
2. B. V. Pavlov, *Acoustic Diagnosis of Mechanisms* (Mashinostroenie, Moscow, 1971).
3. I. A. Birger, *Technical Diagnosis* (Mashinostroenie, Moscow, 1978).
4. W. W. Quinli and F. Fricke, Nat. Conf. Publ.–Inst. Eng. Aust., No. 9, 329 (1990).

5. N. A. Vasil'ev and S. I. Dvornikov, Akust. Zh. **46**, 424 (2000) [Acoust. Phys. **46**, 364 (2000)].
6. S. Oh, H. Kim, and Y. Park, J. Acoust. Soc. Am. **111**, 180 (2002).
7. S. Frikha, G. Coffignal, and J. L. Trolle, J. Sound Vibr. **233** (3), 495 (2000).
8. S. Frikha, M. Gaudin, and G. Coffignal, J. Sound Vibr. **241** (3), 373 (2001).
9. V. A. Yurko, *Inverse Spectral Problems for Linear Differential Operators and Their Applications* (Sarat. Pedagog. Inst., Saratov, 2001; Gordon and Breach, New York, 2000).
10. A. M. Akhtyamov, Differ. Uravn. **35** (8), 1127 (1999).
11. A. M. Akhtyamov, Fundam. Prikl. Mat. **6** (4), 995 (2000).
12. I. Sh. Akhatov and A. M. Akhtyamov, Prikl. Mat. Mekh. **65** (2), 290 (2001).
13. W. Strutt (Lord Rayleigh), *The Theory of Sound* (Macmillan, London, 1929; Gostekhizdat, Moscow, 1940), Vol. 1.
14. *Vibrations in Engineering*, Vol. 1: *Vibrations of Linear Systems*, Ed. by V. V. Bolotin (Mashinostroenie, Moscow, 1978).
15. V. S. Gontkevich, *Free Vibrations of Plates and Shells* (Naukova Dumka, Kiev, 1964).
16. *Strength, Stability, Vibrations. Handbook*, Ed. by I. A. Birger and Ya. G. Panovko (Mashinostroenie, Moscow, 1968), Vol. 1.
17. M. A. Naĭmark, *Linear Differential Operators*, 2nd ed. (Nauka, Moscow, 1969; Ungar, New York, 1967).
18. B. Ya. Levin, *Distribution of Zeros of Entire Functions* (GITTL, Moscow, 1956; American Mathematical Society, Providence, 1980).
19. M. M. Postnikov, *Lectures on Geometry: Linear Algebra and Differential Geometry* (Nauka, Moscow, 1979).

Translated by M. Lyamshev

Acoustical Physics, Vol. 49, No. 3, 2003, pp. 276–284. Translated from Akusticheskiĭ Zhurnal, Vol. 49, No. 3, 2003, pp. 332–341.

Physical and Technological Aspects of Ultrasonic Imaging of Brain Structures through Thick Skull Bones: 1. Theoretical and Model Studies

S. V. Baĭkov*, A. M. Molotilov, and V. D. Svet***

** Andreev Acoustics Institute, Russian Academy of Sciences, ul. Shvernika 4, Moscow, 117036 Russia*

*** OOO AMM-2000, Spasskiĭ tupik 6, Moscow, 129090 Russia*

e-mail: vsvet@akin.ru

Received December 25, 2001

Abstract—The basic effects that restrict the potentialities of the ultrasonic imaging of brain structures by echo sounding through thick skull bones are considered. It is demonstrated that the main interfering factors are the echo signals from multiple reflections in the bone, its unknown inhomogeneity in depth, and the strong attenuation. To eliminate these effects, the use of a matched spatial processing and complex wideband signals with their subsequent correlation compression is proposed. A simulation of the proposed signal processing techniques confirmed the possibility of brain structure imaging with a spatial resolution of about 1 mm by ultrasonic echo sounding with acceptable intensities through bones up to 20 mm thick at frequencies of 1–2 MHz. © *2003 MAIK "Nauka/Interperiodica".*

INTRODUCTION

Ultrasonic methods of medical diagnostics belong to the most popular methods of medical examination. They provide acoustic images of viscera with high resolution and contrast. At the same time, ultrasonic diagnostics of brain structures encounters some difficulties. The major restrictions are caused by the thick skull bones, which attenuate and distort the ultrasonic field. Therefore, transcranial ultrasonic diagnostics is usually conducted through the so-called "acoustic transparence windows," i.e., the regions where the skull bones are thin (temporal regions and eyeballs) [1]. However, the anatomic location of such "windows" and their small area make it impossible to obtain high-quality ultrasonic images.

Investigations of signal processing techniques that eliminate or reduce the interfering effect of thick skull bones were started over 20 years ago [2]. However, certain progress in this area was achieved only in the last six or seven years, when researchers turned their attention to the methods of phase conjugation developed earlier in coherent optics and radar. The methods of phase conjugation are referred to differently in the literature: medium-matched filtration [3, 4], method of time mirrors [5–8], matched space–time processing, etc. The physical meaning of all these methods is the same despite the names: before obtaining the image of an object lying under an inhomogeneous layer, it is necessary to evaluate in some way the parameters of the layer, or, more specifically, its complex transfer function, and adjust the amplitude–phase distributions of the fields in the radiation and reception modes. As for the formulated problem, this means that it is necessary first to measure the profiles of the lower and upper boundaries of the bone, the local thicknesses, and the local transmission factors in the region, through which the diagnostics will be performed. In this case, it is usually assumed that ultrasonic attenuation at some frequency is the same for the whole region of the bone, and its value is determined only by the local thickness. With this data available, it is possible to calculate the amplitude–phase distribution of the exited ultrasonic field in the radiation mode, which is necessary for the field transmitted through this bone region to form a plane or spherical wave. The same operations must be performed in the reception mode. In this approach, it is important that the brain structure under examination is assumed to lie in a medium that can be considered as an analog of free space and is separated from it by an inhomogeneous layer, i.e., by the thick skull bones. It is this assumption that provides an opportunity to calculate the amplitude–phase distributions correcting the wave fronts for all possible angular directions and distances, at which objects can be located, from the measured bone parameters. If the object lies within the inhomogeneous layer, it is necessary to measure (but in what way?) all transfer functions from each point of the object to each elementary receiver to reconstruct the image. This can be accomplished theoretically, but not yet in practice.

The bone parameters can be measured in different ways. In some works on ultrasonic transcranial surgery, when focused ultrasound is used for brain surgery [9–11], the authors suggest first to obtain an X-ray or NMR image of the specified bone region. Then, after measur-

1063-7710/03/4903-0276$24.00

ing its local thickness values, it is possible to calculate the necessary time delays (phases) in all elements of the radiating two-dimensional array and to form a corresponding amplitude–phase distribution by then positioning the array at exactly the same place using precise positioning systems. Despite the complexity of the proposed procedure, it provides an opportunity to measure the bone thickness to a very high accuracy, because the resolution of the X-ray or NMR techniques constitutes fractions of a millimeter and the two-dimensional profile of the bone region is measured rather than the one-dimensional one.

In this paper, we suggest measuring the bone profile with the help of the same multielement ultrasonic sensor that is used for imaging. The measurement accuracy in this case is lower than in the case of NMR techniques, but there are also certain advantages, because such measurements allow one to take into account the local complex transmission factors for the sensor–skin layer–bone system.

Below, we consider the major physical and technological aspects of ultrasonic transcranial diagnostics through thick skull bones in more detail by using the results of the previous investigations [12]. The main goal of the studies presented in the first part of the paper is to develop a full-scale computer model for the whole system and to perform simulation experiments for the determination and optimization of the requirements for the system prototype.

1. MAIN PHYSICAL PHENOMENA AND LIMITATIONS

Attenuation

High ultrasonic attenuation in bones (which can reach 12–45 dB/cm within the frequency range 1–5 MHz [2, 13, 14]) is a negative factor for the penetration of a probing ultrasonic pulse to the brain. The attenuation of sound intensity by four orders of magnitude or more seems catastrophic at first glance, especially if we take into consideration the fact that the acceptable intensity of ultrasound is restricted by severe medical safety standards.

Multiple Reflections

Even if we assume that the level of the reflected useful signal is sufficient to be detected, we encounter another problem: multiple reflections of the probing signal from the outer and inner surfaces of the bone. Simplistically, such a bone behaves as a plate with two reflecting surfaces, and a part of the signal transmitted through the bone is necessarily reflected from the lower bone boundary. Then, part of the reflected signal is transmitted through the upper bone boundary and arrives at the receiver, but the remainder is again reflected from the upper bone boundary and reaches the lower boundary. Then, the whole process will be repeated, and a time sequence of signals with attenuating amplitudes will be represented in the received signal, so that the useful signal occurs among these signals or after them (depending on the distance to the object under examination). If the device operates in a standard pulsed mode, the useful signal can be either "covered" by the multiple reflections or appear somewhere between them. The common processing techniques used for pulsed ultrasonic scanners are incapable of detecting and identifying such a signal.

Curvilinearity and Irregularity of the Lower Bone Boundary

One more obstacle is the curvilinearity and irregularity of the lower bone boundary. The upper boundary of the skull bones is sufficiently smooth but curvilinear, while the lower boundary is both curvilinear and irregular in thickness. For example, within a bone segment 100 mm in length, the bone thickness may randomly vary from 8 to 15 mm. The two-dimensional curvilinearity of the bone and its irregular lower boundary may lead to unpredictable effects of ultrasonic wave refraction and a strong defocusing of the image. In this connection, it should be noted that, today, ultrasonic examinations are mainly performed using one-dimensional arrays with cylindrical lenses, and such a "knife-like" ultrasonic beam may leave the observation plane because of the curvilinearity of the lower boundary.

Scattering Effects

The next effect of ultrasonic interaction with a bone is the scattering. In reality, a bone is not homogeneous. From the physical point of view, it can be represented as a plate with inclusions characterized by different acoustic values of velocity and density and with dimensions comparable to or smaller than the wavelength used for sounding. Such a structure can transform an incident sound wave into a set of waves scattered in different directions. Ultrasonic scattering in bones is rather poorly studied, because such measurements *in vivo* are very difficult for many reasons.

2. PROBLEM FORMULATION, MODELS, AND BASIC PARAMETERS

In the analysis, we proceeded from the following suppositions and the previous experience in detecting and processing weak acoustic signals that propagate in layered inhomogeneous media with scatterers. Not only the signal intensity (or power) is important for the signal detection but also its excess over the noise level, which is characterized by the energy output signal-to-noise ratio. The latter depends on the signal-to-noise ratio at the receiver input, the complexity of the probing signal, and the gain factor of the system, which is governed by the spatial geometry of the radiating and receiving arrays. In the case of a coherent processing of

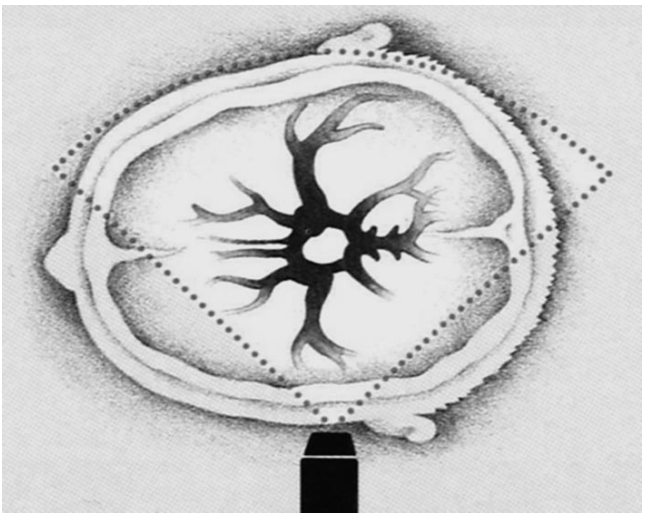

Fig. 1. Sagittal section of skull and major blood vessels of brain (the Velisius circle).

signals, the output signal-to-noise ratio is directly proportional to these parameters. For simplicity, we assume that the gain factor of the system is the product of the number of emitters and the number of receivers divided by the number of the parameters under evaluation. The signal complexity is the product of the probing signal bandwidth by the time of coherent observation. If the pulsed sounding mode is used, which is common to ultrasonic scanners, the signal complexity is the number of pulses used for accumulation. A simple summation of echo signals in a coherent system leads to an amplification of the echo signal (the echo signals are equal for different pulses) and to a reduction of noise (noise is different for different pulses).

Most ultrasonic devices intended for medical examination use probing signals with a low complexity, and, therefore, the gain due to the time processing is usually small. This is connected with the fact that, in echo sounding of open organs, the absorption in soft tissues is not that strong and it is sufficient to use simple pulses. When multielement sensors are used, the angular scan with the number of elements of spatial resolution that is equal to the number of receivers of the array is formed, and, therefore, the gain factor in this case is approximately equal to unity. If all receivers are used to form only one element of resolution (and this is just the case in fully digital systems with electronic scanning), the gain is about 100–512, because modern ultrasonic scanners contain approximately this number of receivers. If time accumulation is used, it has the form of an incoherent accumulation of frames. In this case, the gain increases as the square root of the number of accumulated frames. Thus, the gain due to processing can be about 10^3 (60 dB). The expected low level of an echo signal in the case of sounding through a thick bone means that, for a system to be efficient, the aforementioned effects of multiple reflection and scattering must be approximately at a level of –60 to –70 dB of the probing signal; otherwise, the gain of the processing system must be increased by 60–70 dB. Hence, the summary range of the system must be 110–120 dB with allowance for the fact that it is sufficient to have a tenfold excess of the signal over the noise level at the output of the processing system for the appropriate evaluation of the signal. This means that the use of broadband probing signals with a large base and the application of matched spatial processing should be the only possible solution, because we cannot increase the output beam intensity limited by medical standards.

Figure 1 schematically represents the skull (a sagittal section at the skull base) with the major blood vessels, i.e., the so-called “Velisius circle” formed by the major great arteries. The skull bones have a sufficiently smooth upper surface and an uneven lower boundary. The real thickness of skull bones in different places fluctuates from a few millimeters to 15–18 mm. The blood vessels lie within the brain tissue and have a very complex geometry and different sizes. From the viewpoint of ultrasonic examination, it is important to evaluate the state of vessels with diameters from 1 to 7–8 mm. To set the acoustic properties of a model medium, we use the measurement data from [2, 13, 14]. Specific val-

Parameters of the acoustic computational model

Model component	Density, kg/m^3	Sound velocity, m/s	Frequency, MHz	Attenuation coefficient, m^{-1}
Bone (obstacle)	2000	3400	0.80	92
			1.20	170
			1.60	320
			1.80	430
			2.25	530
Medium studied by echo sounding (brain tissue)	1000	1500	0.30	8.5
			0.87	14
			1.70	18
Object under examination (vessel)	1000–1050	1570	–	–

ues of the acoustic parameters used for simulation are summarized in the table. Most calculations are conducted for a standard detection scheme using a transducer that combines the functions of a radiator and a receiver, because the majority of medical ultrasonic scanners are designed in this way. Since the anatomic structure of a skull is quite complex, we use a simplified model and investigate only the effects that are essential for this analysis. Therefore, for a better understanding of the main phenomena, we represent the computational model as follows.

We consider the brain tissue as a homogeneous medium, into which we place a reflecting object of a simple shape (e.g., a spherical scatterer). On one side, the brain tissue contacts the bone, which we represent (at the first stage) as a homogeneous plate. We do not consider the effects connected with the excitation of transverse waves in either the bone or the medium under examination (brain), because their behavior is analogous to that of longitudinal acoustic waves. The only difference is their smaller propagation velocity. Moreover, we have to exclude from our consideration the processes of scattering from the microstructures of the bone and brain tissues. Therefore, in further calculations, we assume that the media under study are absorbing with the absorption coefficient equal to the attenuation coefficient.

The object under investigation has the form of a sphere filled with a medium that differs from the surrounding medium (brain) in its density and/or the sound velocity. For the simulation, we select the parameters of the simplified acoustic model that are shown in the table.

The scattering amplitude of the object under examination is involved in the algorithm of calculating the field excited by the object in response to a probing wave and determines the amplitude of the echo signal. The theory of scattering gives the following expression for a spherical object:

$$f = 4\pi\frac{k_0^2}{\mu^3}\frac{c_{in}-c_0}{c_0}[\sin(\mu r)-\mu r\cos(\mu r)], \qquad (1)$$

where $k_0 = \omega/c_0$ is the wave number in the medium surrounding the object, ω is the cyclic frequency, c_0 is the sound velocity in the surrounding medium, c_{in} is the sound velocity within the object, $\mu = 2k_0\sin(\vartheta/2)$, ϑ is the angle between the directions of sounding and reception ($\vartheta = \pi$ for a combined transceiver), and r is the object radius. In this study, we proceeded from the assumption that, if the signal is excited by the object, the only obstacle for its detection is the noise comparable to or exceeding the signal. The fact that, in the echo sounding of the brain through the acoustic transparence windows (the bone thickness is ≤2 mm), the signals from internal structures are detected reliably, while, in the case of thicker bones, they vanish, does not mean that the signal is not transmitted through the bone but only points to a decrease in the level of the reflected signal below the dynamic range of the system or to its masking by stray signals combined with noise.

A really difficult situation may arise only when, in the course of the propagation to the object, the probing signal is distorted in such a way that the identification of the reflected signal, which almost does not contain the features of the initial signal, becomes difficult. However, at the first stage, we did not find any physical background for such a situation.

Thus, we can formulate the basic questions for the simulation as follows:

(1) Is it possible to detect ultrasonic signals from the internal brain structures in the case of the echo sounding through thick skull bones, or do some factors make such a detection fundamentally impossible?

(2) What specific effects, apart from attenuation, are caused by the presence of thick bones?

(3) What can be the absolute noise level normalized to acoustic pressure in the detection system?

(4) What intensity of the probing beam is necessary for the level of the signal from the structures of interest to exceed the noise level?

(5) What is the expected level of stray signals, i.e., the signals scattered from other structures, and how do they mask a signal from the object under examination?

(6) How is it possible to suppress or eliminate the stray signals?

3. RESULTS OF SIMULATION

To analyze different variants of signal processing and different choices of the optimal parameters of the system, the ULTRABRAIN-1!H simulation program [12] was used. This program allows one to perform a full-scale simulation of the ultrasonic system. In this paper, we do not describe the details of the program structure and the calculation procedures and present only the results of simulation and the conclusions.

With the ULTRABRAIN-1 program, it is possible, by setting the geometric–acoustic models of a region of the skull bone and brain structures, to obtain their two-dimensional images for

(1) various types of broadband signals;

(2) various algorithms of time processing (square-law and linear detection and correlation processing); and

(3) various types of spatial processing (unfocused or focused images) involving additional subprograms for matched processing (additional programs for a preliminary evaluation of the geometric–acoustic parameters of the bone were developed for this purpose).

It is possible to vary the input parameters of transmitting–receiving arrays, the acoustic parameters of biological structures and signals, and the processing parameters over a wide range to achieve the maximal efficiency of the selected processing scheme and algorithms. The criterion of the processing efficiency is not only the output contrast of the image, which actually is the output

signal-to-noise ratio, and the transmitted dynamic range but also other parameters, such as the spatial resolution in angle and distance, the lateral field level, etc. Regretfully, there is no universal criterion for evaluating the quality of an acoustic image. The standard techniques evaluating the operation of ultrasonic scanners require, e.g., the measurement of more than 16 parameters [1]. Therefore, at the simulation stage, the main criterion of efficiency was chosen to be the degree of similarity of the ultrasonic image of an object to its X-ray image.

Calculation of the Backscattered Field

In calculating the backscattered field, depending on the frequency for spherical objects of different size, it was assumed that the incident field was a plane wave of unit amplitude and the bone thickness was 20 mm. The calculations showed that the expected levels of echo signals in the case of sounding through a 20-mm-thick bone are 10^3–10^5 times smaller than the level of the initial probing signal in a frequency range of 1–3 MHz.

Sounding Radiation Intensity

Knowing the attenuation of echo signals with respect to the probing signal and the level of normalized noise, we can calculate the sounding radiation intensity that is necessary for echo signals to exceed the noise level. In the calculation, we assumed that the signal must exceed the noise by a factor of ten (20 dB) to provide a good enough evaluation. Additionally, it was assumed that the object radius was 1 mm.

The results of calculation showed that, with the ultrasonic intensity 0.15–0.25 W/cm^2, it is possible to "operate" through the skull bones with a thickness up to 21 mm in a frequency range approximately up to 1.2 MHz; in the case of the skull bones with a thickness of 12–15 mm, it is possible to use a frequency up to 2 MHz with the same intensity value. It is necessary to note that the medical limit for the radiation is 1–2 W/cm^2. The calculations were conducted for the intensity at the obstacle surface. At the obstacle–medium boundary, the intensity is approximately one order of magnitude smaller for a 20-mm-thick bone because of the attenuation. Standard Doppler ultrasonic scanners operate with input ultrasonic intensities up to 0.12 W/cm^2, while medical standards allow ultrasonic intensities up to 0.15 W/cm^2 (domestic standards) or 0.3 W/cm^2 (European standards) [1]. In fact, the frequency range of the signal can be wider, since, as indicated above, the irradiation mainly affects the bone tissue, and the main danger for soft tissues, i.e., cavitation, is impossible at these intensities.

Another danger for tissues, apart from cavitation, is heating. However, based on the data of [1] and calculations that are not presented here, we can state that a sufficient excess of the echo signal over the noise level is realized at moderate irradiation intensities that do not cause heating of tissues.

Interfering Echo Signals and the Bone Inhomogeneity

As interfering echo signals, we consider the acoustic fields that are excited by structures extraneous to the study under the effect of the sounding field. These are mainly the echo signals from the obstacle–external space and obstacle–probed medium boundaries. From the given model data, it follows that the acoustic properties of the bone and the brain tissue differ substantially. Therefore, when the probing pulse propagates through their boundary, a rather strong reflected pulse propagates in the opposite direction. Apart from these interfering signals, multiple reflections from the bone tissue are present. The wave fronts undergo unpredictable distortions because of the bone inhomogeneity in thickness. As it was already mentioned, matched spatial processing can eliminate these phenomena or at least considerably reduce their influence. This statement is based on the facts that, first, there is a real possibility to measure the inhomogeneity parameters and, hence, construct an optimal matched filter, and, second, the parameters of such a filter do not change in time but only depend on the spatial coordinates, i.e., on the specific position of the sensor.

In our previous paper [2], we also considered another way to eliminate the signals of multiple reflections, namely, on the basis of the diversity transmission–reception scheme. In this scheme, the multiply reflected signals propagate in the direction of radiation and do not hit the receiver. For this scheme of operation to be efficient, it is necessary that the scattering from the object be close to isotropic. This condition is satisfied, e.g., for the scattering by the form elements of blood. However, for brain structures and vessel walls, the scattering indicatrices are *a priori* unknown, although large practical experience in ultrasonic examination of various internal organs testifies to a wide scattering indicatrix for biological tissues. However, the diversity scheme does not eliminate the problem of the unknown ultrasonic refraction at the curvilinear bone boundary and the problem of the wave front distortions.

Effect of the Instrument Noise

The root-mean-square voltage die to the electric noise in the transducer–amplifier circuit of a high-quality ultrasonic instrument must be about

$$\bar{V}_\mathrm{n} = 3 \times 10^{-9} \sqrt{\Delta\nu},$$

where $\bar{V}_\mathrm{n}$ is the noise voltage in volts and $\Delta\nu$ is the reception bandwidth in hertz. The sensitivity of a modern piezoelectric transducer is about $\gamma \cong 7 \times 10^{-6}$ V/Pa. Using this value, we transform V_n into equivalent acoustic noise:

$$\bar{P}_\mathrm{n} = \frac{\bar{V}_\mathrm{n}}{\gamma} = 4.286 \times 10^{-6} \sqrt{\Delta\nu}\ \text{Pa}.$$

A body emits acoustic noise related to the body temperature by the formula

$$\bar{P}_T^2 = 4\pi\nu^2 c^{-1}\rho kT\Delta\nu,$$

where c is the sound velocity, ρ is the substance density, $k = 1.38 \times 10^{-23}$ J/K is the Boltzmann constant, ν is the radiation frequency, and T is temperature in kelvins. Substituting the values of the velocity and density corresponding to bones and taking $T = 310$ K, we obtain

$$\bar{P}_T^2 = 3.162 \times 10^{-20}\nu^2\Delta\nu,$$

which, at a frequency of 1 MHz, yields

$$\bar{P}_T = 1.778 \times 10^{-4}\sqrt{\Delta\nu}\ \text{Pa}.$$

These estimates demonstrate that, in chosing specific technological solutions, it is necessary to take into account both kinds of noise.

Simulation Examples

The simulation scheme is shown in Fig. 2. The program simulates the positioning of a multi-element transceiver at a preset place on a skull, the generation of signals of a required form, their propagation with allowance for the acoustic parameters of media, the reflection of useful signals, their reception, and the subsequent space–time processing. Figure 3a demonstrates the shape of the signal envelope at the output of the central angular channel in the case of echo sounding through a bone 20 mm thick. A reflecting object 1 mm in size was positioned at a distance of 80 mm. The frequency and duration of the probing pulse were 1.7 MHz and 1.5 μs, respectively, and the number of receiving elements in the array was 128. One can see that signals from multiple reflections are received first, and then, the useful signal. Although the 80-mm distance provides separate reception of the signals reflected from the boundaries and the useful signal, the latter is barely visible.

Figure 3b gives another example, when a complex signal 40 μs in length was used with a subsequent correlation compression and a bone-matched spatial processing. Here, we do not present the detailed algorithms of matched processing. Their various versions can be found in [3–7]. We only note that the local values of the bone thickness under the sensor $d_i(x)$ and the local transmission coefficients $A_i(x)$ are measured first. These data are stored and then used to form the adjusting amplitude–phase distribution $\Phi(x) = A_i(x)\exp\{kd_i(x)\sin\alpha\}$, where α is the variable observation angle in the azimuth plane and k is the wave number. Then, the initial amplitude–phase distribution of the signal in the radiation mode, e.g., a spherical wave of unit amplitude for the selected value of α and distance range, is multiplied by the conjugate adjusting distribution $\Phi^*(x)$ and fed to the receiver elements in the radiation mode. The same distribution is used for the reception of reflected signals.

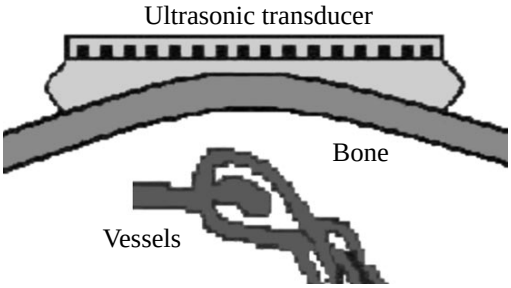

Fig. 2. Simulation scheme.

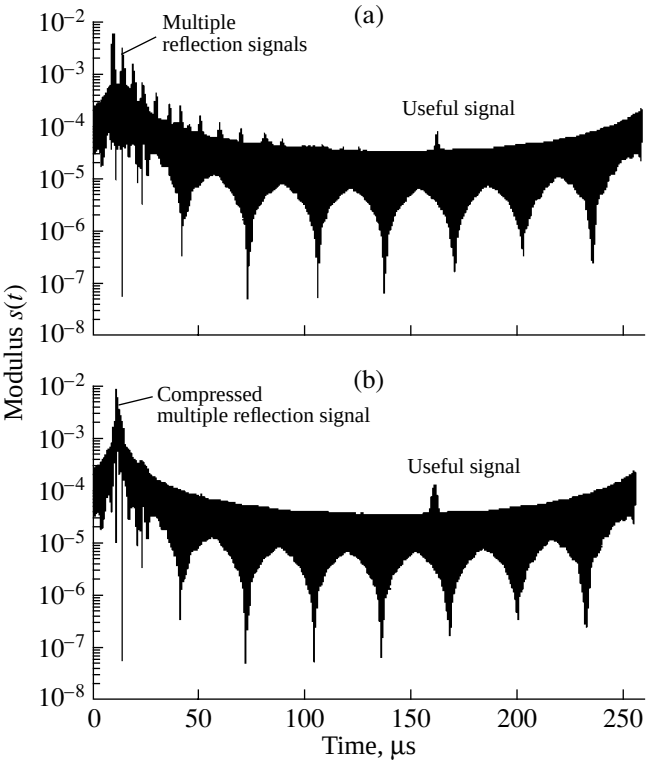

Fig. 3. Signal envelope in the central angular channel (a) in the absence of matched processing and (b) with the bone-matched processing.

Comparing Figs. 3a and 3b, one can see that the matched processing allows one to single out the desired signal against the background of interfering signals, which are compressed into a single narrow pulse.

Figure 4 presents two-dimensional acoustic images of a point object for two cases of processing. The image shown in Fig. 4a is obtained through a thick bone without matched processing. One can see that the image is smeared and the resolution is low. Figure 4b shows the same image after the matching procedure. The indeterminacy of the body size at the 0.7-level almost corresponds to the given parameters of spatial resolution: 1 mm in the azimuth (the X coordinate) and 0.5 mm in the distance (the R coordinate).

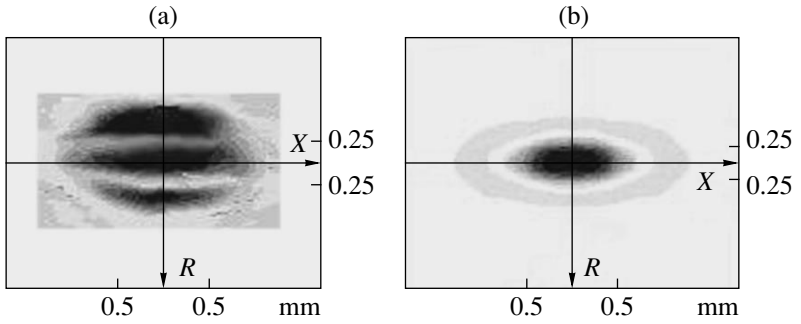

Fig. 4. Image of a point reflector (a) without matched processing and (b) with matched processing.

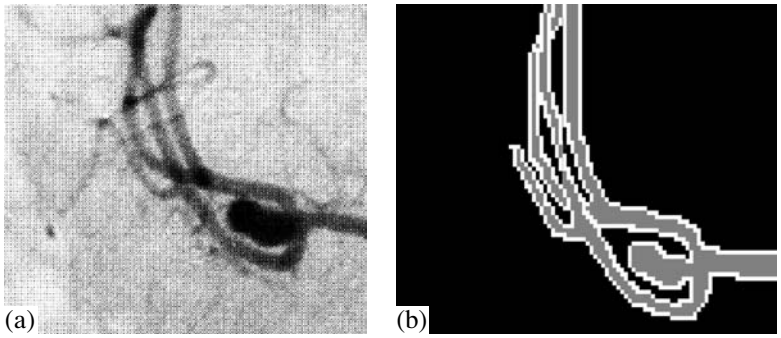

Fig. 5. (a) X-ray image of a brain blood vessel section with an aneurism and (b) the geometric-acoustic model of this area. The density values are 1400, 925, and 1060 kg/m^3 for the bone, brain, and blood, respectively. The sound velocity values are 3360, 1530, and 1550 m/s for the bone, brain, and blood, respectively. The bone thickness is 18 mm.

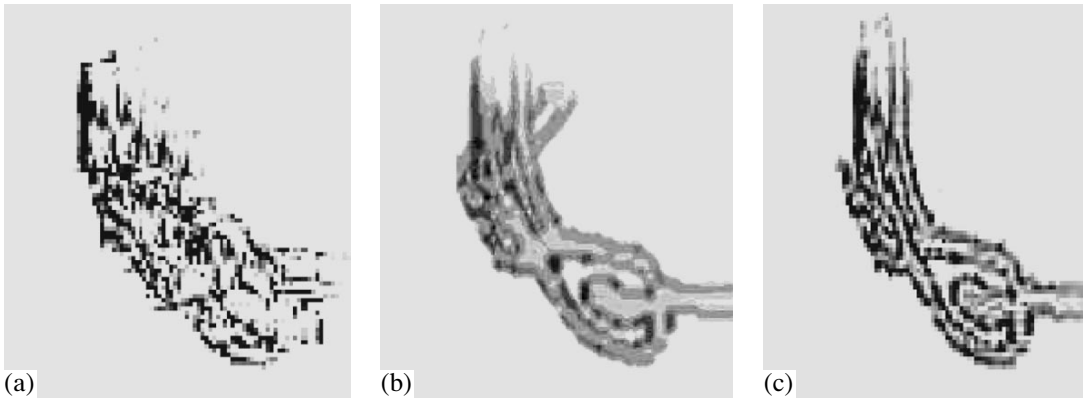

Fig. 6. Reconstructed images of the vessel model: (a) image in the absence of bone-matched processing; (b) reconstructed image with matched processing, the reconstruction only with respect to velocity; and (c) the same image reconstructed taking into account both density and velocity.

Figure 5a presents an angiogram (X-ray image) of a section of brain vessels. On the right-hand side of the picture, at the point of the vessel bifurcation, one can clearly see an aneurism, one of the most dangerous involvements of brain vessels.

A simplified geometric–acoustic model of this area is shown in Fig. 5b. Further, using the anatomic atlas of brain, this vessel model was "placed" under thick skull bones. In this model experiment, we assumed that the bone thickness and the curvatures of the lower and upper surfaces are equal, with a radius of 18 cm.

The proposed processing algorithms provide an opportunity to reconstruct acoustic images of objects with different densities and/or ultrasonic propagation velocities, because only one of these parameters or both of them can change simultaneously in biological structures.

Figure 6a demonstrates the ultrasonic image of the vessel model when the matched processing is not used. One can see that the image quality is very low, and only a certain region that partially resembles of the vessel model is visible. Figures 6b and 6c show the results of a simulation experiment with the bone-matched filtration. Figure 6b demonstrates an ultrasonic image of the reconstructed vessel region when its model differs from the brain tissue only in the ultrasonic propagation velocity. Figure 6c shows the image of the same region in the case when the reconstruction was performed taking into account both velocity and density. This image was obtained using a phase-keyed signal with a carrier frequency of 1.5 MHz and a bandwidth of 900 kHz. The total dynamic range was –130 dB. In the radiation mode, the beam was focused at each element of resolution in angle and in distance with the use of matched processing for both radiation and reception.

CONCLUSIONS

The calculations described above and the results of simulations allow us to make the following conclusions:

(1) To reliably separate the signals reflected from the brain structures in the case of echo sounding through the skull bones whose thickness is 20 mm or more, the ultrasonic system must have a total dynamic range no less than 120–130 dB.

(2) Ultrasonic intensities of the order of 0.2–0.3 W/cm^2 provide the detection of reflected signals in the case of echo sounding through thick skull bones at frequencies within 1–2 MHz. These ultrasonic intensities comply with the medical standards for ultrasonic intensity limits.

(3) The instrument noise and the thermal noise of the sensor-amplifier unit are comparable in their levels, and it is necessary to take into account both types of noise in the system design. It is desirable to have the normalized noise levels of the input amplifiers below (1–3) nV/$\sqrt{\text{Hz}}$. A reduction of the instrument and thermal noise by an order of magnitude allows one to use radiation frequencies up to 3–3.5 MHz.

(4) When the number of elements in the transmitting–receiving array is equal to N = (128–256), the system must provide the radiation and correlation processing of broadband signals with the relative bandwidth $\Delta F/F \geq$ (0.7–1.5). In this case, the focusing must be used in both radiation and reception modes.

(5) The matched spatial processing of signals considerably reduces the effects of multiple reflections in thick bones and the defocusing of wave fronts. To realize the matched processing, it is necessary to preliminarily introduce the calibration of the bone region located under the ultrasonic transducer. The calibration consists in measuring the local thickness of the bone and the transmission coefficients. To provide higher calibration accuracy, it is desirable to perform it at a frequency higher than the frequency used for echo sounding. The values obtained are used for constructing a matched filter and for an automated amplification control in depth with allowance for different attenuation of the signal in frequency and for the local frequency attenuation in the bone.

Our studies confirmed that the main obstacles for echo sounding through thick skull bones are the effects of multiple reflections and the curvilinearity of the lower boundary of the bone rather than the high ultrasonic attenuation. Nevertheless, in contrast to the known ultrasonic scanners for open organs, which operate at frequencies up to 7–10 MHz, the frequency range of the signals utilized in transcranial diagnostics proves to be narrower. In the case of bones with a large thickness (over 20 mm), the utilization of signals with frequencies higher than 3 MHz is problematic. However, the main restriction in this case lies in the relatively high level of intrinsic instrument noise and thermal noise of piezoelectric ceramics and amplifiers rather than in some special physical phenomena. At the same time, the use of frequencies up to 2 MHz provides an opportunity to obtain ultrasonic images of vessels through thick bones with a spatial resolution of the order of 1 mm. The factor least investigated is the ultrasonic scattering in skull bones. Therefore, the only way to clarify its effect is a direct experiment.

The proposed approaches give rise to the new technological requirements for the basic units of an ultrasonic system intended for transcranial diagnostics:

(a) The transmitting and receiving ultrasonic transducers must be broadband and well matched with the bone. In addition, the transverse dimension of the array must be somewhat greater than that of common linear ultrasonic sensors, and the sensor surface should be concave.

(b) The computational means used for the space–time signal processing must be fully digital, sufficiently fast, and multichannel. The best technological solution is the scheme of the elementary channel–A/D converter type.

Note that the purpose of this study was the visualization of the “static” brain structures, i.e., the walls of blood vessels, brain ventricles, etc. The same matched processing technique can be used for the ultrasonic visualization of blood circulation (using the Doppler mapping). However, for the observation of blood circulation through thick skull bones, the use of other methods of signal processing without matched filtration is also possible [15].

The second part of this work will be devoted to the analysis of technological requirements, ways of their technological realization, and some results of experiments with biological phantoms and live objects.

ACKNOWLEDGMENTS

We are grateful to professor E. Bartels from the Munich Neurological Clinic and to professor V.L. Anzimirov from the Institute of Neurosurgery of the Russian Academy of Medical Sciences for fruitful discussions and valuable comments.

REFERENCES

1. L. V. Osipov, *Ultrasonic Diagnostic Devices* (VIDAR, Moscow, 1999).
2. F. J. Fry and J. E. Barger, J. Acoust. Soc. Am. **63**, 1576 (1978).
3. V. D. Svet and N. V. Zuĭkova, Akust. Zh. **39**, 203 (1993) [Acoust. Phys. **39**, 203 (1993)].
4. V. D. Svet, Akust. Zh. **36**, 733 (1990) [Sov. Phys. Acoust. **36**, 412 (1990)].
5. M. Fink, IEEE Trans. Ultrason. Ferroelectr. Freq. Control **39** (5), 555 (1992).
6. M. Tanter, J. F. Aubry, J. Gerber, *et al.*, J. Acoust. Soc. Am. **110**, 37 (2001).
7. J.-F. Aubry, M. Tanter, J. Gerber, *et al.*, J. Acoust. Soc. Am. **110**, 48 (2001).
8. A. R. Brenner, K. Eck, W. Wilhelm, and T. G. Noll, Acoust. Imaging **23**, 122 (1997).
9. J. Sun and K. Hynenen, J. Acoust. Soc. Am. **104**, 1705 (1998).
10. K. Hynenen *et al.*, Magn. Reson. Imaging, No. 5, 259 (1995).
11. K. Hynenen *et al.*, IEEE Trans. Ultrason. Ferroelectr. Freq. Control **45**, 431 (1998).
12. M. Molotilov, V. D. Svet, and S. V. Baykov, in *Proceedings of World Congress on Cerebral Embolism, New Orleans, LA, USA* (1998).
13. R. C. Chivers and R. J. Parry, J. Acoust. Soc. Am. **63**, 940 (1978).
14. *Physical Principles of Medical Ultrasonics*, Ed. by C. R. Hill (Ellis Horwood, Chichester, 1986; Mir, Moscow, 1989).
15. N. V. Zuĭkova, T. V. Kondrat'eva, and V. D. Svet, Akust. Zh. **47**, 664 (2001) [Acoust. Phys. **47**, 578 (2001)].

Translated by M. Lyamshev

Acoustical Physics, Vol. 49, No. 3, 2003, pp. 285–289. Translated from Akusticheskiĭ Zhurnal, Vol. 49, No. 3, 2003, pp. 342–347.

Drifting Underwater Acoustic Antenna Array

V. I. Bardyshev

Andreev Acoustics Institute, Russian Academy of Sciences, ul. Shvernika 4, Moscow, 117036 Russia
e-mail: bvp@akin.ru

Received July 7, 2001

Abstract—Characteristics of a compensated receiving antenna array consisting of four drifting radioacoustic relaying buoys are studied experimentally. The signal frequency is 21 Hz. The array gain is 11.4 dB, and its noise immunity is 3.8 dB. © *2003 MAIK "Nauka/Interperiodica".*

A group of drifting radioacoustic relaying buoys (RARB), which receive underwater signals and transmit them via radio channel to an aircraft or vessel, can be used as a low-frequency, drifting, spatially developed, underwater acoustic antenna array (DAAA). It can be used for detecting and locating sources of low-frequency acoustic signals, e.g., of biological or seismic nature [1–10]. Cetaceous animals are known to transmit intense acoustic pulses at frequencies of 20 and 12.5–200 Hz [1, 2]. Underwater earthquakes and volcanic eruptions are accompanied by acoustic noise whose maximal intensity occurs in the frequency range from several units to several tens of hertz [6–9]; such signals can be used to warn us about catastrophic tsunamis [6]. To receive and study these signals, stationary underwater acoustic arrays [1, 4, 6, 7] and self-contained acoustic buoys [2, 3, 8, 10] were used.

In contrast to RARB, a DAAA offers higher gain and better noise immunity; it can serve to detect low-frequency sound sources and determine their range within the Fresnel zone, which can be rather long if the DAAA aperture is large.

In comparison with stationary underwater arrays, the advantage of the DAAA consists in its mobility, i.e., in the possibility of rapidly deploying it in an arbitrary ocean region; its drawbacks are the limited operation time, which is determined by the capacity of the self-contained power sources, and the constraints imposed by the weather conditions during its transportation.

In comparison with rigid-structure arrays, the advantage of DAAA consists in the possibility of creating a spatially developed aperture 1 to 10 km in length, which provides accurate location of the sources of low-frequency noise; the drawback is the need for additional tools for positioning the drifting receivers with an accuracy sufficiently high for the compensation and coherent summation of signals over the array aperture.

A fundamental difficulty in constructing a DAAA with a large aperture is the possibility of a spatial decorrelation of the signals when the sound speed field is nonuniform in the underwater sound channel (USC) with a stable vertical sound speed distribution or with random space–time variations of the sound speed. In view of these fundamental and technical difficulties, the idea that the DAAA cannot be used in practice was put forward [11].

Here, we present numerical estimates that are evidence of the feasibility of a DAAA, although with some restrictions in its frequency band, aperture, and distance from the signal source. The approximate nature of the estimates leaves space for some doubts. Therefore, this paper presents the description of an in-sea experiment on the implementation of a DAAA.

Because of the inevitable deviations of the RARB units from the target positions, the DAAA proves to be a space-tapered antenna array (AA). The distance separating the reception points (the nodes of the AA) can exceed the signal wavelength. Such an AA can be called a sparse one. In contrast to equidistant AAs, due to different spacings of the sparse compensated random AA, it has no side lobes of the directivity pattern (DP) that have the same level as the main lobe. This feature ensures an unambiguous signal detection [12–14].

Let us estimate the acceptable value of the uncontrolled random rms deviation of the DAAA nodes from the target positions with the known coordinates. Let a tone signal of frequency f propagate in a homogeneous medium with a velocity c. Upon introducing the instrumental time displacement $\tau_i = \Delta r_i/c$ of the signal or its phase rotation by $\varphi_i = 2\pi f \Delta r_i/c$, where Δr_i is the distance of the ith node from the conventional phasing surface, the signals received at the nodes and in the associated AA channels are equalized in their phases and combined in phase. At the summator output, the gain coefficient (in dB) of the AA is $K = 20\log N$, where N is the number of nodes. Random displacements δr of the nodes from the target positions (calculated along the direction towards the signal source) lead to a phase

change $\delta\varphi = 2\pi f \delta r/c$ and to the loss in the AA gain by ΔK [14]:

$$\Delta K = -10\log\left[(1-\delta\varphi^2) + \frac{1}{N^3}\delta\varphi^2\right] \approx -10\log(1-\delta\varphi^2) = -10\log[1-(2\pi f\,\delta r/c)^2]. \quad (1)$$

For definiteness, let us assume that $\Delta K \le 3$ dB is an allowable value for which the AA is efficient. Then, we obtain the conditions

$$\delta\varphi \le 0.7, \quad \delta r \le 0.11c/f, \quad \delta r/\lambda \le 0.11, \quad (2)$$

where λ is the sound wavelength. As the frequency decreases, the requirements for the accuracy of the node positioning become less strict.

To determine the coordinates of the DAAA nodes, the well-developed methods [15] of underwater acoustic positioning can be applied. Systems of underwater navigation use acoustic beacons and provide a positioning accuracy of ±1 to ±0.1 m [15]. With $\delta r = 1$ m, condition (2) is met at the frequencies $f < 160$ Hz. For positioning the DAAA nodes, expendable explosive sound sources or pulse-transmitting buoys can be used.

Random inhomogeneities of the refraction index in water lead to random displacements of the signal phase whose random rms deviation $\delta\varphi$ linearly decreases as the frequency becomes lower [16]:

$$\delta\varphi = 2\pi\frac{f}{c}\sqrt{2\overline{\mu^2}ar}, \quad (3)$$

where a is the mean size of the inhomogeneities and $\overline{\mu^2}$ is the mean square refraction index. According to the measurements in different ocean regions [17], the value of $\overline{a\mu^2}$ is within 2×10^{-9} to 3×10^{-6} m. With such values, in view of Eq. (3), condition (2) is met at $r < 120$–1700 km for the frequency $f = 200$ Hz.

The vertical sound speed distribution is the strongest inhomogeneity of the refraction index; it most strongly affects the misphasing of the signal over the AA aperture. The accuracy of the data on the vertical sound speed distribution along the propagation path is usually insufficient to calculate the signal phase [18], and the numerical statistical modeling of the phase distribution over the aperture of a long AA provides no agreement with the experimental data [19]. Therefore, let us restrict our consideration to approximate estimates.

Let the signal of cyclic frequency ω propagate in an underwater sound channel as a group of modes with phase velocities $v \in [v_1, v_2]$. At point *1* (the distance r_1 from the source), the mode phases are $\varphi_1 \in \left[\omega t - \frac{\omega r_1}{v_1}, \omega t - \frac{\omega r_1}{v_2}\right]$. At point *2* (the distance r_2 from the source), the mode phases are $\varphi_2 \in \left[\omega t - \frac{\omega r_2}{v_1}, \omega t - \frac{\omega r_2}{v_2}\right]$. The phase difference between the modes with the same ordinal numbers at points *1* and *2* is $\Delta\varphi_{12} \in [\omega\Delta r/v_1, \omega\Delta r/v_2]$, where $\Delta r = r_2 - r_1$. Introducing an instrumental phase compensation $\Delta\varphi_a = -\omega\Delta r/v_1$ into the AA channel that corresponds to point *1*, we obtain the phase difference $\Delta\varphi \le \Delta\varphi_{12} - \Delta\varphi_a \in [0, \omega\Delta r\Delta v/v_1 v_2]$, which remains uncompensated. The uncompensated phase difference between points *1* and *2*,

$$\Delta\varphi_{un} \le \omega\Delta r\Delta v/v_1 v_2, \quad (4)$$

decreases as ω and Δr decrease. Assuming that the mode phase difference is uniformly distributed within the interval $\Delta\varphi_{un}$, we arrive at the following rms estimate for the uncompensated phase difference:

$$\delta\varphi_{un} = \frac{\pi}{\sqrt{3}}\Delta r\Delta v/v_1 v_2 \approx 1.8\, f\Delta r\Delta v/v_1 v_2. \quad (5)$$

At some distance from the source, the rapidly decaying modes are absorbed by the sea floor, and the sound field is determined by the discrete spectrum of the modes captured by the USC. Their phase velocities are $v \le c_h$ where c_h is the sound speed in water near the bottom. Then, one can set $v_2 = c_h$. Let the communicating points be near the USC axis where the sound velocity is equal to c_{ax}. Accepting the values $v_1 = c_{ax}$ and $\Delta c = c_h - c_{ax}$, we obtain

$$\delta\varphi_{un} \approx 1.8\, f\Delta r\Delta c/c_{ax}c_h. \quad (6)$$

If, as earlier, the allowable value is $\delta\varphi_{un} \le 0.7$, the condition for the AA efficiency in the zone of the discrete mode spectrum takes the form

$$f < 0.4c_{ax}c_h/\Delta r_m\Delta c, \text{ or } \Delta r_m/\lambda < 0.4c_h/\Delta c, \quad (7)$$

where $\lambda_{ax} = c_{ax}/f$ is the wavelength at the USC axis and Δr_m is the maximal length of the AA along the direction towards the signal source.

To estimate $\Delta\varphi_{un}$ in the far-field zone, we use the ray theory and the formulas presented in the monograph [20]. Let the sea depth be h, the depth of the USC axis be z_{ax}, and the sound speed gradient be $a = \frac{\Delta c}{c_{ax}\Delta z} > 0$ and $a_1 < 0$ under the USC axis and above it, respectively. The maximal depth of the ray is $z_h = ar_h^2/8$, where r_h is the length of the ray cycle. For the ray with the maximal depth h, the corresponding phase velocity at the USC axis is $v_2 = c_{ax}\left(1 + \frac{ar_h^2}{8}\right)$. Introducing the instrumental phase compensation, $\Delta\varphi_a = -\omega\Delta r/c_{ax}$, we obtain from Eq. (4)

$$\Delta\varphi_{un} = \frac{\omega\Delta r}{c_{ax}A_1A_2}\left[1 + \frac{a^2r_1r_2}{8} - A_1A_2\right],$$

where $A_1 = 1 + \frac{a^2 r_1^2}{8}$ and $A_2 = 1 + \frac{a^2 r_2^2}{8}$.

Assuming that $a \ll 1$ and omitting the small term $\frac{r_1^2 r_2^2 a^4}{64}$, we arrive at the estimate

$$|\Delta\varphi| \approx \omega \Delta r a^2 (r_1 r_2 + \Delta r^2)/8 c_{ax}, \quad (8)$$

$$\delta\varphi_{un} \approx 0.23 f \Delta r a^2 (r_1 r_2 + \Delta r^2)/c_{ax}. \quad (9)$$

If the allowable value is $\delta\varphi_{un} \le 0.7$, we obtain the condition for the AA efficiency:

$$f < 3.1 c_{ax}/a^2 \Delta r_m (r_{av}^2 + \Delta r_m^2), \quad (10)$$

where $r_{av} = \sqrt{r_1 r_2}$ is the geometrical mean distance from the source to the AA. Expressions (8)–(10) are valid for $r < r_h = 2\tan\chi_h/a$ and

$$\chi_h = \arccos(c_{ax}/c_h). \quad (11)$$

The loss in the AA gain is

$$\Delta K = -10\log\{1 - 0.053[\Delta r_m f a^2 (r_{av}^2 + \Delta r_m) c_{ax}^{-1}]^2\}. \quad (12)$$

For the northwestern region of the Pacific Ocean, in the warm season, with z_{ax} = 75 m, c_{ax} = 1452 m/s, h = 5.3 km, $a = 1.2 \times 10^{-5}$ m^{-1}, r_{av} = 30 km, Δr_m = 1 km, and $\Delta K \le 3$ dB, Eq. (10) yields $f \le 35$ Hz. If such an AA is focused (i.e., if it is compensated for the cylindrical wave front), the determination of the distance r from the source is possible for $r < d^2/\lambda \approx 20$ km, where d_p = 1 km is the projection of the AA aperture on the plane that is perpendicular to the direction towards the source.

The estimates presented above show the possibility of implementing an efficient DAAA several kilometers long for a distance of several tens of kilometers from the signal source at frequencies of several tens of hertz.

The experiment on the DAAA implementation was carried out in the Black Sea, in the region with the sea depth h = 820 m, at a wind speed of Beaufort 3. The vertical sound speed distribution is shown in Fig. 1. The parameters had the following values: z_{ax} = 60 m, c_{ax} = 1460 m/s, and c_h = 1482 m/s. With the radar of the research vessel, five vessels were observed at the distances 10–20 km, which corresponds to a high-density traffic (4×10^{-3} vessel/km^2). Therefore, the noise of the ship traffic predominated in the interfering noise at frequencies lower than 100 Hz. The experimental layout is illustrated in Fig. 2. As the source of tone signal, an underwater sound projector of 21 Hz was used. It was deployed at a depth of 60 m and was cable-connected to the transmitting vessel. The DAAA consisted of four RARBs whose hydrophones were at a depth of 150 m. The sound speed was c_r = 1465 m/s at the reception depth, the corresponding acoustic wavelength being λ = 69.8 m. The DAAA was located within a rectangle of 830×34 m. The aperture of the DAAA was d = 830 m. The rms deviations of the reception points from the nodes of an equidistant four-node linear AA with an aperture d was δl_a = 100 m ≈ 1.4λ along the baseline and δl_p = 16 m ≈ 0.2λ in the perpendicular direction. The mean distance between the reception points was l_{av} = 277 m ≈ 4λ. The distance from the transmission point to the center of the baseline was r = 2.9 km, $r_{av} \approx r$. The azimuth angle, as measured from the perpendicular to the center of the baseline, was $\theta = 39°$, Δr_m = 520 m. With the radar of the receiving vessel, the coordinates of the transmitting vessel and the RARBs were determined, with rms deviations of about 30 and 15 m, respectively. To improve the positioning of the reception points, the underwater acoustic method was used. A source of tone pulses, with a carrier of 1 kHz, was deployed from the transmitting vessel to a depth of 55 m. From the time differences τ_{i1} in reception of the pulses at the nodes i and 1, the range differences $\Delta r_{i1} = r_i - r_1 = \tau_{i1} c_p$ were determined with the rms deviations $\delta r \approx 2$ m and $\delta r/\lambda \approx 0.03$ m. In this case, condition (2) was met, and, according to Eq. (1), the loss in the gain was ΔK = 0.9 dB. The values of τ_{i1} were specified to compensate the DAAA. The measurements of τ_{i1} were carried out twice in half an hour. During this time interval, the configuration of the DAAA remained unchanged within the measurement accuracy.

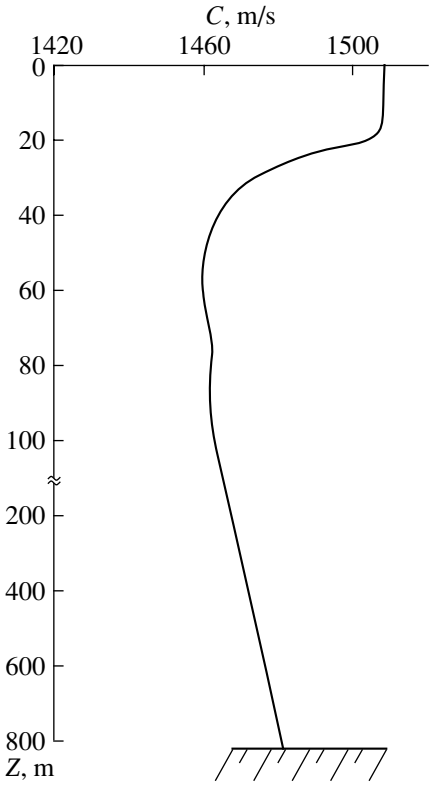

Fig. 1. Vertical sound speed distribution.

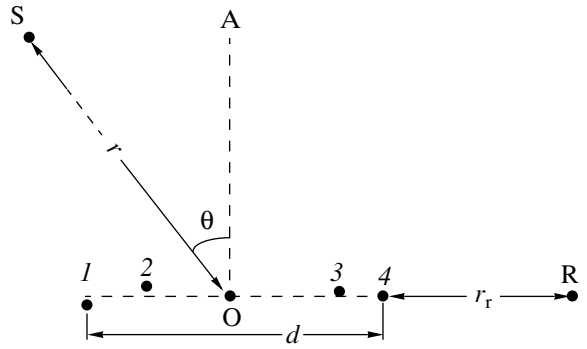

Fig. 2. Experimental layout: (*1–4*) hydrophones of the RARBs; (S) transmitting vessel, from which the sound sources were deployed; (R) receiving vessel, which received the radio signals of the RARBs; d = 830 m is the array aperture; O is the array center (the midpoint of the baseline); AO is the perpendicular to the baseline at its midpoint; $\theta = 39°$ is the azimuth angle to the signal source; r = 2900 m is the distance to the source; r_r = 2000 m is the distance from the array to the receiving vessel.

The positions of the RARBs were also amended when the receiving vessel went along the baseline with a constant speed. In such tacks, the time of crossing the traverse of each RARB was recorded. The rms deviation of the resulting values was no higher than 5 m $\approx 0.07\lambda$.

The radio signals of the RARBs were received at the receiving vessel; then, the underwater acoustic signals were separated and tape recorded. The replayed signals were filtered within the 5-Hz band around the central frequency of 21 Hz, fed to the analog-to-digital converter, and computer-processed in the digital form. The frequency of the signal sampling was 200 Hz, and the number of samples was 4096 for each RARB, which corresponded to the duration T = 20.5 s of a computer-stored realization. The signal processing algorithm was the one conventionally used for a compensated adaptive AA [21]:

$$D_{sp} = \int_0^{T_a} \left[\sum_{i=1}^{4} p_i(t - \tau_{i1}) \right]^2 dt, \qquad (13)$$

where D_{sp} is the energy of the sum of both signal and noise at the output of the processing circuit, $p_i(t)$ is the acoustic signal received at the ith node (channel) of the DAAA, t is the running time, $\tau_{i1} = \Delta r_{i1}/c_p$ is the instrumental delay time in the ith channel, and T_a = 19.5 s is the time of signal integration.

In addition, the energy of the sum of signal and noise was measured at the inputs of all channels within the time interval T_a: $D_{spi} = \int_0^{T_a} p_i^2(t)dt$.

With the sound source switched off and the same compensation, the energy of noise was measured at the channel input and at the output of the processing system: D_{pi} and D_p, respectively. Then, the empirical signal-to-noise ratio (SNR) was calculated at the input, $E_i = (D_{spi} - D_{pi})/D_{pi}$, and at the output, $E_a = (D_{sp} - D_p)/D_p$. The empirical values of E_i ranged from 12 to 47; the mean SNR values were $\bar{E} = \frac{1}{4}\sum_{i=1}^{4} E_i = 25$ and $E_a = 61$ at the input and output, respectively. The mean input energy is given by the formula $\bar{D}_s = \frac{1}{4}\sum_{i=1}^{4}(D_{spi} - D_{pi})$. The empirical gain of the DAAA is $K = 10\log[(D_{sp} - D_p)/\bar{D}_s] = 11.4$ dB. When the signals are in phase and the noise is fully decorellated in all channels, we obtain $K_T = 20\log 4 = 12$ dB. The loss in the gain $K_T - K = 0.6$ dB is close to the estimate obtained above for the multimode sound propagation.

The empirical noise immunity of the DAAA is $\kappa = 10(\log E_a/\bar{E}) = 3.8$ dB. If the signals are in phase and the noise is fully decorrelated for all pairs of the channels, $\kappa_T = 10\log 4 = 6$ dB. The loss in the noise immunity is estimated as $\Delta\kappa = \kappa_T - \kappa = 2.2$ dB and is greater than the loss in gain. Let us show that the loss in the noise immunity can be explained by a partial correlation of noise over the DAAA aperture. Tables 1 and 2 represent the matrices of the normalized empirical cross-correlation values for the signals R_{sij} and the noise R_{pij} in the channel pairs (i, j) at the delay times $\tau_{ij} = \tau_{i1} - \tau_{j1}$ corresponding to the DAAA compensation. If, for the sake of simplicity, we set $E_i = \text{const} = \bar{E}$, we can use the following expression [22]:

$$\kappa = 10\log\left(\sum_{i=1}^{4}\sum_{j=1}^{4} R_{sij}/R_{pij} \right). \qquad (14)$$

Table 1. Cross-correlation matrix of the signals R_{sij} in channel pairs (i, j)

i, j	1	2	3	4
1	1	1	0.8	0.9
2	1	1	0.9	0.9
3	0.8	0.9	1	0.8
4	0.9	0.9	0.8	1

Table 2. Cross-correlation matrix of noise R_{pij} in channel pairs (i, j)

i, j	1	2	3	4
1	1	0.3	0.2	0.3
2	0.3	1	0.2	0.2
3	0.2	0.2	1	0.3
4	0.3	0.2	0.3	1

Using the values from Tables 1 and 2, we obtain κ = 3.2 dB and $\Delta\kappa$ = 2.8 dB. If the noise is fully decorrelated, we assume that $R_{pij} = 0$ at $i \neq j$ and, using the values of R_{sij} from Table 1, we obtain from Eq. (14) κ = 5.7 dB and $\Delta\kappa$ = 0.3 dB. These values show that the loss in the noise immunity, which is caused by a slight decorrelataion of the signal, is insignificant and close to the loss in gain.

The estimates presented above and the experimental data confirm the possibility of using a group of drifting radioacoustic relaying buoys to implement the low-frequency compensated receiving antenna array with an aperture of several kilometers at frequencies of several tens of hertz and with distances of several tens of kilometers to the sound source.

After performing the aforementioned experiments, we developed and successfully tested a specialized digital processor for processing the signals of a 16-channel DAAA.

REFERENCES

1. J. Northrop, W. C. Cummings, and P. O. Thompson, J. Acoust. Soc. Am. **43**, 383 (1968).
2. W. C. Cummings and P. O. Thompson, J. Acoust. Soc. Am. **50**, 1193 (1971).
3. C. Levenson, J. Acoust. Soc. Am. **55**, 1100 (1971).
4. K. M. Stafford, G. C. Fox, and D. S. Clark, J. Acoust. Soc. Am. **104**, 3616 (1998).
5. B. Mohl, W. Wahberg, and A. Heerfort, J. Acoust. Soc. Am. **109**, 434 (2001).
6. S. A. Solov'ev, Vestn. Akad. Nauk SSSR **1**, 77 (1968).
7. S. I. Voronina, N. G. Zhidkov, and R. G. Lyapisheva, Gidrofiz. Okeana (Yuzhno-Sakhalinsk) **28**, 40 (1972).
8. S. I. Voronina and N. G. Zhidkov, Gidrofiz. Okeana (Yuzhno-Sakhalinsk) **28**, 47 (1972).
9. R. S. Dietz and M. J. Sheehy, Geol. Soc. Am. Bull. **65**, 941 (1954).
10. F. Haber and Chien-Cung Yeh, J. Acoust. Soc. Am. **73**, 502 (1983).
11. V. V. Karavaev and V. V. Sazonov, *Statistical Theory of Passive Location* (Radio i Svyaz', Moscow, 1987), p. 79.
12. J. Ruze, Nuovo Cimento Suppl. **9** (3), 364 (1952).
13. Y. T. Lo, IEEE Trans. Antennas Propag. **12**, 257 (1964).
14. Ya. S. Shifrin, *Problems of the Statistical Theory of Antennas* (Sovetskoe Radio, Moscow, 1970).
15. P. H. Milne, *Underwater Acoustic Positioning Systems* (Spon, London, 1982; Sudostroenie, Leningrad, 1989).
16. L. A. Chernov, *Wave Propagation in a Random Medium*, 2nd ed. (Nauka, Moscow, 1975; McGraw-Hill, New York, 1960).
17. *Ocean Acoustics*, Ed. by L. M. Brekhovskikh (Nauka, Moscow, 1974).
18. I. Tolstoy and C. S. Clay, *Ocean Acoustics* (McGraw-Hill, New York, 1966; Mir, Moscow, 1969).
19. V. A. Zverev and N. V. Litvak, Akust. Zh. **45**, 807 (1999) [Acoust. Phys. **45**, 727 (1999)].
20. L. M. Brekhovskikh, *Waves in Layered Media* (Akad. Nauk SSSR, Moscow, 1957; Academic, New York, 1960).
21. N. G. Gatkin, V. A. Geranin, M. I. Karnovskiĭ, and L. G. Krasnyĭ, *Noise Immunity of a Typical Channel of Signal Detection* (Tekhnika, Kiev, 1971).
22. R. J. Urick, *Principles of Underwater Sound* (McGraw-Hill, New York, 1975; Sudostroenie, Leningrad, 1978).

Translated by E. Kopyl

Acoustical Physics, Vol. 49, No. 3, 2003, pp. 290–299. Translated from Akusticheskiĭ Zhurnal, Vol. 49, No. 3, 2003, pp. 348–358.

Inverse Problem of a Statistical Estimation of Scatterer Characteristics and Model Examples

V. A. Burov*, E. E. Kasatkina*, O. D. Rumyantseva*, and E. E. Sukhov**

** Physics Faculty, Moscow State University, Vorob'evy gory, Moscow, 119992 Russia*
e-mail: burov@phys.msu.su
*** Trapeznikov Institute of Control Problems, Russian Academy of Sciences,*
Profsoyuznaya ul. 65, Moscow, 117997 Russia
e-mail: sukhov@ipu.rssi.ru

Received June 5, 2002

Abstract—The inverse scattering problem involving experimental data with errors is considered in its statistical formulation. An algorithm for retrieving regularized estimates of the characteristics of spatially distributed scatterers (the phase velocity and absorption inhomogeneities) is developed. The algorithm takes into account the multiple scattering and generalizes the Wiener filtering to the nonlinear case. For weak scatterers, this nonlinear generalization is reduced to the linear Wiener filtering. The performance of the algorithm is verified by model examples simulating the operation of active acoustic tomography systems against various noise levels. The necessity of taking into account the multiple scattering and the fundamental role of the nonlinear filtering in the regularization procedure is demonstrated. It is remarkable that the noise robustness achieved in the reconstruction of strong scatterers with the optimal regularization algorithm is only slightly inferior to that achieved in the case of weak scatterers. © *2003 MAIK "Nauka/Interperiodica"*.

1. MAXIMAL POSTERIOR PROBABILITY ESTIMATE OF SCATTERER CHARACTERISTICS IN THE PRESENCE OF NOISE

In this paper, we address the problem of reconstructing the acoustic characteristics (e.g., the phase velocity and the absorption coefficient) of scattering inhomogeneities of a medium from noise-distorted scattering data in terms of the statistical approach. This inverse scattering problem belongs to the class of ill-posed problems. Therefore, a stable solution can only be obtained by regularization methods. To date, methods for solving linear ill-posed problems are elaborated. Such problems include, in particular, the linear statistical problems, in which the optimal regularization relies on the prior statistical information [1, 2] and can be reduced to a filtering procedure. However, methods for solving nonlinear ill-posed problems are not sufficiently advanced and are currently under development [3, 4]. The nonlinearity of the solution with respect to raw scattering data and, possibly, a simultaneous nonlinearity of the data with respect to unknown functions (these functions describe the scatterer and its secondary sources or internal fields) make the problem intricate and difficult to solve.

In this paper, we use the general statistical formulation of the inverse scattering problem as the problem of the optimal (in terms of the maximal posterior probability) estimation of the function $\varepsilon(\mathbf{r})$ related to the desired unknown characteristics of the scatterer as follows:

$$\varepsilon(\mathbf{r}) = \omega^2[c_0^{-2} - c^{-2}(\mathbf{r})] - 2i\omega\alpha(\mathbf{r}, \omega)/c(\mathbf{r}), \quad (1)$$

where an $\sim\exp(-i\omega t)$ time dependence is assumed. Here, c_0 and $c(\mathbf{r})$ are the sound velocity in the lossless background medium outside the scatterers and in the scattering region $\Re$, respectively, and $\alpha(\mathbf{r}, \omega)$ is the amplitude absorption coefficient in $\Re$. The algorithm of the solution consists in the minimization of a functional. The functional relies on the discrepancy between the experimental scattering data and their estimates that follow from the Lippmann–Schwinger equations and on the prior information about the correlation properties of noise and the desired characteristics of the scatterer. In addition, the constraining equations are involved, which are included directly into the functional or used as separate additional equations.

It should be noted that a similar statement of the problem was addressed in [5], where a very strong simplifying assumption was made that no nonradiating configurations of secondary sources were present and, as a consequence, the propagation operator with the Green's function as its kernel was invertible. Unfortunately, this assumption is only valid for certain model scatterers when significant prior information about the function describing a particular scatterer is available: for instance, for a scatterer modeled by a set of point inhomogeneities whose strengths are unknown and locations are known. On the contrary, the algorithm reported below is free from such restricting assumptions and it allows for the multiple scattering in the most rigorous mathematical formulation. As a result, we obtain regularized estimates of the velocity and absorption distributions in a scatterer localized in

space. The price of this optimal approach is a more complex resultant system of nonlinear equations and a comparatively high (however, as simulations show, admissible for modern computers) computational burden.

The initial functional can be constructed in the R space (spatial representation) as well as in the K space (momentum representation), which is conjugate to the R space. The earlier paper [6] used the spatial representation, in which the scatterer's function $\varepsilon(\mathbf{r})$ and the total internal field $U(\mathbf{r}, \mathbf{k}_0)$ are estimated (here, $\mathbf{k}_0$ is the wave vector of the incident monochromatic plane wave $\exp(i\mathbf{k}_0\mathbf{r})$). The present paper employs the momentum representation, in which the functions to be estimated are the spatial spectrum $\tilde{\varepsilon}(\mathbf{k}')$ of the scatterer and the spatial spectrum $T(\mathbf{k}', \mathbf{k}_0)$ of the secondary sources $\varepsilon(\mathbf{r})U(\mathbf{r}, \mathbf{k}_0)$ arising in the scattering region:

$$T(\mathbf{k}', \mathbf{k}_0) \equiv \int_{\Re} [\varepsilon(\mathbf{r})U(\mathbf{r}, \mathbf{k}_0)] \exp(-i\mathbf{k}'\mathbf{r})d\mathbf{r},$$
$$\mathbf{k}' \in K, \quad \mathbf{k}_0 \in K_0.$$

The prime means that the vector $\mathbf{k}'$ belongs to the D-dimensional K space of wave vectors of arbitrary direction and length. An unprimed vector belongs to the K_0 space of wave vectors of a fixed length $|\mathbf{k}_0| = k_0$, where k_0 is the wave number in the background medium outside the scatterers. The momentum representation is convenient when the background medium is lossless and homogeneous, the sounding fields are plane, and the plane-wave expansion of the scattered field is used. Below, we assume that these conditions are met. These assumptions do not restrict the generality of the proposed method of constructing the optimal solution and the conclusions that follow from the realization of this method.

The experimental scattering data are the values of the complex scattering amplitude $T_{\exp}(\mathbf{k}, \mathbf{k}_0)$, where $\mathbf{k}, \mathbf{k}_0 \in K_0$. The values of $T_{\exp}$ are related to the desired values of $\tilde{\varepsilon}$ through the Lippmann–Schwinger equation

$$T_{\exp}(\mathbf{k}, \mathbf{k}_0) = \tilde{\varepsilon}(\mathbf{k} - \mathbf{k}_0)$$
$$+ \frac{1}{(2\pi)^D}\int_K \tilde{\varepsilon}(\mathbf{k} - \mathbf{k}')\tilde{G}(|\mathbf{k}'|, k_0)T(\mathbf{k}', \mathbf{k}_0)d\mathbf{k}' + n(\mathbf{k}, \mathbf{k}_0), \quad (2)$$
$$\mathbf{k}, \mathbf{k}_0 \in K_0; \quad \mathbf{k}' \in K,$$

where $\tilde{G}(|\mathbf{k}'|, k_0)$ is the spatial spectrum of the Green's function of the homogeneous infinite medium and $n(\mathbf{k}, \mathbf{k}_0)$ is the noise signal received from the direction $\mathbf{k}$ when the primary plane wave is emitted in the direction $\mathbf{k}_0$. We assume that the functions n and $\tilde{\varepsilon}$ are realizations of Gaussian random processes with the correlation functions N and $\mathfrak{E}$, respectively. Then, the maximal posterior probability estimation procedure amounts to the minimization of the functional F, which is quadratic in the case we consider below:

$$F(\tilde{\varepsilon}, \tilde{\varepsilon}^+, T, T^+)$$
$$= F_0(N^{-1}; \tilde{\varepsilon}, \tilde{\varepsilon}^+, T, T^+) + F_A(\mathfrak{E}^{-1}; \tilde{\varepsilon}, \tilde{\varepsilon}^+), \quad (3)$$

where

$$F_0 = \int_{K_0}\cdots\int \left[T^+_{\exp}(\mathbf{k}_{01}, \mathbf{k}_1) - \tilde{\varepsilon}^+(\mathbf{k}_1 - \mathbf{k}_{01})\right.$$
$$\left. - \frac{1}{(2\pi)^D}\int_K T^+(\mathbf{k}_{01}, \mathbf{k}'_1)\tilde{G}^+(|\mathbf{k}'_1|, k_0)\tilde{\varepsilon}^+(\mathbf{k}_1 - \mathbf{k}'_1)d\mathbf{k}'_1\right]$$
$$\times N^{-1}(\mathbf{k}_1, \mathbf{k}_{01}; \mathbf{k}_2, \mathbf{k}_{02})\left[T_{\exp}(\mathbf{k}_2, \mathbf{k}_{02}) - \tilde{\varepsilon}(\mathbf{k}_2 - \mathbf{k}_{02})\right. \quad (4)$$
$$\left. - \frac{1}{(2\pi)^D}\int_K \tilde{\varepsilon}(\mathbf{k}_2 - \mathbf{k}'_2)\tilde{G}(|\mathbf{k}'_2|, k_0)T(\mathbf{k}'_2, \mathbf{k}_{02})d\mathbf{k}'_2\right]d\mathbf{k}_1$$
$$\times d\mathbf{k}_{01}d\mathbf{k}_2d\mathbf{k}_{02},$$

$$F_A = \int_K\int \tilde{\varepsilon}^+(\mathbf{k}'_1)\beta(\mathbf{k}'_1, \mathbf{k}'_2)\mathfrak{E}^{-1}(\mathbf{k}'_1, \mathbf{k}'_2)\tilde{\varepsilon}(\mathbf{k}'_2)d\mathbf{k}'_1d\mathbf{k}'_2, \quad (5)$$
$$\mathbf{k}_1, \mathbf{k}_{01}, \mathbf{k}_2, \mathbf{k}_{02} \in K_0; \quad \mathbf{k}'_1, \mathbf{k}'_2 \in K.$$

The symbol "+" means Hermitian conjugation. Physically, the term F_0 is a quadratic form of the discrepancy between the scattering amplitude values (or between the wave fields in the spatial representation). These values are, on the one hand, measured experimentally ($T_{\exp}$) and, on the other hand, estimated from Eq. (2) at $n \equiv 0$. The term F_A allows for the prior statistical information about the scatterer characteristics weighted with the function $\beta(\mathbf{k}'_1, \mathbf{k}'_2)$. Without loss of generality, we assume in Eq. (5) that $\langle\tilde{\varepsilon}(\mathbf{k}')\rangle = 0$ for $\forall\mathbf{k}' \in K$, where $\langle\cdot\rangle$ means averaging over an ensemble of scatterers of the class we consider.

Functional (3) should be supplemented with constraining equations of the type of Lippmann–Schwinger equations for the unknown $T(\mathbf{k}', \mathbf{k}_0)$:

$$T(\mathbf{k}', \mathbf{k}_0) = \tilde{\varepsilon}(\mathbf{k}' - \mathbf{k}_0)$$
$$+ \frac{1}{(2\pi)^D}\int_K \tilde{\varepsilon}(\mathbf{k}' - \mathbf{k}'')\tilde{G}(|\mathbf{k}''|, k_0)T(\mathbf{k}'', \mathbf{k}_0)d\mathbf{k}'', \quad (6)$$
$$\mathbf{k}' \in K.$$

Indeed, expression (6) contains exact functions $T(\mathbf{k}', \mathbf{k}_0)$ for all $\mathbf{k}' \in K$, whereas the experimental data $T_{\exp}(\mathbf{k}', \mathbf{k}_0)$ are distorted by noise and known only for $|\mathbf{k}'| = k_0$:

$$T_{\exp}(\mathbf{k}, \mathbf{k}_0) = T(\mathbf{k}, \mathbf{k}_0) + n(\mathbf{k}, \mathbf{k}_0),$$
$$|\mathbf{k}| = |\mathbf{k}_0| = k_0.$$

In the spatial representation, these constraining equations are considered for the wave fields inside the scattering region. It should be noted that the constraining equations can be included directly into the functional F through the undetermined function-valued Lagrange multipliers [6].

When calculating variations of the functional F with respect to the unknown functions $\tilde{\varepsilon}^+(\boldsymbol{\chi})dV_{\boldsymbol{\chi}}$, we introduce the quantity $dV_{\boldsymbol{\chi}}$ representing the elementary volume with the origin at the point $\boldsymbol{\chi} \in K$ in the Cartesian coordinates, where $\boldsymbol{\chi}$ is an arbitrary fixed vector. The equations

$$\delta F(\tilde{\varepsilon}, \tilde{\varepsilon}^+, T, T^+)/\delta[\tilde{\varepsilon}^+(\boldsymbol{\chi})dV_{\boldsymbol{\chi}}] = 0 \qquad (7)$$

together with Eqs. (6) written for all $\mathbf{k}_0$ constitute a complete system of equations for the estimates of the desired quantities $\tilde{\varepsilon}$ and the unknown auxiliary quantities T. Variation (7) can be calculated and the transformations can be performed for the two-dimensional, as well as three-dimensional, problem for arbitrary correlation functions N and $\mathfrak{E}$. The resultant expression is lengthy, but, in essence, simple. For the two-dimensional problem with measurement errors δ-correlated with respect to direction, this expression has the form

$$N^{-1}(\mathbf{k}_1, \mathbf{k}_{01}; \mathbf{k}_2, \mathbf{k}_{02}) \approx (1/n_0)\delta(\mathbf{k}_2 - \mathbf{k}_1)\delta(\mathbf{k}_{02} - \mathbf{k}_{01}),$$
$$\mathbf{k}_1, \mathbf{k}_{01}, \mathbf{k}_2, \mathbf{k}_{02} \in K_0. \qquad (8)$$

The discrete version of relationship (8) for M directions of the incident field and M directions of the scattered field is

$$N^{-1}(\mathbf{k}_1, \mathbf{k}_{01}; \mathbf{k}_2, \mathbf{k}_{02}) \approx (1/W_0)\delta_{\mathbf{k}_1, \mathbf{k}_2}\delta_{\mathbf{k}_{01}, \mathbf{k}_{02}},$$
$$\Delta\varphi = 2\pi/M, \quad \Delta k = k_0\Delta\varphi,$$
$$W_0 \equiv n_0(\Delta k)^2;$$
$$\delta_{\mathbf{k}_1, \mathbf{k}_2} = \{1 \text{ for } \mathbf{k}_1 = \mathbf{k}_2; 0 \text{ for } \mathbf{k}_1 \neq \mathbf{k}_2\},$$

where $\delta_{\mathbf{k}_1, \mathbf{k}_2}$ is the Kronecker delta defined for the discrete vector argument. In terms of our representation, for the two-dimensional problem, $n_0(\Delta k)^2$ is a dimensionless quantity. Physically, this is the power of noise $n(\mathbf{k}, \mathbf{k}_0)$ enclosed in the solid angle $(\Delta k)^2$ at $k_0 = 1$ and defined in the space of pairs of wave vectors $\mathbf{k}, \mathbf{k}_0 \in K_0$ used in the measurements. The dimensional coefficient n_0 has the physical meaning of the noise power density in this space: it is the noise power per unit solid angle.

With expression (8), Eqs. (7) take the following discrete form:

$$\sum_{\boldsymbol{\eta}} A(\boldsymbol{\chi}, \boldsymbol{\eta})\tilde{\varepsilon}(\boldsymbol{\eta}) = T'_{\exp}(\boldsymbol{\chi}) + \Im_1(\boldsymbol{\chi}) + \Im_2(\boldsymbol{\chi}). \qquad (9)$$

The system of equations (9) and (6) implies that the spatial spectrum of the scatterer is localized in a circle of radius $2k_0$. Hence, we can limit our analysis to estimating $\tilde{\varepsilon}(\boldsymbol{\eta})$ only for $|\boldsymbol{\eta}| < 2k_0$. Independent samples are taken over an irregular grid in $\boldsymbol{\eta}$. The grid is irregular, because the measurements use a discrete set of vectors $\mathbf{k}_0, \mathbf{k} \in K_0$ that is uniform in angle. Due to the reciprocity theorem, only half of the directions of the vector $\mathbf{k}$ (index n) are considered for a particular $\mathbf{k}_0$ (index m):

$$\boldsymbol{\eta} \in \{0 \cup (\mathbf{k}^n - \mathbf{k}_0^m)\}, \qquad (10)$$

where

$$\mathbf{k}_0^m = \{k_0, \varphi_0^m\}, \quad \varphi_0^m = \Delta\varphi(m-1);$$
$$\Delta\varphi = 2\pi/M, \quad m = \overline{1, M};$$
$$\mathbf{k}^n = \{k_0, \varphi^n\}, \quad \varphi^n = \Delta\varphi(n-1);$$
$$n = \overline{(m+1), (m+M/2)}.$$

A similar procedure is used to define the independent discrete values of $\boldsymbol{\chi}$ that are the parameters of Eqs. (7) and, consequently, Eqs. (9): $\boldsymbol{\chi} \in \{0 \cup (\mathbf{k}^{n_\alpha} - \mathbf{k}_0^{m_\beta})\}$, where $\mathbf{k}_0^{m_\beta} = \{k_0, \varphi_\beta = \varphi_0^{m_\beta}\}$ and $\mathbf{k}^{n_\alpha} = \{k_0, \varphi_\alpha = \varphi^{n_\alpha}\}$.

The matrix that acts on the unknown quantities $\tilde{\varepsilon}(\boldsymbol{\eta})$ in Eqs. (9) is written as

$$A(\boldsymbol{\chi}, \boldsymbol{\eta}) = E(\boldsymbol{\chi}, \boldsymbol{\eta}) + \beta(\boldsymbol{\chi}, \boldsymbol{\eta})\mathfrak{K}(\boldsymbol{\chi}, \boldsymbol{\eta})W_0\mathfrak{E}^{-1}(\boldsymbol{\chi}, \boldsymbol{\eta}), \qquad (11)$$

where $E(\boldsymbol{\chi}, \boldsymbol{\eta})$ is the unit matrix and

$$\mathfrak{K}(\boldsymbol{\chi}, \boldsymbol{\eta}) = S(\boldsymbol{\chi})S(\boldsymbol{\eta})C(\boldsymbol{\eta})/(2C(\boldsymbol{\chi})).$$

The coefficients S satisfy the conditions

$$S(\boldsymbol{\chi}) = \{|\sin(\varphi_\alpha - \varphi_\beta)| \text{ at } |\boldsymbol{\chi}| \neq 0 \text{ and } |\boldsymbol{\chi}| \neq 2k_0;$$
$$\Delta\varphi/3 \text{ at } \boldsymbol{\chi} = 0 \text{ or } |\boldsymbol{\chi}| = 2k_0\}.$$

For $S(\boldsymbol{\eta})$, the vector $\boldsymbol{\chi}$ is replaced with the vector $\boldsymbol{\eta}$, and the argument $(\varphi_\alpha - \varphi_\beta)$, with the argument $(\varphi^n - \varphi_0^m)$. The coefficient S appears because of the difference in the descriptions of the wave vector spaces K_0 and K, which enter into expressions (4) and (5). This is due to the difference in the physical meanings of the correlation matrices $\mathfrak{E}$ and N, which is also observed in the spatial representation. Indeed, for $\mathfrak{E}(\mathbf{k}'_2, \mathbf{k}'_1) \equiv \langle\tilde{\varepsilon}(\mathbf{k}'_2)\tilde{\varepsilon}^+(\mathbf{k}'_1)\rangle$, the vectors $\mathbf{k}'_1, \mathbf{k}'_2 \in K$ take all admissible discrete values within the region of spatial fre-

quencies of our interest. For $N(\mathbf{k}_2, \mathbf{k}_{02}; \mathbf{k}_1, \mathbf{k}_{01}) \equiv \langle n(\mathbf{k}_2, \mathbf{k}_{02}) n^+(\mathbf{k}_1, \mathbf{k}_{01}) \rangle$, the vectors $\mathbf{k}_1, \mathbf{k}_2, \mathbf{k}_{01}, \mathbf{k}_{02} \in K_0$ vary only in direction.

The coefficient $C(\boldsymbol{\eta})$ is the number of constant vectors $\boldsymbol{\eta} = \mathbf{k} - \mathbf{k}_0$ that can be formed by two vectors $\mathbf{k}$, $\mathbf{k}_0 \in K_0$ when each of the vectors $\mathbf{k}$ and $\mathbf{k}_0$ takes M discrete values:

$$C(\boldsymbol{\eta}) = \{M \text{ at } \boldsymbol{\eta} = 0;$$
$$2 \text{ at } |\boldsymbol{\eta}| \neq 0 \text{ and } |\boldsymbol{\eta}| \neq 2k_0; \quad 1 \text{ at } |\boldsymbol{\eta}| = 2k_0\}.$$

The quantity $C(\boldsymbol{\chi})$ is defined in a similar manner. The quantities $T'_{\exp}(\boldsymbol{\chi})$ are the scattering data averaged over these sets:

$$T'_{\exp}(\boldsymbol{\chi}) = \begin{cases} \dfrac{1}{M}\displaystyle\sum_{m_2=1}^{M} T_{\exp}(\mathbf{k}_0^{m_2}, \mathbf{k}_0^{m_2}) \text{ at } \boldsymbol{\chi} = 0 \\ [T_{\exp}(\mathbf{k}^{n_\alpha}, \mathbf{k}_0^{m_\beta}) + T_{\exp}(-\mathbf{k}_0^{m_\beta}, -\mathbf{k}^{n_\alpha})]/2 \\ \text{at } \boldsymbol{\chi} = \mathbf{k}^{n_\alpha} - \mathbf{k}_0^{m_\beta}, \text{ where } |\boldsymbol{\chi}| \neq 0 \text{ and } |\boldsymbol{\chi}| \neq 2k_0 \\ T_{\exp}(-\mathbf{k}_0^{m_\beta}, \mathbf{k}_0^{m_\beta}) \text{ at } \boldsymbol{\chi} = -2\mathbf{k}_0^{m_\beta} \text{ (i.e., } \mathbf{k}^{n_\alpha} = -\mathbf{k}_0^{m_\beta}). \end{cases}$$

The term $\Im_1(\boldsymbol{\chi})$ has the same structure, but $T_{\exp}$ is replaced by $(\tilde{\varepsilon}(\boldsymbol{\chi}) - T)$. The last term in Eqs. (9), $\Im_2(\boldsymbol{\chi})$, is expressed as

$$\Im_2(\boldsymbol{\chi}) = \frac{S(\boldsymbol{\chi})}{C(\boldsymbol{\chi})}\frac{(\Delta k)^2}{(2\pi)^2}\sum_{m_1=1}^{M}\sum_{n_1=m_1+1}^{m_1+M} T^+(\mathbf{k}_0^{m_1}, \mathbf{k}^{n_1} - \boldsymbol{\chi})$$
$$\times \tilde{G}^+(|\mathbf{k}^{n_1} - \boldsymbol{\chi}|, k_0)[T_{\exp}(\mathbf{k}^{n_1}, \mathbf{k}_0^{m_1}) - T(\mathbf{k}^{n_1}, \mathbf{k}_0^{m_1})];$$
$$\Delta k = 2\pi k_0/M, \quad |\mathbf{k}_0^{m_1}| = |\mathbf{k}^{n_1}| = k_0.$$

The number $M^2/2 + 1$ of algebraic equations (9) is equal to the number of unknown values of $\tilde{\varepsilon}(\boldsymbol{\eta})$. These equations are supplemented with sampled Eqs. (6), which makes it possible to estimate the unknown $T(\mathbf{k}', \mathbf{k}_0)$ for $\mathbf{k}'$ used in Eqs. (9) (in particular, at $|\mathbf{k}'| = k_0$).

It should be noted that scatterer (1) may consist of the velocity component (index c) and dissipation component (index α) simultaneously (the functions $\varepsilon_c(\mathbf{r})$ and $\varepsilon_\alpha(\mathbf{r})$ are real, but their Fourier transforms are not): $\varepsilon(\mathbf{r}) = \varepsilon_c(\mathbf{r}) + i\varepsilon_\alpha(\mathbf{r})$. Therefore, $\tilde{\varepsilon}(\mathbf{k}') = \tilde{\varepsilon}_c(\mathbf{k}') + i\tilde{\varepsilon}_\alpha(\mathbf{k}')$, where $\mathbf{k}' \in K$. Then, the optimal procedure is the one that estimates each of these components separately. When the c and α components are uncorrelated, the term F_A (see Eq. (5)) is replaced with a sum of similar terms for each of them. The variation of the total functional F is calculated independently with respect to both unknown functions $\tilde{\varepsilon}_c$ and $\tilde{\varepsilon}_\alpha$; i.e., variations (7) are replaced with the relationships

$$\delta F/\delta(\tilde{\varepsilon}_c^+(\boldsymbol{\chi})dV_\chi) = 0, \quad \delta F/\delta(\tilde{\varepsilon}_\alpha^+(\boldsymbol{\chi})dV_\chi) = 0.$$

To improve the quality of estimating the c and α components, we can additionally use the prior information that $\varepsilon_c(\mathbf{r})$ and $\varepsilon_\alpha(\mathbf{r})$ are real and that the sign of the function $\varepsilon_\alpha(\mathbf{r})$, which is responsible for the absorption, is known.

To find the correlation function of the scatterer's spatial spectrum $\mathcal{E}(\boldsymbol{\eta}, \boldsymbol{\chi}) = \langle \tilde{\varepsilon}(\boldsymbol{\eta})\tilde{\varepsilon}^+(\boldsymbol{\chi}) \rangle$, one should know the respective prior characteristics of this kind of scatterer or an analytical estimate for the scatterer model being used. Our numerical simulations assumed that each realization of the random scatterer is a single inhomogeneity or a set of inhomogeneities of the same type and that the effective linear size of the region where the inhomogeneities may occur is L. The elementary inhomogeneities, random in amplitude, sign, and location, are uniformly distributed over this region. A full ensemble of single random inhomogeneities is characterized by the following statistical parameters: the mean-square amplitude, the effective linear size l, and the characteristic width of the spatial spectrum $\cong 2\pi/l$. This is a model of the "cluster" scatterer with the mean cluster size $\approx l$. For this model, $\mathcal{E}(\boldsymbol{\eta}, \boldsymbol{\chi}) \approx \mathcal{E}_0\left(\dfrac{\boldsymbol{\eta} + \boldsymbol{\chi}}{2}\right)\Gamma(\boldsymbol{\eta} - \boldsymbol{\chi})$, where $\mathcal{E}_0$ is the scatterer's average statistical spectral "energy" density. It determines the spatial frequency domain where it is necessary to allow for the scatterer's spectral components (the width of the domain is $\cong 2\pi/l$). The function $\Gamma(\boldsymbol{\eta} - \boldsymbol{\chi})$ determines the domain where the correlation between the spectral components $\tilde{\varepsilon}(\boldsymbol{\eta})$ and $\tilde{\varepsilon}^+(\boldsymbol{\chi})$ is significant; this function is related to the overall scatterer size L: the correlation is observed when $|\boldsymbol{\eta} - \boldsymbol{\chi}| \leq 2\pi/L$. In the model we consider below, $\Gamma(\boldsymbol{\eta} - \boldsymbol{\chi}) \approx \exp[-(\boldsymbol{\eta} - \boldsymbol{\chi})^2(L/\pi)^2]$.

To construct the matrix $\mathcal{E}^{-1}(\boldsymbol{\chi}, \boldsymbol{\eta})$, the regularization technique must be used: $\mathcal{E}^{-1}(\boldsymbol{\chi}, \boldsymbol{\eta}) = [\mathcal{E}(\boldsymbol{\eta}, \boldsymbol{\chi}) + \theta E]^{-1}$, where E is the unit matrix and θ is the regularization coefficient chosen in accordance with the maximal value $\max\limits_{(\boldsymbol{\eta}, \boldsymbol{\chi})}|\mathcal{E}(\boldsymbol{\eta}, \boldsymbol{\chi})|$.

2. NUMERICAL SCATTERER RECONSTRUCTION

The experimental scattering data $T^0_{\exp}(\mathbf{k}, \mathbf{k}_0) \equiv T^0_{\exp}(\varphi, \varphi_0)$ in the absence of noise ($T^0_{\exp} \equiv T_{\exp}$ when $n(\mathbf{k}, \mathbf{k}_0) \equiv 0$) were simulated by solving the direct problem[1] with the given scatterer function $\varepsilon(\mathbf{r})$. The Lippmann–Schwinger-type equation (6) was solved by an iterative method, and the values $T(\mathbf{k}', \mathbf{k}_0)$ ($\mathbf{k}' \in K$) found were interpolated onto the Ewald's circle $|\mathbf{k}'| = k_0$ at

[1] We intend to describe the numerical technique used to solve the direct problem in a subsequent paper.

each given $\mathbf{k}_0$. The values T^0_{exp} were distorted by noise uncorrelated in angle (see Eq. (8)) in the form of a zero-mean Gaussian sequence with an rms amplitude deviation σ_n for the components $\text{Re}\,n(\mathbf{k}, \mathbf{k}_0)$ and $\text{Im}\,n(\mathbf{k}, \mathbf{k}_0)$. We assumed that $\sigma_n = qT_{\max}$ ($q \geq 0$), where $T_{\max} \equiv \max_{\mathbf{k}, \mathbf{k}_0 \in K_0} \left|T^0_{\text{exp}}(\mathbf{k}, \mathbf{k}_0)\right|$. The input noise-to-signal amplitude ratio I_n was calculated as the ratio of the noise norm $\|n\|$ to the norm $\left\|T^0_{\text{exp}}\right\|$ of the noise-free scattering data: $I_n = \|n\|/\left\|T^0_{\text{exp}}\right\|$. Here, $\|n\| = \sqrt{\int_0^{2\pi}\int_0^{2\pi} |n(\varphi, \varphi_0)|^2 d\varphi d\varphi_0}$ or, in terms of discrete quantities, $\|n\| = \Delta\varphi \sqrt{\sum_{\mathbf{k}, \mathbf{k}_0} |n(\mathbf{k}, \mathbf{k}_0)|^2}$; in a similar way, we have $\left\|T^0_{\text{exp}}\right\| = \Delta\varphi \sqrt{\sum_{\mathbf{k}, \mathbf{k}_0} \left|T^0_{\text{exp}}(\mathbf{k}, \mathbf{k}_0)\right|^2}$. In the simulations, we introduced independent errors with equal deviations σ_n to two equal sets T^0_{exp}. Accordingly, two realizations of the experimental data $T_{\text{exp}}(\mathbf{k}, \mathbf{k}_0)$ distorted by independent noises were generated. The effective input noise-to-signal ratio was $I'_n = I_n/\sqrt{2}$.

The values $\tilde{\varepsilon}(\boldsymbol{\eta})$ were estimated by solving the inverse problem defined by Eqs. (6) and (9). The solution was interpolated from irregular grid (10) to a regular Cartesian grid, and the final scatterer estimate $\hat{\varepsilon}(\mathbf{r})$ in the R space was calculated through the inverse Fourier transform. The relative rms error in $\hat{\varepsilon}(\mathbf{r})$ was calculated as the ratio of the residual between the estimate $\hat{\varepsilon}(\mathbf{r})$ and the true function $\varepsilon(\mathbf{r})$ to the norm of the function $\varepsilon(\mathbf{r})$: $\nu_\varepsilon = \sqrt{\sum_{\mathbf{r}} |\hat{\varepsilon}(\mathbf{r}) - \varepsilon(\mathbf{r})|^2} / \sqrt{\sum_{\mathbf{r}} |\varepsilon(\mathbf{r})|^2}$.

2.1. Reconstruction of Weak Scatterers

Consider the Born approximation (single scattering) in order to compare the result with that given by the optimal processing in the case of strong scatterers. In the Born approximation, the terms $\Im_1(\boldsymbol{\chi})$ and $\Im_2(\boldsymbol{\chi})$ on the right-hand side of Eqs. (9), which allow for the multiple scattering, are dropped. Additional constraining equations (6) are also unnecessary. Then, with allowance for the prior information about the correlation of the spatial spectra of noise and scatterer, the Born estimate $\tilde{\varepsilon}_{\text{Born}}(\boldsymbol{\eta})$ can be found for $(M^2/2 + 1)$ spatial frequencies $\boldsymbol{\eta}$ (see (10)) from the system of algebraic equations

$$\sum_{\boldsymbol{\eta}} A(\boldsymbol{\chi}, \boldsymbol{\eta}) \tilde{\varepsilon}_{\text{Born}}(\boldsymbol{\eta}) = T'_{\text{exp}}(\boldsymbol{\chi}). \tag{12}$$

In the low-noise approximation, we have $W_0 \longrightarrow 0$ and $A(\boldsymbol{\chi}, \boldsymbol{\eta}) \longrightarrow E(\boldsymbol{\chi}, \boldsymbol{\eta})$, and we obtain $\tilde{\varepsilon}_{\text{Born}}(\boldsymbol{\chi}) = T'_{\text{exp}}(\boldsymbol{\chi})$, which is evident for weak scatterers. As we noted above, for the further comparison with stronger scatterers, we used two realizations of the experimental data. The overdetermined system (12) obtained above was solved by the least-squares method. In the Born approximation, the least-squares solution to the overdetermined problem is equivalent to the solution of the non-overdetermined problem with the scattering data averaged over realizations.

Regularization filtering in the Born approximation is similar to the classical Wiener filtering. In fact, the matrix $[A(\boldsymbol{\chi}, \boldsymbol{\eta})]^{-1}$ in Eq. (12) acts as a filter. According to Eq. (11), the noise-to-signal energy ratio is associated with the quantity $W_0 \mathfrak{E}^{-1}(\boldsymbol{\chi}, \boldsymbol{\eta})$, which enters into Eq. (11) with the weighting function $\beta(\boldsymbol{\chi}, \boldsymbol{\eta})\mathfrak{K}(\boldsymbol{\chi}, \boldsymbol{\eta})$. Choosing the weighting function $\beta(\boldsymbol{\chi}, \boldsymbol{\eta})$ as

$$\beta(\boldsymbol{\chi}, \boldsymbol{\eta}) = 1/\mathfrak{K}(\boldsymbol{\chi}, \boldsymbol{\eta}) \tag{13}$$

adjusts the filtering procedure in Eq. (12) to the Wiener scheme, which provides the optimal solution to the linear inverse problem. The filtering consists in suppressing high spatial frequencies in the spectral estimate $\tilde{\varepsilon}(\boldsymbol{\eta})$. At the same time, at low spatial frequencies, the effect of noise persists. As the noise-to-signal ratio grows, the optimal solution requires a better filtering.

In the numerical experiment, we reconstructed a weak scatterer of Gaussian shape with the maximal phase velocity contrast of $\Delta c/c_0 = 0.01$ and the half-width (measured at a level of $1/e$) $a/\lambda_0 \approx 0.82$. The additional phase shift through the scatterer's central section is $\Delta\psi \cong 0.03\pi$. Each of the two independent data realizations $T_{\text{exp}}(\mathbf{k}, \mathbf{k}_0)$ contained a noise component with $\sigma_n = 0.15T_{\max}$ and $I_n \approx 75\%$; i.e., the input noise-to-signal ratio was high. The results of the numerical reconstruction are reported in [7]. The reconstruction without regularization filtering ignores the prior information about the scatterer and the actual noise, because it assumes that $W_0 = 0$ in Eq. (11). In this case, the relative error of the estimate $\hat{\varepsilon}(\mathbf{r})$ was $\nu_\varepsilon \approx 50\%$, which was almost the same as the effective input noise-to-signal amplitude ratio $I'_n \approx 53\%$. When the reconstruction uses the regularization filtering, the matrix N is formed for the true noise intensity, at which $W_0 = (\sigma_n)^2$ and the optimal factor $\beta(\boldsymbol{\chi}, \boldsymbol{\eta})$ of Eq. (13) is taken. The quality of the estimate $\hat{\varepsilon}(\mathbf{r})$ in the presence of the same errors becomes noticeably better: $\nu_\varepsilon \approx 9\%$.

It should be noted that, independently of whether the filtering was applied or not, at a sufficiently high noise intensity, ν_ε is a linear function of I'_n. At low noise intensities, ν_ε decreases slower due to the discretization errors. It is also important that the estimate $\hat{\varepsilon}(\mathbf{r})$ obtained by the regularization filtering rather weakly depends on the regularization parameters. For example, one can choose $\beta(\boldsymbol{\chi}, \boldsymbol{\eta}) \equiv 1$ and it is sufficient to estimate the matrix $\mathfrak{E}(\boldsymbol{\eta}, \boldsymbol{\chi})$ for approximate values of l and L.

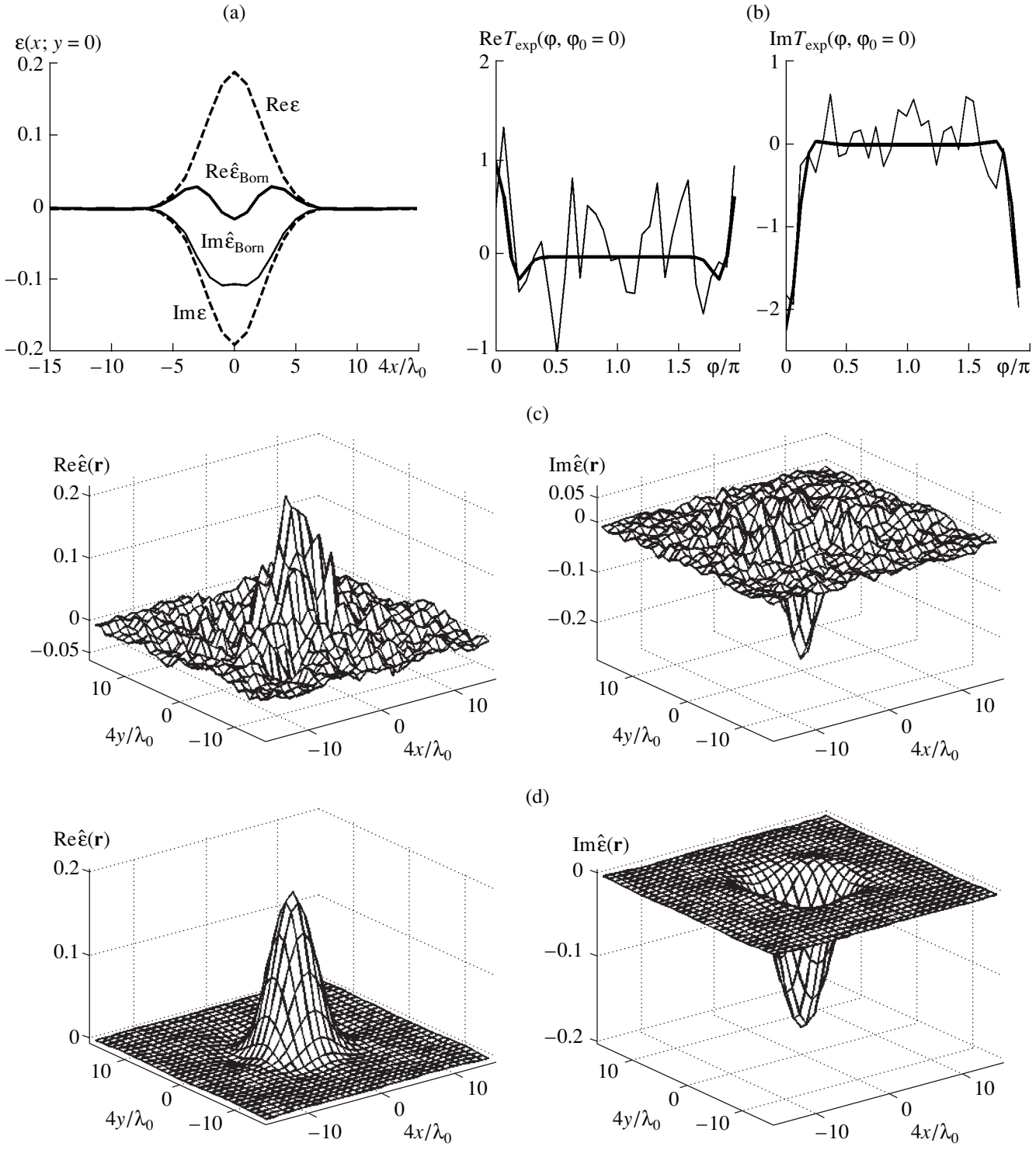

Fig. 1. Middle-power refractive–absorptive scatterer (the velocity contrast is $\Delta c/c_0 = 0.2$, the additional phase shift is $\Delta\psi \cong 0.55\pi$, and the amplitude absorption in the scatterer is 4.2 times): (a) the central sections of the true scatterer (dashed lines) and the scatterer reconstructed in the Born approximation from noise-free data (solid lines); (b) the real and imaginary parts of the scattering data (normalized by the maximum of the noise-free real part) at $\varphi_0 = 0$ in the absence (thick line) and presence of noise with the deviation of $\sigma_n = 0.15T_{max}$ (thin line); and (c, d) the scatterer reconstructed from the noisy data at $\sigma_n = 0.15T_{max}$ (c) by the weak regularization filtering and (d) by the matched filtering.

2.2. Scatterer Reconstruction Taking into Account the Multiple Scattering

To estimate middle-power and strong-power scatterers, it is necessary to solve Eqs. (9) and (6) together. Since the system is nonlinear with respect to the unknown $(\tilde{\varepsilon}, T)$, it must be solved by an iterative technique. In the numerical simulation, we used an iterative scheme that alternatively estimated $\tilde{\varepsilon}$ and T [8, 9]. At every particular iteration step of number j, the estimate $\tilde{\varepsilon}_j(\boldsymbol{\eta})$ is a solution to subsystem (9), whose terms $\Im_1(\boldsymbol{\chi})$ and $\Im_2(\boldsymbol{\chi})$ appearing on the right-hand side are formed from the estimates $\tilde{\varepsilon}_{(j-1)}$ and $T_{(j-1)}$ obtained at the previous step. The initial estimate ($j = 1$) in this iterative procedure is the smoothed Born estimate $\tilde{\varepsilon}_{\text{Born}}(\boldsymbol{\eta})$ [see Eq. (12)]. The use of two realizations of the noise-distorted scattering data T_{exp} makes subsystem (9) overdetermined and suggests that it should be solved in terms of the least-squares method, which additionally improves the convergence of the iterative scheme. It should be noted that multiple scattering causes an implicit nonlinear dependence of the right-hand side of Eqs. (9) on T_{exp}. Therefore, unlike the Born approximation, the least-squares solution to subsystem (9) with redundant data T_{exp} collected from all realizations is not equivalent to the solution of the nonoverdetermined subsystem with the initial data averaged over the realizations.

To avoid the possible oscillating divergence of the iterative solution, we partially (in the relaxation manner) introduce the correction: $\tilde{\varepsilon}'_j = (1-\gamma)\tilde{\varepsilon}_{(j-1)} + \gamma\tilde{\varepsilon}_j$, where $\tilde{\varepsilon}'_j$ is the final spectral estimate on the jth iteration and $0 < \gamma \le 1$ (in the numerical examples described below, $\gamma = 1/8$). Next, we solve subsystem (6) for the estimate $T_j(\mathbf{k}', \mathbf{k}_0)$ based on the particular weighted values $\tilde{\varepsilon}'_j$, after which the calculations are repeated. As is known, since Eqs. (6) contain a convolution, to solve these equations, a domain should be introduced around the support of the function $\hat{\varepsilon}(\mathbf{r})$ ($\tilde{\varepsilon}'_j$ is the spectrum of this function), where the latter is defined to be zero.

The convergence of the iterative procedure was estimated in terms of the current residual $\|T_j - T_{\text{exp}}\| = \Delta\varphi\sqrt{\sum_{\mathbf{k},\mathbf{k}_0}|T_j(\mathbf{k},\mathbf{k}_0) - T_{\text{exp}}(\mathbf{k},\mathbf{k}_0)|^2}$. The iterations were terminated when $\|T_j - T_{\text{exp}}\|$ became comparable with the norm $\|n\|$ of the error due to the noise. Note that, in principle, this reconstruction technique remains operable at any frequency. However, because the scattering power of an acoustic scatterer grows with frequency, the iterative procedure should be improved at high frequencies in order to ensure its convergence (which we will discuss below). In the problems related to medical diagnosis of soft tissues, which is the primary concern of this algorithm, frequencies of a few megahertz are used.

Below, we present the results of our numerical simulations for two refractive–absorptive scatterers $\varepsilon(\mathbf{r}) = \varepsilon_c(\mathbf{r}) + i\varepsilon_\alpha(\mathbf{r})$ of a middle-power intensity. The functions $\mathrm{Re}\,\varepsilon(\mathbf{r}) = \varepsilon_c(\mathbf{r})$ and $\mathrm{Im}\,\varepsilon(\mathbf{r}) = \varepsilon_\alpha(\mathbf{r})$ are modeled by Gaussian inhomogeneities, each of them characterized by the half-width $a/\lambda_0 \approx 0.82$, as in the case of a weak scatterer. The first scatterer has a simple structure (Fig. 1a): its real and imaginary parts are modeled by a single inhomogeneity. The amplitude of the function $\mathrm{Re}\,\varepsilon(\mathbf{r})$ corresponds to the velocity contrast $\Delta c/c_0 = 0.2$, and the additional phase shift through the central section is $\Delta\psi \cong 0.55\pi$. The amplitude of the function $-\mathrm{Im}\,\varepsilon(\mathbf{r})$ corresponds to a maximal amplitude absorption coefficient of ≈ 0.96 Np/λ_0 (see Eq. (1)), and the total absorption along the central section is ≈ 1.44 Np, i.e., the amplitude attenuation is 4.2 times. The second scatterer has a more complex structure (Fig. 2a). The function $\mathrm{Re}\,\varepsilon(\mathbf{r})$ is modeled by four inhomogeneities located asymmetrically with respect to the origin; the function $\mathrm{Im}\,\varepsilon(\mathbf{r})$ is modeled by one inhomogeneity. Two inhomogeneities of $\mathrm{Re}\,\varepsilon(\mathbf{r})$ have equal amplitudes. According to Eq. (1), they correspond to velocity contrasts that are close in magnitude and opposite in sign: $\Delta c/c_0 = 0.1$ and -0.077. The additional phase shift for these inhomogeneities are $\Delta\psi \cong 0.27\pi$ and $\Delta\psi \cong -0.24\pi$, respectively. The two remaining inhomogeneities have lower equal amplitudes and opposite contrasts: $\Delta c/c_0 \approx \pm 0.05$ ($\Delta\psi \cong \pm 0.13\pi$). The amplitude of the function $-\mathrm{Im}\,\varepsilon(\mathbf{r})$ corresponds to a ≈ 0.4-Np/λ_0 attenuation, while the total attenuation along the central section is ≈ 0.58 Np, i.e., the amplitude attenuation is 1.78 times. Although the maximal contrast of the complex scatterer is lower than that of the first scatterer, the norms $\|T^0_{\text{exp}}\|$ of the scattering data are approximately equal for both scatterers.

The fact that the shapes and widths of the refractive and dissipative inhomogeneities were the same allowed us to reconstruct the function $\varepsilon(\mathbf{r})$ as a whole, without using the scheme that estimates the c and α components separately. The number of transmission and reception directions was $M = 32$ for the simple scatterer and 64 for the complex scatterer. The matrix $\mathcal{E}^{-1}(\boldsymbol{\chi}, \boldsymbol{\eta})$ was formed at $L = l = 2a$ for the simple scatterer and at $l = 2a$ and $L = 2l = 4a$ for the complex scatterer; $\theta = 10^{-6}\max_{(\boldsymbol{\eta},\boldsymbol{\chi})}|\mathcal{E}(\boldsymbol{\eta}, \boldsymbol{\chi})|$ in both cases.

The results of the reconstruction of these scatterers demonstrate that it is necessary to allow for the multiple scattering. They also reveal the fundamental role of the nonlinear filtering as regularization. The Born approximation is insufficient for a high-quality reconstruction. Even in the absence of noise, the Born estimate $\hat{\varepsilon}_{\text{Born}}(\mathbf{r})$ obtained from Eq. (12) significantly differs from the true scatterer function: the relative reconstruction error is $\nu_\varepsilon \approx 64\%$ for the simple scatterer (Fig. 1a) and 42% for the complex scatterer (Fig. 2d).

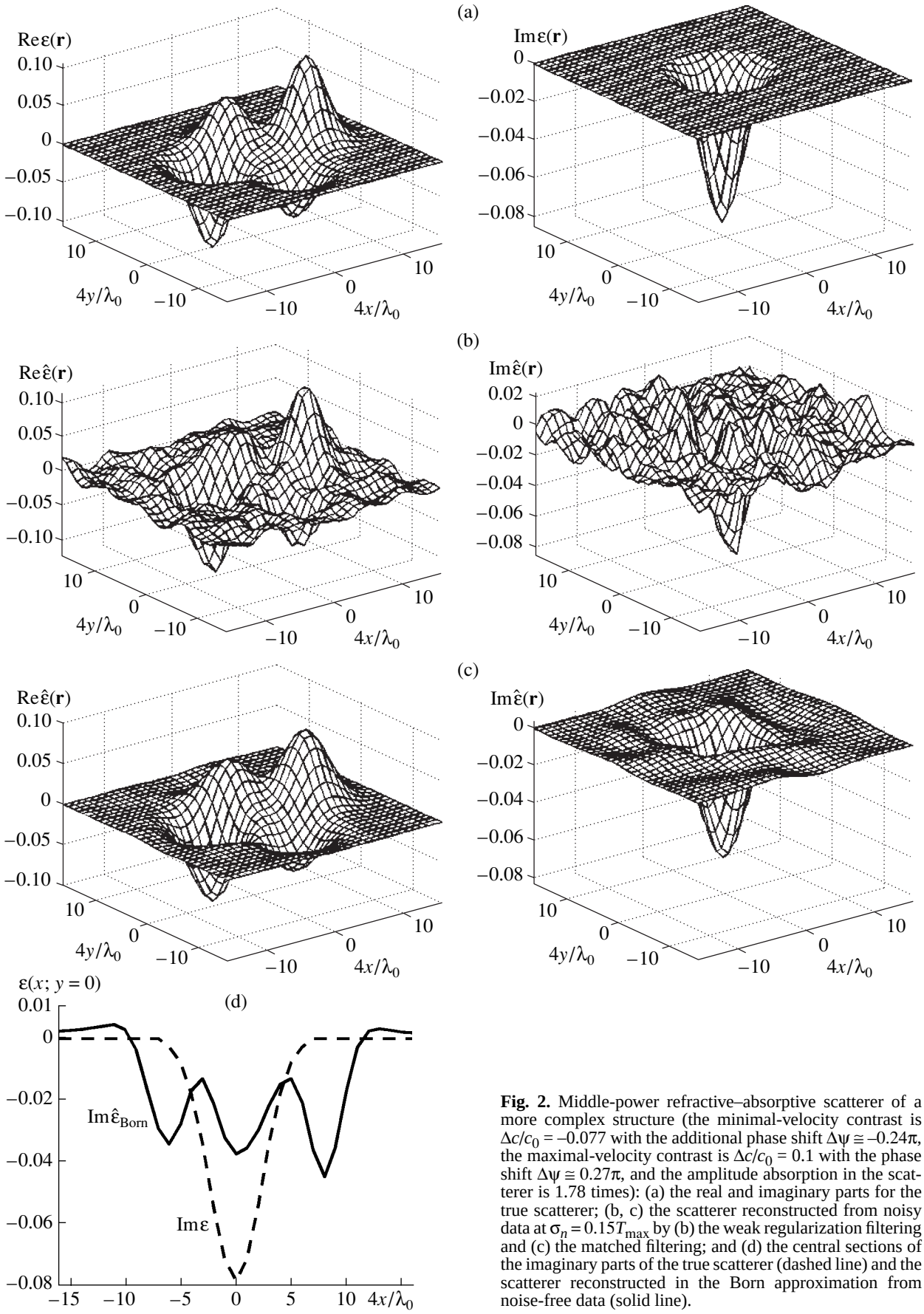

Fig. 2. Middle-power refractive–absorptive scatterer of a more complex structure (the minimal-velocity contrast is $\Delta c/c_0 = -0.077$ with the additional phase shift $\Delta\psi \cong -0.24\pi$, the maximal-velocity contrast is $\Delta c/c_0 = 0.1$ with the phase shift $\Delta\psi \cong 0.27\pi$, and the amplitude absorption in the scatterer is 1.78 times): (a) the real and imaginary parts for the true scatterer; (b, c) the scatterer reconstructed from noisy data at $\sigma_n = 0.15T_{max}$ by (b) the weak regularization filtering and (c) the matched filtering; and (d) the central sections of the imaginary parts of the true scatterer (dashed line) and the scatterer reconstructed in the Born approximation from noise-free data (solid line).

To study the effect of the regularization filtering on the quality of the scatterer estimate in the presence of an intense noise, we used the reconstruction procedure with allowance for the multiple scattering, i.e., with the full system of Eqs. (9) and (6). As in the case of the weak scatterer, two scattering data realizations corresponded to independent errors with the deviation $\sigma_n = 0.15T_{\max}$. Then, for the simple scatterer, $I_n' \approx 56\%$; an intense noise is illustrated by one data realization in Fig. 1b. For the complex scatterer, $I_n' \approx 108\%$ because of the higher error norm.

Our reconstruction procedure successively used the correlation matrix N calculated at two different noise intensities. The regularization filtering matched with the noise intensity assumed that the true error level was such that $W_0 = (\sigma_n)^2 = (0.15T_{\max})^2$. The weak regularization filtering assumed a 150^2 weaker level: $W_0 = (10^{-3}T_{\max})^2$. The reconstruction by the weak filtering, which is necessary to provide the convergence of the iterative procedure on the whole, gives a very low reconstruction quality. For instance, for the simple scatterer, $\nu_\varepsilon \approx 66\%$ (Fig. 1c). This error is somewhat higher than that for the weak scatterer mentioned above (Section 2.1) and reconstructed without filtering at the same input ratio I_n'. For the complex scatterer, $\nu_\varepsilon \approx 55\%$ (Fig. 2b). Thus, the reconstruction error ν_ε after the weak filtering is of the order of the relative input data error.

The matched regularization filtering provides a sufficiently high reconstruction quality. Even with the above intense noise, $\nu_\varepsilon \approx 15\%$ for the simple scatterer (Fig. 1d) and $\nu_\varepsilon \approx 17\%$ for the complex scatterer (Fig. 2c). These values of ν_ε show that, when multiple scattering must be taken into account, additional errors arise (as compared to the result of reconstructing the weak scatterer).

It is important to note that the mechanism of the spectral regularization filtering is always the same irrespective of the iteration number j, because the matrix $A(\boldsymbol{\chi}, \boldsymbol{\eta})$ in Eqs. (9) and (11) remains the same for all iteration steps. This matrix is the one that contains the information about the correlation properties of noise and scatterer. Therefore, at each iteration step, the regularization filtering amounts to the Wiener-type filtering, similar to the filtering in the case of weak scatterers. The solution $\tilde{\varepsilon}_j(\boldsymbol{\eta})$ obtained from Eqs. (9) is similar to Born estimate (12) with the right-hand side corrected for the multiple scattering (based on the results of the previous cycle of iterations). We thus obtained a nonlinear generalization of the Wiener filtering for reconstructing sufficiently strong scatterers, which provides a regularized solution that is close to the optimal one. Note that a simple filtering procedure that cuts off the spatial spectrum of the scatterer at each iteration step, which also improves the convergence, was proposed in [10].

Our simulations revealed the following unexpected effect. It was found that it is sufficient to apply the matched regularization procedure only at the final cycle of the iterative procedure. Indeed, after a preliminary solution with the weak regularization filtering is obtained, one more iteration cycle can be performed with the use of the matched filtering (Figs. 1c, 2b). The reconstruction quality of such a one-step matched filtering is actually the same as that of the multistep matched filtering. This fact is of interest for applications. It allows one first to reconstruct the scatterer using the filtering procedure that assumes a certain noise intensity much lower than the true one. After that, the result is processed once by a different, stronger, filter. By varying the parameters of this additional filter, a variant that is optimal for the particular scatterer and measurement errors can be chosen. However, we failed to theoretically justify this simplified approach. Perhaps, it is only efficient for not too strong scatterers of a rather simple shape.

3. CONCLUSIONS

Thus, an algorithm for the statistical estimation of the scatterer characteristics is proposed and studied. Its performance is corroborated by numerical simulations, although the algorithm is rather complicated in terms of computations. To extend the convergence region of the iterative process for application purposes, it is expedient to simultaneously estimate [11] all the unknown quantities with the filtering applied to each of them. The storage and performance capacities required for this procedure must be much greater than those of a personal computer. In addition, to provide a unique solution in the case of strong scatterers, one should use redundant data; otherwise, the iterative procedure may converge to a false solution [12].

ACKNOWLEDGMENTS

This work was supported by the Russian Foundation for Basic Research, project nos. 01-02-16282 and "Scientific schools" 00-15-96530.

REFERENCES

1. A. N. Tikhonov and V. Ya. Arsenin, *Solution of Ill-Posed Problems* (Nauka, Moscow, 1986; Winston, Washington, 1977).
2. A. M. Fedotov, *Ill-Posed Problems with Random Errors in the Data* (Nauka, Novosibirsk, 1990), p. 280.
3. A. N. Tikhonov, A. V. Goncharskiĭ, V. V. Stepanov, and A. G. Yagola, *Numerical Methods for the Solution of Ill-Posed Problems* (Nauka, Moscow, 1990; Kluwer, Dordrecht, 1995).
4. A. N. Tikhonov, A. S. Leonov, and A. G. Yagola, *Nonlinear Ill-Posed Problems* (Nauka, Moscow, 1995; Chapman and Hall, London, 1998).

5. V. A. Burov and A. A. Goryunov, Vestn. Mosk. Univ., Ser. 3: Fiz., Astron. **18** (6), 95 (1977) [Moscow Univ. Phys. Bull. **32** (6), 77 (1977)].

6. V. A. Burov, E. E. Kasatkina, and O. D. Rumyantseva, Akust. Zh. **43**, 315 (1997) [Acoust. Phys. **43**, 270 (1997)].

7. V. A. Burov, E. E. Kasatkina, E. G. Sukhov, and O. D. Rumyantseva, Acoust. Imaging **25**, 71 (2000).

8. S. A. Johnson, Y. Zhou, M. L. Tracy, *et al.*, Ultrason. Imaging **6** (4), 103 (1984).

9. V. A. Burov and M. N. Rychagov, Akust. Zh. **38**, 844 (1992) [Sov. Phys. Acoust. **38**, 461 (1992)].

10. W. W. Kim, D. T. Borup, S. A. Johnson, *et al.*, in *Proceedings of IEEE Ultrasonics Symposium* (1987), p. 903.

11. V. A. Burov, A. A. Goryunov, A. V. Saskovets, and T. A. Tikhonova, Akust. Zh. **32**, 433 (1986) [Sov. Phys. Acoust. **32**, 273 (1986)].

12. V. A. Burov and O. D. Rumiantseva, Acoust. Imaging **22**, 107 (1996).

Translated by A. Khzmalyan

Acoustical Physics, Vol. 49, No. 3, 2003, pp. 300–304. Translated from Akusticheskiĭ Zhurnal, Vol. 49, No. 3, 2003, pp. 359–364.

Amplitude and Frequency Characteristics of Acoustic Jets

I. V. Lebedeva and A. E. Grushin

Physics Faculty, Moscow State University, Vorob'evy gory, Moscow, 119992 Russia

e-mail: lebedeva@acs373a.phys.msu.su

Received March 27, 2002

Abstract—The prerequisites to formation and the characteristics of a jet that occurs at the open end of a waveguide guiding an intense sound wave are studied. The velocity field is measured by a hot-wire anemometer. The previously developed method of separating the jet velocity V_{jet} from the amplitude of the oscillating particle velocity V_{osc}, which is applicable only when $V_{jet} > V_{osc}$, is supplemented with the method of oscillogram processing applicable for $V_{jet} \le V_{osc}$. Thus, a full picture of the jet evolution in space, starting from the waveguide outlet, is obtained. The experimentally determined spatial distribution of the jet velocity is found to agree well with the numerically simulated dependences reported by other authors. For the oscillating velocity amplitude at the open end of the waveguide, a threshold value, beyond which the formation of the acoustic jet takes place, is revealed. The frequency dependence of this threshold value is determined. The dependence of the maximal jet velocity on the oscillating velocity amplitude in the outlet waveguide cross section is found to be close to linear. © *2003 MAIK "Nauka/Interperiodica".*

In the last few years, acoustic jets have attracted the attention of researchers in connection with the good prospects of their use in aerodynamic systems.

Since the mid-1990s, a series of publications concerned with the design and application of acoustic jet generators have appeared in the AIAA journal and AIAA papers [1–3]. These miniature millimeter-sized devices are made in the form of a Helmholtz resonator whose rear wall performs harmonic oscillations while the front wall has a relatively small opening. The oscillations of the rear wall can be excited electrically, piezoelectrically, or mechanically. When the rear wall moves inside the cavity, an air flow comes out of the cavity through the opening, and its separation from the sharp edges of the opening gives rise to vortices. When the initial velocity is sufficiently high, the separated vortices form an acoustic jet. The motion of the rear wall in the opposite direction gives rise to a flow from the surrounding medium into the cavity of the jet generator. Within each oscillation cycle, the average mass flow through the opening is zero while the momentum of the vortices is nonzero. Since the dimensions of the generators are small, the usual oscillation frequencies are within 1–1.5 kHz. The attractive feature of these devices is their low energy consumption, as well as the fact that the jet is formed from the surrounding medium without any special air supply. The potentialities of the generators, whose acoustic jets may reach velocities above 20 m/s, are rather promising. In particular, they can be used for the fuel agitation in engines to intensify the combustion, cooling solid surfaces, and changing the direction and the degree of turbulization in stationary flows to reduce the flow noise.

The first experimental studies of the characteristics of acoustic jets were described in *Acoustical Physics* years ago [4, 5]. In one experiment [4], the jet was produced by a low-frequency source of a vibration-resonance type. The device was designed and studied in connection with the practical task of powder spraying. In the other experiment [5], the jet was formed as a result of the propagation of intense sound through a hole in a screen placed in the waveguide cross section. This study was performed in connection with the observation of the nonlinear absorption of intense sound by resonant systems [6].

Soon after the generators of acoustic jets found wide application in engineering, an AIAA paper [7] appeared reporting on the first experimental study of the effect of an acoustic jet on a steady flow produced by a fan. This experiment included the measurements of the jet velocity at the generator axis and the measurements of the jet profiles at different distances from the generator outlet. All measurements were performed well away from the outlet (starting from ten calibers).

Almost simultaneously, another AIAA paper reported on the numerical simulation of an acoustic jet [8]. It considered the jet characteristics only outside the generator, while the velocity profile in the outlet cross section was preset analytically. Later on [9], a direct numerical simulation was used to solve nonstationary Navier–Stokes equations with allowance for the compressibility of the medium, which made it possible to determine the resulting field both inside and outside the generator cavity. The authors of the latter paper stressed that the problem they considered was not only of practical significance but also instructive for understanding the fundamental processes in the physics of gases and liquids.

1063-7710/03/4903-0300$24.00 © 2003 MAIK "Nauka/Interperiodica"

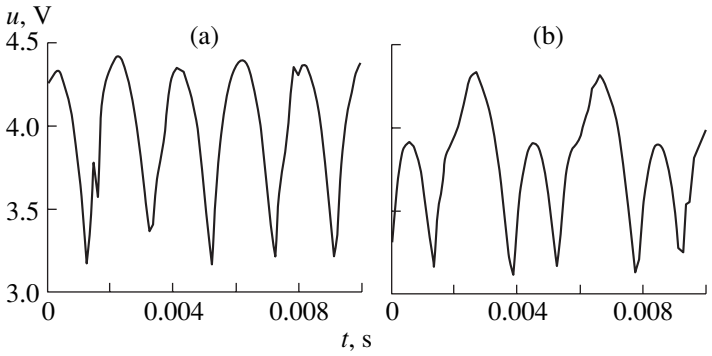

Fig. 1. Oscillograms of the hot-wire anemometer signal (a) in the outlet cross section of the waveguide and (b) at a distance of 4 mm from it; the frequency is 255 Hz.

Experimental values of the jet velocity and the velocity fluctuation along the generator axis were presented in [10]. These values agree well with the calculated ones for distances greater than five calibers and noticeably deviate from the calculations for smaller distances from the outlet. An explanation of this discrepancy will be proposed below.

In our previous publications [11, 12], we studied the spatial evolution of the acoustic jet formed at the open end of a waveguide when an intense sound wave propagates through it. In the present study, we determine the dependence of the maximal velocity of the jet on the amplitude of the oscillating particle velocity in the outlet cross section; we also reveal the threshold value of the latter velocity beyond which the jet begins to form and determine the frequency dependence of this threshold value. As far as we know, these issues were not considered in the literature.

The experimental setup was similar to that described earlier [6]. The waveguide was a circular tube whose inner diameter was d_0 = 2.35 cm, and length, 74 cm. One end of the tube was connected through a tapered concentrator to a loudspeaker, while the other end was open. The velocity field inside and outside the waveguide was measured by a wire probe of a constant-temperature hot-wire anemometer (DISA, Denmark), and the pressure field of the sound wave was measured by a half-inch capacitor microphone (Bruel & Kjaer, Denmark). The measurements were performed at the resonance frequencies of the system, which were determined by the maximal oscillating velocity amplitude in the outlet cross section of the waveguide. For the structure used in our experiment, the resonance frequencies were 175, 255, and 358 Hz.

To process the anemometric data and separate the acoustic jet velocity V_{jet} from the oscillating velocity amplitude V_{osc} caused by both acoustic oscillations and random fluctuations, we used the technique described in [13]. The jet velocity was estimated from the rms value of the signal produced by the hot-wire anemometer, and the oscillating component of the velocity was determined from the standard variance of this signal. It should be noted that this technique is applicable only when $V_{jet} > V_{osc}$. For the opposite case $V_{jet} \le V_{osc}$, we used the direct processing of oscillograms. The latter method is described below.

As was mentioned in [12], at a sound level of 160 dB, which corresponds to an oscillating velocity amplitude of 10 m/s, only a harmonic wave is observed in the waveguide, as well as in its outlet cross section. The oscillogram of this wave is shown in Fig. 1a. Neither the microphone nor the probe of the hot-wire anemometer detect any distortions of the sinusoidal profile. The transformation of the sound energy into the hydrodynamic one begins immediately outside the outlet of the waveguide, the velocities satisfying the inequality $V_{jet} < V_{osc}$. The appearance of a concurrent flow leads to an increase in the oscillation energy within one half-period and to its decrease within the other half-period by the value of the flow velocity (Fig. 1b). In this case, the jet velocity is determined as half of the difference between the average values of the maximal and minimal amplitudes of the measured signal while the oscillating velocity amplitude is determined as the half-sum of these values. The quantitative estimates of V_{jet} and V_{osc} are obtained with allowance for the probe calibration curve recorded in the sound field at a given frequency (since the sensitivity of the probe is frequency dependent). The use of the standard technique at small distances from the outlet leads to erroneous results and to a discrepancy between the experimental and computational data, which presumably was the case in [10].

Figure 2 presents the spatial distributions of the jet velocity V_{jet}, which is normalized to the oscillating velocity amplitude in the outlet waveguide cross section V_0, along the waveguide axis (the x axis) at the three chosen resonance frequencies at a sound level of 160 dB. The distances are expressed in calibers, i.e., normalized to the diameter d_0 of the waveguide opening. One can see that the decrease in the jet velocity with distance is faster at the higher frequency (358 Hz). The behavior of the experimental dependence agrees well with that obtained in [10] from the numerical simulation of the jet formation process.

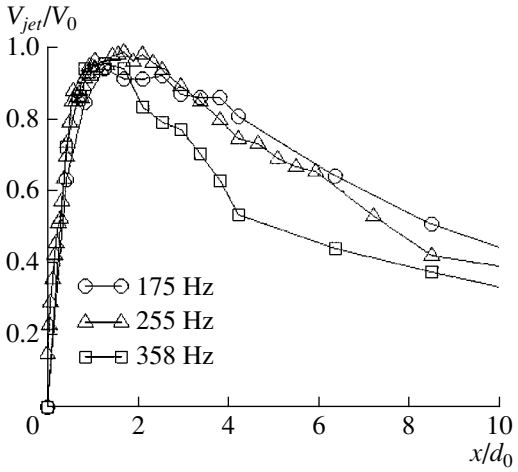

Fig. 2. Distribution of the dimensionless velocity along the waveguide axis.

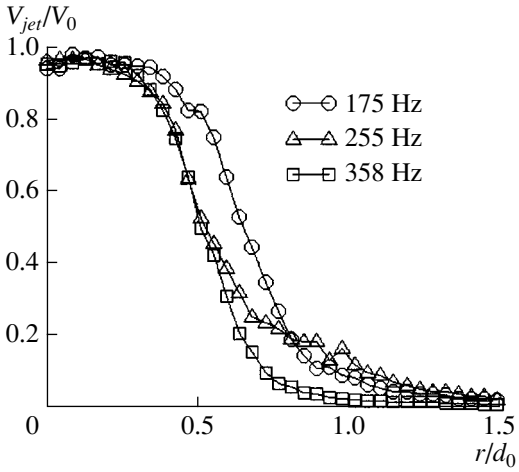

Fig. 3. Dimensionless profile of the maximal jet velocity at a distance of 1.3 calibers.

The evolution of the acoustic jet in space can be represented by three regions. In the first region, which in our experimental conditions covers the distances from one to two calibers, the jet formation occurs due to the sound wave energy decrease. The velocity of the resulting jet reaches its maximal value, which is comparable with the oscillating velocity amplitude in the outlet waveguide cross section. This fact makes the phenomenon under study essentially different from the Rayleigh, Eckart, and Schlichting flows whose velocities are an order of magnitude smaller than the oscillating velocity of the sound wave. Figure 3 shows the transverse profile of the jet at the distance corresponding to its maximal velocity. One can see that the jet width is greater for the lower frequency. The second region covers the distances between two and four calibers and corresponds to the stabilization of the jet. The velocity of the jet varies only slightly in this region, while the Reynolds number reaches a value of 16000. As a result, an active turbulization of the jet begins because of its interaction with the surrounding medium, and this effect is clearly reflected in the power spectrum. The third region is characterized by a decrease in the jet velocity and a broadening of the jet profile. Figure 4 presents the profiles of the jet velocity for the frequency of 358 Hz at distances of 1.3, 2.1, and 6.0 calibers. From this figure, it follows that, at a distance of six calibers, the velocity of the jet decreases by a factor of two while the width of its profile increases by a factor of two.

The error in the determination of the jet velocity is mainly caused by the inaccuracy of the probe calibration and the error in positioning the probe when it is moved along the axis. In our experiments, the total error did not exceed 10%.

The probe of the hot-wire anemometer already stops detecting the sound wave in the second region because of its insufficient sensitivity. Therefore, the sound field outside the waveguide was measured by a half-inch condenser microphone. The results of the sound pressure measurements along the waveguide axis and along straight lines inclined at an angle θ to it are shown in Fig. 5. The sound field formed in our experiment is similar to the field produced by a spherically divergent sound wave generated by a point source.

By varying the sound level in the waveguide over a wide dynamical range from 138 to 166 dB (which corresponds to the variation of V_0 from 0.8 to 15 m/s), we revealed a threshold value of the oscillating velocity amplitude at the open end of the waveguide: when the threshold was exceeded, the acoustic jet emerged. In this respect, the jet under study resembles the Schlichting flow, which is also characterized by a sound intensity threshold; the latter is related to the loss increase due to the convective term in the Navier–Stokes equations.

Figure 6 presents the experimental dependence of the maximal jet velocity V_{jet} on the oscillating velocity amplitude in the outlet waveguide cross section V_0. One can see that, when the oscillating velocity amplitude is smaller than some critical value V_t, the jet is absent.

To determine the threshold value V_t with higher accuracy, we represented the aforementioned experimental dependences using logarithmic coordinates. The resulting plots have the experimental points concentrated along two intersecting straight lines. A change in the slope angle of such a line corresponds to a change in the mechanism of the sound energy loss. Equations describing these straight lines are determined by the least squares method, and the critical value is determined as the point of their intersection. An example of such a processing for a frequency of 175 Hz is shown in Fig. 7. From this figure, it follows that, at the given frequency, we have $V_t = 2.4$ m/s.

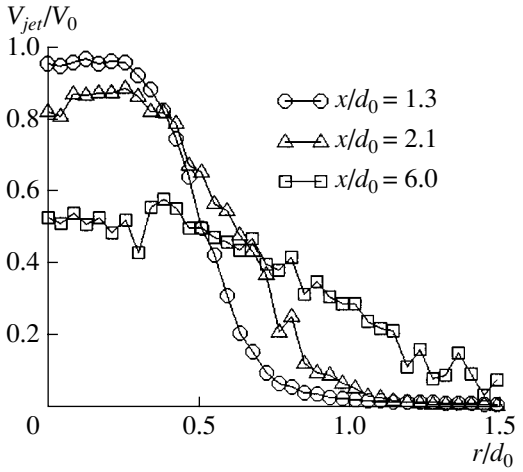

Fig. 4. Dimensionless profile of the jet velocity at different distances from the open end of the waveguide; the frequency is 358 Hz.

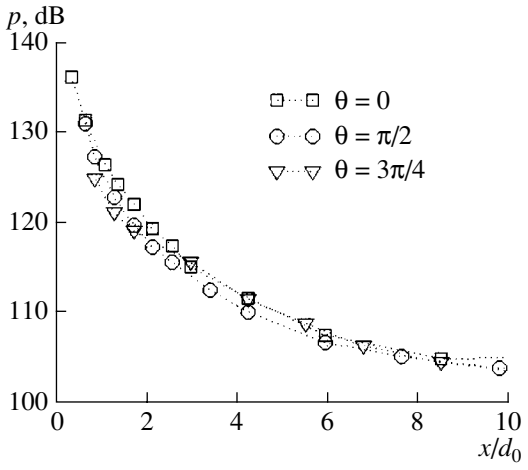

Fig. 5. Distribution of the sound pressure level outside the waveguide along the waveguide axis and at an angle θ to it; the frequency is 358 Hz.

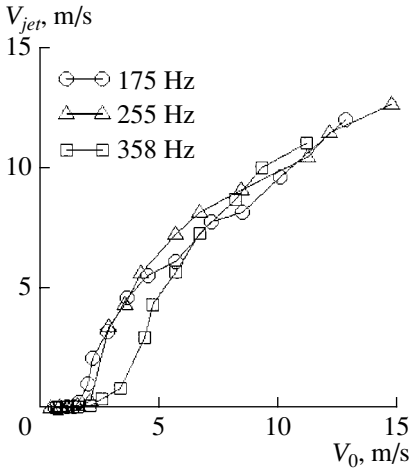

Fig. 6. Dependence of the maximal jet velocity on the oscillating velocity amplitude in the outlet cross section of the waveguide.

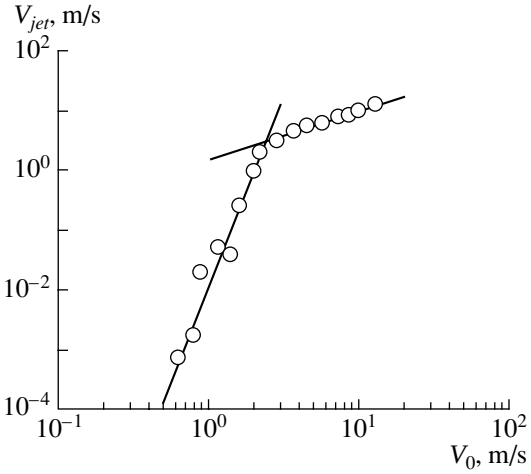

Fig. 7. The same dependence as in Fig. 6, but represented in logarithmic coordinates; the frequency is 175 Hz.

The dependence of V_{jet} on V_0 can be expressed as $V_{jet} \propto V_0^{\varepsilon}$, where the exponent ε can be determined from Fig. 7. This exponent ε is nothing but the slope of the straight line in the region $V_0 > V_t$, and the slope is calculated by the least squares method. For the frequency of 175 Hz, we obtain ε = 0.8.

The experimental data for the two other frequencies were processed in the same way.

An important parameter that determines the condition of the jet formation is known to be the ratio of the displacement amplitude to the characteristic geometric dimension of the system. The table summarizes the critical values obtained for the oscillating velocity amplitude V_t, the corresponding displacement amplitudes ξ_t normalized to the waveguide diameter d_0, and the exponent ε characterizing the dependence of V_{jet} on V_0 for all three frequencies.

The threshold value of the oscillating velocity amplitude V_t increases approximately twofold within one octave. At the same time, the normalized displacement ξ_t/d_0 for the waveguide in use remains approximately the same and is on average equal to 0.09. It should be noted that the value reported in [14] for the corresponding parameter is an order of magnitude greater. This can be explained by the fact that the authors of the cited paper determined this parameter from only the field visualization pattern. As a result, they have found the criterion not for the jet formation threshold but for the conditions of the jet with a fully developed turbulence.

Parameters of the acoustic jet

f, Hz	V_t, m/s	ξ_t/d_0	ε
175	2.4	0.093	0.8
255	3.1	0.082	0.7
358	4.9	0.093	1.1

The average value of the exponent is ε = 0.9; i.e., the dependence under consideration is close to a linear one, and the slight deviation is presumably caused by the spherical spread of the sound wave outside the waveguide.

Thus, by supplementing the standard method of experimental data processing, which is valid only for $V_{jet} > V_{osc}$, by the method of oscillogram processing valid for $V_{jet} \le V_{osc}$, we obtained a full picture of the jet evolution in space, starting from the waveguide outlet. The spatial distribution of the jet velocity obtained from our experiment agrees well with the numerically simulated dependences obtained by other authors [10]. The dependence of the jet velocity on the oscillating velocity amplitude in the outlet cross section of the waveguide is found to be close to a linear one. From the experimental data, we determined the critical value of the oscillating velocity amplitude in the outlet waveguide cross section, so that the jet formation occurs when this value is exceeded. We also determined the dependence of this critical velocity on frequency.

REFERENCES

1. M. Amitay, A. Honohan, M. Trautman, and A. Glezer, AIAA Pap., No. 97-2004 (1997).
2. F. Ross, AIAA Pap., No. 97-1973 (1997).
3. J. F. Donovan, L. D. Kral, and A. W. Cary, AIAA Pap., No. 98-0210 (1998).
4. E. P. Mednikov and B. G. Novitskiĭ, Akust. Zh. **21**, 245 (1975) [Sov. Phys. Acoust. **21**, 152 (1975)].
5. I. V. Lebedeva, Akust. Zh. **26**, 599 (1980) [Sov. Phys. Acoust. **26**, 331 (1980)].
6. S. P. Dragan and I. V. Lebedeva, Akust. Zh. **44**, 206 (1998) [Acoust. Phys. **44**, 167 (1998)].
7. B. L. Smith and A. Glezer, AIAA Pap., No. 97-0213 (1997).
8. L. D. Kral, J. F. Donovan, A. B. Cain, and A. W. Cary, AIAA Pap., No 97-1824 (1997).
9. D. P. Rizetta, M. R. Visbal, and M. J. Stanek, AIAA J. **37** (8), 919 (1999).
10. S. G. Mallinson, G. Hong, and J. A. Reizes, AIAA Pap., No. 99-3651 (1999).
11. A. E. Grushin and I. V. Lebedeva, in *Proceedings of X Session of the Russian Acoustical Society* (Moscow, 2000), Vol. 1, p. 71.
12. I. V. Lebedeva and A. E. Grushin, Vestn. Mosk. Univ., Ser. 3: Fiz., Astron., No. 2, 49 (2002).
13. A. E. Grushin and I. V. Lebedeva, Izmer. Tekh., No. 5, 63 (2001).
14. B. L. Smith and G. W. Swift, AIAA Pap., No. 2001-3030 (2001).

Translated by E. Golyamina

Acoustical Physics, Vol. 49, No. 3, 2003, pp. 305–311. Translated from Akusticheskiĭ Zhurnal, Vol. 49, No. 3, 2003, pp. 365–371.

Diffracting Acoustic Beams of Finite Amplitude in Marine Sediments

Ya. M. Zhileĭkin, Yu. I. Osipik, and N. I. Pushkina

Research Computer Center, Moscow State University, Vorob'evy gory, Moscow, 119992 Russia
e-mail: jam@srcc.msu.su; N.Pushkina@mererand.com

Received February 20, 2002

Abstract—The evolution wave equation that describes the nonlinear propagation of bounded acoustic beams in two-phase marine sediments is derived. The equation is numerically studied in application to marine sediments with different physical parameters. *© 2003 MAIK "Nauka/Interperiodica".*

INTRODUCTION

The propagation of high-intensity acoustic waves in marine sediments finds increasing application in studying the properties of the ocean floor (see, e.g., [1–3]). The propagation of nonlinear one-dimensional sound waves in marine sediments was studied in [4]. The one-dimensional approach is valid for beams that can be treated as unbounded in the transverse direction. Actual beams have finite cross sections, and, if the transverse size of a beam is comparable with the wavelength, diffraction phenomena may be observed. In this paper, along with nonlinear phenomena, we consider the diffraction divergence of a bounded sound beam in the course of its propagation in two-phase marine sediments. We derive an approximate nonlinear wave equation that describes the evolution of a high-intensity three-dimensional beam in which an increase in the front steepness leading to the shock wave formation is accompanied by the diffraction of the beam. Since the complex combination of nonlinear and diffraction processes does not allow one to solve the problem in an explicit form, we perform a numerical analysis of the phenomena at hand.

1. DERIVATION OF APPROXIMATE NONLINEAR WAVE EQUATIONS FOR ACOUSTIC BEAMS IN MARINE SEDIMENTS

To derive the approximate evolution wave equation, we start from the continuity equations for the densities and momenta of the liquid and solid phases of the sediments consisting of a rigid frame and pores filled with water [4]:

$$\frac{\partial}{\partial t} m\rho_f + \frac{\partial}{\partial x_i} m\rho_f v_i = 0,$$

$$\frac{\partial}{\partial t}(1-m)\rho_s + \frac{\partial}{\partial x_i}(1-m)\rho_s u_i = 0,$$

$$\frac{\partial}{\partial t} m\rho_f v_i + \frac{\partial}{\partial x_j} m\rho_f v_i v_j = -\frac{\partial}{\partial x_i} mP, \tag{1}$$

$$\frac{\partial}{\partial t}(1-m)\rho_s u_i + \frac{\partial}{\partial x_j}(1-m)\rho_s u_i u_j = \frac{\partial}{\partial x_j}\sigma_{ij} - \frac{\partial}{\partial x_i}(1-m)P.$$

Here, ρ_f and ρ_s are the densities of the liquid and solid phases, **v** and **u** are the respective velocities, m is the porosity of the sediment frame, P is the pressure in the liquid, and σ_{ij} are the stresses acting on the volume element of the frame. Below, we will show that, in the case at hand, the sound absorption is sufficiently small in the sense that the attenuation length is greater than the distances at which the diffraction or discontinuities can be developed. Therefore, in deriving the evolution equation, we ignore the absorption to simplify the calculations, the main objective of which is far from considering the theoretical aspects of absorption. In the linear approximation, the variable part of the pressure P is given by the expression [5, 6]

$$P^l = G^{-1}\xi - F\mathrm{div}\mathbf{U}, \tag{2}$$

where

$$G = \frac{1-m}{k_s} + \frac{m}{k_f} - \frac{k}{k_s^2};$$

$$F = \left(1 - \frac{k}{k_s}\right)G^{-1}; \quad \xi = m\mathrm{div}(\mathbf{U} - \mathbf{V}).$$

Here, k_f, k_s, and k are the bulk moduli of the fluid, the mineral grains constituting the frame, and the frame itself, respectively; **U** is the displacement of the frame; **V** is the displacement of the fluid; and ξ is the volume of the fluid flowing into the volume element of the medium and out of it. By using the variables $\delta\rho_f$ and $\delta\rho_s$

instead of ξ and $\mathbf{U}$, where $\delta\rho_f = -\rho_{0f}\mathrm{div}\,\mathbf{V}$ and $\delta\rho_s = -\rho_{0s}\mathrm{div}\,\mathbf{U}$, Eq. (2) can be represented in the form

$$P^l = G^{-1}\left(\frac{m}{\rho_{0f}}\delta\rho_f + \frac{\nu}{\rho_{0s}}\delta\rho_s\right), \tag{3}$$

where $\nu = 1 - m - k/k_s$. In what follows, we will omit the subscript "0" for the equilibrium values. According to [4], the linear part of the stress tensor σ_{ij} is

$$\sigma_{ij}^l = \left(k - \frac{2}{3}\mu\right)U_{ll}\delta_{ij} + 2\mu U_{ij} + \frac{k}{k_s}P^l\delta_{ij}, \tag{4}$$

where μ is the shear modulus of the frame and U_{ij} is the strain tensor.

In the general case of finite-amplitude waves, one should take into account the nonlinear parts of the pressure P^n and the stress tensor σ_{ij}^n, which are the next terms in expansions (3) and (4). Their explicit forms will be given below for several limiting cases.

A well-known fact is that the nonlinearity of the medium and the finite beam width lead to distortions of the wave front, both along the propagation direction (the x axis) and across it (the y and z axes). We assume that the perturbations of the medium are small, so that a small parameter can be introduced:

$$\epsilon \sim v_x/c \sim u_x/c \sim \delta\rho_f/\rho_f \sim \delta\rho_s/\rho_s,$$

where c is the speed of sound in the sediment. With this parameter, we can considerably simplify Eq. (1). Taking into account that the beam boundaries are rather sharp in the transverse directions and, hence, the parameters vary more rapidly in these directions than along the propagation path, we introduce new variables [7, 8]

$$x' = \epsilon x, \quad y' = \sqrt{\epsilon}y, \quad z' = \sqrt{\epsilon}z \tag{5}$$

and set $v_{y,z}/c \sim u_{y,z}/c \sim \epsilon\sqrt{\epsilon}$. Substituting variables (5) and the moving coordinate $\tau = t - x/c$ into Eq. (1), we retain the quantities up to the order of ϵ^2 and eliminate the velocities v and u. As a result, we obtain the equations for $\delta\rho_f$ and $\delta\rho_s$ (for simplicity, in the equations presented below, we write ρ_f and ρ_s instead of $\delta\rho_f$ and $\delta\rho_s$ in the derivatives of $\delta\rho_f$ and $\delta\rho_s$):

$$\left(1 - \frac{m}{\rho_f c^2 G}\right)\frac{\partial^2\rho_f}{\partial\tau^2} - \frac{\nu}{\rho_s c^2 G}\frac{\partial^2\rho_s}{\partial\tau^2}$$

$$= -c\left(1 + \frac{m}{\rho_f c^2 G}\right)\frac{\partial^2\rho_f}{\partial x\partial\tau} - \frac{\nu}{\rho_s cG}\frac{\partial^2\rho_s}{\partial x\partial\tau} + \frac{m}{\rho_f G}\Delta\rho_f \tag{6}$$

$$+ \frac{\nu}{\rho_s G}\Delta\rho_s + \frac{1}{\rho_f}\frac{\partial^2\rho_f^2}{\partial\tau^2} + \frac{1}{c^2}\frac{\partial^2 P^n}{\partial\tau^2};$$

$$\left(1 - m - \frac{k + 4/3\mu + \nu^2/G}{\rho_s c^2}\right)\frac{\partial^2\rho_s}{\partial\tau^2} - \frac{m\nu}{\rho_f c^2 G}\frac{\partial^2\rho_f}{\partial\tau^2}$$

$$= -c\left(1 - m - \frac{k + 4/3\mu + \nu^2/G}{\rho_s c^2}\right)\frac{\partial^2\rho_s}{\partial x\partial\tau}$$

$$- \frac{m\nu}{\rho_f cG}\frac{\partial^2\rho_f}{\partial x\partial\tau} + \frac{1}{\rho_s}\left(k + \frac{4}{3}\mu + \frac{\nu^2}{G}\right)\Delta\rho_s + \frac{m\nu}{\rho_f G}\Delta\rho_f \tag{7}$$

$$- \frac{1}{\rho_s}\left(1 - m - \frac{k + 4/3\mu}{\rho_s c^2}\right)\frac{\partial^2\rho_s^2}{\partial\tau^2} + \frac{\nu}{c^2}\frac{\partial^2 P^n}{\partial\tau^2} - \frac{1}{c^2}\frac{\partial^2\tilde{\sigma}_{xx}^n}{\partial\tau^2}.$$

Here, $\Delta = \partial^2/\partial y^2 + \partial^2/\partial z^2$ and $\tilde{\sigma}_{xx}^n = \sigma_{xx}^n - k/k_s P^n$ (the nonlinear stress tensor is considered for the one-dimensional case, which corresponds to the accepted approximations). From here on, we omit the primes for the x, y, and z coordinates. In Eqs. (6) and (7), the left- and right-hand members have the orders of $\sim\epsilon$ and $\sim\epsilon^2$, respectively.

Let us eliminate one of the variables, $\delta\rho_f$ or $\delta\rho_s$, from the linear part of these equations: let it be, e.g., $\delta\rho_s$. Note that Eq. (1) (or Eqs. (6) and (7)) allow two independent longitudinal modes: the so-called fast and slow waves. However, according to [6], the slow wave (in contrast to the fast one) is a strongly attenuated diffusion mode and, therefore, it makes no noticeable contribution to the sound field. In this single-mode case, the elimination of $\delta\rho_s$ leads to the disappearance of the linear part of the equation if c is the velocity of the fast wave. Thus, we arrive at the approximate nonlinear equation for a bounded beam in marine sediments:

$$\left[2(1-m)\left(1 - \frac{m}{\rho_f c^2 G}\right) - \frac{\nu^2}{\rho_s c^2 G}\right.$$

$$\left. + \left(1 - m - \frac{k + 4/3\mu}{\rho_s c^2}\right)\left(1 + \frac{m}{\rho_f c^2 G}\right)\right]\frac{\partial^2\rho_f}{\partial x\partial\tau}$$

$$- c\left(1 - m - \frac{k + 4/3\mu}{\rho_s c^2}\frac{m}{\rho_f c^2 G}\right)\Delta\rho_f$$

$$+ \frac{1}{c}\left[\frac{\nu}{\rho_s}\left(1 - \frac{m}{\rho_f c^2 G}\right)\right. \tag{8}$$

$$\left. - \frac{1}{\rho_f}\left(1 - m - \frac{k + 4/3\mu + \nu^2/G}{\rho_s c^2}\right)\right]\frac{\partial^2\rho_f^2}{\partial\tau^2}$$

$$- \frac{1}{c^3}\left[\left(1 - m - \frac{k + 4/3\mu}{\rho_s c^2}\right)\frac{\partial^2 P^n}{\partial\tau^2} - \frac{\nu}{\rho_s c^2 G}\frac{\partial^2\tilde{\sigma}_{xx}^n}{\partial\tau^2}\right] = 0.$$

In passing from Eqs. (6) and (7) to Eq. (8), the quantity $\delta\rho_s$ involved in the nonlinear parts is expressed through $\delta\rho_f$ by the formula

$$\delta\rho_s = \left(\frac{\nu}{\rho_s c^2 G}\right)^{-1}\left(1 - \frac{m}{\rho_f c^2 G}\right)\delta\rho_f, \tag{9}$$

which can be obtained from the linear equations and is valid to an accuracy of $\sim\epsilon$.

Equation (8) was derived without imposing any limitations on the values of the bulk moduli of the liquid and solid phases. Actually, the ratio k_f/k_s noticeably varies depending on the type of the sea floor (sand, clay, silt, and so on). For instance, in the case of a sandy frame, the bulk modulus k_s of the quartz grains is much greater than that of the water filling the pores. In this case, $G \approx m/k_f$ (if m is not close to zero), and the equation takes the form:

$$\begin{aligned}
&\left\{2(1-m)\left[1-\left(\frac{c_f}{c}\right)^2\right] - \frac{\nu^2}{m}\frac{\rho_f}{\rho_s}\left(\frac{c_f}{c}\right)^2\right.\\
&\left.+\left(1-m-\frac{k+4/3\mu}{\rho_s c^2}\right)\left[1+\left(\frac{c_f}{c}\right)^2\right]\right\}\frac{\partial^2\rho_f}{\partial x\partial\tau}\\
&-c\left[1-m-\frac{k+4/3\mu}{\rho_s c^2}\left(\frac{c_f}{c}\right)^2\right]\Delta\rho_f\\
&+\frac{1}{\rho_f c}\left\{\nu\frac{\rho_f}{\rho_s}\left[1-\left(\frac{c_f}{c}\right)^2\right]\right.\\
&\left.-\left[1-m-\frac{k+4/3\mu}{\rho_s c^2}-\frac{\nu^2}{m}\frac{\rho_f}{\rho_s}\left(\frac{c_f}{c}\right)^2\right]\right\}\frac{\partial^2\rho_f^2}{\partial\tau^2}\\
&-\frac{1}{c^3}\left[\left(1-m-\frac{k+4/3\mu}{\rho_s c^2}\right)\frac{\partial^2 P^n}{\partial\tau^2} - \frac{\nu}{m}\frac{\rho_f}{\rho_s}\left(\frac{c_f}{c}\right)^2\frac{\partial^2\tilde{\sigma}_{xx}^n}{\partial\tau^2}\right] = 0.
\end{aligned} \tag{10}$$

Here, c_f is the speed of sound in water.

It is easy to show that, if the sediment porosity is $m \longrightarrow 1$, Eq. (8) takes the form of the evolution equation for the beam in a homogeneous liquid with $P^n = \frac{1}{2}\partial c_f^2/\partial\rho_f(\delta\rho_f)^2$:

$$-2\frac{\partial^2\rho_f}{\partial x\partial\tau} + c_f\Delta\rho_f + \frac{1}{\rho_f c_f}\left(1+\frac{1}{2}\frac{\rho_f}{c_f^2}\frac{\partial c_f^2}{\partial\rho_f}\right)\frac{\partial^2\rho_f^2}{\partial\tau^2} = 0,$$

which is equivalent to the corresponding equation given in [8]:

$$\frac{\gamma+1}{4\rho c}\frac{\partial^2\rho^2}{\partial\tau^2} - \frac{\partial^2\rho}{\partial x\partial\tau} + \frac{c}{2}\Delta\rho = 0,$$

where γ is the adiabatic index in the equation of state

$$P = P_0 + c^2\delta\rho + \frac{\gamma-1}{2}\frac{c^2}{\rho}(\delta\rho)^2.$$

In the case $m \longrightarrow 0$, in view of Eq. (9), Eq. (8) takes the form of the evolution wave equation in a solid with $\tilde{\sigma}_{xx}^n = (\delta\rho_s)^2/\rho_s^2(3/2k + 2\mu + \tilde{A} + 3\tilde{B} + \tilde{C}) \equiv (\delta\rho_s)^2/\rho_s^2\tilde{M}$, where $\tilde{A}$, $\tilde{B}$, and $\tilde{C}$ are the nonlinear constants in the expansion of the elastic energy of the solid [9]:

$$2\frac{\partial^2\rho_s}{\partial x\partial\tau} - c_s\Delta\rho_s + \frac{1}{\rho_s c_s}\frac{\tilde{M}}{\rho_s c_s^2}\frac{\partial^2\rho_s^2}{\partial\tau^2} = 0;$$

here, c_s is the speed of sound in the solid.

2. NUMERICAL STUDY OF THE SOUND BEAM PROPAGATION IN MARINE SEDIMENTS

To numerically study the propagation of acoustic beams in marine sediments in the presence of nonlinear phenomena and diffraction, we consider Eq. (10) represented in the form

$$a_1\frac{\partial^2\tilde{\rho}_f}{\partial x\partial\tau} + a_2\Delta\tilde{\rho}_f + a_3\frac{\partial^2\tilde{\rho}_f^2}{\partial\tau^2} = 0, \tag{11}$$

with the boundary condition

$$\tilde{\rho}_f\big|_{x=0} = A\bar{\rho}_f(r)f(\omega\tau).$$

Here, since $\rho_f = \rho_{0f} + \delta\rho_f$ and $\rho_s = \rho_{0s} + \delta\rho_s$, the quantity $\tilde{\rho}_f = \delta\rho_f$ is the density perturbation in the medium; the factors a_1, a_2, and a_3 depend on the equilibrium density values ρ_{0f} and ρ_{0s}; A is the density perturbation amplitude at the boundary; ω is the perturbation frequency; and $\bar{\rho}_f(r)$ is the normalized perturbation amplitude, which is a rapidly decaying function of the transverse coordinate r. Equation (11) ignores the dissipation of sound. In two-phase media like sandy marine sediments, the absorption coefficient depends on the frequency almost linearly [10]. The choice of the frequency dependence of the absorption coefficient is known to influence the evolution of nonlinear processes [11]. Therefore, it is advantageous to consider the problem of wave absorption in two-phase media and the form of the corresponding operator in Eq. (11). This problem will be considered in a separate paper. Note the following fact. In Eq. (10), the last two terms involve nonlinear parts of the pressure and the stress tensor. These quantities can be represented as expansions in powers of $\delta\rho_f$ and $\delta\rho_s$, starting from the quadratic terms (the linear terms of these expansions are given by Eqs. (3) and (4)). Therefore, the nonlinearity coefficient a_3 of Eq. (11) also includes the contribution of the last two terms appearing in square brackets in Eq. (10).

Table 1. Physical parameters of marine sediments and the calculated factors for cases 1–5

Parameter	Units	1	2	3	4	5
		[13]	[14, 17]	[18]	[14, 19]	[20]
m		0.4	0.38	0.47	0.36	0.47
c	cm/s	1.7×10^5	1.7×10^5	1.7×10^5	1.7×10^5	1.7×10^5
k	dyn/cm^2	1.08×10^9	1.99×10^9	4.36×10^9	1.00×10^9	4.36×10^8
μ	dyn/cm^2	5.00×10^8	1.19×10^9	2.61×10^8	1.00×10^9	2.61×10^8
k_s	dyn/cm^2	3.60×10^{11}	4.00×10^{11}	3.60×10^{11}	3.60×10^{11}	3.60×10^{11}
		[13, 14]	[14]	[14]	[19]	[14]
ω	s^{-1}	6.28×10^4	6.28×10^4	6.28×10^4	6.28×10^4	6.28×10^4
α	cm^{-1}	4.0×10^{-3}	4.0×10^{-3}	2.0×10^{-3}	3.0×10^{-3}	2.0×10^{-3}
a_1		1.0	1.0	0.9	1.0	0.98
a_2	cm/s	-0.99×10^5	-0.99×10^5	-0.82×10^5	-1.05×10^5	-0.89×10^5
$\lvert a_3 \rvert$	cm^2 s/g	3.04×10^{-5}	2.95×10^{-5}	2.65×10^{-5}	3.05×10^{-5}	2.90×10^{-5}
$\lvert N \rvert$		1.20	1.17	1.27	1.15	1.29
x_k	cm	65.4	63.4	69.0	62.1	69.7
L_{disc}	cm	27.0	27.0	27.0	27.0	27.0
L_{diff}	cm	32.7	31.7	34.5	31.1	34.8
L_{diss}	cm	2.50×10^2	2.50×10^2	5.00×10^2	3.34×10^2	5.00×10^2

Let us introduce the dimensionless variables

$$r' = r/r_0, \quad \tau' = \omega\tau, \quad \tilde{\rho}' = \tilde{\rho}_f/A, \quad x' = x/x_k,$$

where r_0 is the characteristic width of the beam and $x_k = (|a_1/a_2|)\omega r_0^2$. In the further consideration, we omit the prime and "wave" signs to simplify the notations. As a result, we arrive at the equation in the conventional Khokhlov–Zabolotskaya form:

$$N\frac{\partial^2\rho^2}{\partial\tau^2} - \frac{\partial^2\rho}{\partial\tau\partial x} + \Delta_\perp\rho = 0, \tag{12}$$

where $N = (a_3/a_2)A\omega^2 r_0^2$ is the dimensionless generalized coefficient of nonlinearity.

To perform an approximate analysis of the solution of Eq. (12), we consider the equations consisting of the mixed derivative and one of the remaining terms. The solutions to these equations depend on the parameters that have the length dimension and determine the scale of the process evolution. These parameters are the diffraction length $L_{\text{diff}} = 1/2|a_1/a_2|\omega r_0^2$ and the distance of the discontinuity formation $L_{\text{disc}} = 1/2|a_1/a_3|(A\omega)^{-1}$.

To clarify the meaning of the factors in Eq. (11), we compare these parameters with the corresponding quantities for homogeneous media [12]. In the latter case, $L_{\text{diff}} = \omega r_0^2/c$ and $L_{\text{disc}} = 2\rho_0 c(\gamma + 1)^{-1}(A\omega)^{-1}$. Therefore, the quantity $2|a_2/a_1|$ corresponds to the speed of sound c, and the ratio $1/2|a_1/a_3|$ corresponds to the quantity $2\rho_0 c(\gamma + 1)^{-1}$.

The factor N in Eq. (12) can be expressed through the quantities L_{diff} and L_{disc} as $|N| = L_{\text{diff}}/L_{\text{disc}}$. The quantity N characterizes the predominance of one of the processes: the shock front formation or the diffraction. If $N > 1$, nonlinear effects manifest themselves before the diffraction divergence of the beam. If $N < 1$, the beam diverges before the shock front can be formed.

In the numerical study of Eq. (12), we considered the boundary conditions of the form

$$\rho(\tau, r, 0) = e^{-r^2}\sin\tau. \tag{13}$$

According to [12], the solution to the problem defined by Eqs. (12), (13) is a periodic function τ with a period of 2π. To solve this problem numerically, we used the method of conservative finite-difference schemes of gas dynamics [12].

Tables 1 and 2 present the values of the input parameters for ten different cases. These cases cover different properties of marine sediments, which vary over a wide range, depending on the medium constituting the frame (coarse sand, fine sand, clay, and so on), the frame porosity, and other physical characteristics. The upper row in the tables shows the references from which we took the values of the physical parameters for sediments of different types. Along with the parameters, the tables show the calculated values of the factors a_1, a_2, and a_3 together with the values of N, x_k, L_{diff}, L_{disc}, and $L_{\text{diss}} \sim 1/\alpha$, where α is the amplitude absorption coefficient taken from the experiment and L_{diss} is the distance within which the wave is absorbed. In cases 1–7, the sound speed value in marine sediments, $c = 1.7 \times 10^5$ cm/s, is

Table 2. Physical parameters of marine sediments and the calculated factors for cases 6–10

Parameter	Units	6	7	8	9	10
		[14]	[14]	[10]	[10]	[10]
m		0.4	0.36	0.39	0.44	0.47
c	cm/s	1.7×10^5	1.7×10^5	1.84×10^5	1.74×10^5	1.7×10^5
k	dyn/cm^2	5.3×10^{10}	5.3×10^{10}	6.69×10^{10}	5.69×10^{10}	5.12×10^{10}
μ	dyn/cm^2	2.61×10^8	2.61×10^8	1.29×10^9	3.21×10^9	5.00×10^9
k_s	dyn/cm^2	3.60×10^{11}	7.00×10^{10}	3.60×10^{11}	3.60×10^{11}	3.60×10^{11}
ω	s^{-1}	6.28×10^4	6.28×10^4	8.8×10^4	8.8×10^4	8.8×10^4
α	cm^{-1}	4.0×10^{-3}	3.0×10^{-3}	8.0×10^{-3}	8.0×10^{-3}	8.0×10^{-3}
a_1		0.76×10^{-1}	1.7×10^{-1}	0.35×10^{-1}	-1.7×10^{-1}	-2.3×10^{-1}
a_2	cm/s	-0.98×10^4	-1.7×10^4	-1.9×10^4	1.2×10^3	7.6×10^3
$\lvert a_3 \rvert$	cm^2 s/g	2.2×10^{-6}	5.0×10^{-6}	0.95×10^{-6}	4.9×10^{-6}	6.9×10^{-6}
$\lvert N \rvert$		0.90	1.20	0.4	3.3×10^1	6.9
x_k	cm	48.6	64.9	16.8	1272.	267.7
L_{disc}	cm	27	27	21	20	19
L_{diff}	cm	24	32	8.4	64	130
L_{diss}	cm	2.50×10^2	3.34×10^2	12.5×10	12.5×10	12.5×10

taken from [14]. In cases 8–10, the value of the speed c for different sediment components is taken from [10]. In all cases, $A = 10^{-2}$ g/cm^3, $r_0 = 10$ cm, $c_f = 1.5 \times 10^5$ cm/s, $\rho_f = 1.0$ g/cm^3, and $\rho_s = 2.65$ g/cm^3 (the latter value is the density of quartz grains, because the frame is formed by a sandy medium in the case at hand). The values of m, k, k_s, μ, and the absorption coefficient α are taken from the papers referred to in the tables. The factor a_3 is a complex combination of the sediment physical parameters and their density (or pressure) dependences, which are not always known. This factor can be estimated if the nonlinearity coefficient (usually denoted as B/A) is known. This coefficient varies from 8 to 12 for water-saturated sand [15, 16], and, hence, by the order of magnitude, the factor a_3 can be estimated as $|a_3| \sim \frac{1}{2}\frac{B}{A}\frac{|a_1|}{\rho_f c} \approx (4\text{–}6)\frac{a_1}{\rho_f c}$. Note that, in water, the nonlinearity coefficient (B/A) is about 5 to 6; i.e., the nonlinearity of marine sediments is stronger than that of water. According to [15], although the water filling the pores makes the major contribution to the sediment nonlinearity coefficient, the contributions of the bulk and shear moduli of the frame to the sediment nonlinearity prove to be quite significant. Since the sign of a_3 is not determined, the tables present the absolute values of N. As for the factor a_2, which governs the diffraction and affects the value of N, it can change its sign depending on the relation between the sediment porosity and the elastic characteristics of the frame. Therefore, in the general case, N can also change its sign.

To illustrate the results of calculations, we present the plots for the normalized density disturbance ρ at the beam axis ($r = 0$) as a function of τ for different normalized distances x.

For the first seven cases, the results are close to each other. Hence, it is sufficient to analyze one of them (case 1, for instance). Note that, in all cases, the values of L_{diss} noticeably exceed the values of L_{disc} and L_{diff}. This means that, at the distances under consideration, the absorption is relatively small. In case 1, L_{disc} is somewhat smaller than L_{diff} and the nonlinear phenomena progress somewhat faster than the diffraction. Figure 1 shows the decay of the amplitude and a slight

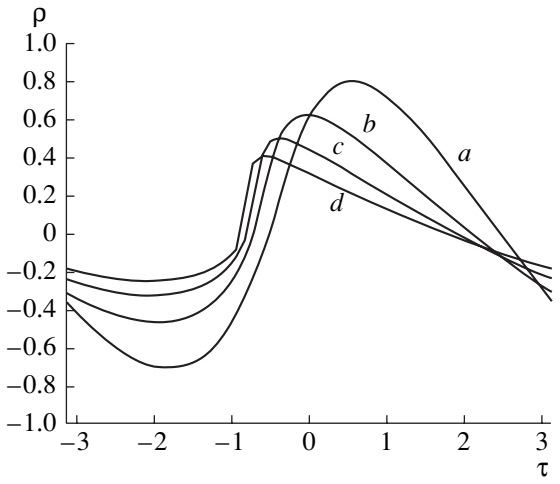

Fig. 1. Wave form of the density disturbance at the beam axis ($r = 0$) versus τ for the following nonnormalized distances: x = (*a*) 13.1, (*b*) 26.2, (*c*) 39.2, and (*d*) 52.3 cm (case 1).

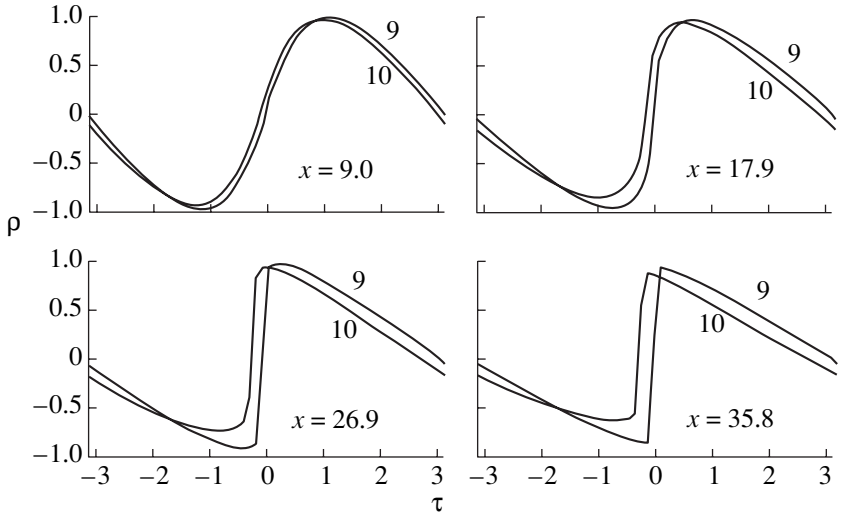

Fig. 2. Wave form of the density disturbance at the beam axis ($r = 0$) versus τ for the indicated nonnormalized distances (cases 9 and 10).

increase in the wave front steepness at the distances $x \sim 2L_{\text{disc}}$. The amplitude decay is mainly governed by the diffraction-caused divergence of the beam.

Case 8 is characterized by a somewhat lower value of L_{disc} and a many-times-lower value of L_{diff}. This means that the nonlinear effects weakly manifest themselves against the background of the diffraction.

Now, we consider cases 9 and 10. In case 9, the value of L_{diff} is about five times greater than in case 10, the values of L_{disc} being approximately the same. In both cases, the values of L_{diff} are many times higher than those of L_{disc}. Therefore, a discontinuity front of the shock wave is formed, which appears nearly vertical in Fig. 2. In view of the relatively small value of L_{diff} in case 10, the nonlinear process progresses along with the less active diffraction of the beam, which leads to a greater phase shift of the beam. Such a behavior is characteristic of the nonlinear propagation of acoustic beams and can be attributed to the interaction of nonlinear and diffraction processes [12, 21]. In the last three cases, the length of discontinuity is somewhat smaller than in the previous cases because of the higher frequency of the exciting wave.

The numerical analysis described above reveals the main features of the high-intensity acoustic beam propagation in water-saturated marine sediments. The analysis shows that the nonlinear distortions and, to some extent, the diffraction divergence of the beam affect the sound propagation in two-phase media of this type, as in the case of the evolution of these phenomena in homogeneous liquids, for which a detailed analysis using a new spectral approach was performed in [11, 22].

ACKNOWLEDGMENTS

We are grateful to V.A. Khokhlova for useful discussions.

This work was supported by the Russian Foundation for Basic Research, project no. 01-02-17039.

REFERENCES

1. R. Carbo and A. C. Molero, J. Acoust. Soc. Am. **108**, 1545 (2000).
2. T. K. Stanton, J. Acoust. Soc. Am. **108**, 551 (2000).
3. T. N. Gardner, J. Acoust. Soc. Am. **107**, 163 (2000).
4. V. G. Bykov and V. N. Nikolaevskiĭ, Akust. Zh. **36**, 606 (1990) [Sov. Phys. Acoust. **36**, 342 (1990)].
5. M. A. Biot, J. Acoust. Soc. Am. **34**, 1254 (1962).
6. R. D. Stoll, *Ocean Seismo-Acoustics, Low-Frequency Underwater Acoustics* (Plenum, New York, 1986).
7. S. A. Akhmanov, A. P. Sukhorukov, and R. V. Khokhlov, Zh. Éksp. Teor. Fiz. **50**, 474 (1966) [Sov. Phys. JETP **23**, 316 (1966)].
8. E. A. Zabolotskaya and R. V. Khokhlov, Akust. Zh. **15**, 40 (1969) [Sov. Phys. Acoust. **15**, 35 (1969)].
9. L. D. Landau and E. M. Lifshitz, *Course of Theoretical Physics*, Vol. 7: *Theory of Elasticity*, 3rd ed. (Nauka, Moscow, 1965; Pergamon, New York, 1986).
10. L. Bjørnø, in *Lecture at Institute of Acoustics, Spring Conference'76, Liverpool* (1976).
11. S. S. Kashcheeva, O. A. Sapozhnikov, V. A. Khokhlova, *et al.*, Akust. Zh. **46**, 211 (2000) [Acoust. Phys. **46**, 170 (2000)].
12. N. S. Bakhvalov, Ya. M. Zhileĭkin, and E. A. Zabolotskaya, *Nonlinear Theory of Sound Beams* (Nauka, Moscow, 1982; Am. Inst. Phys., New York, 1987).

13. A. Turgut and T. Yamamoto, J. Acoust. Soc. Am. **87**, 2376 (1990).
14. N. P. Chotiros, J. Acoust. Soc. Am. **97**, 199 (1995).
15. J. M. Hovem, J. Acoust. Soc. Am. **66**, 1463 (1979).
16. F. A. Boyle and N. P. Chotiros, J. Acoust. Soc. Am. **103**, 1328 (1998).
17. P. R. Ogushwitz, J. Acoust. Soc. Am. **77**, 453 (1985).
18. M. Stern, A. Bedford, and H. R. Millwater, J. Acoust. Soc. Am. **77**, 1781 (1985).
19. J. M. Hovem and G. D. Ingram, J. Acoust. Soc. Am. **66**, 1807 (1979).
20. R. D. Stoll and T. K. Kan, J. Acoust. Soc. Am. **70**, 149 (1981).
21. O. V. Rudenko, S. I. Soluyan, and R. V. Khokhlov, Dokl. Akad. Nauk SSSR **225**, 1053 (1975) [Sov. Phys. Dokl. **20**, 836 (1975)].
22. A. E. Ponomarev, V. A. Khokhlova, and O. A. Sapozhnikov, in *Proceedings of X Session of the Russian Acoustical Society* (GEOS, Moscow, 2000), p. 13.

Translated by E. Kopyl

Acoustical Physics, Vol. 49, No. 3, 2003, pp. 312–315. Translated from Akusticheskiĭ Zhurnal, Vol. 49, No. 3, 2003, pp. 372–375.

Dipole Resonance Scatterer of Sound

N. G. Kanev* and M. A. Mironov**

** Moscow Institute of Physics and Technology, Institutskiĭ per. 9, Dolgoprudnyĭ, Moscow oblast, 141700 Russia*

*** Andreev Acoustics Institute, Russian Academy of Sciences, ul. Shvernika 4, Moscow, 117036 Russia*

e-mail: mironov@akin.ru

Received December 25, 2001

Abstract—A dipole resonance scatterer of sound in the form of a short (in comparison with the quarter-wave) tube closed on one side with a stretched membrane is investigated theoretically and experimentally. The coefficient of sound transmission through the cross section of a measuring tube, into which the resonance scatterer is placed, is calculated and measured. It is shown that the waveguide is totally blocked at the resonance frequency of the resonator. *© 2003 MAIK "Nauka/Interperiodica".*

It is well known that monopole resonators, such as a gas bubble in a liquid or a Helmholtz resonator, are highly efficient scatterers of sound at the resonance frequency [1]. The monopole scattering is caused by the volume velocity produced by the scatterer. In this paper, we consider a resonator of the dipole type. Such a scatterer creates the scattered field due to the force that it applies to the surrounding medium. The strongest scattering effect occurs in waveguides that are narrow in comparison with the wavelength. In what follows, we theoretically and experimentally investigate the scattering of sound by a dipole scatterer in a narrow waveguide.

Suppose that a harmonic wave of frequency ω propagates in a circular tube with a cross-sectional area S. The linear size of the waveguide cross section is assumed to be small in comparison with the sound wavelength. In some cross section of the waveguide, we place a dipole resonator in the form of a body fixed to a spring (Fig. 1). The area of the resonator cross section is assumed to be small in comparison with the cross-sectional area of the waveguide. The solution of the scattering problem in the one-dimensional case consists in the determination of the reflection and transmission coefficients and the conditions that minimize the sound transmission through the waveguide cross section in which the resonator is positioned.

Let u be the particle velocity of the medium in the cross section where the resonator is positioned and v be the particle velocity of the resonator itself. Then, the equation of motion of the resonator has the form [1]

$$m\dot{v} = -\mu(\dot{v} - \dot{u}) - \kappa\int v\,dt - rv, \qquad (1)$$

where m and μ are the mass and the added mass of the body, κ is the elasticity coefficient, and r is the friction coefficient. For harmonic oscillations of frequency ω, Eq. (1) yields the following expression for the force with which the body acts on the medium:

$$F = \mu(\dot{v} - \dot{u}) = \mu(-i\omega)\frac{\omega^2 m - \kappa + i\omega r}{-\omega^2(m+\mu) + \kappa - i\omega r}u. \qquad (2)$$

The reflection V and transmission W coefficients are calculated with the use of the boundary conditions in the cross section where the scatterer lies. These conditions are formulated as the equality of particle velocities and the equality of the pressure drop (i.e., the difference in pressure on the two sides of the cross section) to the force F divided by the area S. The result of the calculation is represented in the form

$$W = \frac{C}{A} = \frac{1}{1 - K/2}, \quad V = \frac{B}{A} = -\frac{K/2}{1 - K/2}, \qquad (3)$$

where

$$K = \frac{i\omega\mu}{\rho c S}\left(\frac{\omega^2}{\omega_0^2}\frac{m}{m+\mu} - 1 + i\omega\frac{r}{\kappa}\right)\Big/\left(\frac{\omega^2}{\omega_0^2} - 1 + i\omega\frac{r}{\kappa}\right) \qquad (4)$$

and

$$\omega_0 = \sqrt{\frac{\kappa}{m+\mu}} \qquad (5)$$

is the resonance frequency of the body oscillation.

The case of the minimal transmission (or maximal reflection) is of most interest. It is clear that the coefficient W is minimal at $\omega = \omega_0$. Introducing the Q-factor of oscillations $Q = \dfrac{\kappa}{\omega_0 r}$ and using Eq. (3) at the reso-

nance frequency, we obtain the minimal coefficient W in the form

$$W(\omega_0) = 1/\left[1 + \frac{\omega_0 Q \mu^2}{2\rho c S(m+\mu)}\right]. \quad (6)$$

In the absence of losses, at the resonance frequency, the transmission coefficient is equal to zero. As follows from Eq. (6), one can reduce the transmission coefficient W by increasing the Q-factor and the added mass. To increase the added mass μ, one can use the following design of the resonator (just this design was used in our experiment).

A tube of length L and cross-sectional area σ ($\sigma \ll S$) is closed at one end by a stretched membrane, and at the other end, it is open (Fig. 3a). In such a resonator, the stretched membrane is the elastic element and the membrane mass is the mass element. The added mass is the mass of the medium in the tube. It is equal to $\mu = \rho\Omega = \rho\sigma L$. With an increase in the tube volume Ω, the added mass also increases. Thus, the efficiency of the scatterer depends on the scatterer volume (Fig. 2). The width of the region, within which the transmission coefficient W does not exceed a certain level, increases with increasing volume. For example, at the level W = 0.3 (–10 dB), it measures $\frac{\Delta\omega}{\omega_0} \approx 0.16 k_0 \frac{\Omega}{S}$.

The resonator in the form of a tube with a membrane can be mounted either inside (Fig. 3b) or outside (Fig. 3c) the waveguide.

Solving the corresponding system of equations that takes into account the finite distance between the tube ends, we find that the transmission coefficient is again given by Eq. (3) with the coefficient K given by Eq. (4), in which resonance frequency ω_0 of the free resonator is replaced by

$$\omega_w = \frac{\omega_0}{\sqrt{1 + \frac{\sigma\mu}{S(m+\mu)}}}. \quad (7)$$

The change (decrease) in the resonance frequency follows from the fact that the added mass μ is increased by the mass of the medium oscillating in the waveguide between the tube ends. Formulas (3), (4), and (7) remain valid as long as the tube length is shorter than 0.2 of the sound wavelength.

The experiments with the dipole resonance scatterer were performed using an automated aeroacoustic interferometer [2, 3]. This instrument is made as a circular waveguide 10 cm in diameter and 2 m in length. The sound source is positioned at one end of the waveguide, and the active absorber (compensator) ensuring the total absorption of the incident wave is mounted at the other end. The specimen is placed in the middle of the waveguide. The reflection and transmission coefficients are measured with two pairs of microphones installed on both sides of the specimen, which in our case is the

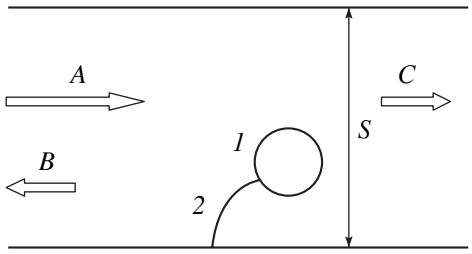

Fig. 1. Dipole resonator in a narrow waveguide: (*1*) the vibrating body of mass m and added mass μ; (*2*) the spring with the elasticity coefficient κ; A is the amplitude of the incident wave, B is the amplitude of the reflected wave, C is the amplitude of the transmitted wave, and S is the area of the waveguide cross section.

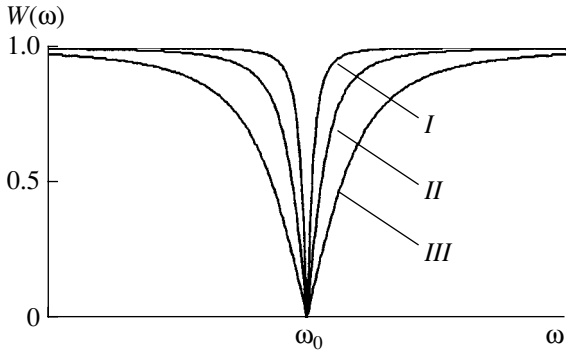

Fig. 2. Transmission coefficient $W(\omega)$ for different resonator volumes: (*I*) Ω, (*II*) 2Ω, and (*III*) 4Ω.

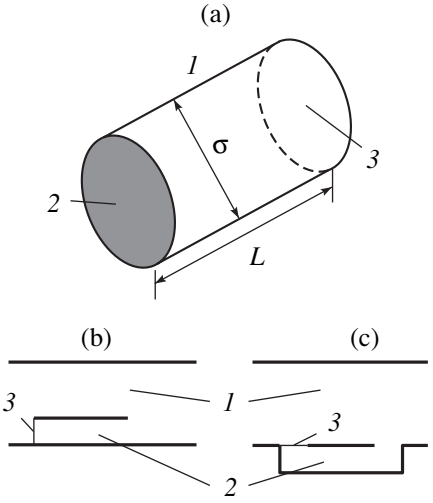

Fig. 3. (a) Actual structure of the dipole resonator: (*1*) the tube of length L and cross-sectional area σ ($\ll S$), (*2*) the membrane stretched over one end of the tube, and (*3*) the open end of the tube. (b, c) Ways of mounting the dipole resonator (b) inside and (c) outside the waveguide: (*1*) the waveguide, (*2*) the dipole resonator, and (*3*) the stretched membrane of the resonator.

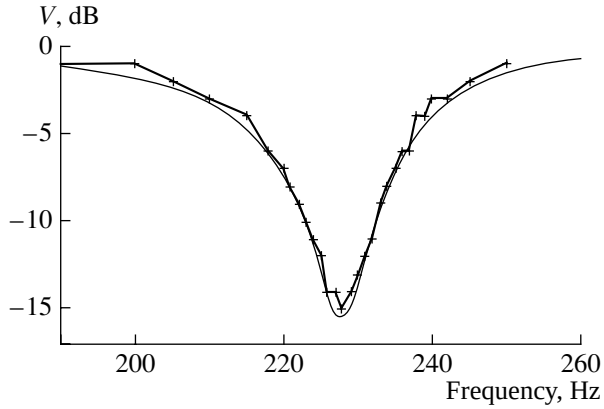

Fig. 4. Transmission coefficient versus frequency: theory (solid line) and experiment (crosses).

dipole resonator. The parameters of the dipole resonator geometry are as follows: the tube length is $L = 20$ cm and the tube diameter is 5.8 cm. The resonator natural frequency measured outside the waveguide is $f_0 = 255$ Hz. Figure 4 shows the measured coefficients W and V. The frequency of minimal transmission was found to be $f_w = 228$ Hz, i.e., lower than the frequency f_0, which is in good agreement with Eq. (7). At the scatterer resonance frequency, the measured transmission coefficient was –15 dB. The relative bandwidth, in which the transmission coefficient is below or equal to –6 dB, measures 0.074. In Fig. 4, the solid line shows the theoretical function $W(\omega)$. To take into account the loss in the resonator, we introduced a small imaginary addition to the natural frequency: $f_0 = 255(1 - i \times 0.005)$ Hz, which corresponds to the resonator's Q-factor $Q = 100$.

As the resonator length L decreases, the mass of air in the tube decreases and, consequently, the resonance frequency increases. Figure 5 shows the transmission coefficient measured for resonator tubes of different length L (the initial resonator was shortened without changing the membrane tension). For $L = 15$ cm, this frequency was $f_{w2} = 254$ Hz; for $L = 10$ cm, it was $f_{w3} = 295$ Hz; for $L = 5$ cm, it was $f_{w4} = 347$ Hz; and, finally, for $L = 2$ cm, it was $f_{w5} = 386$ Hz. At these frequencies, the minimal values of the transmission coefficient appeared to be almost equal. The relative bandwidth decreases with decreasing tube length: for a length of 0.2 m, it measures 0.074, and for a length of 0.02 m, it is only 0.018. From the dependence of the frequency f_w on the tube length, one can estimate the membrane mass m. This mass appeared to be about 1.7×10^{-4} kg, which measures a quarter of the added mass for tube length $L = 0.2$ m. The membrane tension is about 2.2×10^3 N/m.

In Fig. 5, the heavy solid curve (the background) represents the transmission coefficient measured with no specimen in the measuring tube. In this case, only the wave generated by the source propagates in the waveguide, so that $W = 1$ for all frequencies. Deviations of the transmission coefficient from 0 dB are presumably caused by the incomplete absorption of the incident wave by the compensator.

It is of interest to compare the efficiencies of the dipole and monopole scatterers. As a monopole scatterer, we consider a Helmholtz resonator. For a Helmholtz resonator inserted in a narrow waveguide, the coefficient of sound transmission through the cross section in which the resonator is positioned has the form

$$W_m = \frac{1}{1 + i\dfrac{\omega_0^2 \Omega}{2cS}\dfrac{\omega}{\omega^2 - \omega_0^2}}, \qquad (8)$$

where ω_0 is the resonance frequency, S is the area of the waveguide cross section, and Ω is the resonator volume. Equation (8) does not take into account the mechanical

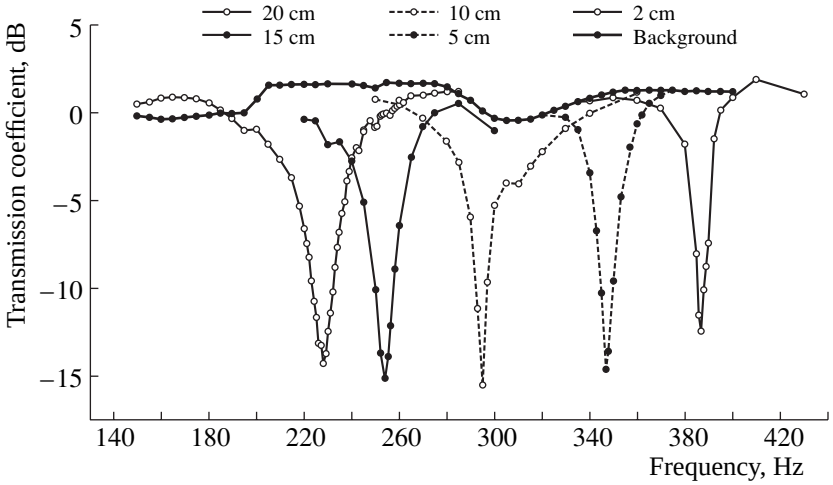

Fig. 5. Transmission coefficient for different resonator lengths.

loss. For the dipole resonator, for $m \ll \mu$ and, again, without taking into account mechanical loss, Eqs. (3) and (4) yield the following expression for W:

$$W_d = 1/\left(1 + i\frac{\omega_0^2\mu}{2\rho c S}\frac{\omega}{\omega^2 - \omega_0^2}\right). \quad (9)$$

Expressing the added mass involved in Eq. (9) through the dipole scatterer volume $\Omega = \mu/\rho$, we find that resonance curves (8) and (9) corresponding to the two types of scatterers under study identically coincide for equal volumes. This means that, in narrow waveguides, both monopole and dipole scatterers provide the sound scattering with identical efficiencies. It should be noted that, in the case of sound scattering in free space, the resonance scattering cross section of a dipole exceeds that of a monopole by a factor of three [5].

The main results of this study are the experimental realization of the dipole resonance scatterer and the corroboration of the fact that the scatterer occupying only a small part of the waveguide cross section can considerably (by 15 dB) decrease the transmitted sound. This property makes it possible to use dipole scatterers as new effective means of noise reduction in different applications. In connection with this, we plan further investigations aimed at increasing the efficiency of the scatterer by active methods [4, 5] and broadening the bandwidth by using several scatterers with identical or different resonance frequencies. In the latter case, the resonance frequencies must be distributed over the working band of the scattering unit according to a certain law. Such a structure resembles the fuzzy structures that have become quite popular in recent years [6, 7].

REFERENCES

1. M. A. Isakovich, *General Acoustics* (Nauka, Moscow, 1978).
2. A. Ya. Gorenberg, F. F. Kamenets, I. I. Sizov, and A. E. Vovk, in *Proceedings of X Session of the Russian Acoustical Society* (GEOS, Moscow, 2000), Vol. 2, p. 68.
3. V. V. Tyutekin, Akust. Zh. **47**, 843 (2001) [Acoust. Phys. **47**, 746 (2001)].
4. G. M. Emms and C. Fox, Appl. Acoust. **62**, 735 (2001).
5. P. A. Nelson and S. J. Elliott, *Active Control of Sound* (Academic, New York, 1992).
6. G. Maidanik and K. J. Becker, J. Acoust. Soc. Am. **104**, 2628 (1998).
7. M. Strasberg, J. Acoust. Soc. Am. **100**, 2878 (1996).

Translated by A. Vinogradov

Acoustical Physics, Vol. 49, No. 3, 2003, pp. 316–327. Translated from Akusticheskiĭ Zhurnal, Vol. 49, No. 3, 2003, pp. 376–388.

Acoustic Phenomena Observed in Lung Auscultation

V. I. Korenbaum, A. A. Tagil'tsev, and Yu. V. Kulakov

Institute of Physics and Information Technologies, Far-East State University, ul. Sukhanova 8, Vladivostok, 690600 Russia

e-mail: v_kor@poi.dvo.ru

Received December 7, 1995; in final form, November 22, 2001

Abstract—The results of studying respiratory noise at the chest wall by the method of acoustic intensimetry reveal the presence of frequency components with different signs of the real and imaginary parts of the cross spectrum obtained for the responses of the receivers of vibratory displacement and dynamic force. An acoustic model is proposed to explain this difference on the basis of the hypothesis that the contributions of both air-borne and structure-borne sound are significant in the transmission of respiratory noise to the chest wall. It is shown that, when considered as an acoustic channel for the basic respiratory noise, the respiratory system of an adult subject has two resonances: in the frequency bands within 110–150 and 215–350 Hz. For adults in normal condition, the air-borne component of the basic respiratory noise predominates in the region 100–300 Hz in the lower parts of lungs. At forced respiration of healthy adults, the sounds of vesicular respiration are generated by the turbulent air flow in the 11th- through 13th-generation bronchi, and the transmission of these sounds to the chest wall in normal condition is mainly through air and is determined by the resonance of the vibratory system formed by the elasticity of air in the respiratory ducts of lungs and by the surface mass density of the chest wall. It is demonstrated that the distance from the chest wall to the sources of structure-borne additional respiratory noise, namely, wheezing with frequencies above 300 Hz, can be estimated numerically from the ratio between the real and imaginary parts of the cross spectrum on the assumption that the source is of the quadrupole type. © *2003 MAIK "Nauka/Interperiodica".*

The auscultation of lungs, i.e., listening to respiratory and vocal sounds transmitted to the chest wall, was proposed by R. Laenec [1] at the beginning of the 19th century. Despite the long history and wide-spread application of this procedure in medical practice, it underwent no radical changes and remained a kind of medical art to this day [2–4]. Numerous attempts to introduce objective acoustic methods into the auscultation of lungs have been made since the 1950s without any substantial results. This situation is likely to be caused by the lack of understanding of the processes underlying the formation (generation and radiation) and propagation (transmission) of sounds in the human respiratory system, such a lack of understanding being acknowledged by all leading specialists in the medical field under discussion [2–9].

STATE OF THE ART

Origin of Respiratory Sounds

The fact that respiratory noise originates from the air flow through the respiratory system is generally recognized [5, 9]. Different features of noise correspond to lung sounds of different types: they include [3] the basic respiratory noise characterizing the normal condition of the respiratory system and the additional respiratory noise associated with deviations from the norm. According to conventional classification, the basic respiratory noise is classed into the bronchial and vesicular noise types. Bronchial noise consists of the sounds detected over the trachea and the projections of the largest ducts of the respiratory tract, i.e., the main bronchi. Experiments carried out by different authors with the aim of determining the characteristic frequency bands of bronchial sounds provided rather contradictory results: 710–1400 Hz [10], 500–1000 Hz [2], 100–800 Hz [6], 60–700 Hz [11], and 75–900 Hz [12]. Vesicular noise is detected over the lower parts of lungs in normal condition. Its frequency band lies below that of bronchial noise, but the experimental estimates obtained for this band from different experiments are also contradictory: 80–400 Hz [13], 180–355 Hz [10], 50–600 Hz [6], and 100–130 Hz (at maximum) [2]. The basic respiratory noise represents broadband processes. The additional respiratory noise falls into two main types: prolonged (more than 250 ms) narrowband processes corresponding to wheezing [5] and short explosive sounds (broadband processes) heard as crackles [4, 5].

The bronchial sounds are believed to result from the air flow through the trachea and large bronchi and caused by the turbulent pressure fluctuations in this air flow [14].

As for the vesicular sounds, several hypotheses have been put forward to explain their origin. The noise detected over a normal lung was called "vesicular respiration" by Laenec [1], because he believed that this noise was caused by the friction between air and the

1063-7710/03/4903-0316$24.00

walls of alveoli (vesicles). This hypotheses was multiply subjected to question. In 1834 [15], the vesicular noise in normal respiration was explained by the air passage through the glottis. The resulting sound was assumed to transform in the course of its propagation through the respiratory ducts of a lung, after which it was transmitted to the chest wall. Subsequent physiological and clinical experiments [2, 4, 5] gave contradictory results, some of them being in favor of the first hypothesis and some, in favor of the second one. Finally, it was demonstrated [16] that the source of vesicular noise does not lie in the alveoli: it lies farther toward the periphery of the bronchial tree, noticeably farther than the source of bronchial noise. These results were confirmed by the determination of the "coherence distances" of the basic respiratory noise on the chest surface [6]. The characteristic size of coherence zones of vesicular noise was found to be about 6 cm for frequencies within 50–600 Hz and 12–18 cm for frequencies within 100–150 Hz. According to the authors of the cited publication [6], these results testify that the vesicular sounds originate from a depth greater than that corresponding to the alveolar hypothesis. The classical interpretation of wheezing sounds attributes them to the excitation of vibrations of the viscous or liquid contents in the air duct lumen [3]. However, wheezing is also observed in the absence of secretion in the bronchi. The hypothesis put forward by Forgacs [4] explains these sounds by the self-oscillation processes that occur when the air flow excites vibrations in compressed parts of the mucous membrane of the respiratory tract. This hypothesis was confirmed by visual observations [17]. Subsequent experiments [18] showed that two types of vibrations are possible: first, with a closure of the respiratory tract (longitudinal vibrations) and, second, without the closure, owing to the vibrations of the mucous membrane areas near the equilibrium position (flexural vibrations).

Transmission of Respiratory Sounds

For years, the transmission of respiratory and vocal sounds to the chest wall through the air ducts of the bronchial tree was believed to be purely airborne [1–4]. Nemerovskiĭ [19] made an attempt to represent this hypothesis in the form of an acoustic model based on the propagation of travelling plane waves through narrow pipes. Although he obtained encouraging results for low frequencies of 80–100 Hz, no agreement with experimental data could be achieved for frequencies above 200 Hz.

In 1989, an acoustic model of a structure-supported transmission of vocal sounds to the chest wall was proposed [20]. This model was based on the vibrations of a quarter-wavelength air column in a single narrow pipe representing the bronchial tree. These vibrations were assumed to be partially transformed due to the finite wall stiffness into pulsating vibrations of the lateral surface of the cylindrical pipe. As a result, cylindrical waves propagated via the lung tissue (structure) to the chest wall. Currently, this model with various improvements [7, 8] is considered as the basic one. However, the quantitative estimates [7, 21] obtained from this model agree well with the measured amplitude–frequency response of the respiratory tract [19, 21] only for frequencies above ~200 Hz. For lower frequencies, the model leads to considerable discrepancies.

Recently, experiments were carried out with the aim of studying the effect of the density of gas inhaled by a subject on the acoustic transfer function and on the time of sound transmission from the trachea to different chest areas when an artificial broadband signal was supplied to the subject's mouth cavity [22, 23]. As a rule, the gas used for breathing in such experiments was heliox (a mixture of helium (80%) and oxygen (20%)). In [24], this approach was used to study the basic respiratory noise. The results of the aforementioned studies testify that, in the frequency range below ~300 Hz, no considerable changes of acoustic characteristics occur when the gas inhaled by the subject changes from air to heliox. The authors of [22] also report on the absence of changes in the frequency band 300–600 Hz; relying on this result, they conclude that the propagation of sound via the lung parenchyma (structure) predominates. On the other hand, the authors of [23] observed considerable changes in the acoustic characteristics within 300–1200 Hz. This result was interpreted as a consequence of a change in the path of sound propagation in the aforementioned frequency band. The authors of [24] reported on noticeable changes in the noise measured on the chest wall at frequencies within 300–600 Hz, while the measurements over the trachea revealed a frequency shift "similar to the shift of the speech formants in helium."

The difficulties in obtaining objective records of acoustic signals propagating in lungs were believed [19] to be related to the masking of some acoustic effects by other acoustic effects. However, it was established [19] that acoustic vibrations of frequency 80–100 Hz supplied to the air channel of the bronchial tree through the mouth propagate predominantly via the air ducts. Only a small part (not exceeding 5%) is transformed and propagates via the lung structure.

One more remarkable result of the aforementioned study [19] is the experimental observation and theoretical explanation of the resonance effect in the so-called acoustic resonant circuit formed by the elasticity of air enclosed in the respiratory ducts of the lung and by the mass of the chest wall. The resonance of the acoustic resonant circuit was expected to lie within 80–100 Hz [19].

The study described below proceeds from the hypothesis of the mutual masking of the air-borne and structure-borne acoustic signals of respiratory noise in lungs. For the case of vocal sounds, this hypothesis was confirmed by our previous experiments [25]. The purpose of the present study is to refine the picture of

acoustic effects in human lungs on the basis of this hypothesis by using the intensimetry approach to studying the sounds transmitted to the chest wall [25].

METHOD OF STUDY

The respiratory noise was recorded by a combination acoustic transducer (CAT) [25] consisting of an accelerometer with a contact base and a microphone with a stethoscopic head, which were mounted coaxially to form a single unit. In our previous publication [25], it was shown that, in the frequency range above 100 Hz, a CAT positioned on the surface of a human chest can be considered as constrained. In these conditions, the microphone of the CAT represents a receiver of vibrational displacement and the accelerometer is a receiver of dynamic force. Synchronous responses of the CAT channels at the points of the human chest surface were subjected to cross-spectral processing [25].

More than 100 realizations of respiratory noise associated with eupnea were recorded by placing the CAT in different positions on the chest surfaces of three adult volunteers. The recording process was controlled by a physician (a pulmonologist) who performed a simultaneous auscultation and a subjective classification of the sounds observed in the experiment. In addition, the state of the subjects tested was verified by the data of the clinical anamnesis, which included the results of X-ray and spirographic examinations.

The signals were recorded by an A-1014 SONY tape recorder with an additional amplification and filtering of signals in the frequency band within 100–1000 Hz. The signals from the tape recorder were supplied to a processing system based on an IBM PC [26]. The sampling frequency was 12048 Hz. The cross-spectral processing was based on the fast Fourier transform procedure. A total of 1024 spectral samples were taken. Weighting was performed with the Humming window, and averaging was done within the duration of a sample containing 8192 time readings with a 75% overlapping of subsamples. The cross spectra of inhalation, exhalation, and segments with additional respiratory noise were calculated separately.

The CAD channels were preliminarily calibrated within 100–1000 Hz by the comparison method [25], and their amplitude–frequency and phase–frequency responses were taken into account in calculating the cross spectra. The forms of the spectra, the frequencies of the main spectral maxima, and the behavior of the sign of the imaginary part of the cross spectrum were characterized by high individual reproducibility [27].

For the theoretical evaluation of the bronchial tree zones responsible for the generation of the basic respiratory noise, the approximate method of determining the frequencies of the spectral maxima of respiratory noise in different parts of the bronchial tree was used [28]. The method is based on the semiempirical model of the air flow noise in ventilation systems [29].

ACOUSTIC MODEL

Generation of Basic Respiratory Noise

The application of the approach described in [28] to the case of eupnea, which is characterized by the maximal values of the instantaneous volume flow rate of about 2–3 l/s, shows that the dominant part in the generation of the basic respiratory noise is played by the turbulent flow noise. Indeed, the velocities that are necessary for the development of the separation phenomena are usually not reached in this case, and the noise of the turbulent boundary layer is too weak to account for the effects observed in the experiment. If we assume that the main spectral maxima of the basic respiratory noise are determined by the flows with the maximal values of the instantaneous volume flow rate, the expression [28] evaluating the frequency of the spectral maximum of a turbulent flow in the bronchi (on the assumption that we deal with a regular dichotomic branching of the bronchial tree) can be represented in the form

$$f_{\max} \approx 0.2V/(2^j d_j^3), \tag{1}$$

where V is the maximal volume flow rate, j is the order of the bronchial tree generation, d_j is the diameter of the bronchi of the jth generation, and the condition of the existence of the turbulent flow noise has the form [29]

$$q = V/(2jd_j^3) > 200. \tag{2}$$

Respiratory Tract

The respiratory system is represented by a branching narrow air-filled pipe surrounded along its perimeter by the lung tissue whose acoustic impedance [7] is much greater than that of air. In addition, according to [19], the air volume in the respiratory parts of the lung, i.e., in the acini represented by a set of branches of terminal bronchioles (the 16th generation of the bronchial tree branches [3]), and the chest wall together form an acoustic resonant circuit. This acoustic system should be characterized by two fundamental resonance frequencies.

The first frequency, i.e., the frequency of the acoustic resonant circuit [19], can be approximately represented in the form [30]

$$f_{\text{arc}} \approx (K/m)^{0.5}/2\pi, \tag{3}$$

where $K = \rho_0 c_0^2/h$ is the stiffness, ρ_0 is the air density, c_0 is the velocity of sound in air, h is the thickness of the air layer of the parenchyma (according to morphometric data [31], its average value is about 5 mm), $m = \rho_w l_w$ is the surface mass density of the chest wall, ρ_w is the chest wall tissue density close to the water density [7], and l_w is the chest wall thickness of about 2–4 cm. With allowance for these values, the eigenfrequency given by Eq. (3) is of the order of 110–150 Hz, which is close to

the results reported in [19]. Thus, if the sound wave propagating through the respiratory tract contains vibrations with frequencies within this band, an efficient vibration excitation occurs in some chest areas, and this excitation characterizes the air-borne component of sound in the whole mechanism of sound transmission. It should be noted that, since the resonance of the vibratory system does not depend on the point of the force application, the adequacy of the frequency values obtained for the acoustic resonant circuit is confirmed by the observations described in [2], which showed that the fundamental frequencies of the percussion tones over healthy lung areas are within 100–130 Hz.

On the other hand, the whole bronchial tree, as a system of narrow acoustic pipes open at the mouth end (from the point of view of the respiration through the mouth and the utterance of vowels), is characterized by a set of wave resonances. Since, for the frequencies $f > f_{arc}$, the impedance of the acoustic resonant circuit is of a mass character and the condition $2\pi fm/\rho_0 c_0 \gg 1$ is satisfied, we can consider a quarter-wave series [30] in compliance with [20, 21]. The velocity of sound in the air ducts of the bronchial tree is practically the same as in air [19], and the length of a branch of the bronchial tree from the larynx to the chest wall can vary within 23–38 cm [31]. Then, the first frequency of the aforementioned series, i.e., the frequency of the quarter-wave resonance, should be of the order of 215–350 Hz.

Thus, at frequencies of 215–350 Hz, a standing wave is excited, and the maximal sound pressure amplitude of this wave should occur at the closed end of the pipe. However, since the total cross section of the pipe increases as the chest wall is approached, the maximal sound pressure amplitudes occur in the region of the large bronchi and the trachea segment lying inside the chest [25]. It is precisely this region where the most efficient excitation of the structure-borne sound takes place as a result of the transformation of part of the standing wave energy into cylindrical pulsations of the respiratory tract, this conclusion being in good agreement with medical observations [3]. According to [7, 8, 21], cylindrical waves formed in the aforementioned way propagate via the tissues, including the parenchyma and the chest wall, and are detected by acoustic receivers as the structure-borne sound component of the total sound transmission. At the same time, the resonance of the air column gives rise to the chest wall vibrations at the closed end of the pipe. These vibrations characterize the air-borne component of voice transmission, which is clearly observed in the lower parts of the lungs [25]. In the upper parts of the lungs in normal condition [25], at the same frequencies, a competition of the air-borne and structure-borne sound components is observed as the source of structure-borne sound is approached. However, at the resonance frequencies of the acoustic resonant circuit, sound transmitted through these lung zones in normal condition is purely air-borne [25, 27].

We note differences in the conditions of excitation of the two types of resonance vibrations described above. The resonance of the acoustic resonant circuit is excited by any sound whose frequency is close to resonance when this sound is transmitted to the chest wall via the air ducts. By contrast, the effective excitation of forced vibrations of the quarter-wavelength pipe [30] requires the presence of acoustic perturbations near the open end of the pipe, i.e., in the region of the trachea and large bronchi.

It should also be noted that, in asthenic persons (at least one such case was observed by us), the resonance of the acoustic resonant circuit may be shifted to higher frequencies, toward the quarter-wave resonance. As a result, the quarter-wavelength pipe proves to have not a rigid but a resonant cover, and the quarter-wave resonance is considerably reduced; i.e., the two-resonance system under consideration may become constrained.

Transmission of Basic Respiratory Noise

As will be shown below, the sources of basic respiratory noise form a fairly complex distributed system. According to the model of noise generation considered above, we assume that this system is a set of pulsating point sources whose pulsations result from the averaging of the turbulent pressure fluctuations at the wall of the respiratory tract. Consider one of these sources and assume that it pulsates in a medium characterized by the average density ρ and sound velocity c with the sound pressure p_{js}. By analogy with [7, 25], in the first approximation, we ignore the rereflected waves because of the strong attenuation. Specifying the wave number in the tissues k_s and the distance r from the source to the outer chest wall via the tissues, according to [32], we obtain the following expressions for the pressure p_s and vibrational particle velocity v_s of the structure-supported wave:

$$p_s = p_{js}(\exp(-ik_s r))/r,$$

$$v_s = p_{js}(1 + 1/ik_s r)(\exp(-ik_s r))/\rho c r. \qquad (4)$$

For the particle displacement in a structure-supported wave at a perfectly soft boundary [25], we have $\xi_s \approx -i2v_s/\omega$, where ω is the circular frequency. The response of the CAT microphone (receiver of vibrational displacement) will presumably be described by the expression $u_{ms} \approx g_m \xi_s$, where g_m is the conversion factor of the microphone together with the stethoscopic chamber in terms of the vibrational displacement [25]. The CAT accelerometer measures the pressure force $F_p \approx -2Sp_s$, where S is the area of the contact region between the sensing element of the accelerometer and the body. Thus, the accelerometer response can be described by the expression $u_{as} \sim -2g_f p_s S$, where g_f is the conversion factor of the accelerometer in terms of the dynamic force. Note that the same electric response at the accelerometer output can be represented in the

form analogous to that in [25]: $u_{as} \sim g_v v_s$, where g_v is the conversion factor of the accelerometer in terms of the vibrational particle velocity. Then, assuming that the wave is locally plane, we obtain $g_f \sim -g_v/(\rho c S)$. Hence, for the accelerometer response, we have $u_{as} \sim -2g_v p_s/\rho c$. Passing to the calculation of the cross spectrum of the microphone and accelerometer channels [25], we obtain (the polarity of the accelerometer is inverse, as in [25])

$$W_s \sim -4g_m g_v p_{js}^2 (i + 1/k_s r)/[\rho^2 r^2 c^2 \omega]. \quad (5)$$

From this expression, it follows that, for the structure-borne component of basic respiratory noise, as well as for the structure-borne component of vocal sound transmission [25], both real and imaginary parts of the cross spectrum are of negative sign.

The air-borne sounds [25] reaching the receivers propagate through a narrow pipe loaded at its end by a concentrated mass characterizing the parameters of the chest wall. Since the concentrated mass moves as a whole, the vibrational particle velocity v_a measured at its outer surface can be calculated through the sound pressure at the pipe end p_t [30]:

$$v_a = -ip_t \exp(i\omega l/c_0)/(\omega m), \quad (6)$$

where l is the pipe length and l/c_0 characterizes the time delay between air-borne and structure-borne sound. The vibrational displacement of the concentrated mass at the pipe end can be determined as

$$\xi_a = -p_t \exp(i\omega l/c_0)/(\omega^2 m). \quad (7)$$

Evidently [25], the microphone (receiver of vibrational displacement) measures the quantity $u_{ma} \approx g_m \xi_a$, and the accelerometer (receiver of dynamic force) responds to the inertial force of both the mass of the medium involved in the vibrations and the dynamic mass of the receiver ($(m_1) - F_i = a_a m_1$). Thus, the response of the receiver of dynamic force is proportional to the acceleration a_a and can be represented in the form $u_{aa} \approx g_v v_a$ [25]. Passing to the calculation of the cross spectrum of the channels, we obtain

$$W_a \sim i[g_m g_v p_t/(\omega^3 m^2)]. \quad (8)$$

As a result, the cross spectrum obtained for air-borne sound proves to be purely imaginary with a positive imaginary part.

The comparison of expressions (6) and (8) shows that the signs of the imaginary part of the cross spectrum of respiratory noise are different for different sound components: the air-borne sound is characterized by spectral components with the positive sign, and the structure-borne sound, by components with the negative sign, which agrees well with the results obtained earlier [25] for vocal sounds. It should be noted that the mutual compensation of the aforementioned spectral components does not occur as a result of the difference in the frequency responses of the air-borne and structure-supported sound transmission channels. In addition, we note that the signs of expressions (5) and (8) depend on the polarity of the accelerometer connection. The essential factor is the difference in the sign (phase) characteristics of the air-borne and structure-borne sound components, which reflects the features of their formation and propagation.

When sound waves are excited in both the air ducts and the lung tissues, the output signals of the receivers have the form

$$\begin{aligned} u_a &\approx g_v\{-ip_{ja}S_j \exp(-ik_a l)/(S_p \omega m) \\ &\quad - 2p_{js}[\exp(-ik_s r)]/\rho c r\}, \\ u_m &\approx g_m\{-p_{ja}S_j \exp(-ik_a l)/(S_p \omega^2 m) \\ &\quad - 2p_{js}(i + 1/k_s r)[\exp(-ik_s r)]/\rho c r \omega\}, \end{aligned} \quad (9)$$

where $p_{ja}S_j/S_p \approx p_t$ (to simplify the expression, we assume that the amplitude–frequency responses of the air and structure transmission channels are implicitly determined in terms of the sound pressures produced by the source in air p_{ja} and in the structure p_{js}, respectively), S_j is the cross-sectional area of the bronchus in which the sound is generated, S_p is the total cross section of the peripheral parts of the bronchial tree, and $k = \omega/c_0$. Performing evident transformations, we arrive at the relations that determine the real and imaginary parts of the cross spectrum of the receivers W and the proper spectra of the microphone F_m and the accelerometer F_a:

$$\begin{aligned} \mathrm{Im}(W) &\sim -g_m g_v\{A_2^2 - A_1^2 - A_1 A_2 c \cos(\omega\tau)/(r\omega)\}/\omega, \\ \mathrm{Re}(W) &\sim -g_m g_v\{A_2^2 c/(r\omega) + 2A_1 A_2 \cos(\omega\tau) \\ &\quad - A_1 A_2 c \sin(\omega\tau)/(r\omega)\}/\omega, \\ F_a &\sim g_v^2\{A_1^2 + A_2^2 - 2A_1 A_2 \sin(\sin\omega\tau)\}, \\ F_m &\sim g_m^2\{A_1^2 + A_2^2 c^2/(r\omega)^2 + A_2^2 \\ &\quad + 2A_1 A_2[c \sin(\omega\tau)/(r\omega) + \cos(\omega\tau)]\}/\omega^2, \end{aligned} \quad (10)$$

where $\tau = r/c - l/c_0$, $A_1 = p_{ja}S_j/(S_p \omega m)$, and $A_2 = 2p_{js}/(\rho c r)$.

With allowance for the fact that, in the presence of both air-borne and structure-borne signals, not only the values of Im(W), Re(W), F_a, and F_m but also the value of the delay τ are determined experimentally (e.g., through the autocorrelation function of the signal of each of the receivers), the system of equations (10) can be used not only for the determination of the parameters of the source of received sounds but also for the source localization.

In particular, if only the structure-borne component is present, we have

$$\begin{aligned} \mathrm{Im}(W) &\sim -g_m g_v A_2^2/\omega, \\ \mathrm{Re}(W) &\sim -g_m g_v A_2^2 c/(r\omega^2). \end{aligned} \tag{11}$$

From relations (11), we derive

$$r \sim [c\,\mathrm{Im}(W)]/[2\pi f\,\mathrm{Re}(W)]. \tag{12}$$

Hence, in principle, from the measurements of the real and imaginary parts of the spectrum of structure-borne sound, one can determine the distance from the chest wall to the source of the detected structure-borne sound via the tissues. This possibility is of special interest for studying the additional respiratory noise. However, an essential difficulty is encountered in this case. Above, we assumed that the source of the basic respiratory noise is of monopole type, whereas, for the additional respiratory noise, this hypotheses is questionable.

Generation and Transmission of Additional Respiratory Noise

Among possible types of additional respiratory noise, we consider wheezing with frequencies above ~300 Hz. The source of this sound [4] is the zone of tissue closure in the bronchus lumen (presumably, no farther than 9th- and 10th-generation bronchi [28]). This zone has a linear configuration and, under longitudinal vibrations [28], causes a ring extension (the positive half-wave) of segments of the respiratory tract wall in the directions perpendicular to the line of the tissue closure. Since the force in the direction parallel to the line of the tissue closure is absent, these segments of the respiratory tract wall experience a ring compression due to the elasticity within the aforementioned half-period. The vibration pattern described above resembles the quadrupole mode of vibrations of a piezoelectric cylinder, i.e., a transverse quadrupole. It should be noted that a similar hypothesis was formulated earlier [33] in application to crackles.

Let us consider a two-dimensional model of the structure-supported transmission of wheezing produced by a source in the form of a transverse quadrupole. The orientation of the source is of no importance, because, by analogy with expression (12), we deal with the relative quantity $\mathrm{Im}(W)/\mathrm{Re}(W)$. The sound pressure of a transverse quadrupole [32] has the form

$$\begin{aligned} p_s &= -ik_s^3 \rho c Q_{xy} \exp(-ik_s r) xy/(4\pi r^3) \\ &\times [1 - 3i/(k_s r) - 3/(k_s r)^2], \end{aligned} \tag{13}$$

where Q_{xy} is the quadrupole strength and $xy/r^2 = \cos(x, r)\cos(y, r)$. After some obvious calculation, the radial part of the particle velocity of a transverse quadrupole (the tangential part can be ignored in view of the features of the subsequent signal processing [25]) can be represented in the form

$$\begin{aligned} v_{sr} &= -k_s^3 Q_{xy} xy/(4\pi r^3)[\exp(-ik_s r)] \\ &\times [i + 6/(k_s r) - 15i/(k_s r)^2 - 15/(k_s r)^3]. \end{aligned} \tag{14}$$

Expressing (as before) the response of the accelerometer (receiver of dynamic force) through the sound pressure given by Eq. (13) and calculating the cross spectrum W of the receiver responses by analogy with expressions (8), (11), and (12), we divide the real part of the spectrum by its imaginary part to obtain

$$\mathrm{Re}(W)/\mathrm{Im}(W) = 3/(k_s r) + 12/(k_s r)^3 + 45/(k_s r)^5. \tag{15}$$

We assume that the experimentally measured value of the ratio of the real and imaginary components of the cross spectrum at the spectral maximum of the wheezing is $\mathrm{Re}(W)/\mathrm{Im}(W) = C$. Introducing the notation $z = 1/k_s r$, we obtain the equation

$$45z^5 + 12z^3 + 3z - C = 0, \tag{16}$$

which can be solved numerically for each specific source of wheezing in the case of the purely structure-supported sound transmission.

Note that the quantity $k_s r = 1/z$ obtained by solving Eq. (16) involves the average velocity of sound in the chest tissues c. Since, according to [7], the propagation of sound in the lung tissue occurs through two media with widely different sound velocities (the parenchyma and the chest wall), we can write the expression

$$\begin{aligned} c &= r/(r_p/c_p + l_w/c_w) \\ &= (r_p + l_w)c_p c_w/(r_p c_w + l_w c_p), \end{aligned} \tag{17}$$

where r_p is the distance to the source via the parenchyma, c_p is the sound velocity in the parenchyma, and c_w is the sound velocity in the chest wall. Taking into account that $k_s r = 2\pi fr/c$ and performing obvious transformations of Eq. (17), we obtain

$$r_p = c_p/(2\pi f z) - l_w c_p/c_w. \tag{18}$$

RESULTS AND DISCUSSION

According to expressions (1) and (2) and the known Weibel morphometry of a statistical average respiratory system of an adult [19], we calculated the frequencies characteristic of noise produced in different parts of the bronchial tree (Table 1) at eupnea (V = 2–3 l/s). Of course, the idealization of the respiratory tract model and the use of the statistical average values of V and d_j allows us to consider the resulting values only as estimates, but the qualitative features of noise generation at eupnea become evident. In particular, at eupnea in normal condition, practically no noise is produced in the lung parenchyma (the bronchial tree branches from 16th to 23rd generations), which coincides with the assumption [4] of the "silence of the lung parenchyma of a healthy subject."

Table 1. Noise generation in the bronchial tree at eupnea (V = 2–3 l/s)

j	q, 1/s	f_{max}, Hz
0	340–515	68–102
1	578–868	116–174
2	874–1312	175–262
3	1423–2135	285–427
4	1371–2057	274–411
5	1457–2186	291–437
6	1423–2135	285–427
7	1248–1926	256–385
8	1214–1821	242–364
9	1069–1604	213–320
10	910–1365	182–273
11	754–1131	150–226
12	569–854	114–170
13	443–664	89–133
14	301–451	60–90
15	212–318	42–64
16	141–211	–
17–23	Below 200	–

Figures 1–5 present the cross spectra obtained experimentally for the responses of the CAT channels (the near-spine and shoulder-blade lines on the left and on the right) in the case of typical respiratory sounds at eupnea.

The cross spectrum shown in Fig. 1 characterizes the inhalation in vesicular respiration. According to the model accepted above, this signal corresponds to an almost purely air-borne sound whose spectral maximum lies within 100–160 Hz, which immediately suggests that the acoustic resonant circuit plays an important role in its formation. Judging from the spectral characteristics of Fig. 1, the noise of the inhalation phase can be formed in the regions of the 11th through 13th generations of the bronchial tree or its zeroth and first generations, in compliance with the data shown in Table 1. However, noise propagating toward the chest wall from the region of the main bronchi is more strongly attenuated because of the increase in the total cross section toward the periphery of the bronchial tree. Thus, the most probable zone of noise generation accompanying a deep inhalation at normal vesicular respiration [34] should be the region of the 11th- through 13th-generation bronchi, which qualitatively agrees with the results reported in [6, 16]. Nevertheless, in the transmission of these sounds to the chest wall (through air, at least), a fundamental role is played by the respiratory part of lungs owing to the mechanism of the acoustic resonant circuit. The latter fact shows that Laenec's [1] understanding of the origin of these sounds was close to reality. We also note that the results obtained by us validate the above model of the structure-supported transmission of basic respiratory noise. According to anatomic data, the distance from the 11th- through 13th-generation bronchi to the chest wall is within several centimeters (of the order of the longitudinal sound wave in the lung parenchyma), and, hence, each of these bronchi can be represented as a pulsating point source described by Eqs. (4).

A sharp change in the imaginary part of the spectrum during inhalation (Fig. 2), which is associated with the attenuation of the amplitudes of positive spectral readings, can be interpreted according to the proposed model as a considerable reduction of noise produced in the 11th- through 13th-generation bronchi directly connected through air ducts with the CAT zone or as a local change in the parameters of the acoustic resonant circuit (a decrease in the air layer of the parenchyma) due to pathology. An increase in the amplitude of the negative spectral components testifies to the enhancement of the structure-supported transmission from the neighboring group of bronchi, which can be related to the presence of carnifications in the lung tissue due to pathological processes. In turn, a sharp noise decrease in the "own" group of bronchi testifies to a reduced ventilation of the given parenchyma region. The latter effect can be caused either by a closure of the corresponding air ducts of the bronchial tree or by pathological changes of the parenchyma region ventilated by this group of bronchi, which agrees well with clinical data (pneumosclerosis).

In the case of exhalation (Fig. 3), the noise spectrum noticeably broadens because of the appearance of components with frequencies within 200–300 Hz. Judging from Table 1, these components may be caused by the noise in the region of the first and second generations of the bronchial tree, as well as in the region of the 9th and 10th generations. By analogy with the previous case, one would take into account the sound attenuation due to the increase in the total cross section at the periphery of the bronchial tree and, hence, choose the second variant. However, the aforementioned frequencies lie in the region of the quarter-wave resonance of the bronchial tree if the latter is considered as an acoustic pipe. This fact does not allow us to exclude the possibility of the forced vibration excitation, which is most efficient in the large bronchi located near the pressure node of the standing wave [30]. In addition, at the phase of inhalation (Figs. 1 and 3 refer to signals from the same chest area of the same patient), although the conditions for the sound propagation from the 9th- and 10th-generation bronchi to the chest wall are more favorable (propagation along the flow [29]), these spectral components are not observed. Hence, the noise of frequencies 200–300 Hz should be attributed to the region of the first- and second-generation bronchi; i.e., it may be interpreted as the noise of bronchial respiration in medical terms. At the same time, the frequency region within 100–160 Hz exhibits no considerable changes

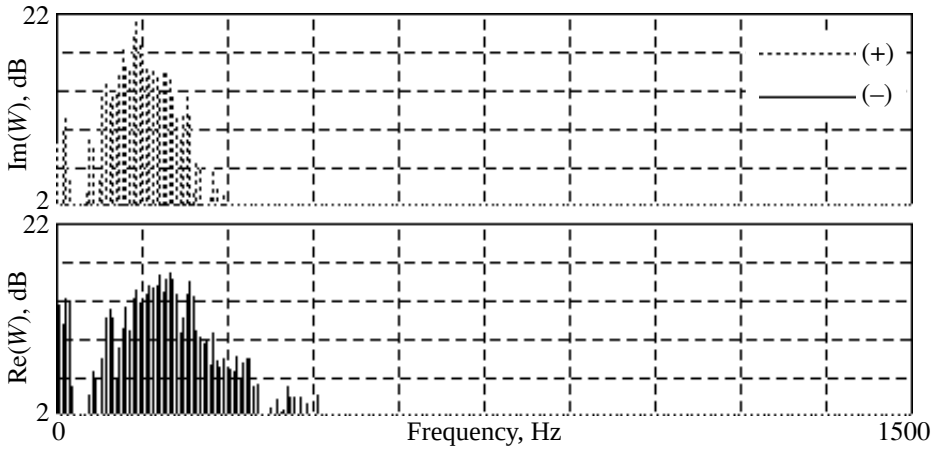

Fig. 1. Imaginary and real parts of the cross spectrum obtained for the responses of the CAT channels at inhalation over the lower zone of the lung in normal condition.

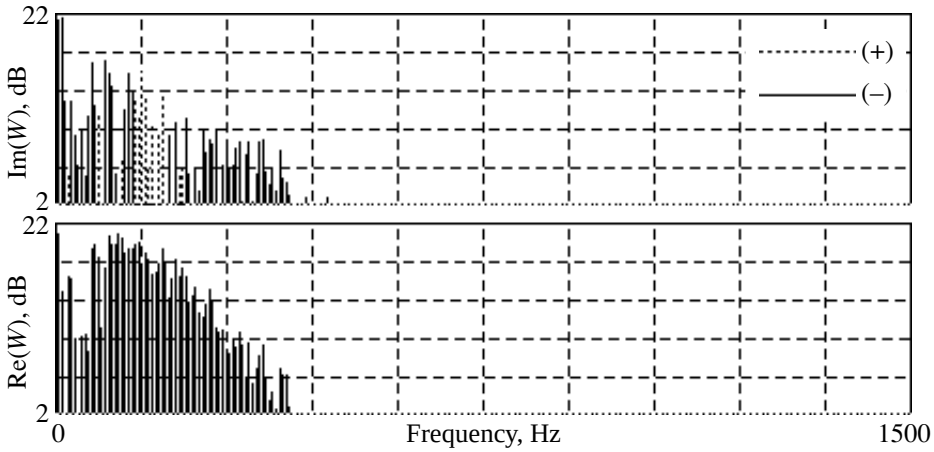

Fig. 2. Imaginary and real parts of the cross spectrum obtained for the responses of the CAT channels at inhalation over the middle zone of the lung at reduced ventilation.

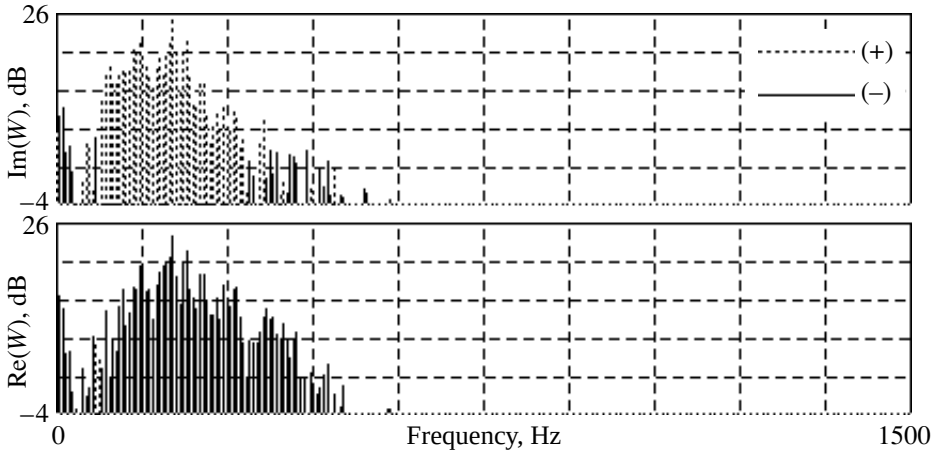

Fig. 3. Imaginary and real parts of the cross spectrum obtained for the responses of the CAT channels at exhalation over the lower zone of the lung in normal condition.

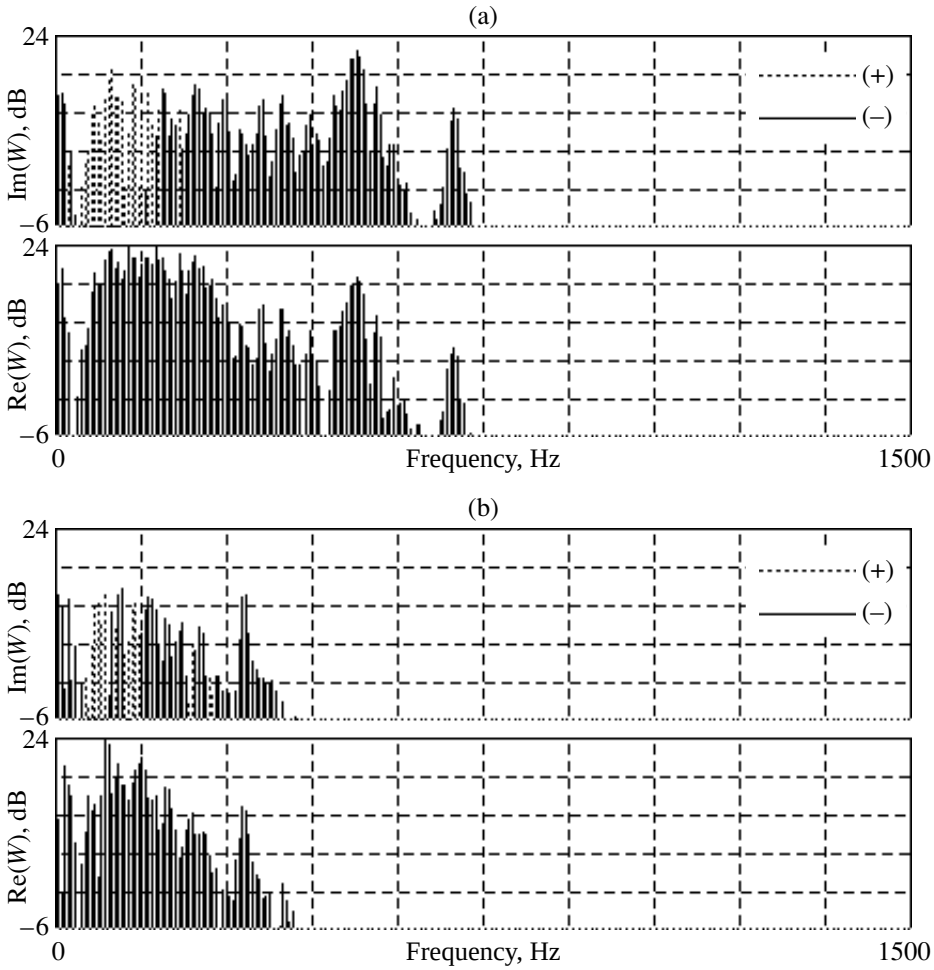

Fig. 4. Imaginary and real parts of the cross spectrum obtained for the responses of the CAT channels at exhalation over the upper zone of the lung (structure-borne additional respiratory noise): (a) the main part of the exhalation and (b) the wheezing before the cough impulse at the end of the exhalation.

compared to the phase of inhalation (Fig. 1) and, presumably, does not differ from it in the mechanism of noise generation. It should also be noted that, according to the anatomic data, the bronchi of the first and second generations, when considered as the sources of the structure-borne basic respiratory noise, evidently satisfy the model of Eqs. (4).

The exhalation shown in Fig. 3 is characterized by the predominance of the air-borne sound transmission and can be considered as normal, while the exhalation shown in Fig. 4a is characterized by weaker air-borne sounds in the high-frequency region and by the appearance of a pronounced structure-borne component in the frequency band 150–400 Hz. This effect can be interpreted as an enhancement of the transmission of bronchial sounds from the neighboring groups of bronchi because of the carnifications in the lung tissue, which agrees well with the X-ray and clinical data.

Now, we consider the pronounced discrete spectral components observed in Fig. 4 (540, 710, and 345 Hz) and in Fig. 5 (300 Hz). From the medical point of view, these acoustic signals are classed as wheezing. Naturally, wheezing may also differ in the way of transmission: it can be air-borne (Fig. 5) or structure-borne (Fig. 4).

By numerically solving Eqs. (16) and (18) with the parameters $c_p = 30$ m/s, $c_w = 2000$ m/s [7], and $l_w = 2$ cm, we determined the distances (Table 2) to the sources of wheezing represented in Fig. 4 (a patient with a clinically confirmed exacerbation of chronic bronchitis). The analysis of the results shown in Table 2 testifies that the calculated distance values are reasonable from the anatomic point of view. Note that the calculated distances (several centimeters) also validate the model of the structure-supported transmission described by Eqs. (13) and (14). An observation of very small distances to the sources of wheezing with different frequencies of spectral maxima (Fig. 4) can be interpreted as the presence of permeability disorders of the respiratory tract in the same chest area. Depending on the constriction of respiratory ducts at different exhalation phases, these disorders cause variation of the frequen-

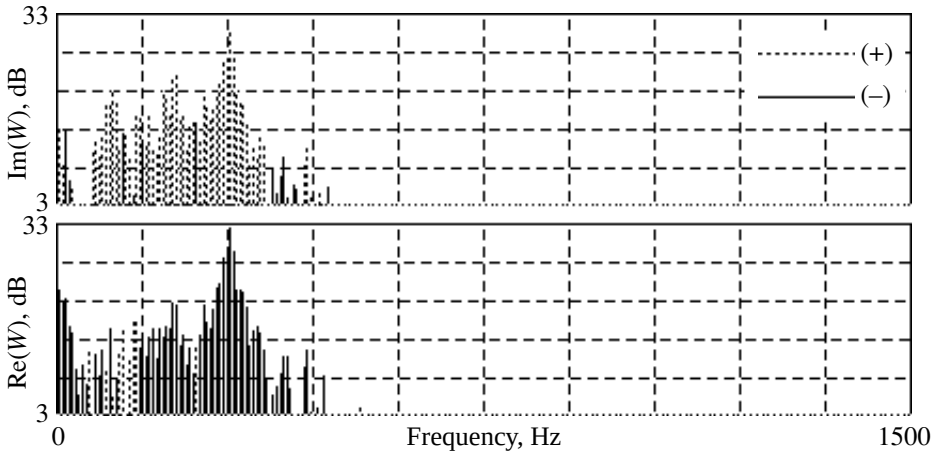

Fig. 5. Imaginary and real parts of the cross spectrum obtained for the responses of the CAT channels at exhalation over the lower zone of the lung (air-borne additional respiratory noise).

cies of the mechanical resonator due to a closure of the respiratory duct walls [28]. The latter effect may be an indication of a local pathological change caused by an inflammation process in the respiratory tract, as well as a deformation of the respiratory tract by adjacent pathologically changed areas of lung tissue. By the simultaneous or sequential calculation of the distance to the source of wheezing from several zones of the chest with the help of the difference distance-measurement methods, one can estimate the position of the source in the lung. Taking into account that different sources of wheezing are statistically independent, it is fundamentally possible to realize the emission acoustic tomography of these sources in the lungs by applying the narrowband spectral analysis. Of course, the verification of the proposed acoustic interpretations and the evaluation of the precision parameters require comprehensive clinical studies, but the fundamental diagnostic potentialities of the proposed approach seem to be rather promising.

Using the acoustic model developed above, let us consider the changes that may occur in the acoustic pattern of respiratory noise when air is replaced by heliox. Note that previous studies of the gas dependence of respiratory sounds [22–24] were performed with the use of the conventional procedure of respiratory sound detection, which did not allow one to judge the type of transmission. However, a certain comparison with the results of these studies is possible for the frequency characteristics of respiratory sounds.

The density of the gas mixture representing the heliox is $\rho_{he} \approx \rho_0/3.1$. The sound velocity in heliox [35] is $c_{he} \approx 1.9c_0$. Using formula (3), we obtain an expression for the resonance frequency of the acoustic resonant circuit in heliox: $f_{\text{arc}he} \approx 1.08 f_{\text{arc}^0}$, which means that the resonance of the acoustic resonant circuit is shifted only slightly. On the other hand, since the sound velocity in heliox is twice as high as in air, the quarter-wave resonance must be shifted from the region 215–350 Hz (in air) to the region 410–670 Hz (in heliox).

In accordance with the model described above, the dominant component of the basic respiratory noise at eupnea is the turbulent flow noise. The dynamic viscosities of air, oxygen, and helium are known to be close to each other. However, the Reynolds number involves the kinematic viscosity whose value in heliox is three times that in air. This fact underlies the conclusion [24] that the change from air to heliox must be accompanied by a change in the characteristics of the basic respiratory noise. However, the turbulent flow considered by us as the main source of the basic respiratory noise represents a motion with a fully developed turbulence [36]. It should be noted that, in the case under study, the fully developed turbulence is achieved not because of the large Reynolds numbers but mainly because of the turbulence of the oncoming flow, which is determined by the configuration of the bronchial tree [9]. For a fully developed turbulence, the parameters of the motion of the large-scale components (of the order of the diameter of the respiratory tract) responsible for the noise given by Eq. (1) are practically independent of the viscosity of the medium [36]. Hence, the spectral characteristics of noise produced in the bronchial tree should not noticeably deviate from those given in Table 1.

Table 2. Distances from the surface of the chest wall to the sources of wheezing

Figure number	Frequency of the spectral maximum, Hz	Distance, cm
Fig. 4a	540	7.5
Fig. 4a	710	8.1
Fig. 4b	345	8.0

Thus, according to the proposed acoustic model, no changes should be expected in the generation and transmission of respiratory noise in heliox, as compared to air, in the frequency region below approximately 200 Hz (the upper edge of the broadband frequency maxima corresponding to the resonance of the acoustic resonant circuit) in both lower and upper parts of lungs. In the parts located near the main bronchi and at the trachea, an attenuation of sounds with frequencies within 215–350 Hz should be observed along with an amplification of sounds within 410–670 Hz. In the lower parts of lungs, because of the filtering properties of the parenchyma [20], only the attenuation of sounds within 215–350 Hz should be observed. These conclusions are in qualitative agreement with most experimental observations described in the cited papers [22–24].

Summarizing the results of our study, we conclude that, using the method described in our previous publication [25] for measuring the respiratory noise at the chest wall, we experimentally revealed the frequency components characterized by different signs of the imaginary part of the cross spectrum obtained for the vibrational displacement and the dynamic force. The acoustic model developed on the basis of combining the results of earlier studies [19, 20, 28] explains the aforementioned difference from the point of view of the hypothesis that the contributions of both air-borne and structure-borne sound components are significant in the mechanism of sound transmission to the chest wall. In the framework of our approach, we made the following inferences:

(1) When considered as an acoustic channel for the basic respiratory noise, the respiratory system of an adult subject has two resonances: first, the resonance of the vibratory system formed by the elasticity of air in the respiratory ducts of lungs and by the surface mass density of the chest wall, this resonance lying within a frequency band of 110–150 Hz, and, second, the quarter-wave resonance of the whole bronchial tree as a system of narrow pipes, which occurs within 215–350 Hz.

(2) For adult subjects in normal condition, the frequency components responsible for the air-borne sound transmission in the basic respiratory noise predominate in the frequency region between 100 and 300 Hz in the lower parts of lungs, while the frequency components responsible for the structure-supported transmission predominate in the higher-frequency region.

(3) Vesicular noise (the sounds of vesicular respiration) observed in healthy adults at forced respiration is generated by the turbulent air flow in the 11th- through 13th-generation bronchi; its transmission to the chest wall in normal condition occurs mainly by air and is determined by the resonance of the vibratory system that is formed by the elasticity of air in the respiratory ducts of lungs and by the surface mass density of the chest wall.

(4) The distance from the chest wall to the sources of structure-borne additional respiratory noise, namely, wheezing with frequencies above 300 Hz, can be estimated numerically from the ratio between the real and imaginary parts of the cross spectrum of vibratory displacement and dynamic force for narrowband spectral components of these sounds on the assumption that the source is of the quadrupole type.

REFERENCES

1. R. T. H. Laenec, *De l'Auscultation Mediate* (Brosson and Chaude, Paris, 1819).
2. M. I. Rederman, Ter Arkh. **61** (4), 113 (1989).
3. N. I. Aleksandrova, A. G. Bobkov, N. A. Bogdanov, *et al.*, in *Respiration Disorders: Manual for Physicians*, Ed. by N. R. Paleev, Vol. 1: *General Pulmanology*, Ed. by N. V. Putov (Meditsina, Moscow, 1989), pp. 9–256.
4. P. Forgacs, Chest **73**, 399 (1978).
5. R. Loudon and R. L. Murphy, Am. Rev. Respir. Dis. **130**, 663 (1984).
6. F. Dalmay, M. T. Antonini, P. Marquet, and R. Menier, Eur. Respir. J., No. 8, 1761 (1995).
7. I. V. Vovk, V. T. Grinchenko, and V. N. Oleĭnik, Akust. Zh. **41**, 758 (1995) [Acoust. Phys. **41**, 667 (1995)].
8. H. Pastercamp, S. Kraman, and G. Wodicka, Am. J. Respir. Crit. Care Med. **156**, 974 (1997).
9. N. Gavriely and D. W. Cugell, J. Appl. Physiol. **80** (1), 5 (1996).
10. I. P. Zamotaev, N. A. Magazannik, L. A. Vodolazskiĭ, *et al.*, Klin. Med. (Moscow) **52** (5), 97 (1974).
11. V. A. McKusik, J. T. Jenkins, and G. N. Webb, Am. Rev. Tuberc. **72** (12), 34 (1955).
12. N. Gavriely, Y. Palti, and G. Alroy, J. Appl. Physiol. **50**, 307 (1981).
13. E. I. Likhacheva, in *Nonspecific Chronic Lung Diseases and Their Resort Treatment* (Kislovodsk, 1968), pp. 37–43.
14. I. V. Vovk, K. É. Zalutskiĭ, and L. G. Krasnyĭ, Akust. Zh. **40**, 762 (1994) [Acoust. Phys. **40**, 676 (1994)].
15. J. H. S. Beau, Arch. Gen. Med. **5**, 557 (1834).
16. S. S. Kraman, Lung **161**, 57 (1983).
17. K. Akasaka, K. Konno, Y. Ono, *et al.*, Tohoku J. Exp. Med. **117**, 323 (1975).
18. R. Beck, M. Odeh, A. Oliven, and N. Gavriely, Eur. Respir. J. **8** (12), 2120 (1995).
19. L. I. Nemerovskiĭ, *Pulmophonography* (Meditsina, Moscow, 1981), pp. 29–73.
20. G. Wodicka, K. Stevens, H. Golub, *et al.*, IEEE Trans. Biomed. Eng. **36**, 925 (1989).
21. G. Wodicka, K. Stevens, H. Golub, and D. Shannon, IEEE Trans. Biomed. Eng. **37**, 1130 (1990).
22. M. Mahagnah and N. Gavriely, J. Appl. Physiol. **78** (3), 928 (1995).
23. S. Patel, S. Lu, P. C. Doerschuk, and G. R. Wodicka, Med. Biol. Eng. Comput. **33** (4), 571 (1995).
24. H. Pasterkamp and I. Sanchez, Am. J. Respir. Crit. Care Med. **153** (3), 1087 (1996).
25. V. I. Korenbaum, A. A. Tagil'tsev, and Yu. V. Kulakov, Akust. Zh. **44**, 380 (1998) [Acoust. Phys. **44**, 322 (1998)].

26. V. V. Kryukov and K. I. Shakhgel'dyan, in *Proceedings of International Conference on Personal Computers in the Design and Study of Mechanisms and Aggregates* (St. Petersburg, 1996), p. 79.
27. V. I. Korenbaum, Ju. V. Kulakov, and A. A. Tagiltsev, Biomed. Instrum. Technol. **32** (2), 147 (1998).
28. V. I. Korenbaum, Yu. V. Kulakov, and A. A. Tagil'tsev, Akust. Zh. **43**, 78 (1997) [Acoust. Phys. **43**, 66 (1997)].
29. *Taschenbuch der Techischen Akustik*, Ed. by K. Heckl and H. A. Müller (Springer, Berlin, 1975; Sudostroenie, Leningrad, 1980).
30. M. A. Isakovich, *General Acoustics* (Nauka, Moscow, 1973), pp. 147–229.
31. *Physiology of Respiration*, Ed. by I. S. Breslav and G. G. Isaev (Nauka, St. Petersburg, 1994), pp. 7–120.
32. E. Skudrzyk, *The Foundations of Acoustics* (Springer, New York, 1971; Mir, Moscow, 1976), Vol. 2.
33. J. J. Fredberg and S. K. Holford, J. Acoust. Soc. Am. **73**, 1036 (1983).
34. V. I. Korenbaum, Yu. V. Kulakov, and A. A. Tagil'tsev, Fiziol. Cheloveka **23**, 133 (1997).
35. A. L. Prostakov and N. A. Stoptsov, *Electronics for Professional Divers and Sport Divers* (Sudostroenie, Leningrad, 1983), pp. 35–36.
36. L. D. Landau and E. M. Lifshitz, *Course of Theoretical Physics*, Vol. 6: *Fluid Mechanics* (Nauka, Moscow, 1986; Pergamon, New York, 1987).

Translated by E. Golyamina

Acoustical Physics, Vol. 49, No. 3, 2003, pp. 328–338. Translated from Akusticheskiĭ Zhurnal, Vol. 49, No. 3, 2003, pp. 389–399.

Energy Distribution between Seismic Waves of Different Types Produced in an Elastic Half-Space by a Source with an Arbitrary Radiation Pattern

G. A. Maximov, M. E. Merkulov, and V. Yu. Kudryavtsev

Moscow State Engineering Physics Institute (Technical University), Kashirskoe sh. 31, Moscow, 115409 Russia

e-mail: maximov@dpt39.mephi.ru

Received August 27, 2001

Abstract—The energy distribution between different types of seismic waves produced by a source of longitudinal and transverse waves with an arbitrary radiation pattern in an elastic half-space is considered. With an appropriate choice of the angular distribution functions, this source can model an earthquake source. A direct theoretical comparison of the energy distributions of seismic waves generated by an underground explosion and an earthquake is carried out. Analytical relationships that describe the dependence of the energy distribution between different types of waves on the parameters of the medium and the source are derived. © *2003 MAIK "Nauka/Interperiodica".*

In recent years, various methods of monitoring underground nuclear explosions (UNEs) have undergone extensive development. Of particular interest are the seismic methods. An important area of application of the seismic monitoring methods is discrimination between UNEs and other seismic sources, such as earthquakes and regular industrial explosions. The problem of discriminating between UNEs and industrial explosions has been studied in [1–4] and is not considered in this paper.

There are different methods for discriminating between earthquakes and UNEs, which use the characteristics of seismic signals observed at teleseismic and regional distances. One of the most used and efficient methods is the one based on the so-called magnitude criterion $m_b : M_S$, which represents the difference between the magnitudes of bulk P waves and surface waves produced by the same source [5–8]. The magnitude is understood as the logarithm of the wave amplitude-to-period ratio [5, 7, 9]. This method has a solid experimental basis, but its theoretical corroboration has not been completed. For this purpose, it is important to substantiate the criterion not only qualitatively but also quantitatively, because only in this case is it possible to predict the situations in which it becomes inoperative.

For heavy explosions or earthquakes (>10 kilotons), which are observed at teleseismic distances, the magnitude criterion is quite reliable. The analysis of experimental data [5, 8] and some theoretical results [7] show that the magnitude difference between the bulk and surface waves, $m_b - M_S$, for UNEs is greater than for earthquakes approximately by unity. However, for low-power sources (<2 kilotons), which can only be observed at regional distances, no reliable criteria exist [9]. This occurs, because the low-power sources produce waves of short wavelength, and it is therefore necessary to take into account the inhomogeneity of the earth's crust. The structure of the seismic fields becomes complex, consisting of bulk longitudinal and transverse waves along with surface and channel waves refracted by and reflected from the inhomogeneities. Therefore, a correct reconstruction of the parameters characterizing the seismic source is a very intricate and laborious problem. Difficulties associated with the magnitude description of the energy characteristics also refer to the bulk waves produced by earthquakes, whose seismic field strongly depends on a large number of parameters that determine the source's orientation in space and can be used efficiently only after averaging over many observation points. Also, a low-power source excites the fundamental mode of the earth less efficiently, so it may not be detected against other quasi-Rayleigh waves.

Although the magnitude criterion is a very convenient tool in experimental practice, its use in theoretical analysis encounters a number of problems associated with the insufficiently clear, from the physical viewpoint, definition of magnitude. In particular, in terms of the magnitude of the bulk or surface waves, the earthquake intensity is evaluated for a rather narrow frequency band, while the main part of the energy may be concentrated in another frequency range. This

1063-7710/03/4903-0328$24.00 © 2003 MAIK "Nauka/Interperiodica"

is why quantities are being sought that would take into account the source spectrum more adequately. In particular, the "energy" magnitude based on an estimate of the P wave energy, which is calculated by integrating the source function spectrum, has been proposed [10]. By all means, the magnitude criteria actually characterize the energy relationships. Therefore, it seems reasonable to perform theoretical analysis directly in terms of the energy characteristics, which have a clear physical meaning.

The energy distribution among various types of waves in an elastic half-space has been considered in a number of publications [11–15].

This paper continues the previous study [14] where this problem was considered for waves generated by a spherically or cylindrically symmetric source embedded in the elastic half-space. Here, we will study a point source of longitudinal or transverse waves with an arbitrary radiation pattern and, accordingly, the energy distribution between seismic waves of various types produced by such a source in the half-space. With an appropriate choice of the angular distribution functions, this source can be used as a model of an earthquake source. We perform a direct theoretical comparison of the energy distributions of seismic waves produced by an underground explosion and earthquake. We also derive analytical relationships that describe the dependence of the energy distribution between different types of waves on the parameters of the medium and the source.

1. ORIGINAL EQUATIONS

We define the energy carried by a wave as the energy flux transferred in the form of this wave within the whole emission time through a closed surface Σ enclosing the region where the wave is formed [12, 14]:

$$E^\alpha = \oint_\Sigma dSn_i \int_0^\infty dt q_i^\alpha(\mathbf{r}, t),$$

where $q_i^\alpha(\mathbf{r}, t) = V_j^\alpha(\mathbf{r}, t)\sigma_{ij}^\alpha(\mathbf{r}, t)$ is the energy flux density in the ith direction; $V_j^\alpha(\mathbf{r}, t)$ and $\sigma_{ij}^\alpha(\mathbf{r}, t)$ are the mass velocity and the stress tensor in the wave, respectively; the index α indicates that the quantity refers to the particular wave type; and n_i are the components of the vector orthogonal to the surface.

It is convenient to choose the surface Σ so that its normal coincides with the energy flux direction. For example, for bulk waves, this will be a spherical surface; for surface waves, a cylindrical one.

It should be noted that not all of the energy that is transferred through the surface Σ can be attributed to the wave. Part of it is spent for the static deformations in the medium. It has been shown that the expression for the energy carried by the wave is as follows [14]:

$$\begin{aligned} E^\alpha &= \oint_\Sigma dSn_i \frac{1}{2\pi}\int_{-\infty}^{\infty} d\omega \frac{i\omega}{2}\{u_j^\alpha(\mathbf{r}, \omega)\sigma_{ij}^\alpha(\mathbf{r}, -\omega) \\ &\quad - u_j^\alpha(\mathbf{r}, -\omega)\sigma_{ij}^\alpha(\mathbf{r}, \omega)\} \\ &= \oint_\Sigma dSn_i \frac{1}{2\pi}\int_{-\infty}^{\infty} d\omega i\omega \operatorname{Im}\{u_j^\alpha(\mathbf{r}, \omega)\sigma_{ij}^{\alpha *}(\mathbf{r}, \omega)\}, \end{aligned} \quad (1)$$

where $u_j^\alpha(\mathbf{r}, \omega)$ and $\sigma_{ij}^\alpha(\mathbf{r}, \omega)$ are the frequency spectra of the displacement vector and of the stress tensor. The energy of static deformations can be written as follows:

$$E_{st}^\alpha = \frac{1}{2}\oint_\Sigma dSn_i u_j^\alpha(\mathbf{r}, t = \infty)\sigma_{ij}^\alpha(\mathbf{r}, t = \infty).$$

Consider an embedded seismic point source placed a distance h from the surface of an isotropic elastic half-space. The source generates longitudinal elastic P waves and transverse S waves with respective radiation patterns.

Let us represent the wave field in terms of displacement potentials of the longitudinal waves, $\Phi(r, \varphi, z)$, and transverse waves, $\mathbf{\Psi}(r, \varphi, z)$:

$$\mathbf{u} = \operatorname{grad}\Phi + \operatorname{rot}\mathbf{\Psi}. \quad (2)$$

To find the wave fields, note that it is convenient to represent the S wave as a superposition of vertical and horizontal components, SV and SH. To this end, represent the potential $\mathbf{\Psi}$ of the transverse wave in the cylindrical coordinate system (r, φ, z) as a superposition of two vectors [16]:

$$\mathbf{\Psi} = \operatorname{rot}(0, 0, \Psi_{SV}) + (0, 0, \Psi_{SH}). \quad (3)$$

In this case, the displacement $\mathbf{u}_{SH} = \operatorname{rot}(0, 0, \Psi_{SH})$ will lie in the horizontal plane, which corresponds to the SH wave, and $\mathbf{u}_{SV} = \operatorname{rot}\operatorname{rot}(0, 0, \Psi_{SV})$ will correspond to the SV wave.

The system of wave equations for the potentials in the cylindrical coordinates is as follows:

$$\begin{cases} \Delta\Phi + \left(\dfrac{\omega}{c_l}\right)^2 \Phi = -\dfrac{Q_l(\omega)}{2\pi} f_l(\theta, \varphi)\delta(z-h)\dfrac{\delta(r)}{r} \\ \Delta\Psi_{SV} + \left(\dfrac{\omega}{c_s}\right)^2 \Psi_{SV} \\ = -\dfrac{Q_{SV}(\omega)}{2\pi}\dfrac{c_s}{\omega} f_{SV}(\theta, \varphi)\delta(z-h)\dfrac{\delta(r)}{r} \\ \Delta\Psi_{SH} + \left(\dfrac{\omega}{c_s}\right)^2 \Psi_{SH} \\ = -\dfrac{Q_{SH}(\omega)}{2\pi} f_{SH}(\theta, \varphi)\delta(z-h)\dfrac{\delta(r)}{r}, \end{cases} \tag{4}$$

where $f_l(\theta, \varphi)$, $f_{SV}(\theta, \varphi)$, and $f_{SH}(\theta, \varphi)$ are the patterns of the P, SV, and SH waves in spherical coordinates and $Q_\alpha(\omega)$ are their spectra. It should be noted that, due to relationship (3), for the functions $Q_{SV}(\omega)$ and $Q_{SH}(\omega)$ to have the same dimensionality, the special multiplier $Q_{SV}(\omega)$ is deliberately factored out from c_s/ω.

The boundary conditions that require the normal and tangential stress on the free surface of the half-space to be zero, $(\sigma_{zr}, \sigma_{z\varphi}, \sigma_{zz}) = (0, 0, 0)|_{z=0}$, lead to the following equations [16–18]:

$$\left.\begin{cases} 2\dfrac{\partial\Phi}{\partial z} + \dfrac{\partial^2\Psi_{SV}}{\partial z^2} - \Delta_{r\varphi}\Psi_{SV} = 0 \\ (2\mu+\lambda)\dfrac{\partial^2\Phi}{\partial z^2} - 2\mu\dfrac{\partial}{\partial z}(\Delta_{r\varphi}\Psi_{SV}) + \lambda\Delta_{r\varphi}\Phi = 0 \\ \dfrac{\partial^2\Psi_{SH}}{\partial\varphi\partial z} = 0. \end{cases}\right|_{z=0} \tag{5}$$

To find the fields, we will use the Fourier-series expansion in the angle φ in Eqs. (4) and (5), the Hankel transform in the epicentral distance ($r \longrightarrow s$), and the Laplace transform in the coordinate $z \longrightarrow \xi$ [19].

Finally, the potentials of the seismic waves in the half-space can be represented as

$$\Phi(r, z, \varphi, \omega) = \sum_{n=-\infty}^{\infty} e^{-in\varphi}\int_0^\infty r dr J_n(rs)\Phi_n(r, z, \omega)$$

with similar formulas for Ψ_{SV} and Ψ_{SH}, where

$$\begin{cases} \Phi(s, \varphi, z) = \dfrac{1}{2\pi}\sum_{n=-\infty}^{n=\infty} e^{in\varphi}\left[\dfrac{Q_l(\omega)}{2\pi}\dfrac{f_{ln}(s)}{2\nu_l}\right. \\ \times\left(e^{-|z-h|\nu_l} + \dfrac{D_+}{D_-}e^{-(z+h)\nu_l}\right) \\ \left. + \dfrac{Q_{SV}(\omega)}{2\pi}\dfrac{c_s}{\omega}\dfrac{f_{SVn}(s)}{2\nu_l}e^{-\nu_s h}e^{-\nu_l z}\dfrac{2s^2 - \left(\dfrac{\omega}{c_s}\right)^2}{\nu_s D_-}\right] \\ \Psi_{SV}(s, \varphi, z) \\ = \dfrac{1}{2\pi}\sum_{n=-\infty}^{n=\infty} e^{in\varphi}\left[\dfrac{Q_l(\omega)}{2\pi}\dfrac{f_{ln}(s)}{2\nu_s}e^{-\nu_l h}e^{-\nu_s z}\dfrac{2s^2 - \left(\dfrac{\omega}{c_s}\right)^2}{s^2\nu_l D_-}\right. \\ \left. + \dfrac{Q_{SV}(\omega)}{2\pi}\dfrac{c_s}{\omega}\dfrac{f_{SVn}(s)}{2\nu_s}\left(e^{-|z-h|\nu_s} + \dfrac{D_+}{D_-}e^{-(z+h)\nu_s}\right)\right] \\ \Psi_{SH}(s, \varphi, z) \\ = \dfrac{1}{2\pi}\sum_{n=-\infty}^{n=\infty} e^{in\varphi}\left[\dfrac{Q_{SH}(\omega)}{2\pi}\dfrac{f_{SHn}(s)}{2\nu_s}(e^{-|z-h|\nu_s} + e^{-(z+h)\nu_s})\right], \end{cases} \tag{6}$$

$\nu_l = \sqrt{s^2 - \left(\dfrac{\omega}{c_l}\right)^2}$, $\nu_s = \sqrt{s^2 - \left(\dfrac{\omega}{c_s}\right)^2}$, and $D_\pm = 1 \pm \dfrac{\left(2s^2 - \left(\dfrac{\omega}{c_s}\right)^2\right)^2}{4s^2\nu_s\nu_l}$ is the Rayleigh dispersion function.

As we see from (6), the expression for the potential of the longitudinal wave consists of the direct longitudinal P wave emitted by the source and of the longitudinal PP and SP waves reflected from the surface. A similar structure is observed in the potential of the transverse SV wave, which consists of the direct S wave produced by the source and of the reflected SS and PS waves. The potential of the SH wave consists of two terms: the direct and reflected SH waves.

At large distances from the source, the P and S waves are separated and, therefore, the energies they carry can be considered independently. To determine how much energy is emitted in the form of bulk longitudinal and transverse waves in the elastic half-space, consider the energy flux through a hemisphere of a large radius R. To this end, we change from the cylindrical to spherical coordinates, $(r, \varphi, z) \longrightarrow (R, \theta, \varphi)$.

2. ENERGY OF THE P WAVES

The displacement field of the longitudinal wave and its potential Φ are related as

$$\mathbf{u}^p = \operatorname{grad}\Phi = \frac{\partial\Phi}{\partial R}\mathbf{e}_R + \frac{1}{R}\frac{\partial\Phi}{\partial\theta}\mathbf{e}_\theta + \frac{1}{R\sin\theta}\frac{\partial\Phi}{\partial\varphi}\mathbf{e}_\varphi$$
$$= u_R^p\mathbf{e}_R + u_\theta^p\mathbf{e}_\theta + u_\varphi^p\mathbf{e}_\varphi.$$

Using asymptotic formulas for the Bessel functions for large arguments, the longitudinal potential can be written as

$$\Phi(r, \varphi, z, \omega) \xrightarrow[sr\to\infty]{} \frac{1}{2\pi}\sum_n e^{in\varphi}\frac{(-i)^n}{2}\int_{-\infty}^{\infty} ds|s|\sqrt{\frac{2}{\pi isr}}e^{isr}\Phi_n(s, 0, \omega)e^{-z\nu_l}. \quad (7)$$

Here, $\Phi_n(s, 0, \omega)$ is the value of the potential at the boundary of the half-space.

By taking a derivative of expression (7) with respect to R and retaining only the first-order terms in R, we obtain the radial component of the displacement

$$u_R^p = \frac{\partial}{\partial R}\Phi = \frac{1}{2\pi}\sum_n e^{in\varphi}\frac{(-i)^n}{2} \times \int_{-\infty}^{\infty} ds|s|\sqrt{\frac{2}{\pi isr}}\Phi_n(s, 0, \omega) \times e^{isR\sin\theta - \nu_l R\cos\theta}(is\sin\theta - \nu_l\cos\theta).$$

Assuming that R is a large parameter $\left(R\frac{\omega}{c_l} \gg 1\right)$, this integral can be estimated by the method of saddle points. It can be shown that the saddle point is at $s^* = -\frac{\omega}{c_l}\sin\omega$ and the radial component of the displacement is

$$u_R^p = \frac{1}{2\pi}\sum_n e^{in\varphi}(-i)^p\Phi_n\left(-\frac{\omega}{c_l}\sin\theta, 0, \omega\right) \times \frac{e^{-iR\frac{\omega}{c_l}}}{R}\frac{\omega}{c_l}\left|\frac{\omega}{c_l}\right|\cos\theta. \quad (8)$$

Using a similar technique to calculate the θ and φ components of the displacement, we can see that they have a higher order of smallness in R; i.e., in our approximation, $u_\theta^p \longrightarrow 0$ and $u_\varphi^p \longrightarrow 0$. Therefore, to calculate the energy of the P wave, it is sufficient to know only the radial component of the stress tensor

$$\sigma_{RR} = (\lambda + 2\mu)\frac{\partial u_R}{\partial R} + 2\lambda\frac{u_R}{R}. \quad (9)$$

Due to the symmetry of Eq. (1), the contribution of the second term in Eq. (9) is zero. In addition, in the chosen approximation, we have $\frac{\partial u_R^p}{\partial R} \longrightarrow -\frac{i\omega}{c_l}u_R$. Therefore, the energy of the P wave can be written as

$$E^P = \frac{\rho}{c_l^3}\frac{1}{2\pi}\int_{-\infty}^{\infty} d\omega\omega^6\int_0^{\pi/2} d\theta\cos^2\theta\sin\theta\frac{1}{2\pi} \times \sum_n \Phi_n(\omega)\Phi_{-n}(-\omega). \quad (10)$$

Next, let us evaluate the energy of the P wave emitted by the source into the half-space. From Eqs. (6), we determine the potential of the direct longitudinal wave at the boundary:

$$\Phi_n^P(s, \varphi, 0) = \frac{Q_l(\omega)}{2\pi}\frac{f_{ln}(s)}{2\nu_l}e^{h\nu_l}. \quad (11)$$

Then, by substituting Eq. (11) into Eq. (10), we obtain

$$E^P = \frac{\rho}{16\pi^3 c_l}\int_0^{\infty}\omega^4|Q_l(\omega)|^2 d\omega\int_0^{\pi/2}\sin\theta d\theta\int_0^{2\pi} f_l^2(\theta, \varphi)d\varphi. \quad (12)$$

The energy of the longitudinal PP and SP waves reflected from the surface can be obtained in a similar manner. The respective potentials are as follows:

$$\Phi_n^{PP}(s, \varphi, 0) = \frac{Q_l(\omega)}{2\pi}\frac{f_{ln}(s)}{2\nu_l}\frac{D_+}{D_-}e^{-h\nu_l}, \quad (13)$$

$$\Phi_n^{SP}(s, \varphi, 0) = \frac{Q_{SV}(\omega)}{2\pi}\frac{c_s}{\omega}\frac{f_{SVn}(s)}{2\nu_l}e^{-\nu_s h}\frac{2s^2 - \left(\frac{\omega}{c_s}\right)^2}{\nu_s D_-}. \quad (14)$$

By substituting Eqs. (13) and (14) into Eq. (10), we obtain the following expressions for the energy of the reflected longitudinal waves:

$$E^{PP} = \frac{\rho}{16\pi^3 c_l}\int_0^{\infty}\omega^4|Q_l(\omega)|^2 d\omega \times \int_0^{\pi/2}\left|\frac{\tilde{D}_+(\theta)}{\tilde{D}_-(\theta)}\right|^2\sin\theta d\theta\int_0^{2\pi} f_l^2(\theta, \varphi)d\varphi, \quad (15)$$

$$E^{SP} = \frac{\rho}{16\pi^3 c_s}\int_0^{\infty}\omega^4|Q_{SV}(\omega)|^2 d\omega \times \int_0^{\pi/2}\left|\frac{\cos 2\theta}{\tilde{\tilde{D}}_-(\theta)}\right|^2\frac{c_l}{c_s}\frac{\sin\theta}{\cos\theta\sqrt{1 - \left(\frac{c_l}{c_s}\right)^2\sin^2\theta}}d\theta\int_0^{2\pi} f_{SV}^2(\theta, \varphi)d\varphi, \quad (16)$$

where

$$\tilde{D}_{\pm}(\theta) = 1 \mp \left(\frac{c_l}{c_s}\right)^3 \frac{\left(1 - 2\left(\frac{c_s}{c_l}\right)^2 \sin^2\theta\right)^2}{4\sin^2\theta\cos\sqrt{1 - \left(\frac{c_s}{c_l}\right)^2 \sin^2\theta}},$$

$$\tilde{\tilde{D}}_{\pm}(\theta) = 1 \mp \left(\frac{c_l}{c_s}\right) \frac{(\cos 2\theta)^2}{4\sin^2\theta\cos\theta\sqrt{1 - \left(\frac{c_l}{c_s}\right)^2 \sin^2\theta}}.$$

Expressions (12) and (15) are written in terms of the P-wave angles, whereas expression (16) uses the angles of the transverse wave. These angles are related through the Snell's law:

$$\sin\theta_s = \frac{c_s}{c_l}\sin\theta_l.$$

3. ENERGY OF THE SV WAVES

Now, let us determine the energy of the transverse SV wave produced by the source. The vector potential of the SV wave in the cylindrical coordinates (r, φ, z) can be written as

$$\mathbf{\Psi}_{SV} = \mathrm{rot}(0, 0, \Psi_{SV}).$$

Changing to the spherical coordinates (R, φ, θ), we obtain

$$\mathbf{\Psi}_{SV} = \mathrm{rot}(\Psi_{SV}\cos\theta, 0, \Psi_{SV}\sin\theta).$$

We are interested in the field on a hemisphere of a large radius, for which we obtain that the displacement is primary determined by the orbital component, while the radial and azimuthal components have a higher order of smallness in R and, hence, can be set equal to zero:

$$\mathbf{u}_{SV} = \mathrm{rot}\,\mathbf{\Psi}_{SV} \approx -\sin\theta\frac{\partial^2}{\partial R^2}\Psi_{SV}\mathbf{e}_\theta.$$

By analogy with Eq. (7), we write

$$\Psi_{SV}(r, \varphi, z, \omega) \xrightarrow[sr\to\infty]{} \frac{1}{2\pi}\sum_n e^{in\varphi}\frac{(-i)^n}{2}\int_{-\infty}^{\infty} ds|s|\sqrt{\frac{2}{\pi isr}}e^{isr}\Psi_{SVn}(s, 0, \omega)e^{-zv_s}.$$

Then, the orbital displacement component is given by the expression

$$u_\theta^{SV} = -\sin\theta\frac{\partial^2}{\partial R^2}\Psi_{SV} = -i\frac{1}{2\pi}\sum_n e^{in\varphi}(-i)^n \times \Psi_{SVn}\left(-\frac{\omega}{c_s}\sin\theta, 0, \omega\right)\frac{e^{-iR\frac{\omega}{c_s}}}{R}\left|\frac{\omega}{c_s}\right|^3\cos\theta\sin\theta. \quad (17)$$

Since, in this case, the radial and azimuthal displacement components vanish, it is sufficient to know only the ($R\theta$) component of the stress tensor for calculating the energy of the SV wave:

$$\sigma_{R\theta} = \mu\left(\frac{\partial u_\theta}{\partial R} - \frac{u_\theta}{R}\right). \quad (18)$$

Due to the symmetry of Eq. (1), the contribution of the second term in Eq. (18) is zero, and, in our approximation, $\frac{\partial u_\theta^{SV}}{\partial R} \longrightarrow -\frac{i\omega}{c_s}u_\theta^{SV}$. This leads to the expression

$$E^{SV} = \frac{\rho}{c_s^5}\frac{1}{2\pi}\int_{-\infty}^{\infty} d\omega\omega^8\int_\theta d\theta\cos^2\theta\sin^3\theta\frac{1}{2\pi} \times \sum_n \Psi_n(\omega)\Psi_{-n}(-\omega). \quad (19)$$

Expressions for the energy carried by the direct and reflected bulk SV waves are obtained in the same way as those for the longitudinal waves:

$$E_{SV}^S = \frac{\rho}{16\pi^3 c_s}\int_0^\infty \omega^4|Q_{SV}(\omega)|^2 d\omega \times \int_0^{\pi/2}\sin^3\theta d\theta\int_0^{2\pi} f_{SV}(\theta, \varphi)^2 d\varphi, \quad (20)$$

$$E_{SV}^{SS} = \frac{\rho}{16\pi^3 c_s}\int_0^\infty \omega^4|Q_{SV}(\omega)|^2 d\omega \times \int_0^{\pi/2}\sin^3\theta\left|\frac{\tilde{\tilde{D}}_+(\theta)}{\tilde{\tilde{D}}_-(\theta)}\right|^2 d\theta\int_0^{2\pi} f_{SV}(\theta, \varphi)^2 d\varphi, \quad (21)$$

$$E_{SV}^{PS} = \frac{\rho}{16\pi^3 c_l}\left(\frac{c_l}{c_s}\right)^3\int_0^\infty \omega^4|Q_l(\omega)|^2 d\omega \times \int_0^{\pi/2}\sin\theta\frac{\cos\theta}{\sqrt{1 - \left(\frac{c_s}{c_l}\right)^2\sin^2\theta}}\left|\frac{1 - 2\left(\frac{c_s}{c_l}\right)^2\sin^2\theta}{\tilde{D}_-(\theta)\sin\theta\cos\theta}\right|^2 d\theta \times \int_0^{2\pi} f_l(\theta, \varphi)^2 d\varphi. \quad (22)$$

Expressions (20) and (21) are written in terms of the transverse wave angles, whereas expression (22) uses the angles of the longitudinal wave.

Using Eqs. (12), (15), (16), and (20)–(22), one can show that $E^P = E^{PP} + E^{PS}$ and $E^{SS}_{SV} = E^{SS}_{SV} + E^{SP}_{SV}$.

4. ENERGY OF THE SH WAVES

The energy of the direct and reflected SH waves can be determined in a similar manner. Since the transverse SH wave, being reflected from the interface, does not transform into other wave types, the energy of the direct wave emitted by the source towards the interface is equal to the energy of the reflected SH wave. Therefore, it is sufficient to find only the energy of the SH wave produced by the source.

The vector potential of the SH wave in the cylindrical coordinates is

$$\mathbf{\Psi}_{SH} = (0, 0, \Psi_{SH}).$$

In the spherical coordinates,

$$\mathbf{\Psi}_{SH} = (\Psi_{SH}\cos\theta, 0, \Psi_{SH}\sin\theta).$$

At large distances from the source, the azimuthal displacement component predominates:

$$\mathbf{u}_{SH} = \mathrm{rot}\,\mathbf{\Psi}_{SH} \approx \sin\theta\frac{\partial}{\partial R}\Psi_{SH}\mathbf{e}_\varphi. \tag{23}$$

Therefore, the stress tensor component of interest ($R\varphi$) is

$$\sigma_{R\varphi} = \mu\frac{\partial u_\varphi}{\partial R}.$$

Following the same procedure as with the P waves and SV waves, we obtain the expression for the energy of the SH wave:

$$E^S_{SH} = E^{SS}_{SH} = \frac{\rho}{16\pi^3 c_s}\int_0^\infty \omega^4 |Q_{SH}(\omega)|^2 d\omega \int_0^{\pi/2} \sin^3\theta d\theta \int_0^{2\pi} f_{SH}(\theta, \varphi)^2 d\varphi. \tag{24}$$

5. ENERGY OF THE RAYLEIGH WAVES

The Rayleigh wave generated by a point source is a cylindrical wave. Therefore, it is convenient to use the cylindrical coordinates for calculating its energy flux.

The Rayleigh wave corresponds to a pole of the integrands in Eqs. (6). It can easily be seen that the potential of the SH wave and the terms in the potentials of the P and SV waves that are associated with the direct waves have no poles. Therefore, they do not contribute to the Rayleigh wave.

With Eqs. (2) and (3) taken into account, the relation between the components of the displacement vector and the stress tensor, on the one hand, and the potentials of the longitudinal and transverse waves Φ and Ψ_{SV}, on the other hand, becomes as follows:

$$\begin{cases} u_r(r, \varphi, z, \omega) = \dfrac{\partial\Phi}{\partial r} + \dfrac{\partial^2\Psi_{SV}}{\partial z\partial r} \\ u_\varphi(r, \varphi, z, \omega) = \dfrac{1}{r}\dfrac{\partial\Phi}{\partial\varphi} + \dfrac{1}{r}\dfrac{\partial^2\Psi_{SV}}{\partial z\partial\varphi} \xrightarrow[sr\to\infty]{} 0 \\ u_z(r, \varphi, z, \omega) = \dfrac{\partial}{\partial z}\Phi - \Delta_{r\varphi}\Psi_{SV}, \end{cases} \tag{25}$$

$$\begin{cases} \sigma_{rr} = 2\mu u_{rr} + \lambda\,\mathrm{div}\,\mathbf{u} = 2\mu\left(\dfrac{\partial^2\Phi}{\partial r^2} + \dfrac{\partial^3\Psi_{SV}}{\partial z\partial r^2}\right) + \lambda\Delta\Phi \\ \sigma_{r\varphi} = \mu\left(\dfrac{\partial u_\varphi}{\partial r} - \dfrac{u_\varphi}{r} + \dfrac{1}{r}\dfrac{\partial u_r}{\partial\varphi}\right) \xrightarrow[sr\to\infty]{} 0 \\ \sigma_{rz} = \mu\left(\dfrac{\partial u_r}{\partial z} + \dfrac{\partial u_z}{\partial r}\right) \\ = \mu\left(2\dfrac{\partial^2\Phi}{\partial r\partial z} + \dfrac{\partial^3\Psi_{SV}}{\partial z^2\partial r} - \dfrac{\partial}{\partial r}(\Delta_{r\varphi}\Psi_{SV})\right). \end{cases} \tag{26}$$

By applying the Fourier transform in the azimuthal angle and the Hankel transform in the epicentral distance, Eqs. (25) and (26) can be represented as

$$\begin{cases} u_z(r, \varphi, z, \omega) = \dfrac{1}{2\pi}\sum_n e^{in\varphi}\dfrac{1}{2}\int_{-\infty}^{\infty} ds|s| H^{(1)}_n(sr) \\ \times[-\nu_l\Phi_n(s, z, \omega) + s^2\Psi_{SVn}(s, z, \omega)] \\ u_r(r, \varphi, z, \omega) = \dfrac{1}{2\pi}\sum_n e^{in\varphi}\dfrac{1}{2}\int_{-\infty}^{\infty} ds|s| H^{(1)}_{n+1}(sr) \\ \times[-s\Phi_n(s, z, \omega) + s\nu_s\Psi_{SVn}(s, z, \omega)] \\ \sigma_{rz} = \dfrac{\mu}{2\pi}\sum_n e^{in\varphi}\dfrac{1}{2}\int_{-\infty}^{\infty} ds|s| H^{(1)}_{n+1}(sr) \\ \times[2s\nu_l\Phi_n - s\Psi_{SVn}(2\nu_s^2 + (\omega/c_s)^2)] \\ \sigma_{rr} = \dfrac{\mu}{2\pi}\sum_n e^{in\varphi}\dfrac{1}{2}\int_{-\infty}^{\infty} ds|s| H^{(1)}_n(sr) \\ \times[-\Phi_n(2\nu_l^2 + (\omega/c_s)^2) + 2s^2\nu_s\Psi_{SVn}]. \end{cases} \tag{27}$$

When deriving system (27), we implied that the radius of the surface Σ is much longer that the wavelength. The Rayleigh dispersion relation has the form $D_-(s, \omega) = 0$, which is equivalent to the equation

$$4s^2\nu_s\nu_l - (2s^2 - (\omega/c_s)^2)^2 = 0.$$

A root of this equation can be represented as $s_R = \frac{\omega}{c_R}$, where c_R is the velocity of the Rayleigh wave. By virtue of the residue theorem, system (27) can be reduced to

$$\begin{cases} u_z^{Rj} = \sum_n e^{in\varphi}\frac{i}{2}|s_R|H_n^{(1)}(s_j r)[-|s_R|\nu_l^R\tilde{\Phi}_n + s_R^2\tilde{\Psi}_{SVn}] \\ u_r^{Rj} = \sum_n e^{in\varphi}\frac{i}{2}|s_R|H_{n+1}^{(1)}(s_R r)[s_{Rj}\tilde{\Phi}_n + s_R|s_R|\nu_s^R\tilde{\Psi}_{SVn}] \\ \sigma_{rz}^{Rj} = \sum_n e^{in\varphi}\frac{\mu i}{2}|s_R|H_{n+1}^{(1)}(s_R r) \\ \times\left[2s_R|s_R|\nu_l^R\tilde{\Phi}_n - s_R^3\left(2\nu_s^R + \frac{c_R^2}{c_s^2}\right)\tilde{\Psi}_{SVn}\right] \\ \sigma_{rr}^{Rj} = \sum_n e^{in\varphi}\frac{\mu i}{2}|s_R|H_n^{(1)}(s_R r) \\ \times\left[-s_R^2\left(2\nu_l^R + \frac{c_R^2}{c_s^2}\right)\tilde{\Phi}_n + 2s_R^2|s_R|\nu_s^R\tilde{\Psi}_{SVn}\right], \end{cases}$$

where $\tilde{\Phi} = \operatorname{res}_{s=s_R}\Phi(s, z, \omega)$; $\tilde{\Psi} = \operatorname{res}_{s=s_R}\Psi(s, z, \omega)$, and

$$\nu_l^R = \sqrt{1-\left(\frac{c_R}{c_l}\right)^2}, \quad \nu_s^R = \sqrt{1-\left(\frac{c_R}{c_s}\right)^2}.$$

By substituting the expressions for the residues and integrating with respect to the vertical coordinate z, the following expression for the Rayleigh wave energy is obtained:

$$\begin{aligned} E^R = \frac{\rho}{16\pi^2 c_R}\int_0^\infty d\omega\omega^4\int_0^{2\pi} d\varphi[B_1|f_l|^2|Q_l|^2 e^{-2|s_R|\nu_l^R h} \\ + B_2|f_{SV}|^2|Q_{SV}|^2 e^{-2|s_R|\nu_s^R h} \\ + B_3\mathrm{Re}(f_l f_{SV}^* Q_l Q_{SV}^*)e^{-|s_R|(\nu_l^R+\nu_s^R)h}]. \end{aligned} \tag{28}$$

Here, the coefficients B_i are given by the expressions

$$B_1 = \left(\frac{c_s}{c_R}\right)^2\frac{1}{(\nu_l^R d_-)^2}\left[\frac{1}{\nu_l^R}\alpha_l + \frac{1}{\nu_s^R}\alpha_s\frac{\nu_l^R}{\nu_s^R} - \gamma\beta_s\right],$$

$$B_2 = \left(\frac{c_s}{c_R}\right)^4\frac{1}{(\nu_s^R d_-)^2}\left[\frac{1}{\nu_l^R}\alpha_l\frac{\nu_s^R}{\nu_l^R} + \frac{1}{\nu_s^R}\alpha_s - \gamma\beta_l\right],$$

$$B_3 = \left(\frac{c_s}{c_R}\right)^3\frac{1}{\nu_l^R\nu_s^R(d_-)^2}2\mathrm{Re}\left[\frac{1}{\nu_l^R}\alpha_l\beta_l + \frac{1}{\nu_s^R}\alpha_s\beta_s - \gamma\right],$$

where

$$d_- = \frac{2+(c_R/c_s)^2}{2-(c_R/c_s)^2} - \frac{1}{2}\left(\frac{1}{\nu_{lR}^2} + \frac{1}{\nu_{sR}^2}\right),$$

$$\alpha_l = 4(\nu_l^R)^2 + \frac{c_R^2}{c_s^2}, \quad \alpha_s = 4(\nu_s^R)^2 + \frac{c_R^2}{c_s^2},$$

$$\beta_l = \frac{(2-c_R^2/c_s^2)}{2\nu_l^R}, \quad \beta_s = \frac{(2-c_R^2/c_s^2)}{2\nu_s^R},$$

$$\gamma = \frac{2(\nu_s^R 2 - 2(\nu_l^R)^2 + \alpha_l) + \nu_l^R(2-2(\nu_s^R)^2 + \alpha_s)}{\nu_l^R + \nu_s^R}.$$

It can easily be seen that, at $f_{SV} = 0$ and $f_l = 1$, expression (28) is reduced to the formula for the energy of the Rayleigh wave produced by an isotropic point source of P waves in the half-space [14].

6. DISTRIBUTION OF THE SEISMIC ENERGY PRODUCED BY AN EARTHQUAKE

Thus far, in our calculations, we have not specified the source functions that appear on the right sides of Eqs. (4). Now, we will try to define them in such a manner that the displacements in the longitudinal and transverse waves produced by the point source in the far-field region coincide with the respective displacements produced by a shear crack source. This model provides a fairly complete characterization of the processes accompanying the propagation of waves generated by a real seismic earthquake source.

The most wide-spread view of the earthquake source is that it has the form of a surface on which shear displacements evolve (a discontinuity plane) [16]. Given a shear discontinuity on the discontinuity plane Σ, displacements at any point of the medium can be calculated. For the sake of simplicity, assume that the direction of the displacement jump is constant over the discontinuity plane and is determined by the vector $\mathbf{\nu}$:

$$U_j(\boldsymbol{\xi}, t) = \nu_j\Delta U(\boldsymbol{\xi}, t).$$

In this case, the frequency-domain representation of the displacement in the far-field region is as follows:

$$\begin{cases} U_P(\omega) = \frac{2n_\gamma\nu_\gamma}{4\pi c_l R}S_{\text{eff}}i\omega\left(\frac{c_s}{c_l}\right)^2\Delta u(\omega)e^{-\frac{i\omega R}{c_l}} \\ U_{SV}(\omega) = \frac{[\nu_{SV}n_\gamma + \nu_\gamma n_{SV}]}{4\pi c_s R}S_{\text{eff}}i\omega\Delta u(\omega)e^{-\frac{i\omega R}{c_s}} \\ U_{SH}(\omega) = \frac{[\nu_{SH}n_\gamma + \nu_\gamma n_{SH}]}{4\pi c_s R}S_{\text{eff}}i\omega\Delta u(\omega)e^{-\frac{i\omega R}{c_s}}. \end{cases} \tag{29}$$

Here, $\boldsymbol{\gamma}$ is the unit radius vector, $\mathbf{n}$ is the vector orthogonal to the discontinuity plane,

$\nu_{SV} = (\mathbf{\nu e}_\theta)$, $\nu_{SH} = (\mathbf{\nu e}_\varphi)$, and $\nu_\gamma = \mathbf{\nu\gamma} \equiv (\mathbf{\nu e}_R)$.

Displacements for the direct bulk waves, which follow from Eqs. (8), (17), and (23) after the potential at the interface is substituted in them, acquire the following form:

$$u_R^P = F_l(\varphi, \theta, \omega) e^{i\frac{\omega h}{c_l}\cos\theta} \frac{Q_l(\omega)}{4\pi} \frac{e^{-iR\frac{\omega}{c_l}}}{R} \frac{i\omega}{c_l}, \quad (30)$$

$$u_\theta^{SV} = F_{SV}(\varphi, \theta, \omega)\sin\theta \frac{e^{-iR\frac{\omega}{c_s}}}{R} \frac{Q_{SV}(\omega)}{4\pi} \frac{\omega}{c_s} e^{i\frac{\omega h}{c_s}\cos\theta}, \quad (31)$$

$$u_\varphi^{SH} = F_{SH}(\varphi, \theta, \omega)\sin\theta \frac{e^{-iR\frac{\omega}{c_s}}}{R} \frac{Q_{SH}(\omega)}{4\pi} \frac{i\omega}{c_s} e^{i\frac{\omega h}{c_s}\cos\theta}, \quad (32)$$

where

$$F_l(\varphi, \theta, \omega) = -\frac{1}{2\pi}\sum_n e^{in\varphi}(-i)^n f_{ln}(\theta, \omega),$$

$$F_{SV}(\varphi, \theta, \omega) = -\frac{1}{2\pi}\sum_n e^{in\varphi}(-i)^n f_{SVn}(\theta, \omega),$$

and $F_{SH}(\varphi, \theta, \omega)$ is analogous to $F_{SV}(\varphi, \theta, \omega)$.

The comparison of Eqs. (30) with Eqs. (31)–(32) shows that they are equivalent when the following conditions are met:

$$\begin{cases} Q_{SH}(\omega) = S_{\text{eff}}\Delta u(\omega) \\ Q_{SV}(\omega) = iS_{\text{eff}}\Delta u(\omega) \\ Q_l(\omega) = \left(\frac{c_s}{c_l}\right)^2 S_{\text{eff}}\Delta u(\omega), \end{cases} \quad (33)$$

$$\begin{cases} F_l(\varphi, \theta, \omega) = 2n_\gamma \nu_\gamma \\ F_{SV}(\varphi, \theta, \omega) = (\nu_{SV} n_\gamma + \nu_\gamma n_{SV})/\sin\theta \\ F_{SH}(\varphi, \theta, \omega) = (\nu_{SH} n_\gamma + \nu_\gamma n_{SH})/\sin\theta. \end{cases} \quad (34)$$

In these expressions, the factors like $\exp\left(i\frac{\omega h}{c}\cos\theta\right)$ are deliberately omitted, because they account for the fact that, in our coordinate system, the source is located at $z = h$ rather than at $z = 0$.

To render the angular distribution functions concrete, let us choose the coordinate system such that the vector **n** lies in the *zy* plane and introduce the χ and Ω angles as follows: χ is the angle between the vector **n** and the *z* axis and Ω is the angle between the vector **ν** and the *zy* plane (Fig. 1). In this case, the vectors **n** and **ν** can be written in terms of $\boldsymbol{\gamma}$, $\mathbf{e}_\theta$, and $\mathbf{e}_\varphi$ as

$$\begin{cases} \mathbf{n} = \boldsymbol{\gamma}[\sin\chi\sin\theta\cos\varphi + \cos\chi\cos\theta] \\ -\mathbf{e}_\theta[\sin\chi\cos\theta\cos\varphi - \cos\chi\sin\theta] + \mathbf{e}_\varphi\sin\chi\sin\varphi \\ \boldsymbol{\nu} = \boldsymbol{\gamma}[\cos\Omega\cos\chi\sin\theta\cos\varphi + \sin\Omega\sin\theta\sin\varphi \\ -\cos\Omega\sin\chi\cos\theta] - \mathbf{e}_\theta[\cos\Omega\cos\chi\cos\theta\cos\varphi \\ +\sin\Omega\cos\theta\sin\varphi + \cos\Omega\sin\chi\sin\theta] \\ +\mathbf{e}_\varphi[\cos\Omega\cos\chi\sin\varphi - \sin\Omega\cos\varphi]. \end{cases} \quad (35)$$

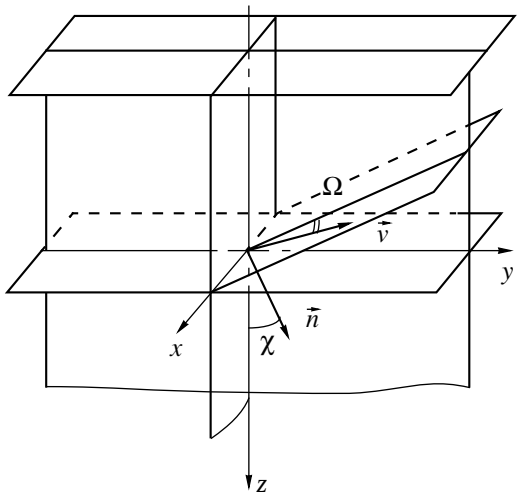

Fig. 1. Coordinate system and the angles Ω and χ.

By substituting Eqs. (35) into Eqs. (34), the radiation pattern can be expressed in terms of the angles φ, θ, χ, and Ω. We also note that expressions (10), (19), and (24) for the energies contain only quadratic forms of displacements integrated over the azimuthal angle. Taking into account that $\int_0^{2\pi} F_\alpha(\varphi, \omega)F_\beta(\varphi, -\omega)d\varphi = \int_0^{2\pi} f_\alpha(\varphi, \omega)f_\beta(\varphi, -\omega)d\varphi$, the following expression for the energy of the direct longitudinal wave is obtained:

$$E^P = \frac{\rho}{16\pi^3 c_l}\int_0^\infty \omega^4 |Q_l(\omega)|^2 d\omega \left[\frac{8}{15}\pi\right].$$

This means that the energy of the emitted P wave is independent of the source orientation in space.

Expressions for the energies of the SV and SH waves in terms of the S-wave angles are as follows:

$$E_{SV}^S = \frac{\rho}{16\pi^3 c_s}\int_0^\infty \omega^4 |Q_{SV}(\omega)|^2 d\omega$$

$$\times\left[\frac{1}{3}\pi\left(\cos^2\chi - \cos 2\chi\cos^2\chi\cos^2\Omega + \cos^2\Omega + \frac{2}{5}\right)\right],$$

$$E_{SH}^S = \frac{\rho}{16\pi^3 c_s}\int_0^\infty \omega^4 |Q_{SH}(\omega)|^2 d\omega$$

$$\times\left[\frac{1}{3}\pi(2 - \cos^2\chi + \cos 2\chi\cos^2\chi\cos^2\Omega - \cos^2\Omega)\right].$$

Due to Eqs. (33), we find that the energy of the S wave is also independent of the angles χ and Ω and is given by the expression

$$E^S = \frac{\rho}{16\pi^3 c_s}\int_0^\infty \omega^4 |Q_{SH}(\omega)|^2 d\omega \left[\frac{4}{5}\pi\right].$$

Let us take a particular spectral function of the source in Eqs. (36). Let it be

$$\Delta u(\omega) = \frac{U_0}{i\omega(1+i\omega\tau)^2}, \quad (36)$$

where τ is the characteristic radiation time and U_0 is the maximal displacement on the elastic radius. Such a function has been used for estimating an explosion [14]. This function is chosen, because explosions and earthquakes with similar spectral functions are most difficult to discriminate, and also in view of our attempt to formulate a discrimination criterion based on the difference in the angular distribution functions. Thus, for spectral function (36), we obtain

$$E^P = \frac{\rho}{8\pi c_l \tau^3}\frac{(S_{\text{eff}}U_0)^2}{15}\left(\frac{c_s}{c_l}\right)^4,$$

$$E^S = \frac{\rho}{16\pi c_s \tau^3}\frac{(S_{\text{eff}}U_0)^2}{5}.$$

To calculate the integrals with respect to frequency for the Rayleigh wave, we use the embedded source approximation: $h \gg (c_R\tau)/2\nu_s^R$. In this case, due to the rapid decay of the exponential, the low-frequency asymptotics of the source function makes the dominant contribution to the integral. Then, expression (28) is reduced to

$$E^R = \frac{\rho(S_{\text{eff}}U_0)^2}{16\pi^2 c_R}\frac{c_R^3}{4h^3}\int_0^{2\pi} d\varphi \left[B_1|f_l|^2\left(\frac{c_s}{c_l}\right)^4\frac{1}{(\nu_l^R)^3}\right.$$

$$\left. + B_2|f_{SV}|^2\frac{1}{(\nu_s^R)^3} - B_3\left(\frac{c_s}{c_l}\right)^2\frac{8\,\text{Re}(I^* f_l f_{SV}^*)}{(\nu_l^R+\nu_s^R)^3}\right].$$

The three terms in the brackets above are the contributions to the Rayleigh wave made by the longitudinal waves, transverse waves, and interference of these, respectively. Omitting the interference term, the bulk-to-surface wave energy ratio can be written as

$$E^R/E^P = \frac{15(c_l\tau)^3}{8\pi h^3}\left(\frac{c_R}{c_l}\right)^2$$

$$\times\left[B_1\frac{1}{(\nu_l^R)^3}\int_0^{2\pi}|f_l|^2 d\varphi + B_2\left(\frac{c_l}{c_s}\right)^4\frac{1}{(\nu_s^R)^3}\int_0^{2\pi}|f_{SV}|^2 d\varphi\right]. \quad (37)$$

Relationship (37) allows us to calculate $\log E^P$ as a function of $\log E^R$, which is similar to the regression relationship $m_b : M_S$. Taking a logarithm of this expression, we obtain

$$\log E^P = \log E^R + A(\sigma, \Omega, \chi) + B(\sigma^*) + C(h),$$

where

$$A(\sigma, \Omega, \chi) = 2\log\left(\frac{c_l}{c_s}\right) - \log\left(\frac{15}{8\pi}\left(\frac{c_R}{c_s}\right)^2\right.$$

$$\left.\times\left[B_1\frac{1}{(\nu_l^R)^3}\int_0^{2\pi}|f_l|^2 d\varphi + B_2\left(\frac{c_l}{c_s}\right)^4\frac{1}{(\nu_s^R)^3}\int_0^{2\pi}|f_{SV}|^2 d\varphi\right]\right);$$

$$B(\sigma^*) = 3\log\left(\frac{h^*}{c_l\tau}\right); \quad C(h) = 3\log\left(\frac{h}{h^*}\right).$$

The term $A(\sigma, \Omega, \chi)$ here is only determined by the orientation of the shear crack and by Poisson's ratio of the medium (or by the velocity ratio of the longitudinal and transverse waves) at the earthquake site. The term $B(\sigma^*)$ is a logarithm of the ratio of the reduced depth h^* to the emitted wavelength $c_l\tau$. It is independent of the earthquake intensity and is primarily determined by the strength of the medium, σ^*, at the place where the earthquake occurred. The last term, $C(h)$, characterizes the effect of the deviation of the real depth from the reduced one.

For an explosive source, a similar relationship was obtained in [14]. It differs from the relationship presented above by the term $A_{EXPL}(\sigma)$:

$$A_{EXPL}(\sigma) = 2\log\left(\frac{c_l}{c_s}\right) - \log\left(\frac{B_1}{2(\nu_l^R)^3}\left(\frac{c_R}{c_s}\right)^2\right).$$

Figure 2 shows ratio (37) versus the angles Ω and χ, which determine the crack orientation and the direction of the shear.

As we see from Fig. 2, the energy of the Rayleigh waves can vary over a sufficiently wide range, depending on the crack orientation and the direction of the shear.

Figure 3 presents $\log E^P$ versus $\log E^R$ for explosions and earthquakes in a medium with Poisson's ratio $\sigma = 0.2$, all other parameters being the same. The energy is measured in kilotons. Note that, since the energy of the seismic waves is but a few percent of the explosion energy, the variation in $\log E^P$ in Fig. 3 from –2 to 0 corresponds to an explosive force of 1 to 100 kt, which corresponds to a bulk wave magnitude m_b of 4 to 6 units. The "Earthquakes" region refers to earthquakes whose depth is equal to the explosion depth; the "Deep

Earthquakes" region, to the earthquakes that are three times as deep.

The boundaries of the earthquake region are determined by the maximal and minimal energy of the Rayleigh wave, depending on the orientation of the shear crack. As we see in Fig. 3, at the same depth, the explosion line and the earthquake region are about two units apart. Since even shallow-focus earthquakes occur at greater depths than UNEs, due to the $C(h)$ term in the expression obtained above for $\log E^P$, the earthquake region in Fig. 3 will move toward the UNE region. Thus, at depths about three times as deep as the those of the UNEs, these regions will be displaced with respect to each other by unity, as shown in Fig. 3.

To compare our results with experimental data, we include Fig. 4 borrowed from Marshall and Basham [6]. It presents an experimental distribution of $m_b : M_S$ for UNEs and earthquakes observed in central Eurasia. The comparison between Figs. 3 and 4 visually indicates that the energy function $\log E^P : \log E^R$ quite adequately follows the magnitude criterion $m_b : M_S$.

Thus, we have studied the energy distribution between different seismic waves produced by an embedded source of P and S waves with an arbitrary radiation pattern in an elastic half-space.

Explicit formulas are obtained for the energies of the emitted (direct and reflected) longitudinal and transverse bulk waves and the Rayleigh wave. The spectral and angular source functions being chosen appropriately, these results may correspond to an explosive source or earthquake source.

The energy relationships between different types of seismic waves produced by UNEs and earthquakes in an elastic half-space are used to construct the functions $\log E^P : \log E^R$, which are similar to the magnitude ratio $m_b : M_S$. Explosions and earthquakes of the same spectral distribution and with equal seismic moments were found to differ by two magnitude units. This is a large margin for discriminating between them, even when the earthquakes occur at greater depths than the explosions. It is also shown that the energy of the surface Rayleigh waves produced by earthquakes strongly depends on the crack orientation and the direction of the shear.

Note that the solution to the problem of energy distribution in a homogeneous half-space should only be regarded as the first necessary step in solving the real problem of discriminating between UNEs and low-intensity earthquakes, because, in a homogeneous half-space, no higher-order surface quasi-Rayleigh and Love waves are excited. At the same time, these modes of surface waves predominate at regional distances. These are the so-called Log waves. For these waves to occur, the presence of a stratified structure consisting of at least one stratum is necessary.

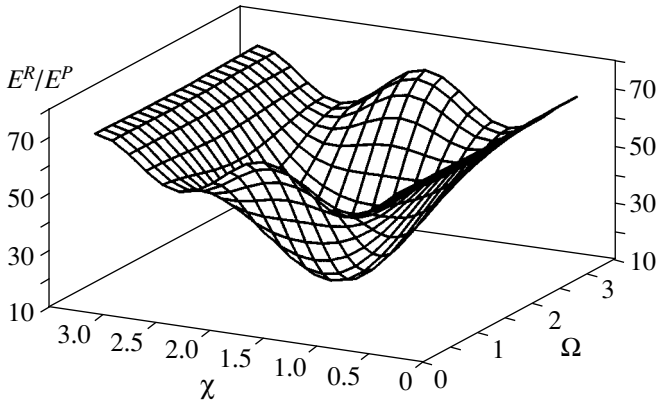

Fig. 2. Ratio E^R/E^P as a function of the orientation of the shear crack and of the direction of the shear.

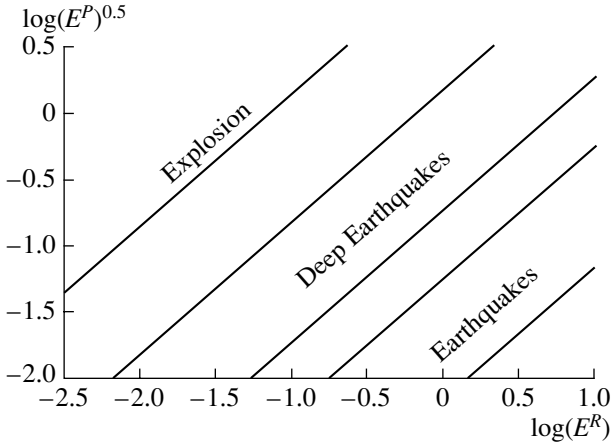

Fig. 3. Dependence of $\log E^P$ on $\log E^R$ for explosions and earthquakes in a medium with Poisson's ratio $\sigma = 0.2$. The "Earthquakes" region refers to earthquakes whose depth is equal to that of explosions; the "Deep Earthquakes" region, to earthquakes three times as deep.

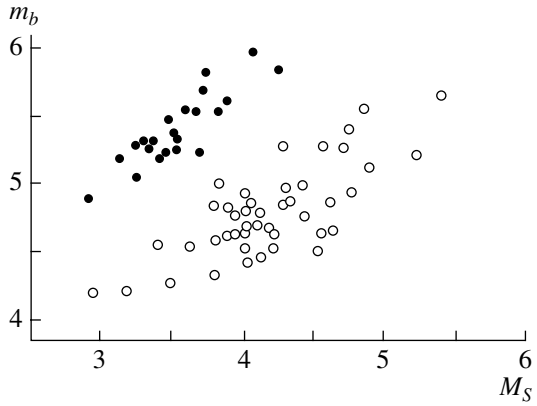

Fig. 4. Experimental distribution of m_b versus M_S for UNEs (the full dots) and earthquakes (the empty dots) observed in central Eurasia (following [6]).

In our opinion, the next step in this direction will be the solution to the problem of the energy distribution produced by a source with an arbitrary radiation pattern in a stratified elastic medium.

REFERENCES

1. A. T. Smith, Bull. Seismol. Soc. Am. **79**, 1089 (1989).
2. D. B. Harris and G. A. Clark, Bull. Seismol. Soc. Am. **70**, 2037 (1990).
3. M. A. H. Hedlin, J. B. Minster, and J. A. Orcutt, Bull. Seismol. Soc. Am. **80B**, 2143 (1990).
4. A. T. Smith, Bull. Seismol. Soc. Am. **83**, 160 (1993).
5. I. P. Pasechnik, G. G. Dashkov, L. A. Polikarpova, and N. G. Gamburtseva, Izv. Akad. Nauk SSSR, Fiz. Zemli, No. 1, 28 (1970).
6. P. P. Marshall and P. W. Basham, Geophys. J. R. Astron. Soc. **28**, 431 (1972).
7. J. L. Stevens and S. M. Day, J. Geophys. Res. **90** (B4), 3009 (1985).
8. O. K. Kedrov, in *Complex Research on Physics of the Earth*, Ed. by M. A. Sadovskiĭ (Nauka, Moscow, 1989), pp. 189–203.
9. D. Carr, in *Seismic Verification* (Technology Department Sandia Natl. Lab., Albuquerque, New Mexico, 1994), Report No. SAN 94-0086, pp. 11–21.
10. T. B. Yanovskaya, Yu. V. Roslov, and E. L. Lyskova, Fiz. Zemli, No. 1, 3 (1996).
11. G. F. Miller and H. Persey, Proc. R. Soc. London, Ser. A **223** (1192), 55 (1955).
12. S. Ya. Kogan, *Seismic Energy and Methods of Its Determination* (Nauka, Moscow, 1975).
13. V. V. Gushchin, V. P. Dokuchaev, Yu. M. Zaslavskiĭ, and I. D. Konyukhova, in *Study of the Earth by Nonexplosive Seismic Sources* (Nauka, Moscow, 1981), pp. 113–118.
14. G. A. Maksimov, Fiz. Zemli, No. 11, 31 (1996).
15. H. Levine and G. C. Gaunaurd, J. Acoust. Soc. Am. **110**, 31 (2001).
16. K. Aki and P. G. Richards, *Quantitative Seismology, Theory and Methods* (Freeman, San Francisco, 1980; Mir, Moscow, 1983), Vols. 1, 2.
17. L. D. Landau and E. M. Lifshits, *Course of Theoretical Physics*, Vol. 7: *Theory of Elasticity*, 4th ed. (Nauka, Moscow, 1987; Pergamon, New York, 1986).
18. L. M. Lyamshev, Akust. Zh. **10**, 81 (1964) [Sov. Phys. Acoust. **10**, 65 (1964)].
19. G. A. Korn and T. M. Korn, *Mathematical Handbook for Scientists and Engineers* (2nd ed., McGraw-Hill, New York, 1968; 5th ed., Nauka, Moscow, 1984).

Translated by A. Khzmalyan

Acoustical Physics, Vol. 49, No. 3, 2003, pp. 339–343. Translated from Akusticheskiĭ Zhurnal, Vol. 49, No. 3, 2003, pp. 400–404.

Acoustic Streaming in a Sound Field near a Free Boundary

V. A. Mourga

St. Petersburg State Marine Technical University,
ul. Lotsmanskaya 3, St. Petersburg, 190008 Russia
e-mail: rector@smtu.ru

Received August 7, 2000

Abstract—Stationary acoustic streaming that occurs near the free boundary of a compressible viscous liquid in the field of a standing sound wave excited along this boundary is theoretically investigated. © *2003 MAIK "Nauka/Interperiodica".*

Flows near a moving boundary occupy a special place in the theory of acoustic streaming (see, e.g., [1–3]) primarily because of the necessity to take into consideration the deformation (perturbation) of the boundary. The stationary flow generated in an incompressible liquid by a surface oscillation (a wave on the water surface) that was predetermined in the form of a traveling or standing wave was investigated in [4]. The flow arising in the sound field near the boundary between two liquids whose corresponding parameters have comparable values was considered in [5]; the deformation of the boundary was shown to be negligible in this case. The present paper considers a compressible liquid in which acoustic streaming is caused by sound waves incident of the free flat boundary from the side of the liquid. In this case, the perturbation of the surface plays an essential role. In addition, one cannot restrict the consideration to the boundary layer approximation (see below). The flows considered here appear to be much weaker in comparison with the flow considered in [5]; nevertheless, in the absence of other stationary flows, it may significantly affect the transfer processes, such as heat transfer (cooling of the liquid surface by sound).

The effect of the boundary deformation cannot be described by conventional methods of the perturbation theory (decomposition of the solution in power series) because of the presence of a thin acoustic boundary layer. Therefore, it is necessary to use a coordinate system in which the surface of the liquid coincides with the coordinate surface; hence, the coordinate system must be curvilinear and moving.

Let the unperturbed surface of the liquid be the horizontal plane $Y = 0$ in the Cartesian coordinate system X, Y, Z, where the Y axis is directed upward and the liquid fills the lower halfspace ($Y < 0$). We assume that the pattern of the process is two-dimensional and is independent of Z. Additionally, we introduce the curvilinear coordinate system x, y, z in which the x coordinate runs along the surface (deformed in the general case), the y coordinate is measured from the surface and runs in the upward direction (not along the normal), and the z axis coincides in direction with the Z axis. Thus, the latter coordinate system is nonorthogonal (in contrast to the orthogonal system used in [4]). The surface of the liquid coincides with the coordinate surface $y = 0$ at any time. Within the accuracy adequate for our purposes, we have

$$x = \int_0^X \sqrt{1+\zeta'^2}\,dX \approx X, \quad y = Y - \zeta,$$
$$\frac{\partial}{\partial X} = \frac{\partial}{\partial x} - \zeta'\frac{\partial}{\partial y}, \quad \frac{\partial}{\partial Y} = \frac{\partial}{\partial y}, \quad \mathbf{e}_x \cdot \mathbf{e}_y = \zeta', \tag{1}$$
$$\frac{\partial \mathbf{e}_x}{\partial x} = \mathbf{e}_y\zeta'', \quad a_X = a_x, \quad a_Y = a_y + a_x\zeta',$$

where $\zeta(x, t)$ is the (vertical) displacement of an oscillating element of the boundary from its unperturbed position, $\zeta' = \partial\zeta/\partial x$, $\zeta'' = \partial^2\zeta/\partial x^2$, t is time, $\mathbf{e}_x$ and $\mathbf{e}_y$ are the base vectors of the coordinate system, $\mathbf{a}$ is an arbitrary vector expressed as $\mathbf{a} = a_x\mathbf{e}_x + a_y\mathbf{e}_y$, and a_X and a_Y are the components of the vector $\mathbf{a}$ in the Cartesian coordinate system. Using expressions (1), we can obtain the differential relationships required for the further consideration:

$$\nabla = \mathbf{e}_x\left(\frac{\partial}{\partial x} - \zeta'\frac{\partial}{\partial y}\right) + \mathbf{e}_y\left(\frac{\partial}{\partial y} - \zeta'\frac{\partial}{\partial x}\right),$$
$$\nabla \cdot \mathbf{a} = \frac{\partial a_x}{\partial x} + \frac{\partial a_y}{\partial y},$$
$$\nabla^2 = \frac{\partial^2}{\partial x^2} + \frac{\partial^2}{\partial y^2} - \frac{2\zeta'\partial^2}{\partial x\partial y} - \frac{\zeta''\partial}{\partial y}, \tag{2}$$
$$(\nabla \times \mathbf{a})_z = \frac{\partial a_y}{\partial x} - \frac{\partial a_x}{\partial y} + \zeta'\left(\frac{\partial a_x}{\partial x} - \frac{\partial a_y}{\partial y}\right) + a_x\zeta''.$$

1063-7710/03/4903-0339$24.00 © 2003 MAIK "Nauka/Interperiodica"

Note that the expression for the divergence of a vector coincides in form with the corresponding expression in the Cartesian coordinates. In what follows, this fact will allow us to introduce the current function of a stationary flow in a very simple manner, which justifies the use of the nonorthogonal coordinate system.

Let two identical harmonic plane waves propagate in the *xy* plane from the bulk of the liquid to the surface so as to form a symmetric pattern with respect to the *y* axis. Together with the reflected waves, they form a standing sound field extending along the surface of the liquid. In the first (acoustic) approximation, the deformation of the boundary can be neglected, so the *x* and *y* coordinates are Cartesian. We assume that the inequality

$$\left(\frac{\nu\omega}{c^2}\right)^{1/2} = \frac{k_0\delta}{\sqrt{2}} = \varepsilon \ll 1$$

is satisfied, where ν is the kinematic viscosity, ω is the oscillation frequency, c is the sound velocity, $k_0 = \omega/c$, and δ is the thickness of the boundary layer. We represent the oscillating velocity vector $\mathbf{v}$ as the sum $\mathbf{v} = \mathbf{v}_1 + \mathbf{v}_2$, where $\mathbf{v}_1$ and $\mathbf{v}_2$ are the potential and solenoidal vectors, respectively; the projections of the oscillating velocity vector on the *x* and *y* axes are $u = u_1 + u_2$ and $v = v_1 + v_2$. In the first approximation, the initial equations are as follows:

$$\frac{\partial\mathbf{v}}{\partial t} = -\frac{1}{\rho_0}\nabla p' + \nu\nabla^2\mathbf{v} + \frac{1}{3}\nu\nabla\nabla\cdot\mathbf{v},$$
$$\frac{\partial\rho'}{\partial t} + \rho_0\nabla\cdot\mathbf{v} = 0, \quad p' = \rho' c^2. \tag{3}$$

Here, ρ_0 is the unperturbed density of the liquid, ρ' is the acoustic density, and p' is the acoustic pressure. At the free boundary ($y = 0$), the normal and tangential components of the stress tensor must vanish:

$$p' - 2\nu\rho_0\frac{\partial v}{\partial y} + \frac{2}{3}\nu\rho_0\nabla\cdot\mathbf{v} = 0,$$
$$\frac{\partial u}{\partial y} + \frac{\partial v}{\partial x} = 0. \tag{4}$$

Equations (3) are equivalent to the following equations for complex amplitudes (here and below, we omit the temporal factor $\exp(-i\omega t)$):

$$\nabla^2\mathbf{v}_1 + \frac{\omega^2}{c^2}\left(1 + \frac{4}{3}\frac{i\nu\omega}{c^2}\right)\mathbf{v}_1 = 0,$$
$$p' = -\frac{i\rho_0 c^2}{\omega}\nabla\cdot\mathbf{v}_1, \tag{5}$$
$$\nabla^2\mathbf{v}_2 + \frac{i\omega}{\nu}\mathbf{v}_2 = 0, \quad \nabla\cdot\mathbf{v}_2 = 0.$$

Neglecting small quantities of the order of $\sim\varepsilon^2$, we rewrite the first boundary condition (4) in the form $\nabla\cdot\mathbf{v}_1 = 0$; the particular solution to Eqs. (5) can be written as

$$u_1 = \cos kx(e^{i\gamma y} + Ae^{-i\gamma y}),$$
$$v_1 = \frac{\gamma i}{k}\sin kx(e^{i\gamma y} - Ae^{-i\gamma y}), \tag{6}$$
$$u_2 = B\cos kx e^{i\sigma y}, \quad v_2 = -\frac{iBk}{\sigma}\sin kx e^{i\sigma y},$$

where $k^2 + \gamma^2 = k_0^2$, $k = k_0\sin\theta$, $\gamma = k_0\cos\theta$, θ is the angle of wave incidence on the boundary, A is the reflection coefficient, the combined amplitude of the longitudinal (along the *x* axis) oscillating velocity of two incident waves is equal to unity, $\sigma = -(1 + i)/\delta$, and B is an unknown constant. It is clear that $|k_0/\sigma| \sim \varepsilon$. From the boundary conditions, we obtain $A = -1$ and $B = -4\gamma/\sigma$; thus, we find that Eqs. (6) reduce to

$$u_1 = 2i\cos kx\cdot\sin\gamma y, \quad v_1 = \frac{2i\gamma}{k}\sin kx\cdot\cos\gamma y,$$
$$u_2 = -\frac{4\gamma}{\sigma}\cos kx\exp(i\sigma y), \tag{7}$$
$$v_2 = \frac{4k\gamma i}{\sigma^2}\sin kx\exp(i\sigma y).$$

As can be seen from Eqs. (7), the order of magnitude of v_2 is $\sim\varepsilon^2$; nevertheless, this expression is valid, because it is obtained from the equation of continuity and the expression for u_2, and the latter, in turn, is valid because its order of magnitude is $\sim\varepsilon$. In the boundary layer approximation, all quantities with the order of magnitude $\sim\varepsilon$ and higher should be discarded, so the constant B becomes equal to zero and the field is purely potential.

In the second approximation, quadratic in the oscillation amplitude, one has to take into account that the coordinate system is both curvilinear and moving. For the absolute motion of liquid, equations of motion have the form

$$\rho\frac{\partial\mathbf{w}}{\partial t} + \rho[(\mathbf{w} - \mathbf{v}_0)\cdot\nabla]\mathbf{w}$$
$$= -\nabla p + \eta\left(\nabla^2\mathbf{w} + \frac{1}{3}\nabla\nabla\cdot\mathbf{w}\right), \tag{8}$$
$$\frac{\partial\rho}{\partial t} + \nabla[\rho(\mathbf{w} - \mathbf{v}_0)] = 0.$$

Here, $\mathbf{w}$ is the total velocity of liquid particles, which is a sum of oscillating and stationary components; $\mathbf{v}_0$ is the velocity of the boundary element along the *y* axis, $v_0 = \dot{\zeta}$; η is the dynamic viscosity, which is assumed to be positive; and $\rho = \rho_0 + \rho'$. The differential operators have the form given in Eqs. (2), excluding the fact that nonlinear corrections in the quadratic terms in Eqs. (8)

should be neglected in these operators, so that the latter acquire the Cartesian form. Applying the curl operator to both sides of the first equation and averaging over time, we obtain from Eqs. (8) the following equations valid to the second-order terms (in the oscillation amplitude):

$$\begin{aligned}&\langle \mathbf{\Omega}\nabla\cdot\mathbf{v} - \mathbf{v}\times\nabla\nabla\cdot\mathbf{v} + \nabla\times[\mathbf{\Omega}\times(\mathbf{v}-\mathbf{v}_0)]\rangle \\ &= \nu\nabla^2(\nabla\times\mathbf{V}) + \nu\left\langle 4\zeta'\frac{\partial^3 u_2}{\partial x\partial y^2} + 2\zeta''\frac{\partial^2 u_2}{\partial y^2}\right\rangle\cdot\mathbf{e}_z, \\ &\nabla\cdot\left[\mathbf{V} + \left\langle\frac{\rho'}{\rho_0}(\mathbf{v}-\mathbf{v}_0)\right\rangle\right] = 0.\end{aligned} \tag{9}$$

Here, the angular brackets mean averaging over time at fixed x and y coordinates; $\mathbf{V}$ is the average (Euler) velocity of liquid particles; $\mathbf{v}$ is the (real) oscillating velocity whose components have the complex amplitudes given in Eqs. (7), so that $\mathbf{w} = \mathbf{V} + \mathbf{v}$; and $\mathbf{\Omega} = \nabla\times\mathbf{v}$. In Eqs. (9), the operators ∇ and ∇^2 have the Cartesian form, because the second term on the right-hand side of the first equation allows for the curvilinear character of the coordinate system; this term appears because of the nonlinear corrections (2) to the Laplasian and curl operators. From the equation of continuity (the second equation in Eqs. (9)), it follows that vector $\mathbf{U} = \mathbf{V} + \langle\rho'(\mathbf{v}-\mathbf{v}_0)/\rho_0\rangle$ is the vector of the average velocity of the liquid mass transfer. Excluding ρ' with the use of the continuity equation (in the acoustic approximation) and using the complex amplitudes of the oscillating velocity, we represent this vector in the form

$$\mathbf{U} = \mathbf{V} + \frac{i}{2\omega}(\mathbf{v}-\mathbf{v}_0)\nabla\cdot\mathbf{v}^*, \tag{10}$$

where the asterisk means the complex conjugate quantity; only the real part of the above expression is physically meaningful. Now, we introduce the function of current Ψ:

$$U_x = \partial\Psi/\partial y, \quad U_y = -\partial\Psi/\partial x. \tag{11}$$

Using Eqs. (10), (11), and (7) and performing some calculations, we obtain the following equation for the function of current instead of Eqs. (9):

$$\begin{aligned}\nabla^4\Psi &= \frac{\sin 2kx}{\omega}\gamma^2 k\sigma^* e^{-i\sigma^* y} \\ &\times\left[\frac{\gamma^2 y^2}{k^2}\sigma^{*2} + 4e^{i\sigma y}(1+i) + 2iy\sigma^*\left(1+\frac{3k_0^2}{k^2}\right) - \frac{8\gamma^2}{k^2}\right].\end{aligned} \tag{12}$$

Here, again, only the real part of the expression is physically meaningful. Only two boundary conditions are necessary at the liquid boundary: the kinematic condition and the condition that the tangential force acting on the surface is zero. In our coordinate system, the first condition has the form

$$\frac{\partial f}{\partial t} + [(\mathbf{w}-\mathbf{v}_0)\cdot\nabla]f = 0, \tag{13}$$

where $f(x, y, t) = 0$ is the equation describing the surface of the liquid. However, in our case, this equation is $y = 0$; for this reason, we have $\partial f/\partial t = 0$, $\partial f/\partial x = 0$, and $\partial f/\partial y = 1$.

Using Eqs. (1), for the arbitrary vector $\mathbf{a}$, we have

$$\begin{aligned}\mathbf{a}\cdot\nabla &= a_X\frac{\partial}{\partial X} + a_Y\frac{\partial}{\partial Y} = a_x\left(\frac{\partial}{\partial x} - \zeta'\frac{\partial}{\partial y}\right) \\ &+ (a_y + a_x\zeta')\frac{\partial}{\partial y} = a_x\frac{\partial}{\partial x} + a_y\frac{\partial}{\partial y}.\end{aligned}$$

Taking into account the relationships above, from Eq. (13), we obtain $w_y = v_0$. By averaging over time, we obtain

$$\langle w_y\rangle = V_y = 0 \text{ at } y = 0, \tag{14}$$

because v_0 is a purely periodic function of time, which corresponds to the assumption that the drift of the boundary is absent. The second condition expressed in the Cartesian coordinates has the form

$$\sum_{i,k=1}^{2}\left(\frac{\partial w_i}{\partial X_k} + \frac{\partial w_k}{\partial X_i}\right)n_k\tau_i = 0, \tag{15}$$

where $X_i (i = 1, 2)$ denotes the coordinates X and Y, n_i are the projections of the unit vector normal to the surface of the liquid, and τ_i are the projections of the unit vector tangential to the surface of the liquid. Approximately, we can write $\tau_X = 1$, $\tau_Y = \zeta'$, $n_x = -\zeta'$, and $n_Y = 1$. Changing in Eq. (15) to curvilinear coordinates according to the rules formulated in Eqs. (1), we obtain, after averaging over time,

$$\begin{aligned}&\frac{\partial V_x}{\partial y} + \frac{\partial V_y}{\partial x} + \left\langle u\zeta'' - \zeta'\left(\frac{\partial u}{\partial x} - \frac{\partial v}{\partial y}\right)\right\rangle = 0 \\ &\text{at } y = 0.\end{aligned} \tag{16}$$

As earlier, in Eq. (16), we use only the first-approximation quantities in the nonlinear terms.

Assume that the desired solution to Eq. (12) has the form (the final result will justify this assumption)

$$\Psi(x, y) = [\Phi(y) + \varphi(y)]\sin 2kx, \tag{17}$$

where Φ is the solution to the homogeneous equation and φ is the particular solution to Eq. (12). The latter can be calculated by the fourfold integration of the right-hand side of Eq. (12) with respect to y. At $y = 0$, we have in particular

$$\frac{d^2\varphi}{dy^2} = \frac{\gamma^2 k\delta}{\omega}\left(\frac{\gamma^2}{k^2} - 6\right). \tag{18}$$

The function Φ satisfies the equation

$$\Phi^{(4)} - 8k^2\Phi^{(2)} + 16k^4\Phi = 0$$

(the figures in parentheses mean the order of the derivative with respect to y), whose bounded solution is

$$\Phi = e^{2ky}(N + Py), \tag{19}$$

where N and P are unknown constants. Using Eqs. (10), (11), and (17), we rewrite the first boundary condition (14) in the form $\Phi + \varphi = 0$. Assuming that the function φ is small in comparison with the function Φ (this assumption will be justified below), we find from Eq. (19) that $N = 0$ at $y = 0$. For the second boundary condition, the calculation of the expression in angular brackets gives

$$\langle \ldots \rangle = \frac{k\gamma^2\delta}{\omega}\sin 2kx \quad \text{at} \quad y = 0. \tag{20}$$

Then, according to Eq. (10), we have

$$\begin{aligned} \frac{\partial V_x}{\partial y} &= \frac{\partial U_x}{\partial y} - \frac{i}{2\omega}\frac{\partial}{\partial y}(u\nabla \cdot \mathbf{v}^*) \\ &= \frac{\partial U_x}{\partial y} - \frac{k_0^2\gamma^2\delta}{k\omega}\sin 2kx, \quad \frac{\partial V_y}{\partial x} = \frac{\partial U_y}{\partial x}. \end{aligned} \tag{21}$$

Taking into account Eqs. (11), (17), (18), (20), and (21), we rewrite condition (16) in the form

$$\frac{d^2\Phi}{dy^2} + 4k^2\Phi = \frac{6k\gamma^2\delta}{\omega} \quad \text{at} \quad y = 0. \tag{22}$$

Finally, using solution (19) for Φ and neglecting the small terms, we obtain from Eq. (22)

$$P = -3\gamma^2\delta/2\omega.$$

Consequently, we have the following expression for the function of current

$$\Psi = -\frac{3\gamma^2\delta}{2\omega}e^{2ky}y\sin 2kx.$$

The components of the vector of average velocity of mass transfer can be written in the form

$$\begin{aligned} U_x &= -\frac{3\gamma^2\delta}{2\omega}e^{2ky}(1 + 2ky)\sin 2kx, \\ U_y &= \frac{3\gamma^2\delta}{\omega}kye^{2ky}\cos 2kx, \end{aligned} \tag{23}$$

where, again, the partial solution φ and $d\varphi/dy$ is neglected.

In the general case, the velocity of mass transfer $\mathbf{U}$ does not coincide with the average velocity of an individual liquid particle $\mathbf{U}_L$ (which is the Lagrange velocity). According to Rayleigh [6], the velocity of an individual particle in a moving coordinate system is

$$\mathbf{U}_L = \mathbf{V} + \langle(\boldsymbol{\xi} \cdot \nabla)\mathbf{v}_R\rangle,$$

where $\boldsymbol{\xi}$ is the radius vector connecting the point that coincides with particle position averaged over the oscillation period and the point where the particle occurs at the given instant, and $\mathbf{v}_R$ is the relative oscillating velocity of the particle. By virtue of (10), one can show that the Lagrange velocity is related to the velocity of mass transfer through the relationship

$$\mathbf{U}_L = \mathbf{U} + \frac{1}{2}\nabla \times (\mathbf{v}_R \times \boldsymbol{\xi}). \tag{24}$$

The calculation of the second term in Eq. (24) with allowance for the fact that $\mathbf{v}_R = \mathbf{v} - \mathbf{v}_0 = \dot{\boldsymbol{\xi}}$ gives a quantity whose order of magnitude is determined by the expression

$$\sim\frac{\gamma^2\delta}{\omega}e^{-y/\delta} \cdot k_0\delta\sin 2kx.$$

The comparison of this result with Eqs. (23) shows that the correction to U in Eq. (24) has a relative magnitude of the order of $\sim\varepsilon$ and should be omitted. Thus, in the case under consideration, we have $\mathbf{U} = \mathbf{U}_L$.

The velocity of mass transfer is maximal at the boundary of the liquid ($y = 0$) and is equal to

$$U_{\max} = \frac{3\gamma^2\delta}{2\omega}.$$

If we write the total amplitude of the longitudinal oscillating velocity as $2u_0\sin\theta$ (u_0 is the velocity amplitude of each of the incident waves), the expression above is rearranged to the form

$$U_{\max} = \frac{3}{2}\frac{u_0^2}{c}k_0\delta\sin^2 2\theta. \tag{25}$$

From this expression, one can see that the most intense streaming appears when the waves are incident on the surface at an angle of $\pi/4$. The velocities of mass transfer in the Rayleigh flow near a rigid wall [6] and near a boundary between two liquids, whose corresponding parameters have comparable values [5], are, on the order of magnitude, equal to $\sim u_0^2/c$ and $u_0^2/ck_0\delta$, respectively. The comparison of these quantities with Eq. (25) shows that the acoustic streaming considered in this paper is relatively weak. The structure of the streaming is similar to that considered in [5]: the

streaming consists of large-scale vortices that occur along the boundary and have a characteristic size of the half-wavelength of sound.

REFERENCES

1. L. K. Zarembo and V. A. Krasil'nikov, *Introduction to Nonlinear Physical Acoustics* (Nauka, Moscow, 1966).
2. *Physical Acoustics: Principles and Methods*, Ed. by W. P. Mason (Academic, New York, 1965; Mir, Moscow, 1969), Vol. 2, Part B.
3. Zhao Xiaoliang, Zhu Zhemin, and Du Gonghuan, J. Acoust. Soc. Am. **104**, 583 (1998).
4. M. S. Longuet-Higgins, Philos. Trans. R. Soc. London, Ser. A **245**, 535 (1953).
5. V. A. Murga, Akust. Zh. **46**, 526 (2000) [Acoust. Phys. **46**, 456 (2000)].
6. J. W. Strutt (Lord Rayleigh), *The Theory of Sound* (Macmillan, London, 1894; Gostekhizdat, Moscow, 1955), Vol. 2.

Translated by A. Vinogradov

Acoustical Physics, Vol. 49, No. 3, 2003, pp. 344–353. Translated from Akusticheskiĭ Zhurnal, Vol. 49, No. 3, 2003, pp. 405–415.

Wave Processes in Media with Hysteretic Nonlinearity. Part I

V. E. Nazarov, A. V. Radostin, L. A. Ostrovsky, and I. A. Soustova

Institute of Applied Physics, Russian Academy of Sciences,
ul. Ul'yanova 46, Nizhni Novgorod, 603950 Russia
e-mail: nazarov@hydro.appl.sci-nnov.ru

Received May 4, 2001

Abstract—Two phenomenological models of hysteretic equations of state for media with imperfect elasticity are described and compared. On the basis of these equations, a theoretical study of nonlinear effects caused by the acoustic wave propagation in an unbounded medium is performed. The profiles, parameters, and spectra of waves are determined. The distinctive features of nonlinear wave processes in such media are revealed, so that these features can be used to choose the appropriate hysteretic equation of state for analytically describing the experimental data. *© 2003 MAIK "Nauka/Interperiodica".*

1. INTRODUCTION

Traditionally, the propagation and interaction of acoustic waves in various solid media is described in terms of the five-constant (or nine-constant) elasticity theory [1, 2]. This theory, being essentially mathematical, determines the nonlinear (in the quadratic or cubic approximations, respectively) equation of state for homogeneous media (i.e., the dependence of the elastic stress tensor σ_{ij} on the components of the elastic strain tensor ε_{ij}). For longitudinal stresses σ and strains ε, the equation of state can be formally derived from the Taylor expansion of a smooth single-valued differentiable (i.e., analytic) function $\sigma = \sigma(\varepsilon)$ to the terms quadratic (or cubic) in ε:

$$\sigma(\varepsilon) = E\left(\varepsilon - \frac{\gamma}{2}\varepsilon^2 + \ldots\right), \qquad (1)$$

where $E = \left.\frac{\partial\sigma(\varepsilon)}{\partial\varepsilon}\right|_{\varepsilon = 0}$ is the elastic modulus, $\gamma = -E^{-1}\left.\frac{\partial^2\sigma(\varepsilon)}{\partial\varepsilon^2}\right|_{\varepsilon = 0}$ is the parameter of the quadratic nonlinearity, and $|\gamma\varepsilon| \ll 1$. In homogeneous solids, such a nonlinearity is caused by the dependence of intermolecular forces on the molecular displacements, and the parameter γ is rather small and does not exceed a value of 10 [2]. The simplest nonlinear effect that accompanies the propagation of a harmonic wave is the generation of its higher harmonics. In such media (at small distances from the source, well before the shock front formation), the amplitude of the *n*th harmonic is proportional to the *n*th power of the amplitude of the initial wave propagating with a constant velocity without attenuation.

In describing microinhomogeneous media, which include most types of rock and some metals and structural materials (because of their complex structure and the presence of microdefects like cracks, grains, dislocations, etc.), such an approach is inapplicable. For these media, the equations of state correspond to the type and number of defects in them and, as a rule, are nonanalytic (i.e., nonsmooth and nondifferentiable). For example, the presence of cracks in a solid may lead to a difference between its elastic moduli of compression and tension. A granular structure of the material may change the power of the nonlinear term in the equation of state, specifically, from an integer of 2, as in the five-constant elasticity theory, to a fractional power of 3/2 [3, 4]. One-dimensional defects of the crystal lattice, i.e., dislocations, lead to a hysteretic (ambiguous) stress–strain dependence $\sigma = \sigma(\varepsilon, \dot{\varepsilon})$ (where $\dot{\varepsilon}$ is the strain rate) for polycrystals [5, 6]. As a rule, the effective nonlinear parameter of microinhomogeneous media exceeds the corresponding parameter of homogeneous media and materials by three to four orders of magnitude. Therefore, the character of the nonlinear effects accompanying the propagation and interaction of elastic waves may be not only quantitatively but also qualitatively different for different microinhomogeneous media. This fact can be used in the diagnostics and nondestructive testing of such media. From the viewpoint of the latter applications, a favorable factor is that the nonlinear acoustic properties of such media are more sensitive to the presence of defects, as compared to the linear properties.

In recent years, in acoustics (and seismoacoustics [7]), the nonlinear wave processes occurring in various microinhomogeneous media have been more and more often described by equations of state containing a hysteretic nonlinearity. In our previous publications [3, 8–14], hysteretic equations of state with quadratic and cubic nonlinearities were derived from the analysis of experimental amplitude dependences of the nonlinear loss, the resonance frequency shift, and the levels of

higher harmonics, which were observed in various metal (copper, zinc, and lead) and rock (granite, marble) resonators. The equations were used to study nonlinear wave processes in an unbounded medium and in a bar resonator by the perturbation method. The comparison of the analytic calculations with the experimental results made it possible to determine the values of the hysteretic nonlinear parameters of these media. In a series of theoretical and experimental studies [15–18], the main results of which were described in a review [19], hysteretic dependences were obtained by numerically simulating the behavior of a medium containing an ensemble of Priesach–Mayergoys elements [20, 21], which possess a trigger-type hysteresis. In the framework of the hysteresis obtained in this way, a numerical study of the nonlinear distortion of an initially harmonic wave was carried out, and from the comparison of the numerical calculations with experimental data, the values of the effective nonlinear parameters were determined for sandstone, limestone, and concrete. In the following publications [22–26], on the basis of the results obtained in [15, 16], an analytic (in the quadratic approximation) description of such a hysteresis was proposed and a theoretical study of the propagation and interaction of initially harmonic waves and triangular pulses was performed. However, in some of the cited papers [22, 24, 26], the form of the hysteresis was determined by a single parameter and was strictly symmetric, which is more likely to correspond to the behavior of real solids undergoing shear deformation rather than compressional or tensile one. Other papers [23, 25] used the assumption that the parameters determining the average slope of the hysteresis loop and its quadratic nonlinearity are identical. All these rather stringent constraints considerably narrow the class of media described by the cited theory.

Hysteretic properties are typical of many microinhomogeneous media and, especially, of "soft" metals and rock. However, one should not expect that all such media can be described by a single universal equation of state with different numerical values of nonlinear parameters for different media (just as the linear deformation of homogeneous and isotropic media is described by the same Hooke law [1, 2] with different elastic coefficients for different media). The nonlinear acoustic properties of microinhomogeneous media are widely diversified (as compared to those of homogeneous media), because even a single medium can exhibit different behavior in different amplitude and frequency ranges. For example, in experimental studies of the nonlinear effects of amplitude-dependent internal friction in acoustic bar resonators, the dependences of the resonance frequency shift and nonlinear loss on the wave amplitude were found to obey different power laws: for unannealed copper, the exponent in the power law was equal to 1, and for annealed copper, to 1/2 [3, 8, 9]; for unannealed and annealed zinc, the exponents were equal to 1 and 2, respectively [13, 14]; for lead, the exponent was equal to 2 at small amplitudes and to 1/2 at large amplitudes [12]; for granite and sandstone, it was equal to 1 [11, 27, 28]; and for marble, to 2 [11]. In the cited review [19], the authors also mentioned the linear dependence of the resonance frequency shift on the excitation amplitude of resonators made of sandstone, limestone, and concrete. The manifestation of identical dependences of the propagation velocity variation and the nonlinear loss on the wave amplitude testifies that the medium possesses a hysteretic nonlinearity. Another manifestation of such a nonanalytic nonlinearity is the identical power-law dependence (with the hysteretic nonlinearity exponent) of the level of higher harmonics generated in the medium on the wave amplitude at the fundamental frequency [8–10]. Precisely these kinds of dependences were observed in [3, 8, 9, 11, 14].

In the cited publications [3, 8–19, 22–26], different kinds of hysteresis were used, and, presumably, there still exists no unified approach to choosing the hysteretic equation of state for one or another medium. In connection with this, the elaboration of principles for making such a choice is a topical problem of nonlinear acoustics (and seismoacoustics). We believe that some progress in this direction may be achieved by studying and comparing different nonlinear effects that occur in media with different kinds of hysteretic nonlinearity, because the character of nonlinear wave processes is governed by the nonlinearity of the medium.

In this paper, which consists of two parts, we theoretically study the effects of nonlinear propagation of continuous and pulsed longitudinal acoustic waves in media whose equations of state possess a hysteretic nonlinearity. First, we describe two basic (asymmetric in the general case) models of hysteretic equations of state, and then, in the framework of these equations, we study the evolution and nonlinear distortion of the continuous (Part I) and pulsed acoustic waves in an unbounded medium and in a ring resonator (Part II). On the basis of these studies, we reveal the distinctive features that characterize the nonlinear processes in such media and allow one to choose the appropriate hysteretic equation of state for an analytic description of experimental results. In describing such nonlinear processes, we assume that the nonlinearity of the equation of state of a medium predominates over the kinematic nonlinearity of the equations of motion, so that the latter can be ignored. In this approximation, we can assume that $\varepsilon = U$ and $\rho = \text{const}$ (U is the longitudinal displacement and ρ is the density), and the equations of the elasticity theory in the Lagrangian and Eulerian forms coincide.

2. HYSTERETIC EQUATIONS OF STATE FOR MEDIA WITH AN IMPERFECT ELASTICITY

Many phenomenological equations of state have been constructed for media with hysteretic nonlinearity, and their detailed description can be found in the literature [29–31]. The first analytic description of a

mechanical hysteresis was proposed in 1938 by Davidenkov [32] for explaining the amplitude-dependent internal friction in materials with the so-called imperfect elasticity; the internal friction itself was attributed to the microplastic deformation of the material. In 1956, Granato and Lucke developed the physical theory of amplitude-dependent internal friction in polycrystals [5, 6] on the basis of the Koehler's string model of dislocations [33]. In both these theories, the equation of state of the medium contains a hysteresis: the area of the hysteresis loop determines the nonlinear loss, and the wave-period average of the derivative $\sigma_\varepsilon(\varepsilon, \dot{\varepsilon})$ determines the defect of the elastic modulus. In different hysteresis models, the nonlinear loss and the defect of the elastic modulus depend on the strain wave amplitude in different ways, but their ratio r (at relatively small amplitudes) is constant and amplitude-independent in most cases [29–31]. Presumably, there is no general factor responsible for the hysteretic behavior of various materials. However, for polycrystals, the hysteresis was found to be caused by the separation of dislocations from impurity atoms [5, 6, 34]. (The idea that the mechanical hysteresis is caused by the defects of the crystal lattice was first put forward by Prandtl as early as in 1913 [35]. In 1940, Read proved experimentally that plastic deformation affects the amplitude-dependent internal friction of metals, and he explained this phenomenon on the basis of the dislocation motion [36].) The Granato–Lucke theory provides a fairly good qualitative (and sometimes, quantitative) explanation of the experimental data on the amplitude dependences of the nonlinear loss and the defect of the elastic modulus only for certain sufficiently pure polycrystals. The nonlinear effects that occur in other solids with imperfect elasticity are described by phenomenological hysteretic equations.

In this paper, we use the simplest dependences $\sigma = \sigma(\varepsilon, \dot{\varepsilon})$ that reflect the main and characteristic features of the hysteresis manifesting itself in some metals and rocks, such as unannealed copper [3, 8, 9] and zinc [18], granite [11], sandstone [19, 27, 28], and limestone [19]:

—each hysteresis branch is a quadratic function of strain;

—the transition from one branch to another occurs with a change of sign of ε and (or) $\dot{\varepsilon}$ while the function $\sigma = \sigma(\varepsilon, \dot{\varepsilon})$ remains continuous;

—for infinitely small strains, the hysteretic nonlinearity is negligibly small;

—the ratio r of the nonlinear damping decrement to the defect of the elastic modulus (at small strain amplitudes) is constant.

It should be noted that the first of the aforementioned features is not universal and common to all solids in which mechanical hysteresis manifests itself, because, for marble [11], lead [12], and annealed zinc [13, 14], each hysteresis loop is a cubic rather than quadratic function of strain (this case is not considered in our paper).

In the general case, the equation of state of a medium can be represented in the form

$$\sigma(\varepsilon, \dot{\varepsilon}) = E[\varepsilon - f(\varepsilon, \dot{\varepsilon})], \tag{2}$$

where $f(\varepsilon, \dot{\varepsilon})$ is a nonlinear function of strain and strain rate and $|f_\varepsilon(\varepsilon, \dot{\varepsilon})| \ll 1$. (Note that, in equations of state (1) and (2), it is also necessary to take into account the linear term $\eta\dot{\varepsilon}$ [1, 2]. However, since it is not this term that determines the character of nonlinear wave processes, we assume that it is small and can be ignored. Then, the formulas obtained below will be valid at the distances $x \ll L_0 = 2C_0^3/\eta\omega^2$, where η is the viscosity of the medium, C_0 is the velocity of a small-amplitude longitudinal wave, and ω is the wave frequency.)

In the first model of hysteresis, the nonlinear function has the form

$$f(\varepsilon, \dot{\varepsilon}) = \alpha\varepsilon_m\varepsilon + \begin{cases} \frac{\beta_1}{2}\varepsilon^2 - \frac{\beta_1 + \beta_2}{4}\varepsilon_m^2, & \dot{\varepsilon} > 0 \\ -\frac{\beta_2}{2}\varepsilon^2 + \frac{\beta_1 + \beta_2}{4}\varepsilon_m^2, & \dot{\varepsilon} < 0, \end{cases} \tag{3}$$

where $|\alpha|\varepsilon_m \ll 1$, $|\beta_{1,2}|\varepsilon_m \ll 1$, and $|\beta_{1,2}| \gg 1$. This equation involves three independent nonlinear parameters, α and $\beta_{1,2}$, which are responsible for the defect of the elastic modulus and for the nonlinear loss. Generally speaking, the nonlinearities of the first and second terms in Eq. (3) can also be independent, but for the ratio r (at small strain amplitudes) to be independent of the wave amplitude ε_m, it is necessary to set the power of the first term to be equal to the power of the hysteretic nonlinearity, i.e., equal to 2. One can easily see that, at $\alpha = 0$ and $\beta_1 + \beta_2 = 0$, the defect of the elastic modulus and the nonlinear loss are equal to zero, and Eqs. (3) describe a quadratic nonlinearity, as the five-constant elasticity theory. From Eq. (3), it follows that, when $\beta_1 + \beta_2 \neq 0$, zero stresses (strains) correspond to nonzero strains (stresses). Usually, such nonzero strains are called microplastic ones, and nonzero stresses, residual ones. According to this terminology, we call the first hysteresis (Fig. 1a) inelastic. This kind of hysteresis was proposed by Davidenkov [32]; later, it was observed in the experiments on static deformation of Australian sandstone, South-African quartzite [37], and LiF and NaCl crystals [38–41] and used for describing the amplitude-dependent internal friction (the damping decrement and the defect of elastic modulus) in these crystals.

In the second model of hysteresis, the nonlinear function has the form

$$f(\varepsilon, \dot{\varepsilon}) = \begin{cases} \frac{\gamma_1}{2}\varepsilon^2, & \varepsilon > 0, \quad \dot{\varepsilon} > 0 \\ -\frac{\gamma_2}{2}\varepsilon^2 + \frac{\gamma_1 + \gamma_2}{2}\varepsilon_m^+\varepsilon, & \varepsilon > 0, \quad \dot{\varepsilon} < 0 \\ -\frac{\gamma_3}{2}\varepsilon^2, & \varepsilon < 0, \quad \dot{\varepsilon} < 0 \\ \frac{\gamma_4}{2}\varepsilon^2 + \frac{\gamma_3 + \gamma_4}{2}\varepsilon_m^-\varepsilon, & \varepsilon < 0, \quad \dot{\varepsilon} > 0, \end{cases} \tag{4}$$

where $|\gamma_{1,2}\varepsilon_m^+| \ll 1$, $|\gamma_{3,4}\varepsilon_m^-| \ll 1$, $|\gamma_{1-4}| \gg 1$, $\varepsilon_m^+ > 0$, and $\varepsilon_m^- < 0$. This model contains four nonlinear parameters, γ_{1-4}. Depending on their relationship, Eqs. (2) and (4) describe a broad class of media: when $\gamma_1 = -\gamma_2 = -\gamma_3 = \gamma_4$, we have Eq. (1); when $\gamma_{2,4} = 0$, we obtain an equation with a linear return branch (as in the Granato–Lucke model [5, 30]). For such a medium (at small wave amplitudes), both the damping decrement and the defect of elastic modulus are proportional to the wave amplitude and, hence, we automatically obtain r = const [10]. In this model, zero stresses correspond to zero strains and vice versa, and, therefore, we call the second hysteresis (Fig. 1b) an elastic one. This hysteresis was proposed in [10] and used for describing the results of experimental studies of nonlinear acoustic effects in bar resonators made of polycrystalline metals and different kinds of rock [3, 11–14].

In Eqs. (3) and (4), the quantities ε_m and $\varepsilon_m^\pm$ (unlike the parameters α, $\beta_{1,2}$, and γ_{1-4}) do not characterize the medium itself but are determined by its maximal and minimal strain. In the first model of hysteresis, the hysteresis branches are interdependent and, hence, ε_m is the wave amplitude ($\varepsilon_m > 0$). In the second model of hysteresis, its positive ($\varepsilon > 0$) and negative ($\varepsilon < 0$) branches are defined independently and, therefore, in the general case, the quantities $|\varepsilon_m^\pm|$ are different; i.e., $\varepsilon_m^+ \neq -\varepsilon_m^-$. (The values of ε_m^+ and ε_m^- correspond to the amplitudes of the positive and negative half-periods of the wave.) For the inelastic hysteresis, the nonlinear function is nonanalytic at two points, $\varepsilon = \varepsilon_m$ and $\varepsilon = -\varepsilon_m$, and for the elastic hysteresis, at three points: $\varepsilon = \varepsilon_m^+$, $\varepsilon = \varepsilon_m^-$, and $\varepsilon = 0$. We also note that, in the hysteresis models, a positive nonlinear loss corresponds to the clockwise motion of the working point in the stress–strain diagram $\sigma = \sigma(\varepsilon, \dot{\varepsilon})$. This corresponds to the condition that the sums of nonlinear parameters satisfy the inequalities $\beta_1 + \beta_2 > 0$ and $\gamma_{1,3} + \gamma_{2,4} > 0$. So far, we impose no other conditions on the parameters α, $\beta_{1,2}$, and γ_{1-4} in addition to these inequalities and assume that these parameters are different, which reflects the asymmetry of the stress–strain diagram of a solid at its compression and tension. The presence of this asymmetry is confirmed, in particular, by the results of experimental studies of the amplitude-dependent internal friction in some metals and rocks. For example, for polycrystalline copper (depending on its granular structure, which changes under annealing), the values of the parameters $\gamma_1 + \gamma_3$ and $\gamma_2 + \gamma_4$ varied from 6.6×10^2 and 1.8×10^3 to 1.9×10^4 and 1.5×10^5, respectively [3]; for unannealed polycrystalline zinc, these parameters were equal to 6.3×10^3 and 2.6×10^4 [14]; and for granite, they were 9.2×10^3 and 7×10^3 [11]. The wide difference (several times) in the parameters $\gamma_1 + \gamma_3$ and $\gamma_2 + \gamma_4$ testifies to a wide difference in the parameters γ_{1-4}. Despite the fact that both hysteresis models contain only the terms that are linear and quadratic in strain, the nonlinear function $f = f(\varepsilon, \dot{\varepsilon})$ is a function of a general form; i.e., it contains both even and odd components that depend on the strain in the same way (quadratically in the case under consideration). As a result, at small distances from the source, where the nonlinear attenuation of the initial wave is insignificant, the amplitudes of all its higher harmonics (both even and odd) are proportional to the square of the strain amplitude of the ini-

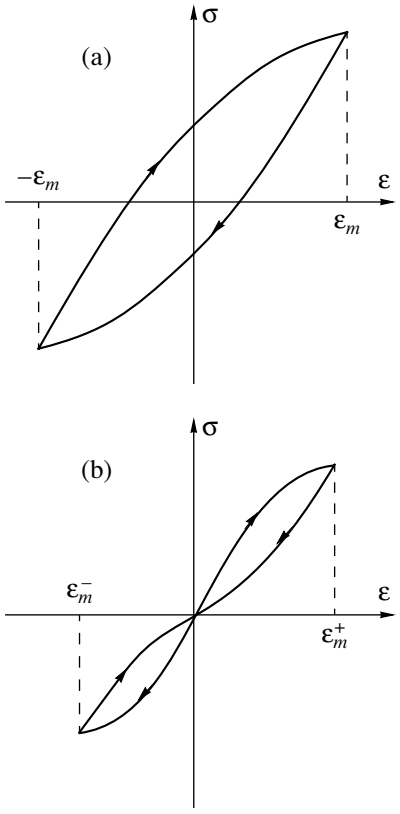

Fig. 1. Dependence $\sigma = \sigma(\varepsilon, \dot{\varepsilon})$ for media with (a) an inelastic hysteresis and (b) an elastic hysteresis.

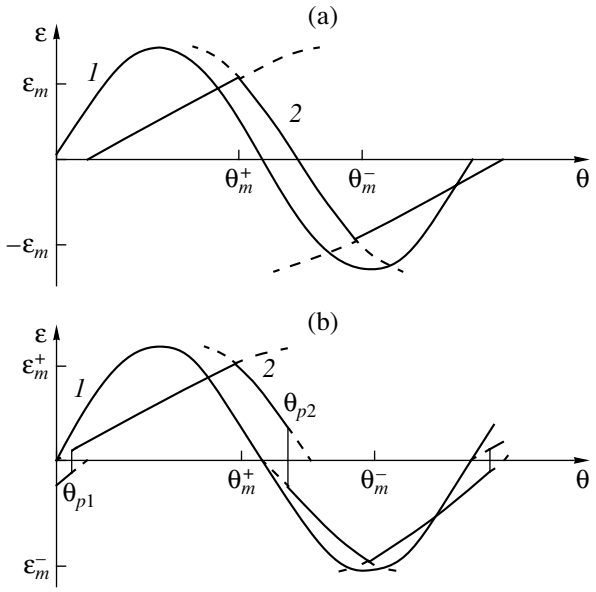

Fig. 2. Evolution of an initially harmonic wave in media with (a) an inelastic hysteresis and (b) an elastic hysteresis for (*1*) $x = 0$ and (*2*) $x > 0$.

tial harmonic wave [10]. For media with a cubic hysteretic nonlinearity, the amplitudes of higher harmonics (at the same small distances) are proportional to the cube of the strain amplitude of the initial wave. This distinctive feature allows one to determine the power of the nonlinear term in the hysteretic equation of state [3, 11–14].

The hysteretic equations presented above noticeably differ from one another: the second equation cannot be derived from the first one, and the first equation, from the second one. In addition, unlike the second equation, the first equation is not an evolutionary one. This fact specifically manifests itself in that, in the inelastic hysteresis, both hysteresis branches depend on the strain amplitude ε_m, which should not take place, because, in this case, the residual stress is determined by the wave amplitude ε_m, and such a dependence violates the causality principle: before being affected, the medium already "knows" the future strain amplitude and the velocity with which the wave will propagate in it. Therefore, the first hysteretic equation can be used only for describing steady-state periodic waves, whereas, for describing transient processes and propagation of unipolar pulses (or disturbances), it is inapplicable. However, in this paper, taking into account the limited applicability of the first equation, we study the propagation of continuous waves and pulsed disturbances in the framework of both hysteretic equations and then, with the aim of revealing the common and distinctive qualitative features of nonlinear acoustic effects in such media, we perform a comparative analysis of the results.

3. ELASTIC WAVES IN AN UNBOUNDED MEDIUM

Hysteretic equations of state (2)–(4) together with the equation of motion [42–44]

$$\rho\frac{\partial^2 U}{\partial t^2} = \frac{\partial\sigma(\varepsilon, \dot\varepsilon)}{\partial x} \tag{5}$$

allow us to study nonlinear wave processes in media with imperfect elasticity. To solve these equations, we use the method of "sewing together" simple waves corresponding to each hysteresis branch. This method was proposed in [45] and then developed in [22–26]. Substituting Eqs. (2)–(4) in Eq. (5) and changing to the variables $\tau = t - x/C_0$ and $x = x$, we obtain an equation for the waves travelling in the positive direction along the x axis [42–44]:

$$\frac{\partial\varepsilon}{\partial x} = -\frac{1}{2C_0}\frac{\partial f(\varepsilon, \dot\varepsilon)}{\partial\tau}, \tag{6}$$

where $C_0 = (E/\rho)^{1/2}$. This equation describes simple strain waves for each hysteresis branch. For an initially harmonic wave $\varepsilon(x = 0, t) = \varepsilon_0\sin\omega t$, its solution (for the first and second hysteresis models) has the form

$$\varepsilon(x, \theta) = \varepsilon_0\begin{cases}\sin\left(\theta - \dfrac{\beta_1}{2}\varepsilon kx - \dfrac{\alpha}{2}k\displaystyle\int_0^x\varepsilon_m(x')dx'\right), & \dot\varepsilon > 0\\ \sin\left(\theta + \dfrac{\beta_2}{2}\varepsilon kx - \dfrac{\alpha}{2}k\displaystyle\int_0^x\varepsilon_m(x')dx'\right), & \dot\varepsilon < 0;\end{cases} \tag{7}$$

$$\varepsilon(x, \theta) = \varepsilon_0\begin{cases}\sin\left(\theta - \dfrac{\gamma_1}{2}\varepsilon kx\right), & \varepsilon > 0, \quad \dot\varepsilon > 0\\ \sin\left(\theta + \dfrac{\gamma_2}{2}\varepsilon kx - \dfrac{\gamma_1 + \gamma_2}{2}k\displaystyle\int_0^x\varepsilon_m^+(x')dx'\right), & \varepsilon > 0, \quad \dot\varepsilon < 0\\ \sin\left(\theta + \dfrac{\gamma_3}{2}\varepsilon kx\right), & \varepsilon < 0, \quad \dot\varepsilon < 0\\ \sin\left(\theta - \dfrac{\gamma_4}{2}\varepsilon kx - \dfrac{\gamma_3 + \gamma_4}{2}k\displaystyle\int_0^x\varepsilon_m^-(x')dx'\right), & \varepsilon < 0, \quad \dot\varepsilon > 0,\end{cases} \tag{8}$$

where $\theta = \omega\tau$ and $k = \omega/C_0$.

Figures 2a and 2b show the profiles of simple waves described by Eqs. (7) and (8) at a distance x from the source. From these plots, one can see that, within each period, ambiguities are formed in the wave (because of the nonanalytic character of functions (3) and (4)) near

the points $\varepsilon = \pm\varepsilon_m$ for the first hysteresis model and near the points $\varepsilon = \varepsilon_m^{\pm}$ and $\varepsilon = 0$ for the second model. For the latter, two types of ambiguities are possible: the first type, near the points $\varepsilon = \varepsilon_m^{\pm}$, where simple waves intersect (as in the first model at $\varepsilon = \pm\varepsilon_m$), and the second type, near the points $\varepsilon = 0$, where the superposition of simple waves takes place. The elimination of ambiguities associated with the superposition of simple waves is achieved by introducing discontinuities in the wave profile, which are determined from the momentum conservation law [42–44]. In a medium described by Eq. (1), the discontinuities of the wave profile are formed at the "trailing edge" ($\dot{\varepsilon} < 0$) when $\gamma > 0$ and at the "leading edge" ($\dot{\varepsilon} > 0$) when $\gamma < 0$. Then, in the first hysteresis model in the case of $\beta_{1,2} \geq 0$ (we will mainly consider this case in our study), no discontinuities will be formed in the wave at all, and the ambiguities near the points of intersection of simple waves can be eliminated by sewing them together at these points. From Eq. (7), we can easily determine the values of the wave amplitude $\varepsilon_m(x)$ and the phases $\theta_m^{\pm}(x)$ corresponding to the points of intersection of simple waves (Fig. 2a):

$$\varepsilon_m(x) = \varepsilon_0 \cos\left[\frac{(\beta_1 + \beta_2)\varepsilon_m(x)kx}{4}\right],$$

$$\theta_m^+(x) = \frac{\pi}{2} + \frac{\beta_1 - \beta_2}{4}\varepsilon_m kx + \frac{\alpha}{2}k\int_0^x \varepsilon_m(x')dx', \qquad (9)$$

$$\theta_m^-(x) = \frac{3\pi}{2} - \frac{\beta_1 - \beta_2}{4}\varepsilon_m kx + \frac{\alpha}{2}k\int_0^x \varepsilon_m(x')dx'.$$

Let us consider the asymptotic profile of wave (7) at small and large distances from the source. From Eqs. (7) and (9), it follows that, when $x \ll x_0 = 4/(\beta_1 + \beta_2)\varepsilon_0 k$, the wave form is close to the initial one and $\varepsilon_m \cong \varepsilon_0$, and when $x \geq x_0$, the wave profile becomes triangular:

$$\varepsilon(x, \theta) = \varepsilon_0 \begin{cases} \dfrac{\theta - \dfrac{\pi\alpha}{\beta_1 + \beta_2}\ln\left(1 + \dfrac{\beta_1 + \beta_2}{4}\varepsilon_0 kx\right)}{1 + \beta_1\varepsilon_0 kx/2}, \\ \theta_m^- - 2\pi \leq \theta < \theta_m^+ \\ \dfrac{\pi - \theta + \dfrac{\pi\alpha}{\beta_1 + \beta_2}\ln\left(1 + \dfrac{\beta_1 + \beta_2}{4}\varepsilon_0 kx\right)}{1 + \beta_2\varepsilon_0 kx/2}, \\ \theta_m^+ \leq \theta < \theta_m^-. \end{cases} \qquad (10)$$

The amplitude and propagation velocity of this wave are determined by the expressions

$$\varepsilon_m(x) = \frac{2\pi\varepsilon_0}{4 + (\beta_1 + \beta_2)\varepsilon_0 kx} \ll \varepsilon_0,$$
$$C(x) = \frac{C_0}{1 + \alpha\varepsilon_m(x)/2}. \qquad (11)$$

Thus, at large distances from the source ($x \gg x_0$), an initially harmonic wave propagating in the medium with an inelastic hysteresis is transformed to a wave with a triangular profile with an amplitude ε_m, which is independent of the initial amplitude and decays according to the law $\varepsilon_m(x) \sim x^{-1}$.

Consider the evolution of the wave spectrum. At small distances, we have

$$\varepsilon(x, \theta) = \left(1 - \frac{\beta_1 + \beta_2}{3\pi}\varepsilon_0 kx\right)\left[\varepsilon_0 \sin(\theta - \alpha\varepsilon_0 kx/2)\right.$$
$$- \frac{\beta_1 - \beta_2}{8}\varepsilon_0^2 kx \sin 2(\theta - \alpha\varepsilon_0 kx/2) + \frac{\beta_1 + \beta_2}{\pi}\varepsilon_0^2 kx \qquad (12)$$
$$\left.\times \sum_{n=1}^{\infty} \frac{(-1)^n}{(2n-1)(2n-3)} \sin(2n+1)(\theta - \alpha\varepsilon_0 kx/2)\right],$$

while the damping decrement δ and the relative variation of the wave velocity $\Delta C/C_0$ are determined by the expressions

$$\delta = \frac{2(\beta_1 + \beta_2)}{3}\varepsilon_0, \quad \frac{\Delta C}{C_0} = \frac{\alpha}{2}\varepsilon_0. \qquad (13)$$

At large distances ($x \gg x_0$), we obtain

$$\varepsilon(x, \theta) = \frac{4(\beta_1 + \beta_2)}{\pi\beta_1\beta_2 kx}\sum_{n=1}^{\infty}\frac{1}{n^2}\sin\left(\frac{\pi n\beta_1}{\beta_1 + \beta_2}\right)\sin n\left[\theta - \frac{\pi\alpha}{(\beta_1 + \beta_2)kx}\right], \qquad (14)$$

$$\delta = (\beta_1 + \beta_2)\varepsilon_m, \quad \frac{\Delta C}{C_0} = \frac{\alpha}{2}\varepsilon_m. \qquad (15)$$

From Eq. (14), it follows that the relative level ζ of the first harmonic in the triangular wave is determined by the expression

$$\zeta = \frac{\varepsilon_1}{\varepsilon_m} = \frac{2(1 + \beta_1/\beta_2)^2}{\pi^2}\cos\left(\frac{\pi}{2}\frac{1 - \beta_2/\beta_1}{1 + \beta_2/\beta_1}\right). \qquad (16)$$

Note that, when $\beta_1 < 0$ (or $\beta_2 < 0$) and $\beta_1 + \beta_2 \geq 0$, a discontinuity is formed in the wave at its leading (or trailing) edge at the point $\varepsilon = 0$ at the distance $x^* = 2/|\beta_{1,2}|\varepsilon_0 k$. In this case, Eqs. (9) will be valid up to the coordinate $x_1 = x^*(\chi/\sin\chi) > x^*$, where $\chi = \pi|\beta_{1,2}|/(|\beta_{1,2}| + |\beta_{2,1}|)$; at this distance, the discontinuity

amplitude becomes equal to the wave amplitude. At large distances, the wave will contain discontinuities whose amplitude is determined as $\varepsilon_m(x) = 2\pi/|\beta_{1,2}|kx$.

Now, we determine the form of the wave and its parameters in a medium with an elastic hysteresis. To simplify the calculations, we assume that $\gamma_{1-4} > 0$. In this case, the first type of ambiguities is also eliminated by sewing together simple waves at the point of their intersection. From Eq. (8), we obtain

$$\pi \mp 2\arcsin\left(\frac{\varepsilon_m^{\pm}}{\varepsilon_0}\right) \mp \frac{\gamma_{1,3} + \gamma_{2,4}}{4}\varepsilon_m^{\pm}kx$$
$$\pm \frac{\gamma_{1,3} + \gamma_{2,4}}{4}k\int_0^x \varepsilon_m^{\pm}(x')dx' = 0.$$

This equation yields

$$\left|\varepsilon_m^{\pm}(x)\right| = \sqrt{\frac{\sqrt{1 + 4\mu_{\pm}^2\varepsilon_0^2} - 1}{2\mu_{\pm}^2}},$$

$$\theta_m^{+}(x) = \arcsin\left(\frac{\varepsilon_m^{+}}{\varepsilon_0}\right) + \frac{\gamma_1}{2}\varepsilon_m^{+}kx, \qquad (17)$$

$$\theta_m^{-}(x) = \pi + \arcsin\left|\frac{\varepsilon_m^{-}}{\varepsilon_0}\right| + \frac{\gamma_3}{2}\left|\varepsilon_m^{-}\right|kx,$$

where $\mu_{\pm} = (\gamma_{1,3} + \gamma_{2,4})kx/8$.

From the first of equations (17), it follows that, as in the medium with an inelastic hysteresis, at small distances from the source ($x \ll x_0 = \min[4/(\gamma_1 + \gamma_2)\varepsilon_0 k; 4/(\gamma_3 + \gamma_4)\varepsilon_0 k]$), the relation $\left|\varepsilon_m^{\pm}(x)\right| \cong \varepsilon_0$ is valid, but at large distances ($x \gg x_0$), the wave amplitude decreases according to a different law: $\left|\varepsilon_m^{\pm}(x)\right| = \sqrt{\varepsilon_0/\mu_{\pm}} \sim (\varepsilon_0/x)^{1/2}$.

To eliminate the ambiguities of the second type, in the wave profile, we introduce discontinuities determined from the following condition: the area cut off by the given discontinuity below the curve $\varepsilon = \varepsilon(x, \theta)$ at $\varepsilon > 0$ should be equal to that at $\varepsilon < 0$ (Fig. 2b) [42–44]. Since (at $\gamma_{1-4} > 0$) at small and large distances from the source, relations $\left|\varepsilon_{p1,2}^{\pm}(x)\right| \ll \varepsilon_0$ are valid, we can find the amplitudes $\varepsilon_{p1,2}^{\pm}(x)$ and phases $\theta_{p1,2}(x)$ of the discontinuities by using the approximate expression for $\varepsilon = \varepsilon(x, \theta)$ that follows from Eq. (8) and is valid near the discontinuities at any distances, and outside the discontinuities, at large distances:

$$\varepsilon(x, \theta) = \varepsilon_0\begin{cases} \dfrac{\theta}{1 + \dfrac{\gamma_1}{2}\varepsilon_0 kx}, & \theta_{p1} \le \theta < \theta_m^{+} \\ \dfrac{\pi - \theta + \theta_{+}^{*}}{1 + \dfrac{\gamma_2}{2}\varepsilon_0 kx}, & \theta_m^{+} \le \theta < \theta_{p2} \\ \dfrac{\pi - \theta}{1 + \dfrac{\gamma_3}{2}\varepsilon_0 kx}, & \theta_{p2} \le \theta < \theta_m^{-} \\ \dfrac{\theta - 2\pi - \theta_{-}^{*}}{1 + \dfrac{\gamma_4}{2}\varepsilon_0 kx}, & \theta_m^{-} \le \theta < 2\pi + \theta_{p1}; \end{cases} \qquad (18)$$

where $\theta_{\pm}^{*}(x) = 4\mu_{\pm}\left|\varepsilon_m^{\pm}(x)\right| + 2\arcsin\left|\dfrac{\varepsilon_m^{\pm}(x)}{\varepsilon_0}\right| - \pi$.

From the condition that the areas cut off by the discontinuities below the curve $\varepsilon = \varepsilon(x, \theta)$ are equal, at the discontinuity points $\theta_{p1,2}(x)$, we obtain

$$\varepsilon_{p1}^{+}(x) = \frac{\varepsilon_0\theta_{-}^{*}(x)}{(1 + \mu_1)\left(1 + \dfrac{\gamma_1}{2}\varepsilon_0 kx\right)},$$

$$\varepsilon_{p1}^{-}(x) = -\mu_1\frac{\varepsilon_0\theta_{-}^{*}(x)}{(1 + \mu_1)\left(1 + \dfrac{\gamma_4}{2}\varepsilon_0 kx\right)},$$

$$\theta_{p1}(x) = \frac{\theta_{-}^{*}(x)}{1 + \mu_1},$$

$$\varepsilon_{p2}^{+}(x) = \mu_2\frac{\varepsilon_0\theta_{+}^{*}(x)}{(1 + \mu_2)\left(1 + \dfrac{\gamma_2}{2}\varepsilon_0 kx\right)}, \qquad (19)$$

$$\varepsilon_{p2}^{-}(x) = -\frac{\varepsilon_0\theta_{+}^{*}(x)}{(1 + \mu_2)\left(1 + \dfrac{\gamma_3}{2}\varepsilon_0 kx\right)},$$

$$\theta_{p2}(x) = \pi + \frac{\theta_{+}^{*}(x)}{1 + \mu_2},$$

where $\mu_{1,2} = \sqrt{\dfrac{1 + \gamma_{4,2}\varepsilon_0 kx/2}{1 + \gamma_{1,3}\varepsilon_0 kx/2}}$.

Thus, at large distances, in a medium with an elastic hysteresis, the positive and negative half-periods of an initially harmonic wave acquire a pentagonal shape with the amplitudes decreasing according to the law $\left|\varepsilon_m^{\pm}(x)\right| \sim (\varepsilon_0/x)^{1/2}$.

Consider the spectral composition of the wave. At small distances, by analogy with Eq. (12), we have

$$\varepsilon(x,\theta) = \left(1-\frac{a_1\varepsilon_0 kx}{2\pi}\right)\Bigg[\varepsilon_0\sin(\theta - b_1\varepsilon_0 kx) + \varepsilon_0^2 kx\sum_{n=2}^{\infty} n\sqrt{a_n^2+b_n^2}\sin[n(\theta - b_1\varepsilon_0 kx)+\Psi_n]\Bigg], \tag{20}$$

$$\delta = a_1\varepsilon_0, \quad \Delta C/C_0 = b_1\varepsilon_0, \tag{21}$$

where

$$a_1 = \frac{\gamma_1+\gamma_2+\gamma_3+\gamma_4}{12}, \quad b_1 = \frac{1}{6\pi}\left\{\gamma_1-\gamma_2+\gamma_3-\gamma_4+\frac{3\pi}{8}(\gamma_1+\gamma_2+\gamma_3+\gamma_4)\right\},$$

$$a_2 = \frac{1}{12\pi}\left\{\gamma_1+\gamma_2-\gamma_3-\gamma_4+\frac{3\pi}{8}(\gamma_1-\gamma_2-\gamma_3+\gamma_4)\right\}, \quad b_2 = \frac{\gamma_1+\gamma_2-\gamma_3-\gamma_4}{24\pi},$$

$$a_n = \frac{\gamma_1+\gamma_2-(-1)^n(\gamma_3+\gamma_4)}{4\pi}\left\{\frac{(n^2-2)\sin\frac{\pi n}{2}}{(n^2-4)n} - \frac{(-1)^n + n\sin\frac{\pi n}{2}}{n^2-1}\right\},$$

$$b_n = \frac{2(n^2-1)[\gamma_1+(-1)^n(\gamma_2-\gamma_3)-\gamma_4]+[\gamma_1+\gamma_2-(-1)^n(\gamma_3+\gamma_4)]\cos\frac{\pi n}{2}}{4\pi n(n^2-1)(n^2-4)}, \quad \tan\Psi_n = \frac{a_n}{b_n}, \quad n>2.$$

At large distances (at $\gamma_1 = \gamma_4$, $\gamma_2 = \gamma_3$, when $\mu_+ = \mu_-$ and $\varepsilon_m^+ = |\varepsilon_m^-| = \varepsilon_m$), we obtain

$$\varepsilon(x,\theta) = \frac{2}{\pi\gamma_1\gamma_2}\sqrt{\frac{2(\gamma_1+\gamma_2)\varepsilon_0}{kx}} \times \sum_{n=1}^{\infty}\frac{\gamma_2-(-1)^n\gamma_1}{n}\sin n[\theta-\mu_+\varepsilon_m(x)], \tag{22}$$

$$\delta = \frac{\pi(\gamma_1+\gamma_2)}{2}\frac{\varepsilon_m^2}{\varepsilon_0}, \quad \frac{\Delta C}{C_0} = \frac{\gamma_1+\gamma_2}{8}\varepsilon_m. \tag{23}$$

From Eq. (22), it follows that the relative level of the first harmonic in this wave is determined by the simple expression

$$\zeta = \frac{\varepsilon_1}{\varepsilon_m} = \frac{1}{\pi}\frac{(\gamma_1+\gamma_2)^2}{\gamma_1\gamma_2}. \tag{24}$$

Expressions (16) and (24) will be used in the second part of our study to determine the amplitude of a steady-state wave in a ring resonator.

4. CONCLUSIONS

The comparison of Eqs. (12), (13) with Eqs. (20), (21) shows that, for small distances, the expressions obtained for the damping decrement, the variation of the wave velocity, and the amplitude of the second harmonic in the framework of the two hysteresis models are similar. Hence, by measuring these parameters, one can conclude whether the medium possesses (or does not possess) a hysteretic nonlinearity, but the type of hysteresis cannot be uniquely determined (without using additional physical considerations). However, certain distinctions manifest themselves in the wave profiles: in a medium with an inelastic hysteresis, the wave has no discontinuities, while in a medium with an elastic hysteresis, two discontinuities occur within one wave period. These distinctions lead to a difference in the spectral composition of waves: in a medium with an inelastic hysteresis, even harmonics higher than the second one are absent, while in a medium with an elastic hysteresis, these harmonics are present.

From Eqs. (12) and (13), it follows that, for the determination of the three independent nonlinear parameters of the inelastic hysteresis, α and $\beta_{1,2}$, it is necessary to measure at least three independent parameters of the wave: the damping decrement, the relative velocity variation, and the amplitude of the second harmonic. Then, the amplitudes of higher harmonics will be uniquely determined by these quantities. On the other hand, from the experimentally measured amplitude of one of these higher harmonics (e.g., the third one), it is also possible to determine independently the

value of the parameter $\beta_1 + \beta_2$, which was found earlier from the measurement of the damping decrement. The comparison of the values of $\beta_1 + \beta_2$ obtained from the two independent measurements allows one to judge whether the inelastic hysteresis is valid (if the values are close) or invalid (if the values are different) for describing the medium under study.

From Eqs. (20) and (21), it follows that, to determine the four independent nonlinear parameters γ_{1-4} of the elastic hysteresis, it is necessary to measure no less than four independent parameters of the wave at a given distance x: the damping decrement, the relative velocity variation, the amplitude of an even (e.g., second) harmonic, and its phase Ψ_2 (relative to the second harmonic of the fundamental frequency wave received at the same distance x). In this case, the amplitudes of higher harmonics and their phases Ψ_n (relative to the phase of the nth harmonic of the fundamental frequency wave at the same distance) will be uniquely determined by these quantities. (The phase of the second harmonic in the medium should be determined with respect to the phase of the second harmonic of the wave received at the fundamental frequency. For this purpose, one should take the square of the received fundamental frequency wave and select from it the second "instrumental" harmonic. After this, the phase of the wave corresponding to the second harmonic in the medium should be compared with the phase of the aforementioned "instrumental" second harmonic.)

Using the experimentally measured amplitudes and phases of higher harmonics, it is possible to determine independently the values of the parameters a_n and b_n, and, from the latter, to derive the values of the parameters a_1 and b_1. The comparison of the values obtained for the parameters a_1 and b_1 from two pairs of independent measurements allows one to judge whether the elastic hysteresis is suitable (or unsuitable) for describing the given medium. A similar procedure has been used earlier [3, 8, 9, 11, 14] for analytically describing the nonlinear acoustic effects in bar resonators made of metals and rocks whose equations of state were determined by an elastic hysteresis. In the cited publications, the values of the nonlinear parameters determined from the resonance frequency shift, the nonlinear loss, and the level of higher harmonics were in good agreement with each other.

As one can see from Eqs. (14), (15) and (22), (23), the qualitative distinctive features that allow one to choose the appropriate type of hysteresis for describing a given medium manifest themselves in the wave at large distances $x \ll x_0 \sim (\gamma_0 k\varepsilon_0)^{-1}$, where $\gamma_0 = [(\beta_1 + \beta_2)/4, \max\{(\gamma_1 + \gamma_2)/4, (\gamma_3 + \gamma_4)/4\}]$ is the effective parameter of hysteretic nonlinearity. These features manifest themselves in the wave form, the amplitude dependence of the damping decrement, and the dependences of the wave amplitude on the initial amplitude and the distance. However, it should be noted that not every medium with hysteretic nonlinearity allows the realization of highly nonlinear wave propagation. This is explained by the fact that the expressions derived above are valid for distances $x \ll L_0 = 2C_0^3/\eta\omega^2$, while considerable nonlinear distortions of a wave occur at the distances $x \geq x_0$. Therefore, strictly speaking, for the realization of such wave propagation conditions, the following inequality should be satisfied: $x_0 \ll L_0$, or $\varepsilon_0 \gg \vartheta/2\pi\gamma_0$, where $\vartheta = \pi\eta\omega/C_0^2$ is the damping decrement. Estimates show that, e.g., for annealed copper and for granite, at $\vartheta \cong 10^{-2}$, $\eta = 1.6 \times 10^2$ cm^2/s, $\gamma_0 \cong 10^4$ [3, 11, 46], and $\omega \cong 2 \times 10^4$ s^{-1} ($L_0 = 10^4$ cm, $x_0 = 1.6 \times 10^3$ cm), the amplitude ε_0 should be greater than 2×10^{-7} ($\gamma_0 \mathrm{Re} = 2\gamma_0\rho C_0^2\varepsilon_0/\eta\omega \geq 6 \times 10^2$). Nevertheless, the proposed procedure of determining the type of hysteretic equation of state can also be used at smaller strains and for other solids with the damping decrement ϑ greater and the nonlinear parameter γ smaller than the chosen values, because the character of the nonlinear wave processes (the amplitude dependence of the nonlinear loss and the variations of the wave velocity and the levels of higher harmonics) is determined by the nonlinearity of the solid rather than by its viscosity η (or damping decrement ϑ).

ACKNOWLEDGMENTS

This work was supported by the Russian Foundation for Basic Research, project nos. 01-05-64417 and 00-05-64252.

REFERENCES

1. L. D. Landau and E. M. Lifshitz, *Course of Theoretical Physics*, Vol. 7: *Theory of Elasticity*, 4th ed. (Nauka, Moscow, 1987; Pergamon, New York, 1986).
2. L. K. Zarembo and V. A. Krasil'nikov, *Introduction to Nonlinear Acoustics* (Nauka, Moscow, 1966).
3. V. E. Nazarov, Fiz. Met. Metalloved. **37** (1), 150 (1991).
4. V. Yu. Zaĭtsev, A. B. Kolpakov, and V. E. Nazarov, Akust. Zh. **45**, 235 (1999) [Acoust. Phys. **45**, 196 (1999)].
5. A. Granato and K. Lucke, J. Appl. Phys. **27** (5), 583 (1956).
6. *Ultrasonic Methods for Studying Dislocations*, Ed. by L. G. Merkulov (Inostrannaya Literatura, Moscow, 1963).
7. O. V. Pavlenko, Bull. Seismol. Soc. Am. **91** (2), 381 (2001).
8. V. E. Nazarov, L. A. Ostrovsky, I. A. Soustova, and A. M. Sutin, Phys. Earth Planet. Inter. **50** (1), 65 (1988).
9. V. E. Nazarov, L. A. Ostrovskiĭ, I. A. Soustova, and A. M. Sutin, Akust. Zh. **34**, 491 (1988) [Sov. Phys. Acoust. **34**, 285 (1988)].
10. V. E. Nazarov and A. M. Sutin, Akust. Zh. **35**, 711 (1989) [Sov. Phys. Acoust. **35**, 410 (1989)].
11. S. V. Zimenkov and V. E. Nazarov, Fiz. Zemli, No. 1, 13 (1993).

12. V. E. Nazarov, Fiz. Met. Metalloved. **88** (4), 82 (1999).
13. V. E. Nazarov, Akust. Zh. **46**, 228 (2000) [Acoust. Phys. **46**, 186 (2000)].
14. V. E. Nazarov and A. B. Kolpakov, J. Acoust. Soc. Am. **107**, 1915 (2000).
15. K. R. McCall and R. A. Guyer, J. Geophys. Res. **99**, 23887 (1994).
16. K. R. McCall and R. A. Guyer, Nonlinear Processes Geophys. **3**, 89 (1996).
17. J. A. TenCate, K. E.-A. Van Den Abeele, T. J. Shanklad, and P. A. Johnson, J. Acoust. Soc. Am. **100**, 1383 (1996).
18. K. E.-A. Van Den Abeele, P. A. Johnson, R. A. Guyer, and K. R. McCall, J. Acoust. Soc. Am. **101**, 1885 (1997).
19. R. A. Guyer and P. A. Johnson, Phys. Today, No. 4, 30 (1999).
20. F. Priesach, Z. Phys. **94**, 277 (1935).
21. I. D. Mayergoyz, J. Appl. Phys. **57**, 3803 (1985).
22. V. Gusev, C. Glorieux, W. Lauriks, and J. Thoen, Phys. Lett. A **232**, 77 (1997).
23. V. Gusev, W. Lauriks, and J. Thoen, J. Acoust. Soc. Am. **103**, 3216 (1998).
24. V. Gusev, Acoust. Lett. **22** (2), 30 (1998).
25. V. Gusev, H. Bailliet, P. Lotton, and M. Bruneau, Wave Motion **29**, 211 (1999).
26. V. Gusev, J. Acoust. Soc. Am. **107**, 3047 (2000).
27. V. E. Nazarov, A. V. Radostin, and I. A. Soustova, in *Proceedings of 3rd Scientific Conference on Radiophysics*, Ed. by A. V. Yakimov (Nizhni Novgor. Gos. Univ., Nizhni Novgorod, 1999), p. 246.
28. V. E. Nazarov, A. V. Radostin, and I. A. Soustova, Akust. Zh. **48**, 85 (2002) [Acoust. Phys. **48**, 76 (2002)].
29. G. S. Pisarenko, *Vibrations of Mechanical Systems with Allowance for Imperfect Elasticity of Material* (Naukova Dumka, Kiev, 1970).
30. S. Asano, J. Phys. Soc. Jpn. **29** (4), 952 (1970).
31. A. B. Lebedev, Fiz. Tverd. Tela (St. Petersburg) **41**, 1214 (1999) [Phys. Solid State **41**, 1105 (1999)].
32. N. N. Davidenkov, Zh. Tekh. Fiz. **8** (6), 483 (1938).
33. J. S. Koehler, *Imperfections in Nearly Perfect Crystal* (Wiley, New York, 1952).
34. *Physical Acoustics: Principles and Methods*, Ed. by W. P. Mason (Academic, New York, 1966; Mir, Moscow, 1969), Vol. 4, Part A.
35. *Physical Acoustics: Principles and Methods*, Ed. by W. P. Mason (Academic, New York, 1966; Mir, Moscow, 1969), Vol. 3, Part A.
36. T. A. Read, Phys. Rev. **58**, 371 (1940).
37. N. G. W. Cook and K. Hodson, J. Geophys. Res. **70**, 2883 (1965).
38. S. B. Kustov, S. N. Golyandin, and B. K. Kardashev, Fiz. Tverd. Tela (Leningrad) **30**, 2167 (1988) [Sov. Phys. Solid State **30**, 1248 (1988)].
39. S. B. Kustov, S. N. Golyandin, A. V. Nikiforov, and B. K. Kardashev, Fiz. Tverd. Tela (Leningrad) **31** (2), 260 (1989) [Sov. Phys. Solid State **31**, 326 (1989)].
40. S. N. Golyandin and S. B. Kustov, Fiz. Tverd. Tela (Leningrad) **34**, 3796 (1992) [Sov. Phys. Solid State **34**, 2031 (1992)].
41. S. N. Golyandin and S. B. Kustov, Fiz. Tverd. Tela (St. Petersburg) **37**, 3248 (1995) [Phys. Solid State **37**, 1786 (1995)].
42. L. D. Landau and E. M. Lifshitz, *Course of Theoretical Physics*, Vol. 6: *Fluid Mechanics*, 4th ed. (Nauka, Moscow, 1986; Pergamon, New York, 1987).
43. K. A. Naugol'nykh and L. A. Ostrovskiĭ, *Nonlinear Wave Processes in Acoustics* (Nauka, Moscow, 1990).
44. O. V. Rudenko and S. I. Soluyan, *Theoretical Foundations of Nonlinear Acoustics* (Nauka, Moscow, 1975; Consultants Bureau, New York, 1977).
45. V. E. Nazarov, Akust. Zh. **43**, 225 (1997) [Acoust. Phys. **43**, 192 (1997)].
46. *Physical Acoustics: Principles and Methods*, Ed. by W. P. Mason (Academic, New York, 1965; Mir, Moscow, 1968), Vol. 3, Part B.

Translated by E. Golyamina

Acoustical Physics, Vol. 49, No. 3, 2003, pp. 354–360. Translated from Akusticheskiĭ Zhurnal, Vol. 49, No. 3, 2003, pp. 416–424.

Reconstruction of the Normal Velocity Distribution on the Surface of an Ultrasonic Transducer from the Acoustic Pressure Measured on a Reference Surface

O. A. Sapozhnikov, Yu. A. Pishchal'nikov, and A. V. Morozov

Physics Faculty, Moscow State University, Moscow, 119992 Russia

e-mail: oleg@acs366.phys.msu.ru

Received May 8, 2002

Abstract—In piezoceramic ultrasonic transducers, the thickness vibrations are usually accompanied by the excitation of Lamb waves, which are difficult to control. Therefore, the normal velocity distribution over the radiating surface is unknown. As a result, the ultrasonic field generated by the transducer cannot be predicted with the desired accuracy. The purpose of this study is to develop and experimentally validate a new method for evaluating the normal velocity distribution over the surface of an ultrasonic transducer. The method consists in measuring the amplitude and phase of the acoustic pressure field over a certain reference surface and then calculating the acoustic field at the transducer by using the Rayleigh integral. The accuracy and stability of the method are illustrated numerically. The method is tested experimentally with a focused piezoceramic transducer. In the experiment, the reference surface is represented by a plane perpendicular to the axis of the acoustic beam. The ultrasonic field is scanned by a needle hydrophone, which is moved by a micropositioner. The measurements show that the method provides an accurate prediction of the acoustic field generated by a source with an unknown nonuniform normal velocity distribution. © *2003 MAIK "Nauka/Interperiodica"*.

INTRODUCTION

Piezoceramic transducers are widely used in visualization, ultrasonic therapy, nondestructive testing, and acoustic microscopy. To theoretically predict the acoustic fields they emit, it is necessary to know the normal velocity and acoustic pressure distributions on the radiating surface. The Rayleigh integral approximation [1], which represents the acoustic pressure at a given point in space as a superposition of spherical waves whose amplitudes are proportional to the normal velocity component at the corresponding points of the transducer, is most commonly used. For simplicity, it is usually assumed that the vibrations of a piezoceramic plate are determined by the thickness mode, i.e., that they are uniform over the radiating surface. However, the accuracy of this approximation is not very high, because the thickness vibrations of piezoceramic transducers are accompanied by other modes that are difficult to control, in particular, by the Lamb waves [2, 3]. Therefore, the distribution of the normal velocity over the transducer surface is nonuniform. It is difficult to theoretically predict the structure of the elastic vibrations of a piezoceramic plate, because the boundary conditions, which depend on the manner the plate is fixed to the body, and the electromechanical parameters of the piezoceramic material are known with a limited accuracy. At first sight, the optical interferometry method can be used to directly measure the normal velocity of the transducer surface vibrations. However, such measurements are only possible for a source operated in air. If the transducer operates in water, the acoustooptical interaction in the liquid plays a significant role. As a result, the signal from the interferometer cannot be explicitly related to the displacement of the surface [2]. Thus, the normal velocity (and, all the more so, the acoustic pressure) distribution over the piezoelectric transducer is actually unknown.

In this paper, we propose a method for reconstructing the normal velocity and the acoustic pressure on the surface of a transducer. The idea of the method is to use the time reversibility of the wave process [4]. The reconstruction procedure consists of two stages. First, the amplitude and phase of the wave is measured over a certain reference surface in front of the transducer. Second, the phase of the wave is reversed and the acoustic field is calculated numerically on the surface of the transducer by using the Rayleigh integral over the reference surface. Similar approaches were proposed earlier for calculating the acoustic fields produced by transducers. One of them represents the transducer as a multielement antenna array. The acoustic pressure measured experimentally at a number of points on the reference surface is expressed as a superposition of spherical waves produced by individual array elements and,

1063-7710/03/4903-0354$24.00 © 2003 MAIK "Nauka/Interperiodica"

then, the resultant system of linear algebraic equations is solved for the particle velocity on these elements [5]. The method has a clear limitation associated with the necessity to numerically solve systems of complex linear equations of a very high order. For example, if the pressure is measured over a 100×100 grid, the number of equations is 10000, which makes the solution of the problem by a personal computer actually impossible. The other method relies on the angular spectrum calculated from the parameters of the wave measured over the reference surface perpendicular to the acoustic axis. Theoretically, the field at other points in space can be calculated exactly from the angular spectrum and, in particular, the source distribution over an emitting surface can be reconstructed. In the practical realization, the accuracy of reconstructing the spatial source distribution can be limited by irregularities greater than the wavelength, because small-scale features of the distribution correspond to exponentially decaying (inhomogeneous) components of the angular spectrum. If the inhomogeneous waves are taken into account, the accuracy proves to be rather high. Such an approach is the basis of the so-called near-field acoustic holography [6–8]. Unfortunately, it is only applicable to comparatively low-frequency waves, for which the field can be measured at distances from the transducer that are smaller than or comparable to the wavelength. In the megahertz frequency range (medical applications and nondestructive testing), the distance between the measurement plane and the transducer is, as a rule, much longer than the wavelength. Therefore, the information on the high-frequency components of the angular spectrum is lost and, for the reconstruction algorithm to be stable, the inhomogeneous components of the spectrum must be set equal to zero [9–11]. As we noted above, this leads to a certain smoothing of the reconstructed distribution, as compared to the true one. A similar limitation is also inherent in the method considered in this paper. However, it should be noted that, unlike the angular spectrum method, the approach proposed below calculates a two-dimensional integral only once (the angular spectrum method performs the two-dimensional integration twice). In addition, in the phase reversal method, the surface over which the wave parameters are measured can be nonplanar. This advantage may be very useful in the studies of transducers that generate strongly divergent acoustic beams.

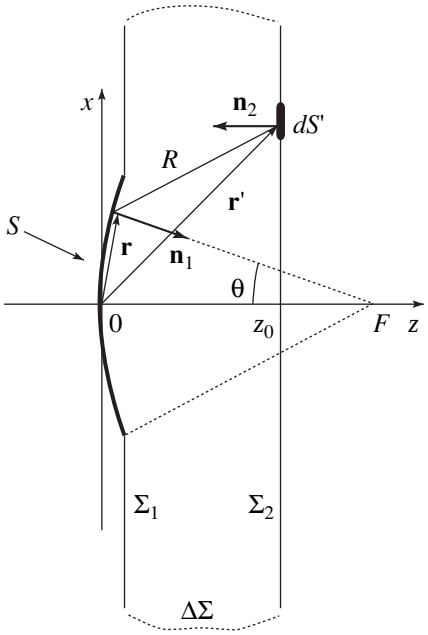

Fig. 1. Geometry of the problem.

THEORY

Consider an acoustic transducer built into a planar screen. Let the surface of the transducer with the screen be Σ_1 (Fig. 1), and let the acoustic pressure $p_2(\mathbf{r}, t)$ be measured on a plane surface Σ_2 that is parallel to the screen. The question arises of whether it is possible to reconstruct the acoustic field $p_1(\mathbf{r}, t)$ over the surface Σ_1 from the known distribution $p_2(\mathbf{r}, t)$. An affirmative answer to this question follows from the time reversibility of the wave process. In fact, the wave equation in a lossless medium, $\Delta p - c^{-2}\partial^2 p/\partial t^2 = 0$, does not change under the substitution $t \longrightarrow -t$. If the transducer is enclosed in a surface that is a perfect time-reversing (or, to put it differently, wave-front-reversing) mirror, the wave propagating to the transducer after the reflection from such a mirror completely reproduces its original parameters. As such a closed surface, we may take the surface consisting of Σ_1, Σ_2, and a side surface $\Delta\Sigma$ removed to infinity (see Fig. 1). However, the contribution due to $\Delta\Sigma$ vanishes, because the solid angle subtended by this surface tends to zero. The contribution of the surface Σ_1 can also be neglected, because the radiation in this direction is small. Hence, we can assume that, if the acoustic pressure on the plane Σ_2 is known, this data is sufficient to reconstruct the field on the transducer surface. The accuracy of the method is limited to about a wavelength; i.e., finer features are smoothed out. Indeed, the field reconstruction at a certain point on the transducer surface can be thought of as focusing of the phase-reversed field, so that the well-known diffraction limitation on the size of the focal spot necessarily manifests itself.

We restrict our analysis to a monochromatic source. In this case, the acoustic pressure can be represented as $p(\mathbf{r}, t) = |A|\cos(\omega t - \varphi) = (Ae^{-i\omega t} + A^* e^{i\omega t})/2$, where $|A|$ and φ are the wave amplitude and phase and ω is the circular frequency, so that $A(\mathbf{r}) = |A|e^{i\varphi}$ is the complex wave amplitude. We assume that the acoustic pressure on the reference plane Σ_2 is known from the measurements. If we mentally place a time-reversing mirror on Σ_2, the acoustic pressure in the reflected wave will have

the form $p(\mathbf{r}, -t) = (Ae^{i\omega t} + A^*e^{-i\omega t})/2 = (A_{\text{rev}}e^{-i\omega t} + A^*_{\text{rev}}\, e^{i\omega t})/2$; i.e., the amplitude of the time-reversed wave will be a complex conjugate of that of the incident wave: $A_{\text{rev}} = A^*$. To calculate the reflected wave on the left of Σ_2, we can use the Kirchhoff–Helmholtz integral, which represents the amplitude of the acoustic field emitted by a surface in terms of the normal velocity and acoustic pressure distributions over this surface. As is known, if the emitting surface is planar, the Kirchhoff–Helmholtz integral can be reduced to integrals that contain the distribution of either normal velocity or acoustic pressure alone [12]. In particular, if we use the acoustic pressure distribution, the Kirchhoff–Helmholtz integral has the form

$$A_{\text{rev}}(\mathbf{r}) = 2\int_{\Sigma_2} A_{\text{rev}}(\mathbf{r}')\frac{\partial G(\mathbf{r}, \mathbf{r}')}{\partial n_2(\mathbf{r}')}dS', \qquad (1)$$

where $G(\mathbf{r}, \mathbf{r}') = e^{ik|\mathbf{r}-\mathbf{r}'|}/4\pi|\mathbf{r}-\mathbf{r}'|$ is the Green's function of free space, k is the wave number, $\mathbf{n}_2(\mathbf{r}')$ is the unit outer normal to the surface Σ_2, and dS' is the element of this surface (Fig. 1). Since $A_{\text{rev}} = A^*$, we arrive at the expression for the original wave on the left of the plane Σ_2 in terms of the known wave amplitude distribution on Σ_2:

$$A(\mathbf{r}) = 2\int_{\Sigma_2} A(\mathbf{r}')\frac{\partial G^*(\mathbf{r}, \mathbf{r}')}{\partial n_2(\mathbf{r}')}dS'. \qquad (2)$$

With the position vector $\mathbf{r}$ placed on the surface Σ_1, this formula yields the unknown amplitude of the acoustic pressure on the transducer and the screen. To find the normal velocity component, we use the equation of motion. Let $V_n(\mathbf{r})$ be the complex amplitude of the normal component of the particle velocity $\mathbf{v}$. The equation of motion $\rho_0\partial\mathbf{v}/\partial t = -\nabla p$ yields $V_n(\mathbf{r}) = -(i/\omega\rho_0)\partial A/\partial n_1$, where ρ_0 is the density of the medium and $\mathbf{n}_1$ is the unit normal to the surface Σ_1. With Eq. (2), we have

$$V_n(\mathbf{r}) = -\frac{2i}{\omega\rho_0}\int_{\Sigma_2} A(\mathbf{r}')\frac{\partial^2 G^*(\mathbf{r}, \mathbf{r}')}{\partial n_1(\mathbf{r})\partial n_2(\mathbf{r}')}dS'. \qquad (3)$$

Expressions (2) and (3) constitute the theoretical basis of the method. As we can see, the acoustic pressure and the normal velocity component on the emitting surface can rather easily be reconstructed from the measured amplitude and phase distributions of the acoustic pressure over a certain reference surface Σ_2. Theoretically, the distance between the plane Σ_2 and the transducer can be arbitrary.

Note that formula (3) is derived under the assumption that the transducer is planar. For nonplanar transducers, an error associated with multiple reflections from the curved emitting surface takes place. However, for transducers with a small curvature and large wave dimensions of their surfaces, which are of interest in most applications, the error should be insignificant.

NUMERICAL MODELING OF A FOCUSED TRANSDUCER

In view of the experiment described in the following section, we consider an acoustic transducer in the form of a spherical bowl (surface S in Fig. 1). Such concave piezoelectric plates are widely used to produce focused ultrasonic beams in medical applications and in nondestructive testing. Due to the axial symmetry of the transducer, there is no need in measuring the amplitude and phase over the entire plane Σ_2. It is sufficient to perform one-dimensional measurements along the radius.

We consider only the normal velocity component on the transducer surface. Introducing the notation

$$K(\mathbf{r}, \mathbf{r}') = -\frac{2i}{\omega\rho_0}\frac{\partial^2 G^*(\mathbf{r}, \mathbf{r}')}{\partial n_1(\mathbf{r})\partial n_2(\mathbf{r}')}, \qquad (4)$$

we represent Eq. (3) in the form

$$V_n(\mathbf{r}) = \int_{\Sigma_2} A(\mathbf{r}')K(\mathbf{r}, \mathbf{r}')dS'. \qquad (5)$$

Here, A is the measured complex amplitude of the sinusoidal wave in the plane Σ_2. Let us make use of the axial symmetry of the problem. We characterize the position of the observation point on the spherical surface of the transducer by the angle θ between the symmetry axis and the straight line that passes through the observation point and the center of curvature of the transducer surface. To calculate integral (5), we introduce the polar coordinates (ξ, ψ) on the Σ_2 plane: $\mathbf{r}' = (\xi\cos\psi, \xi\sin\psi, z_0)$. Calculating the derivatives that enter into Eq. (4) along the normals by taking into account their directions (Fig. 1), we arrive at the following expression for kernel (4):

$$K(\mathbf{r}, \mathbf{r}') = \tilde{K}(\xi, \psi, \theta)$$
$$= -\frac{i}{\omega\rho_0}\frac{e^{-ikR}}{2\pi}\left\{(3\gamma + \cos\theta)\left(\frac{1}{R^3} + \frac{ik}{R^2}\right) - \gamma\frac{k^2}{R}\right\}, \qquad (6)$$

where

$$R = \{F^2 + \xi^2 + (F - z_0)^2$$
$$- 2F\xi\sin\theta\cos\psi - 2F(F - z_0)\cos\theta\}^{1/2}$$

is the distance between the observation point $\mathbf{r}$ and the point $\mathbf{r}'$ on the surface and $\gamma = [F(1 - \cos\theta) - z_0][F - \xi\sin\theta\cos\psi - (F - z_0)\cos\theta]/R^2$. The reference plane Σ_2 is at the distance z_0 from the center of the transducer,

and the center of curvature of the emitting surface, at the distance F (Fig. 1). Integral (5) takes the form

$$V_n(\theta) = \int_0^{2\pi} d\psi \int_0^{\xi_{\max}} \tilde{K}(\xi, \psi, \theta) A(\xi) \xi d\xi, \qquad (5a)$$

where $V_n(\theta)$ is the amplitude of the normal velocity on the transducer surface at the points corresponding to the angle θ, $A(\xi)$ is the pressure amplitude on the reference plane at the distance ξ from the symmetry axis, and $\xi_{\max}$ is the radius of the measurement region. The functions V_n and A depend on one variable each because of the axial symmetry. Integral (5a) can be calculated approximately as a sum over small surface elements of nearly the same area into which the circular measurement region of radius $\xi_{\max}$ is divided.

When implementing this method in practice, a number of questions arise, in particular, the questions of where is the best place for the reference plane; how wide the limits should be, where the field is measured on the reference plane, and what the step size should be; how does the error in the sound velocity affect the reconstruction accuracy; etc. To answer these questions, we used mathematical simulations. We studied a focused monochromatic transducer. Using the Rayleigh integral [13]

$$A(\mathbf{r}') = -i\frac{\rho_0 \omega}{2\pi} \int_{\Sigma_1} \frac{V_n(\mathbf{r}) e^{ik|\mathbf{r}-\mathbf{r}'|}}{|\mathbf{r}-\mathbf{r}'|} dS, \qquad (7)$$

we numerically calculated the acoustic pressure amplitude $A(\mathbf{r}')$ at different points of the reference plane. The initial normal velocity distribution was taken to be uniform: $V_n(\mathbf{r}) = 1$. Assuming that the calculated data $A(\mathbf{r}')$ represent some experiment, we used formula (5) to reconstruct the normal velocity distribution on the transducer surface. The result was compared with the initial (uniform) distribution $V_n(\mathbf{r})$.

Figure 2 shows the amplitude and phase of the velocity $V_n(\mathbf{r})$ on the transducer surface that were reconstructed for different positions of the reference plane. The horizontal axis represents the angle θ at which the points on the transducer surface are seen (θ = 0° corresponds to the center of the transducer, and θ = 14°, to its edge). The calculations were performed with the same parameters as the experiment described in the next section: the ultrasonic frequency was f = 1.1 MHz, the velocity of sound was c_0 = 1476 m/s, the radius of the measurement region was $\xi_{\max}$ = 6 cm, the transducer diameter was 10 cm, the transducer surface curvature radius was F = 22 cm, and the measurement step was 0.3 mm. As we see from this figure, the position of the reference plane, in which the acoustic pressure is measured, actually does not affect the reconstructed normal velocity.

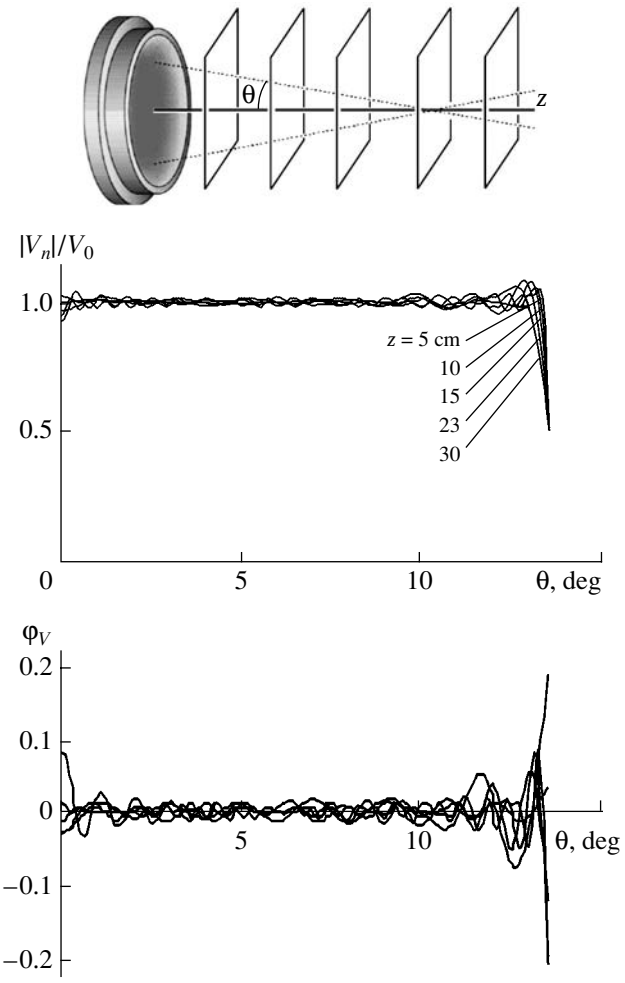

Fig. 2. Reconstruction of the normalized amplitude $|V_n|/V_0$ and phase φ_V (in radians) of the normal velocity on the transducer surface for different distances between the reference plane and the transducer: z_0 = 5, 10, 15, 23, and 30 cm; the horizontal axis represents the angle at which the points of the transducer surface are seen from the focal point: θ = 0° corresponds to the center of the transducer, and θ = 14°, to its edge.

Another source of error in the reconstructed distribution $V_n(\mathbf{r})$ may be an error in the value of the sound velocity. We estimated this effect on the accuracy of the method through the appropriate numerical modeling. As we described above, we calculated the field distribution in the reference plane from the Rayleigh integral under the assumption that the particle velocity distribution over the transducer surface is uniform. This "measured" distribution of the complex pressure amplitude was used to reconstruct the velocity at the transducer surface from formula (5) with another, perturbed, sound velocity value. Figure 3 presents the normal velocity reconstructed with the error Δc = 25 m/s introduced into the velocity of sound, which corresponds to a 10°C variation in the water temperature. For the sake

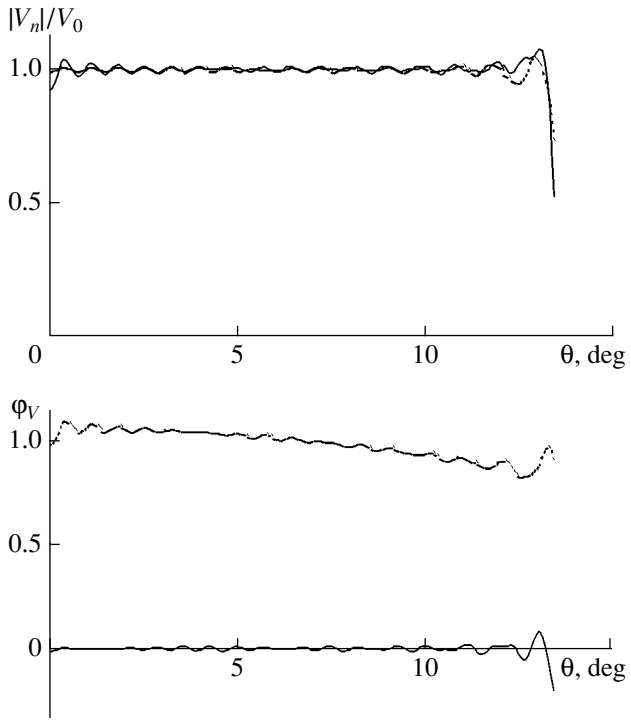

Fig. 3. Effect of the error Δc = 25 m/s introduced into the velocity of sound c_0 = 1476 m/s (which corresponds to a 10°C variation in the water temperature) on the normalized amplitude $|V_n|/V_0$ and phase φ_V (in radians) distributions of the normal velocity over the transducer surface.

of comparison, the dotted line shows the result of reconstruction for the unperturbed velocity of sound c_0 = 1476 m/s. Since the velocity of sound has changed, the phase acquires a certain shift. However, the initial uniform velocity amplitude distribution proves to be almost insensitive to the variation in the velocity of sound and is reconstructed with a sufficiently high accuracy.

EXPERIMENT

A concave piezoceramic transducer with a curvature radius F = 22 cm, a diameter of 10 cm, and a resonance frequency of 1.1 MHz was placed into a $60 \times 24 \times 30$-cm dish filled with settled tap water. The acoustic pressure was measured with a PVDFZ44-0400 SEA needle hydrophone with a sensitive region of 0.4 mm in diameter. After a preamplification, the hydrophone signal was recorded with a 520A Textronix digital oscilloscope. The hydrophone could be moved in three orthogonal directions with an accuracy of 0.01 mm by a Velmex-Unislide micropositioning system. A computer, which ran programs from the National Instruments (Austin, Tex.) in LabView language, was used to control the micropositioner and to read the signals from the oscilloscope. To avoid the effect of reverberation, the measurements used the pulsed operating mode. A rectangular high-frequency electric pulse was supplied to the transducer from an HP 33120A signal source. To model the operation in the CW mode, the pulse duration and the measurement time window were chosen so that the transient processes in the transducer and the hydrophone would be terminated while the signals reflected from the hydrophone body, the walls of the dish, etc. would not yet be received.

The experiment was conducted as follows. At first, we found the position of the symmetry axis (the 0z axis in Fig. 1), whose direction generally coincided with none of the micropositioner axes. To this end, the acoustic pressure amplitude distribution was measured at a certain distance from the transducer in a plane that was approximately orthogonal to the transducer axis. Based on these measurements, the program plotted the equiamplitude lines on the computer screen. They had the form of concentric circles with the center assumably lying on the symmetry axis of the transducer. Then, the hydrophone was placed at this point (center), and the time delay in the signal arrival was measured. After that, the hydrophone was moved a certain distance away from the transducer and the measurement procedure was repeated to determine the second point lying on the axis and to measure the delay in the signal arrival. The coordinates of the two points uniquely determined the symmetry axis, while the velocity of sound in water was calculated from the two delays and the distance between the points. Subsequently, special programs were used to measure the field in the plane orthogonal to the symmetry axis determined above. One of the resulting amplitude and phase distributions of acoustic pressure is shown in Fig. 4. The two-dimensional (upper) images illustrate the amplitude (on the left) and phase (on the right) distributions of acoustic pressure. The phase was measured relative to the signal fed to the transducer from the oscillator. As we see from these distributions, the axial symmetry of the acoustic field is quite pronounced. This means that the time taken to perform the experiment can be considerably reduced using the one-dimensional scan in any direction orthogonal to the symmetry axis instead of the two-dimensional scan. The corresponding one-dimensional amplitude and phase distributions are presented in the lower part of Fig. 4.

After the transverse amplitude and phase distributions of acoustic pressure were measured, the corresponding complex amplitude distribution of the field in the reference plane was calculated. Following the method proposed above, we used Eqs. (5a) and (6) to numerically reconstruct the distribution of the complex amplitude of the velocity over the transducer surface. Figure 5 shows the result of the reconstruction in the form of the dependences of the amplitude and phase of the normal particle velocity component on the angle θ. The acoustic pressure was measured at a distance z_0 =

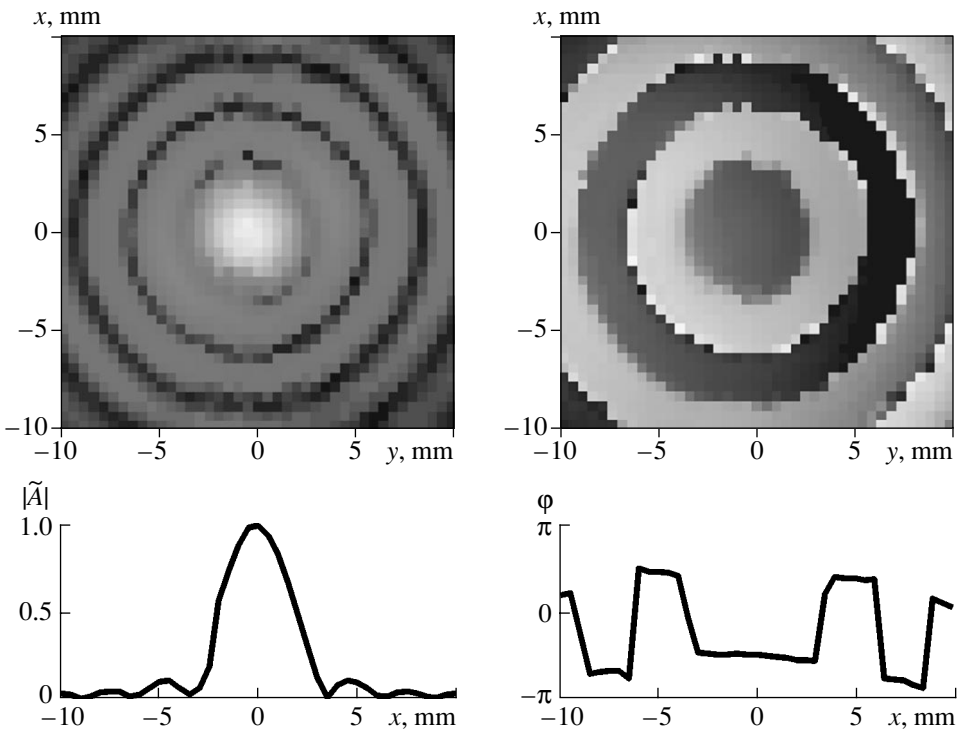

Fig. 4. Measured distributions of the normalized amplitude $|\tilde{A}| = |A|/A_0$ and phase φ of the acoustic pressure in the focal plane z = 220 mm. The upper panels show the two-dimensional distributions in the (x, y) coordinates represented as shades of gray with higher values corresponding to lighter shades. The point $(x, y) = (0, 0)$ corresponds to the hydrophone position on the transducer axis. The lower panels show the one-dimensional amplitude and phase (in radians) distributions along the transverse x axis.

214 mm from the transducer. One can see that the reconstructed amplitude and phase distributions of the particle velocity are nonuniform. They exhibit pronounced maxima and minima associated with the Lamb waves in the piezoceramic plate [2]. In particular, the velocity amplitude maximum at the center of the transducer (θ = 0°) is almost twice as high as the average amplitude of the particle velocity. For comparison, the thin line illustrates the numerical simulation under the assumption that the initial velocity distribution is uniform (see the previous section).

Note that the velocity reconstruction from the acoustic pressure measured at different distances from the transducer gives the same results. Figure 6 shows the normal velocity distributions reconstructed from the pressure measured at z_0 = 136, 165, and 214 mm. The plots demonstrate a qualitatively similar behavior; in particular, the positions and amplitudes of their maxima and minima almost coincide. Minor differences occur, because real transducers are not exactly axially symmetric and, in the general case, the reconstruction procedure should use the acoustic pressure measured over the entire plane rather than along a single line.

Using Rayleigh integral (7) and the reconstructed normal velocity on the transducer surface, one can calculate the acoustic field at any point of space. The comparison of this field with the field measured experimen-

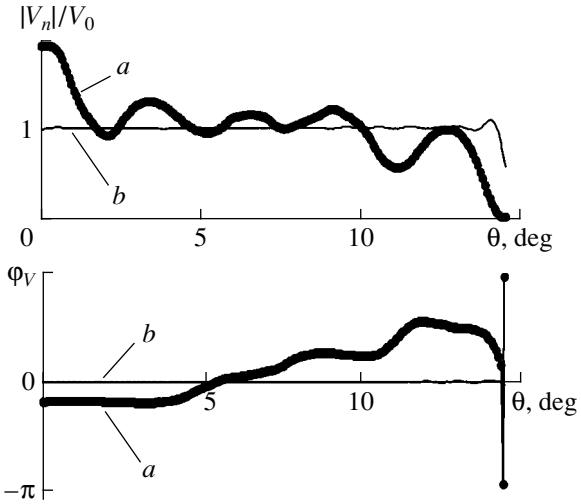

Fig. 5. Reconstruction of the normalized amplitude $|V_n|/V_0$ and phase φ_V distributions of the particle velocity over the transducer surface from the acoustic pressure measured along the transverse x axis at the distance z_0 = 214 mm from the transducer (curves *a*). The thin lines (curves *b*) show the distributions reconstructed from the theoretical pressure distributions created by a piston transducer at this distance. The angle θ = 0° corresponds to the center of the transducer, and the angle θ = 14°, to its edge.

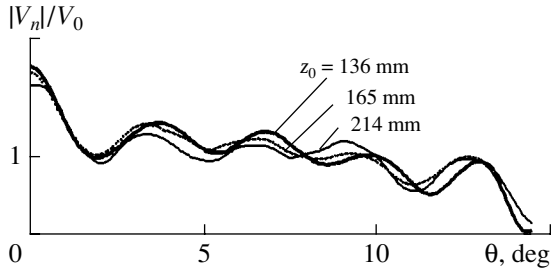

Fig. 6. Reconstruction of the velocity distributions over the transducer surface from the pressure measured along the normal to the acoustic axis at the distances z_0 = 136, 165, and 214 mm from the transducer.

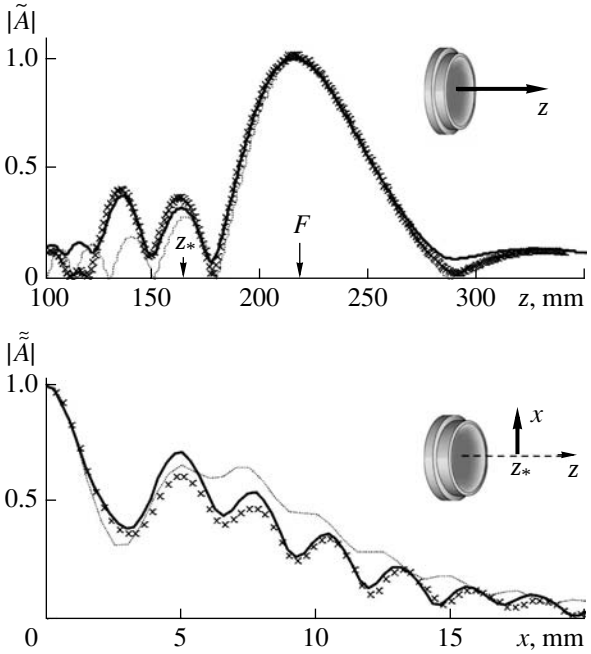

Fig. 7. Measured and calculated acoustic pressure. The upper panel shows the normalized pressure amplitude $|\tilde{A}| = |A|/A_F$ along the transducer axis. The lower panel shows the normalized pressure amplitude $|\tilde{\tilde{A}}| = |A|/A_*$ versus x coordinate for $z = z_* = 165$ mm. Here, $A_F = A(z = F)$ and $A_* = A(z = z_*)$ are the acoustic pressure amplitudes at the focus and on the axis of the transducer at $z = z_*$, respectively. The measured values are indicated by oblique crosses. The solid lines are calculated using the normal particle velocity distribution over the transducer surface that was reconstructed from the pressure measurements at z_0 = 214 mm. The dotted line represents the calculations for a piston transducer.

tally can serve as an implicit validity test for the curves in Fig. 5. To this end, we performed additional measurements of the wave amplitude. The upper panel in Fig. 7 shows the acoustic pressure distribution measured along the transducer axis, and the lower panel, the pressure distribution measured along the normal to the axis at the distance z_0 = 165 mm from the transducer. The thick solid lines are calculated from the reconstructed particle velocity, and the oblique crosses show the experimental results. Note that these calculations used the distribution reconstructed from the pressure measured at a different distance (z_0 = 214 mm) from the transducer. For the sake of comparison, the dotted lines show the pressure reconstructed from the uniform distribution of the normal particle velocity over the transducer. One can see that the calculation based on the reconstructed velocity distribution describes the true field structure much better. Minor differences between the calculations and the experiment can be attributed to the violation of the axial symmetry of the field generated by the transducer (Fig. 4). As was noted above, this effect was ignored in our calculations.

The proposed method of reconstructing the velocity field was also applied to other transducers. The results were similar, which allows us to conclude that the method can be used to reconstruct the normal particle velocity on the surfaces of different transducers.

ACKNOWLEDGMENTS

This work was supported by the Russian Foundation for Basic Research (project nos. 02-02-16999 and 02-02-17029), by the CRDF (grant no. RP2-2384-MO-02), and by the NIH-Fogarty (grant no. R03-TW006150-01).

REFERENCES

1. A. D. Pierce, *Acoustics* (Acoust. Soc. Am., Woodbury, NY, 1989).
2. D. Cathignol, O. A. Sapozhnikov, and J. Zhang, J. Acoust. Soc. Am. **101**, 1286 (1997).
3. D. Cathignol, O. A. Sapozhnikov, and Y. Theillere, J. Acoust. Soc. Am. **105**, 2612 (1999).
4. M. Fink, Phys. Today **50**, 34 (1997).
5. X. Fan, E. G. Moros, and W. L. Straube, J. Acoust. Soc. Am. **102**, 2734 (1997).
6. E. G. Williams and J. D. Maynard, Phys. Rev. Lett. **45**, 554 (1980).
7. E. G. Williams, J. D. Maynard, and E. Skudrzyk, J. Acoust. Soc. Am. **68**, 340 (1980).
8. E. G. Williams, *Fourier Acoustics: Sound Radiation and NAH* (Academic, London, 1999).
9. P. R. Stepanishen and K. C. Benjamin, J. Acoust. Soc. Am. **71**, 803 (1982).
10. M. E. Schafer and P. A. Lewin, J. Acoust. Soc. Am. **85**, 2202 (1989).
11. G. T. Clement and K. Hyhynen, J. Acoust. Soc. Am. **108**, 441 (2000).
12. E. L. Shenderov, *Emission and Scattering of Sound* (Sudostroenie, Leningrad, 1989).
13. D. Cathignol and O. A. Sapozhnikov, Akust. Zh. **45**, 816 (1999) [Acoust. Phys. **45**, 735 (1999)].

Translated by A. Khzmalyan

Acoustical Physics, Vol. 49, No. 3, 2003, pp. 361–362. Translated from Akusticheskiĭ Zhurnal, Vol. 49, No. 3, 2003, pp. 425–426.

SHORT COMMUNICATIONS

Sound Propagation in a Medium Containing Particles with Biased Centers of Mass

I. N. Didenkulov, A. B. Ezerskiĭ, and D. A. Selivanovskiĭ

Institute of Applied Physics, Russian Academy of Sciences,
ul. Ul'yanova 46, Nizhni Novgorod, 603950 Russia
e-mail: din@hydro.appl.sci-nnov.ru

Received November 19, 2002

The problem on the oscillation of a small (less than the sound wavelength in size) foreign particle in a medium in which an acoustic wave propagates has been known since Rayleigh [1]. Usually, when the interaction of an acoustic field with particles suspended in a liquid is considered, only monopole and dipole oscillations are taken into account [2, 3]. As we know, dipole oscillations of particles occur along the direction of propagation of the acoustic wave. However, in certain situations, the center of mass of a particle may not coincide with the point of application of the buoyancy force. In this case, the particle in an acoustic field experiences a turning moment alternating with the sound wave frequency. Evidently, the angular oscillations of the particle will be accompanied by a viscous friction in the liquid and by the corresponding acoustic energy loss.

One might expect that this mechanism of the interaction between the acoustic field and the solid particles suspended in liquid is widespread, because the coincidence of the center of mass and the point of application of the buoyancy force is hardly probable in the general case. The angular oscillations of a particle are noticeable when the density is distributed nonuniformly inside it. This situation may take place when the particle is formed by several particles of different density that are stuck together. This may be, in particular, the materials subjected to any kind of ultrasonic machining or biological objects in the ocean, such as phyto- and zooplankton. We are not aware of any publications concerned with studying this effect in acoustics. In this paper, we describe the solution of the problem on the angular oscillations of a spherical particle with a biased center of mass in an acoustic field and we derive the relationship and present the estimates of the additional sound attenuation in an suspension of such particles.

Figure 1 schematically represents the model under consideration. A spherical particle with a point mass at its periphery is in the field of a plane acoustic wave. The point mass may be either positive or negative. The latter case corresponds to a spherical particle with a small gas bubble stuck to it. The orientation of the particle in terms of the angle α between the radius vector that is directed from the center of the particle to the point mass and the direction of incidence of the acoustic wave is assumed to be random. We also assume that the condition of neutral buoyancy is satisfied, i.e., the mean density of the particle is equal to the density of the surrounding liquid, and the point mass Δm is much smaller than the total mass m of the particle: $|\Delta m| \ll m$.

Under these assumptions, the equation of rotational oscillatory motion of such a particle under the action of the acoustic field has the form

$$J\ddot{\alpha} = M_{in} + M_{fr},$$

where

$$M_{fr} = -\frac{8}{3}\nu\rho R^3\dot{\alpha}\frac{3 + 6b + 6b^2 + 2b^3 - 2ib^2(1 + b)}{1 + 2b + 2b^2}, \quad (1)$$

$$M_{in} = -i\frac{k(-\Delta m)R\sin\alpha p(t)}{\rho}, \quad b = \frac{R}{\delta(\omega)}.$$

Here, M_{in} is the moment of inertial forces that acts on a spherical particle of mass m and moment of inertia $J = (2/5)mR^3$ in the acoustic field because of the presence of a point mass (Δm) at its periphery, $p(t)$ is the pressure amplitude of the sound wave, k is the wave number, ρ is the density of the liquid, $\delta(\omega) = \sqrt{2\nu/\omega}$ is the thickness of the oscillating boundary layer (OBL), ν is the kinematic viscosity of the liquid, and M_{fr} is the moment of the viscous friction forces in the rotational oscillations of the sphere [3].

Solving Eq. (1) for a harmonic field of frequency ω, we obtain the expression for the viscous power loss in

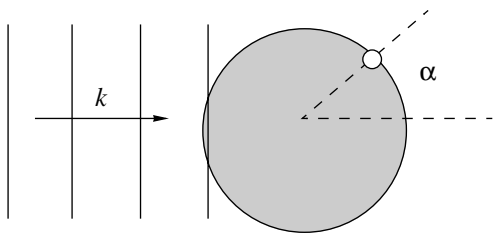

Fig. 1. Schematic representation of the problem.

1063-7710/03/4903-0361$24.00

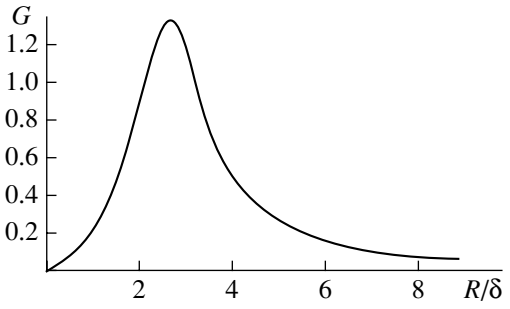

Fig. 2. Parameter G as a function of the ratio of the particle radius to the thickness of the viscous boundary layer.

rotational oscillations of the particle in the acoustic field:

$$W = -\frac{\omega\rho^2\sin^2\alpha}{2\rho C^2}V\left(\frac{\Delta\rho}{\rho}\right)^2 b^2\frac{\gamma}{\gamma^2+\chi^2}, \qquad (2)$$

where

$$\gamma = \frac{3+6b+6b^2+2b^3}{1+2b+2b^2}, \quad \chi = 2b^2\frac{4+3b-2b^2}{1+2b+2b^2},$$

$V = (4/3)\pi R^3$ is the particle volume, $\Delta\rho$ is the excess of density of the particle material over its mean density, and C is the speed of sound.

We consider now the additional attenuation of sound in a medium containing a great number of such particles. If the concentration of particles in the medium is n, the total power loss is related to the plane wave field intensity I and the sound attenuation coefficient by the formula

$$Wn = -\varepsilon I = -\varepsilon p^2/2\rho C.$$

Assuming that the orientations of the particles are uniformly distributed in all directions, we derive the expression for the loss factor

$$\varepsilon = \frac{\omega}{2C}nV\left(\frac{\Delta\rho}{\rho}\right)^2 G(R,\omega), \qquad (3)$$

where

$$G(R,\omega) = b^2\frac{\gamma}{\gamma^2+\chi^2}.$$

The parameter $G(R, \omega)$ describes the efficiency of the development of such rotational motions of particles in the acoustic field of frequency ω. The dependence of the parameter G on the dimensionless ratio $R/\delta(\omega)$ is shown in Fig. 2. This dependence exhibits a maximum at $R/\delta = 2.5$.

Thus, in this paper we proposed a mechanism of rotational oscillatory motion of solid particles that have biased centers of mass and are suspended in liquid in an acoustic field. A simple model of these particles in the form of spheres with added point masses is considered. For this model, the additional attenuation of the sound wave through the viscous loss in the angular oscillations of particles is calculated.

Let us estimate the possible magnitude of this effect. For a suspension of particles in water with the parameters $R = 25$ μm, $nV = 0.01$, $\Delta\rho/\rho = 0.15$, and $\nu = 10^{-6}$ m^2/s, the sound attenuation due to the mechanism under discussion is estimated as $\varepsilon \approx 6$ dB/km at a frequency of 2.8 kHz and $\varepsilon \approx 10$ dB/km at a frequency of 8 kHz. A further study of this effect may be useful for interpreting the experimental data on the sound propagation in various suspensions.

ACKNOWLEDGMENTS

This work was supported by the Russian Foundation for Basic Research, project nos. 01-02-17653, 01-02-16938, and 00-15-96741.

REFERENCES

1. Lord Rayleigh, *Theory of Sound* (Dover, New York, 1945; GITTL, Moscow, 1955), Vols. 1, 2.
2. M. A. Isakovich, *General Acoustics* (Nauka, Moscow, 1973).
3. L. D. Landau and E. M. Lifshitz, *Course of Theoretical Physics*, Vol. 6: *Fluid Mechanics*, 4th ed. (Nauka, Moscow, 1988; Pergamon, New York, 1987).

Translated by A. Svechnikov

Acoustical Physics, Vol. 49, No. 3, 2003, pp. 363–364. Translated from Akusticheskiĭ Zhurnal, Vol. 49, No. 3, 2003, pp. 427–428.

SHORT COMMUNICATIONS

Resonance Wave Absorbers in Narrow Tubes and Rods

A. D. Lapin

Andreev Acoustics Institute, Russian Academy of Sciences, ul. Shvernika 4, Moscow, 117036 Russia
e-mail: mironov@akin.ru

Received March 28, 2002

The lossless Helmholtz resonator is known to be an efficient sound reflector in an infinite narrow tube [1–3]. At the resonance frequency, the incident sound wave is totally reflected from the resonator, and no traveling wave occurs behind the resonator. Before the resonator, the total sound field is equal to the sum of the incident wave and the reflected wave and has the form of a standing wave. Assume that we insert the second, dissipative Helmholtz resonator, whose resonance frequency coincides with that of the first (lossless) resonator, at an antinode of this standing wave. One can expect that, at a certain dissipation in the second resonator, the latter will efficiently absorb the sound [1], and, in the region before this (second) resonator, the reflected traveling wave will disappear. Below, it is shown that, combining a lossless resonator with a certain dissipative resonator (its friction resistance is equal to the radiation resistance), one can totally absorb the sound at the resonance frequency in an infinite narrow tube. Note that a single resonator with optimal friction absorbs at most half of the incident wave energy. The acoustic coupling of two closely positioned Helmholtz resonators in free space was investigated in [4].

In a narrow (in comparison with the wavelength) tube, the pressure and the particle velocity depend only on the x coordinate measured along the tube axis. Let two Helmholtz resonators be connected to the tube at the points $x = x_1 > 0$ and $x = x_2 < x_1$ and let a harmonic sound wave with the pressure $p_0(x) = \exp(ikx)$, where k is the wave number and the temporal factor $\exp(-i\omega t)$ is omitted, be incident on the resonators from the left. The incident wave excites the resonators, and they generate the fields

$$\begin{aligned} p_1(x) &= \frac{\rho c V_1}{2S}\exp(ik|x - x_1|), \\ p_2(x) &= \frac{\rho c V_2}{2S}\exp(ik|x - x_2|), \end{aligned} \tag{1}$$

where V_1 and V_2 are the volume velocities of the first and second resonators, respectively; ρ is the density of the medium in the tube; c is the sound velocity in this medium; and S is the area of the tube cross section. The total filed in the tube is $p = p_0 + p_1 + p_2$. We desire to find the resonators' parameters that ensure the total absorption of the incident wave:

$$p(x > x_1) = 0, \quad p(x < x_2) = \exp(ikx).$$

We obtain the volume velocities V_1 and V_2 from the equations of motion of the resonators:

$$\begin{aligned} &m_1\ddot{\xi}_1 + r_1\dot{\xi}_1 + \kappa_1\xi_1 \\ &= -\sigma_1[p_0(x_1) + p_1(x_1) + p_2(x_1)]\exp(-i\omega t), \end{aligned} \tag{2}$$

$$\begin{aligned} &m_2\ddot{\xi}_2 + r_2\dot{\xi}_2 + \kappa_2\xi_2 \\ &= -\sigma_2[p_0(x_2) + p_1(x_2) + p_2(x_2)]\exp(-i\omega t), \end{aligned} \tag{3}$$

where $\xi(t)$, m, r, κ, and σ are the displacement, the mass, the friction resistance, the elasticity coefficient, and the cross-sectional area of the resonator throat, respectively, and the indices 1 and 2 indicate the number of the resonator characterized by the corresponding quantity.

The volume velocities V_1 and V_2 are equal to $\sigma_1 v_1$ and $\sigma_2 v_2$, respectively, where $v_1 = \dot{\xi}_1(t)\exp(i\omega t)$ and $v_2 = \dot{\xi}_2(t)\exp(i\omega t)$ are the complex amplitudes of the particle velocities. We transform Eqs. (2) and (3) to the form

$$(Z_{10} + Z_{11})v_1 + Z_{21}v_2 = -\sigma_1\exp(ikx_1), \tag{4}$$

$$Z_{12}v_1 + (Z_{20} + Z_{22})v_2 = -\sigma_2\exp(ikx_2), \tag{5}$$

where

$$\begin{aligned} Z_{10} &= r_1 + i(\kappa_1/\omega - \omega m_1), \\ Z_{20} &= r_2 + i(\kappa_2/\omega - \omega m_2), \\ Z_{11} &= \frac{\sigma_1 p_1(x_1)}{v_1} = \frac{\rho c\sigma_1^2}{2S}, \\ Z_{22} &= \frac{\sigma_2 p_2(x_2)}{v_2} = \frac{\rho c\sigma_2^2}{2S}, \\ Z_{12} &= \frac{\sigma_2 p_1(x_2)}{v_1} = Z_{21} \\ &= \frac{\sigma_1 p_2(x_1)}{v_2} = \rho c\frac{\sigma_1\sigma_2}{2S}\exp[ik(x_1 - x_2)]. \end{aligned}$$

1063-7710/03/4903-0363$24.00

Determining the complex amplitudes of the velocities $v_1 = V_1/\sigma_1$ and $v_2 = V_2/\sigma_2$ from Eqs. (4) and (5) and substituting them into Eqs. (1), we obtain the scattered fields p_1 and p_2. The total field in the tube is

$$p(x) = \exp(ikx) - \frac{\rho c\sigma_1}{2S\Delta}[(Z_{20} + Z_{22})\sigma_1 \exp(ikx_1) - Z_{21}\sigma_2 \exp(ikx_2)]\exp(ik|x - x_1|)$$

$$- \frac{\rho c\sigma_2}{2S\Delta}[(Z_{10} + Z_{11})\sigma_2 \exp(ikx_2) - Z_{12}\sigma_1 \exp(ikx_1)]\exp(ik|x - x_2|),$$

where

$$\Delta = (Z_{10} + Z_{11})(Z_{20} + Z_{22}) - Z_{12}Z_{21}.$$

We use this general formula to obtain the fields behind the resonators (for $x > x_1$) and before the resonators (for $x < x_2$):

$$p(x > x_1) = \frac{Z_{10}Z_{20}}{\Delta}\exp(ikx),$$

$$p(x < x_2) = \exp(ikx) - \frac{1}{\Delta}\{Z_{22}(Z_{10} + Z_{11}) + Z_{11}(Z_{20} - Z_{22})\exp[i2k(x_1 - x_2)]\}\exp[-ik(x - 2x_2)].$$

In the two latter formulas, we set

$$\mathrm{Im}Z_{10} = \mathrm{Im}Z_{20} = 0,$$

$$r_1 = 0, \quad k(x_1 - x_2) = (2n + 1)\pi/2,$$

where n is an arbitrary integer. Such settings mean that both resonators are characterized by identical resonance frequencies, the first resonator is lossless, and the resonators are spaced by an odd number of quarter-wavelength. With these parameters, we obtain

$$p(x > x_1) = 0,$$

$$p(x < x_2) = \exp(ikx) + \frac{Z_{11}}{\Delta}(r_2 - 2Z_{22})\exp[-ik(x - 2x_2)].$$

For $r_2 = 2Z_{22} = \rho c\sigma_2^2/S$ (the second resonator is characterized by the friction resistance coincident with the radiation resistance), the reflected wave disappears before the resonators. This means that the resonators totally absorb the incident wave at the frequency equal to the resonance frequency of the resonators. We note that a total absorption is impossible when $r_1 \neq 0$. For $r_1 \ll Z_{11}$, the amplitudes of the transmitted and reflected waves are approximately equal to $r_1/2Z_{11}$ and $r_1/4Z_{11}$, respectively.

One can construct a similar resonance absorber for flexural waves in a thin infinite rod. The simplest resonator is a spring loaded with a weight [5, 6]. Being located perpendicularly to the rod and attached to the rod by the spring, such a resonator strongly dissipates flexural waves. At the resonance frequency, the incident flexural wave is totally reflected from the lossless resonator. The total field before the resonator has the form of a standing wave. Assume that we insert the dissipative resonator, whose resonance frequency coincides with that of the first resonator, at a displacement antinode of this standing wave. At a certain value of the dissipation coefficient, the reflected wave disappears before the resonators, and no traveling wave is present behind the resonators. Calculations show that the total absorption of the incident flexural wave occurs when the following relationships take place:

$$\mathrm{Im}(Y_1 + Y) = \mathrm{Im}(Y_2 + Y) = 0,$$

$$\mathrm{Re}Y_1 = 0, \quad \mathrm{Re}Y_2 = 2\mathrm{Re}Y,$$

where Y is the compliance of the infinite road under a point force, Y_1 and Y_2 are the compliances of the first and second resonators, and the spacing between the resonators must measure an odd number of quarter-wavelengths.

Note that the absorption of flexural waves by dissipative resonators was experimentally investigated in [7, 8].

REFERENCES

1. M. A. Isakovich, *General Acoustics* (Nauka, Moscow, 1973).
2. S. N. Rzhevkin, *Lectures on the Theory of Sound* (Mosk. Gos. Univ., Moscow, 1960).
3. P. Morse and U. Ingard, *Theoretical Acoustics* (McGraw-Hill, New York, 1968).
4. T. Johansson and M. Kleiner, J. Acoust. Soc. Am. **110**, 1315 (2001).
5. M. A. Isakovich, V. I. Kashina, and V. V. Tyutekin, USSR Inventor's Certificate No. 440,509, Byull. Izobret., No. 31 (1974).
6. M. A. Isakovich, V. I. Kashina, and V. V. Tyutekin, Akust. Zh. **23**, 384 (1977) [Sov. Phys. Acoust. **23**, 214 (1977)].
7. I. I. Klyukin, Akust. Zh. **6**, 213 (1960) [Sov. Phys. Acoust. **6**, 209 (1960)].
8. V. V. Tyutekin and A. P. Shkvarnikov, Akust. Zh. **18**, 441 (1972) [Sov. Phys. Acoust. **18**, 369 (1972)].

Translated by A. Vinogradov

Acoustical Physics, Vol. 49, No. 3, 2003, pp. 365–366. Translated from Akusticheskiĭ Zhurnal, Vol. 49, No. 3, 2003, pp. 429–430.

CHRONICLE

Irina Borisovna Andreeva (January 20, 1918–December 5, 2002)

On December 5, 2002, Irina Borisovna Andreeva—one of the founders of Soviet and Russian ocean acoustics, Doctor of Science (Phys.–Math.), Leading Researcher of the Andreev Acoustics Institute, and a winner of the USSR State Award—passed away.

Andreeva was born and educated in St. Petersburg. In 1939, she graduated from the Polytechnical Institute and started working as an engineer. In 1940, she moved to Moscow and began her career in science at the Institute of Theoretical Geophysics of the Academy of Sciences of the USSR. During World War II, Andreeva worked at one of the design offices, where she continued her research in radio engineering. Her outstanding scientific and organizational abilities allowed her to progress from engineer to head of a laboratory within the period from 1943 to 1956. The results of her studies performed during the war and postwar years served as a basis for her candidate dissertation. In 1953, Andreeva got her candidate of science degree in engineering.

In 1956, already being recognized as an excellent specialist in her area of research, Andreeva started working at the Acoustics Institute, which remained her main place of work to the last day of her life. She organized a sector (a special research group) for investigating the sound scattering by oceanic inhomogeneities of different origins. Andreeva headed this sector for more than 30 years. During this period, she displayed her talent for both experimental studies and organization of research. She took active part in the design of the unique research vessels *Sergeĭ Vavilov* and *Petr Lebedev* and then participated in many expeditions on board these ships. The experimental data obtained by Andreeva herself and by other researchers under her supervision formed the basis of her doctoral dissertation. In 1971, she received the degree of doctor of science in physics and mathematics. Owing to these studies, Andreeva gained world-wide recognition as a prominent specialist in sound scattering from biological objects and

1063-7710/03/4903-0365$24.00

deep scattering layers in the ocean. To this day, every scientific publication concerned with this subject contains references to her pioneering works. However, the scope of Andreeva's scientific interests was not restricted to this area of research. She was also widely known as the author of fundamental publications on sound scattering from the ocean surface and on long-range reverberation. Andreeva's list of publications contains several hundred scientific papers and reports and three monographs. One of the monographs, *Ocean Acoustics*, earned her the USSR State Award in 1976.

Andreeva was deeply involved in pedagogical activities. She supervised many graduate and postgraduate projects carried out by the students and postgraduates of Moscow State University; Moscow Institute of Radio Engineering, Electronics, and Automation; and Moscow Institute of Physics and Technology. Today, many of her former students are excellent scientists—candidates and doctors of science. The scientific-organizational activities of Andreeva are well known. She has chaired the organizing committees of different symposia, seminars, and conferences on ocean acoustics. She has also been the scientific editor of a number of books and collections of papers.

For her services rendered to the progress of science, Andreeva received several state awards.

In the last few years, Andreeva continued her active work in science. She supervised the projects supported by the Russian Foundation for Basic Research and aimed at the development of a unique database generalizing the results of the long-term studies of deep scattering layers in the ocean. Unfortunately, Andreeva had not enough time to complete this important work.

The shining memory of Irina Borisovna Andreeva will forever remain in the hearts of her numerous students, colleagues, friends, and all those who knew her.

Translated by E. Golyamina

Acoustical Physics, Vol. 49, No. 3, 2003, pp. 367–368. Translated from Akusticheskiĭ Zhurnal, Vol. 49, No. 3, 2003, pp. 431–432.

CHRONICLE

Mikhail Kuz'mich Rumyantsev (On His 80th Birthday)

Mikhail Kuz'mich Rumyantsev—Distinguished Professor of Moscow State University, a well-known Russian linguist, and the founder of the oriental school of experimental phonetics—is now 80 years old.

Rumyantsev was born on November 17, 1922, near the city of Gzhatsk (Smolensk region) to a peasant family. Before World War II, Rumyantsev took a great interest in theatrical art and studied for more than two years at a dramatic studio that followed the ideas of Meierhol'd. With the outbreak of war on Russian territory, Rumyantsev became a soldier of the Soviet Army. After completing a short course at an antitank artillery college, he took part in military operations and moved with the Soviet Army from Ukraine to Prague, first, as the commander of a gunnery platoon and, then, as the commander of an artillery battery. The evidence of this period of Rumyantsev's life are many orders, medals, and wounds.

After the war, Rumyantsev was demobilized from the Soviet Army and started studying at the Chinese Division of the Moscow Institute of Oriental Studies, where, under the guidance of Professor N.N. Dragunov, his research interests in the field of phonetics of oriental languages were formed. In 1962, Rumyantsev organized the Laboratory of Experimental Phonetics (LEP) at the Institute of Asian and African States of Moscow State University. The laboratory was intended for studying vocal speech of oriental languages on the basis of the experience gained by Rumyantsev from the work at the Laboratory of Experimental Phonetics and Speech Psychology of the Moscow State Pedagogical Institute of Foreign Languages, which was headed by professor V.A. Artemov.

The foundation and formation of the LEP became the main goal of Rumyantsev's activities for almost 40 years. For a long time, the laboratory was probably

1063-7710/03/4903-0367$24.00 © 2003 MAIK "Nauka/Interperiodica"

the only place in the Soviet Union where phonetic–phonological problems of linguistics were studied using acoustic methods. These methods helped to reveal the mechanism of a linguistic phenomenon of vocal speech. The LEP met the requirements of that time and realized Rumyantsev's ideas about the role of the major research center for experimental phonetics of Oriental and African languages. Postgraduates and lecturers from many linguistic departments of the institute, as well as foreign postgraduates, worked and successfully completed their candidate theses at this laboratory. During his work at the Institute of Oriental Languages and, starting from 1956, at the Institute of Asian and African States of Moscow State University, Rumyantsev educated many disciples working now at universities and institutes of the Academies of Sciences of Russia and other CIS countries. During these years, Rumyantsev developed and delivered the most important linguistic theoretical courses on phonetics, phonology, and grammar of the Chinese language. He also worked hard on his doctoral thesis. In 1972, Rumyantsev's book *Tone and Intonation in the Chinese Language* was published. Many generations of experts in phonetics and philology, who majored in the field of speech prosody, were trained using the materials and ideas of this book. It is necessary to note that numerous experiments conducted at the LEP were performed using the electroacoustic equipment specially developed there.

In the mid-1970s, in addition to the research in the acoustic analysis of sounds, studies of the synthesis of vocal speech were begun at the laboratory. Special attention was given to the simulation of prosodic units. Syllables, syllable tones, word rhythmics, and communicative, modal, and stylistic intonations were simulated using the Chinese, Hindi, Persian, Singhalese, Russian, and Yoruba languages. Rumyantsev's astounding intuition in research manifested itself in this change from analysis to synthesis. He was one of the first researchers who could see the potentialities of this method for the theoretical comprehension of many phonetic and phonological processes, as well as for the practical applications, e.g., in designing a human–machine dialog system. Rumyantsev has set a global task for the researchers working at his laboratory: to develop acoustic alphabets for tonal (isolating) languages of the Far East, South-Eastern Asia, and Western Africa. He generalized the tremendous amount of data obtained as the result of experiments and research conducted in the laboratory in the book *Computer Simulation of Speech Units (By the Example of the Chinese Language)*, which was published in 1990.

The scientific works by Rumyantsev are widely used in Russian and foreign linguistics. They deal with the hottest problems of the modern science of language. Rumyantsev's 80th birthday coincides with the 40th anniversary of the Laboratory of Experimental Phonetics founded by him at the Institute of Asian and African States of Moscow State University. Rumyantsev continues heading this laboratory to this day.

Colleagues and numerous disciples of Mikhail Kuz'mich Rumyantsev wish him further success in his creative scientific and pedagogical activities.

Translated by M. Lyamshev